Single-impulse magnetic focusing of launched cold atoms

Smith, David Alexander

Single-Impulse Magnetic Focusing of Launched Cold Atoms

David Alexander Smith

A thesis submitted in partial fulfilment
of the requirements for the degree of
Doctor of Philosophy

Department of Physics
Durham University
UK
September 2005

Single-Impulse Magnetic Focusing of Launched Cold Atoms

David Alexander Smith

Submitted for the degree of Doctor of Philosophy, University of Durham, September 2005

Abstract

This thesis concerns the use of pulsed magnetic lenses with cold atoms. Specifically, an experiment was designed and built to focus a launched cloud of cold rubidium atoms. An atomic fountain was realised, based on launching a compact cold cloud of atoms using the technique of moving molasses.

Analytical and numerical simulations were conducted to formulate the optimum strategies for focusing. Focusing aberrations are investigated and characterised, and techniques for minimising their deleterious effects are presented.

A Baseball Lens was constructed to enable the experimental 3-dimensional focusing of launched cold atoms with a single magnetic impulse.

Typically 7×10^{7} ^{85}Rb atoms were loaded into a magneto-optical trap (MOT), before undergoing an optical molasses stage. Subsequently a moving molasses phase was realised to launch the atoms vertically at a speed of approximately 2 m s^{-1} to bring them to an apex 20.5 cm above the MOT in a remote vacuum chamber. During their flight the atoms were pumped into the weak-field-seeking $5^{2}S_{1/2}\left|F=3,m_{F}=3\right\rangle$ state. The centre of the Baseball Lens was located 16.5 ± 0.2 cm above the MOT. Fluorescence images were taken at the apex of flight to characterise the width of the focussed cloud.

Results were obtained for four different configurations of the Baseball Lens, which varied the relationship between the axial and radial angular frequencies of the lens. Compact focussed clouds were seen for all four configurations with a minimum observed volume of 60 ± 3 mm^{3}, which is a factor of 17 smaller than the unfocussed cloud.

3-dimensional magnetic focusing of cold atoms with a single magnetic impulse has been observed for the first time.

Declaration

I declare that no part of the material presented has been previously submitted by myself for a degree in this or any other university.

David Alexander Smith
November 2005

Acknowledgements

First and foremost, I wish to thank my supervisor Ifan Hughes. His enthusiasm for the research and teaching of physics has had a great effect upon me. I particularly wish to thank him for his understanding of problems both inside and outside of physics when times were tough.

I owe a debt to Charles Adams, for not only introducing me to the field of laser cooling, but also for his acute and valuable advice. Simon MacLeod's vacuum expertise was extremely valuable during the construction of the vacuum chamber, along with his tales of rabbit shooting. I also wish to thank Simon Cornish, particularly for his coil winding techniques and technical knowledge. I am grateful to Aidan Arnold for his theoretical work.

Nick and Griff, thanks for all the good times, and for cable-tying me to the canopy in the laboratory and taking pictures. Graham, cheers for sharing a lab with me, playing your 'dad' music and telling your 'dad' jokes. Matt, thanks for writing numerical simulation codes and for being a valued friend. Kev, good luck with the bambino! Thanks to the rest of the Durham AtMol group, past and present, for being a good bunch.

I wish to thank the technical and secretarial staff in the physics department, particularly John Scott for his help and perseverance with the current-pulse circuit problems.

Thanks to all my other friends and family for their help and support.

And, of course, S.

Contents

Abstract

Acknowledgements

Contents

List of Figures

1 Introduction.....1-1

1.1 General Introduction.....1-2

1.2 The Application of Pulsed Magnetic Lenses.....1-2

1.3 Pulsed Magnetic Fields and Cold Neutral Atoms.....1-3

1.4 The Aims of this Project.....1-7

1.5 Thesis Outline.....1-7

2 Experimental Theory and Set-up.....2-1

2.1 Laser Cooling and Trapping.....2-2

2.1.1 Experimental Overview.....2-2

2.1.2 Rubidium-85.....2-2

2.1.3 Doppler Cooling Theory in 1D.....2-3

2.1.4 Magneto-optical Trap Theory in 1D.....2-4

2.1.5 Magneto-optical Trap in the Laboratory.....2-8

2.1.6 The Lasers.....2-8

2.1.7 Optical Layout and Components.....2-16

2.1.8 RF Electronics and Acousto-optic Modulators.....2-19

2.1.9 The Vacuum System.....2-23

2.1.10 Cancellation of Unwanted Magnetic Fields.....2-31

2.1.11 Laser Beams in the Vacuum Chamber.....2-33

2.1.12 Magnetic Field for the Magneto-optical Trap.....2-34

2.1.13 Magneto-optical Trap Characterisation.....2-36

2.1.14 Computer Control of the Experiment.....2-43

2.1.15 Imaging in the MOT Chamber.....2-45

2.1.16 Making Temperature Measurements.....2-47

2.1.17 Sub-Doppler Cooling.....2-48

2.2 Launching Cold Atoms.....2-51

2.2.1 Moving Molasses Theory.....2-51

2.2.2 Evolution of a Launched Cloud.....2-53

2.2.3 Moving Molasses and Imaging at the Apex of Flight: 15mm ($1/e^2$) radius Laser Beams.....2-55

2.2.4 Improved Moving Molasses and Imaging at the Apex of Flight: 10mm ($1/e^2$) radius Laser Beams.....2-59

3 Theoretical Single-impulse Magnetic Focusing.....3-1

3.1 Basic Pulsed Magnetic Lens Theory and Matrix Representation.....3-2

3.2 Current Carrying Coils for the Formation of Pulsed Magnetic Lenses.....3-5

3.2 Definition of Departure from Harmonicity.....3-15

4 Numerical Simulations of Single-impulse Magnetic Spatial Focusing.....4-1

4.1 Numerical Simulations.....4-2

4.2 Matrices: A Good Starting Point.....4-3

4.3 What about Real Magnetic Fields?.....4-6

4.4 Axial (1-dimensional) and Radial (2-dimensional) Focusing.....4-7

4.5 3-Dimensional Focusing.....4-10

4.6 Conclusions and Choice of Lens for Experimentation.....4-12

5 The Baseball Lens: Design and Testing.....5-1

5.1 Current Pulse Test Circuit.....5-2

5.2 The Supply of the Gate-Emitter Voltage to IGBTs for Large Current Pulses.....5-6

5.3 Baseball Lens Construction.....5-8

5.4 Baseball Lens Characterisation.....5-13

5.5 Baseball Lens Operation and Conditions for an Isotropic Lens.....5-20

6 Experimental Spatial Focusing of a Launched Cold Atom Cloud.....6-1

6.1 Preliminary Results using the Baseball Coil Only.....6-2

6.2 Change of Laser Beams – Improved Launching.....6-12

6.3 Determination of the Initial Cloud Widths.....6-12

6.4 Results from the four configurations of the Baseball Lens.....6-14

6.5 $\mathfrak{ABCD}$-Matrix Analysis.....6-29

6.6 Numerical Simulations for Analysis.....6-36

7 Conclusions.....7-1

List of Figures

Figure 2.1. Relevant Energy Level Diagram for Laser Cooling of ^{85}Rb on the D_2-line.

Figure 2.2. Diagram of the simplest transition on which the magneto-optical trap can operate.

Figure 2.3. The Repumping Laser.

Figure 2.4. The Trap Laser.

Figure 2.5. Schematic of polarisation spectroscopy.

Figure 2.6. Polarisation spectroscopy signal (trap).

Figure 2.7. A polarisation spectroscopy signal (repump).

Figure 2.8. Laser Locking Circuit.

Figure 2.9. Optical Bench Plan View.

Figure 2.10. Optical Set-up for AOMs in a 'double-pass' arrangement.

Figure 2.11. Schematic of the RF Electronics used to supply the acousto-optic crystals.

Figure 2.12. Graph of frequency output of Minicircuits ZOS-100 VCO against Coarse voltage output from the National Instruments PCI-6713 Analogue Card.

Figure 2.13 Graph of frequency stability over time for the ZOS-100 VCOs supplying the two Trap AOMs that are used for the moving molasses stage.

Figure 2.14. Vacuum System Schematic.

Figure 2.15. Photograph of the vacuum chamber.

Figure 2.16. The final cooling curve for the vacuum system

Figure 2.17. Schematic of the rubidium dispenser mounting.

Figure 2.18 Photograph of the mounting of the rubidium dispenser.

Figure 2.19. Schematic of the laser beams through the vacuum chamber.

Figure 2.20. Photograph of the MOT coils mounted on the vacuum chamber.

Figure 2.21. Collection of MOT fluorescence for atom number calculation.

Figure 2.22. MOT fill-curves for a detuning of $\Delta = -2\pi \times 11$ MHz and a magnetic field gradient of 11 G cm^{-1}.

Figure 2.23. Variation of the scattering rate with the value of saturation intensity.

Figure 2.24. A graph of atom number against magnetic field gradient.

Figure 2.25. A graph showing how fill time and atom number vary with continuous dispenser current.

Figure 2.26. A graph showing how fill time and atom number vary with negative detuning from resonance with the $5S_{1/2}\ F = 3$ to $5P_{3/2}\ F' = 4$ cooling transition.

Figure 2.27. Screen-shot of LabVIEW front panel showing an illustration of the analogue lines for output to the National Instruments PCI-6713 Analogue Card.

Figure 2.28. Screen-shot of the LabVIEW front panel showing an illustration of the digital lines for output to the National Instruments PCI-DIO-32HS Digital Input/Output card.

Figure 2.29. Plot of the square of the cloud standard deviation against the square of the expansion time

Figure 2.30. Diagram of the laser beam set-up for moving molasses.

Figure 2.31. Graph of linear detuning δ for moving molasses against launch height h.

Figure 2.32. Evolution of the standard deviation of clouds (of initial standard deviation 1 mm) launched to an apex of 20.5 cm above its initial position.
Figure 2.33. Evolution of the standard deviation of clouds (of initial standard deviation 1 mm) launched to an apex of 20.5 cm above its initial position.
Figure 2.34. Graph of both the launch speed u, and the time taken to reach the apex of flight t_{apex}, against the launch height h.

Figure 2.35. Intensity Chart from the LabVIEW front panel showing a sequence of images (separated by 1 ms) of a cloud in the process of launching.

Figure 2.36. Typical 'binned' vertical (top) and horizontal (bottom) line profiles of a single image taken of the upper chamber with no atoms present.

Figure 2.37. Typical 'binned' vertical (top) and horizontal (bottom) line profiles of a single image taken 202 ms after launch, in the upper chamber with no atoms present.

Figure 2.38. Visual representation of the parameters R (the ramp time) and C (the moving molasses constant time).

Figure 2.39. Columns of images showing the launch of 10^7 ^{85}Rb atoms.

Figure 2.40. (a) Typical single-shot image of a launched cloud in the quartz cell.

Figure 2.41 (a) Typical single-shot image of the quartz cell with no atoms.

Figure 2.42. (a) Single-shot image of a launched cloud in the quartz cell.

Figure 3.1. Schematics of Strategies I-VI.

Figure 3.2. The relevant magnetic field information corresponding to Strategies I-VI.

Figure 3.3. The Departure from Harmonicity $\epsilon[R,Z]$.

Figure 4.1. Island plots.

Figure 4.2. Simulation of 500 atoms going through a 10 000 Amp-turn strategy I lens.

Figure 4.3. The radial expansion factor, at $T = 212$ ms, for radially converging lenses is plotted against λ.

Figure 4.4. A simulation of 500 atoms sent through an isotropic baseball coil lens (strategy VI).

Figure 5.1. Diagram of the general circuit used to form current pulses.

Figure 5.2. Current through the load of the current pulse test circuit for varying load wire diameters (1 mm, 2 mm, and 3 mm).

Figure 5.3. Current pulse from three 12V 1150 A-max. Volvo Truck batteries.

Figure 5.4. Schematic of the Baseball Coil.

Figure 5.5. Baseball Coil during construction upon the aluminium former.

Figure 5.6. Photograph of the completed Baseball Coil.

Figure 5.7. Photograph of bias coil construction.

Figure 5.8. Photograph of the completed bias coil pair in Helmholtz configuration.

Figure 5.9. Photograph of the completed Baseball Lens.

Figure 5.10. Schematic of whole Baseball Lens showing principle directions.

Figure 5.11. Graph of $B_z'(z)$ against z, where the z-direction is along the axis of the baseball coil.

Figure 5.12. (a) shows $B_x'(x)$ against x, and (b) shows $B_y'(y)$ against y for the baseball coil.

Figure 5.13. Plot of the magnitude of the axial magnetic field $B_z(z)$ against the axial direction z, over the central 2 cm of the bias coil pair.

Figure 5.14. Plot of the magnitude of the axial magnetic field $B_z(z)$ against the axial direction z, over the central 4 cm of the bias coil pair.

Figure 5.15. Circuit diagram of the electronics for the current pulse through the Baseball Lens.

Figure 5.16. Graph showing the current through the baseball coil (only).

Figure 5.17. Graph showing the current through the Lens, with a 20 ms long IGBT gate-pulse, using the circuit in Figure 5.15 with $R_{\text{TUNE}} = R_{\text{BIAS}}/2$.

Figure 5.18. Graph showing the current through the Lens, with a 20 ms long IGBT gate-pulse, using the circuit in Figure 5.15 with $R_{\text{TUNE}} = R_{\text{BIAS}}$.

Figure 5.19. Graph showing the current through the Lens, with a 20 ms long IGBT gate-pulse, using the circuit in Figure 5.15 with R_{TUNE} removed.

Figure 6.1. Image of the quartz cell on top of the vacuum chamber when no magnetic impulse acts on the atoms during their ballistic flight from the MOT chamber to the quartz cell.

Figure 6.2. Image of a focused cloud that has experienced a pulse duration of $\tau = 18$ ms, starting 104 ms after launch.

Figure 6.3. Image of a focussed cloud that has experienced a pulse duration of $\tau = 32$ ms, starting 98 ms after launch.

Figure 6.4. Image of a focused cloud that has experienced a pulse duration of $\tau = 9$ ms, starting 107 ms after launch.

Figure 6.5. Plot of the cloud standard deviation in the x-direction σ_x against pulse duration τ.

Figure 6.6. Graph of measured horizontal cloud standard deviation σ_x against image light pulse duration.

Figure 6.7. Optimisation of the orientation of the quarter-wave plate for optical pumping.

Figure 6.8. Graph of Peak Pixel Count against optical pumping pulse duration.

Figure 6.9. Image of an atom cloud at the point the launch beams are switched off.

Figure 6.10. Varying pulse duration τ for the Baseball Coil only, i.e. no bias field.

Figure 6.11. Variation of σ_x and σ_z with pulse duration τ for the baseball coil only.

Figure 6.12. Variation of cloud volume $\sigma_x^2\sigma_z$ with pulse duration τ.

Figure 6.13. Varying pulse duration τ for the Baseball Lens with $R_{\mathrm{TUNE}} = R_{\mathrm{BIAS}}/2$.

Figure 6.14. Variation of σ_x and σ_z with pulse duration τ for Baseball Lens with $R_{\mathrm{TUNE}} = R_{\mathrm{BIAS}}/2$.

Figure 6.15. Variation of cloud volume $\sigma_x^2\sigma_z$ with pulse duration τ for the Baseball Lens with $R_{\mathrm{TUNE}} = R_{\mathrm{BIAS}}/2$.

Figure 6.16. Varying pulse duration τ for the Baseball Lens with $R_{\mathrm{TUNE}} = R_{\mathrm{BIAS}}$.

Figure 6.17. Variation of σ_x and σ_z with pulse duration τ for Baseball Lens with $R_{\mathrm{TUNE}} = R_{\mathrm{BIAS}}$.

Figure 6.18. Variation of cloud volume $\sigma_x^2\sigma_z$ with pulse duration τ for the Baseball Lens with $R_{\mathrm{TUNE}} = R_{\mathrm{BIAS}}$.

Figure 6.19. Varying pulse duration τ for the Baseball Lens with R_{TUNE} removed.

Figure 6.20. Variation of σ_x and σ_z with pulse duration τ for the Baseball Lens with R_{TUNE} removed.

Figure 6.21. Variation of cloud volume $\sigma_x^2\sigma_z$ with pulse duration τ for the Baseball Lens with R_{TUNE} removed.

Figure 6.22. Graph of the theoretical variation of (position) standard deviation (at $T = 204$ ms) against pulse duration τ for various values of lens angular frequency ω.

Figure 6.23. Matrix theory prediction and fit to the experimental standard deviation in the x-direction when using the baseball coil only.

Figure 6.24. Matrix theory prediction and fit to the experimental standard deviation in the x-direction when using the Baseball Lens configured with $R_{\mathrm{TUNE}} = R_{\mathrm{BIAS}}/2$.

Figure 6.25. Matrix theory prediction and fit to the experimental standard deviation in the x-direction when using the Baseball Lens configured with $R_{TUNE} = R_{BIAS}$.

Figure 6.26. Matrix theory prediction and fit to the experimental standard deviation in the x-direction when using the Baseball Lens configured with R_{TUNE} removed.

Figure 6.27. Numerical simulation of the variation of the standard deviation in the x-direction when using the baseball coil only.

Figure 6.28. Numerical simulation of the variation of the standard deviation in the x-direction when using the Baseball lens in the configuration with $R_{TUNE} = R_{BIAS} / 2$.

Figure 6.29. Numerical simulation of the variation of the standard deviation in the x-direction when using the lens in the configuration with $R_{TUNE} = R_{BIAS}$.

Figure 6.30. Numerical simulation of the variation of the standard deviation in the x-direction when using the lens in the configuration with R_{TUNE} removed.

Figure 6.31. Numerical simulation of the variation of the standard deviation in the z-direction when using the lens in the configuration with R_{TUNE} removed.

Figure 6.32. Numerical simulation of the variation of the standard deviation using an ideal Baseball Lens with $\omega_x = \omega_z = 40\,\mathrm{s}^{-1}$.

Chapter 1

Introduction

1.1
General Introduction

The advent of laser-cooling [1, 2] has brought about a revolution in atom-optics [3, 4]. The large frictional force from optical scattering can be used to cool atoms all the way from room temperatures to microKelvin temperatures. Upon achieving these cold temperatures, atoms can then be manipulated using optical [5] and magnetic [6] fields. Magnetic atom-optical elements that reflect [7, 8], refract [9, 10] and guide [11, 12, 13, 14] have been developed for use with cold atoms.

This thesis will concentrate on the magnetic atom-optical element of a pulsed magnetic lens, specifically single-impulse magnetic lenses for launched cold atoms.

1.2
The Application of Pulsed Magnetic Lenses

Pulsed magnetic fields find application in many areas of science, from efforts to affect chicken embryos [15] and analgesia in land snails [16], to pumping liquid oxygen for space rockets [17], as well as in the research area discussed within this thesis. Below is a brief discussion of the possible applications of pulsed magnetic lenses for cold atoms.

Applications of Pulsed Magnetic Lenses for Cold Atoms

The density of a freely expanding atom cloud can be increased by many orders of magnitude with pulsed magnetic lenses, or lenses can be used to reduce significantly the velocity spread, i.e. temperature, of a cloud. It is therefore possible to use pulsed magnetic lenses in a multitude of ways. One could foresee a cloud of atoms being spatially focussed to enhance loading into magnetic guides [12, 18], optical guides [19], and storage rings [20, 21, 22], or even used for lithographic techniques [23]. Pulsed magnetic lenses also offer the facility of transferring cold atoms created in a magneto-optical trap to a remote vacuum chamber of lower background pressure [24] for other uses, e.g. the manufacture of Bose-Einstein Condensate [25].

This project will concentrate on the transfer of cold atoms from a magneto-optical trap to a remote vacuum chamber, using a pulsed magnetic lens to focus spatially the atom cloud at the apex of flight.

1.3
Pulsed Magnetic Lenses and Cold Neutral Atoms

Before this work, three research groups had published significant experimental work with pulsed magnetic lenses for cold atoms. The first, lead by C. Wieman in the early 1990s, investigated the focusing of caesium atoms that were subsequently loaded into an ac magnetic trap. Whilst their 1991 publication in Physical Review Letters, *Multiply Loaded, ac Magnetic Trap for Cold Atoms* [26], concentrates on the ac magnetic trap, C. Monroe's 1992 thesis, *Experiments with Optically and Magnetically Trapped Cesium Atoms* [27] offers more detail of the group's work.

Monroe *at al.* loaded 10^7 caesium atoms into a magneto-optical trap (MOT) which had three mutually orthogonal counter-propagating pairs of laser beams. The beams were arranged such that one pair was horizontal and the other two pairs were at 45° to the horizontal. The beam orientation and set-up allowed an optical fountain in the vertical direction. An atom cloud at 4 μK was launched at a speed of approximately 170 cm s^{-1} to come to rest in 170 ms at an apex 15 cm above the MOT. Just after launch, the atoms were pumped into the strong-field-seeking (SFS) state with $F = 4,\ m_F = -4$. The atom cloud was then focussed in 3-D using an alternate-gradient method [28] utilising two temporally separated magnetic pulses. The lenses were constructed from a total of two circular coils – the first lens utilising just one coil and the second lens utilising both coils. The first coil had a radius of 2.15 cm and the second a radius of 1.65 cm, the coils being separated by 3.3 cm. The first impulse occurred when the centre-of-mass of the atom cloud was in the centre of the first coil (70 ms after launch). The pulse of the coil had a magnitude of 15000 Amp-turns-ms. The second impulse occurred when the centre of mass of the atom cloud was 2 cm above the first coil (8 ms after the first pulse). For the second impulse, the first coil was set at 10000 Amp-turns-ms and the second coil at 23000 Amp-turns-ms. Both the first and the second impulse each lasted approximately 3 ms. The crucial factor in this alternate-gradient method is that the first pulse focuses the atom cloud in the

vertical direction, but defocuses in the horizontal direction. The second pulse defocuses in the vertical direction, but focuses in the horizontal direction. By over-focusing with the first lens, the defocusing of the second lens can bring the atom cloud to focus (in both vertical and horizontal directions) at the apex of flight. The initial cloud, upon launch, is quoted as being approximately $1\times1\times1$ mm, with the best final size being $2.5\times2.5\times3.5$ mm, where the numbers refer to (1/e) full-width Gaussian fits, the last number being in the vertical direction.
Monroe *et al.* attribute the lack of 1:1 imaging as being due to the atom cloud sampling anharmonic regions of the lens. However, they do not discuss either theoretical or experimental methods to decrease the image aberration, or methods to optimise focusing.

Another research group to have conducted experiments with pulsed magnetic lenses is that lead by A. M. Steinberg. Following H. Ammann and N. Christensen's theoretical work on delta kick cooling [29], Myrskog *et al.* [30] used their two MOT coils to cool a cloud of rubidium atoms in one dimension, i.e. to focus the atoms in velocity space. The MOT coils could be used to create an axicon [23] with magnetic field gradient of 180 G cm^{-1}, (by having the currents in the two coils run in the opposite sense to eachother); or to create an approximately harmonic potential with magnetic field curvature of 60 G cm^{-2}, (by having the currents in the two coils run in the same sense to eachother). The circular coils had 200 turns, radii of 4 cm and were separated by 8 cm.
10^8 ^{85}Rb atoms were collected in a MOT and then cooled to 7.5 μK in an optical molasses phase. After 11 ms of free expansion a quadrupole magnetic pulse (using the MOT coils) was applied for 3 ms. This impulse was used to cool atoms in the weak-field-seeking (WFS) state $5^2S_{1/2}\left|F=3,m_F=3\right\rangle$ of ^{85}Rb to 1.2 μK in 1-D. In a similar experiment, using a magnetic pulse from the (approximately) harmonic field with 60 G cm^{-2}, the atom cloud was cooled from 9 μK to 700 nK in 1-D, a temperature decrease of more than a factor of ten.

The third group to research pulsed magnetic focusing for cold atoms was that of O. Gorceix around the early part of this century. They published work on both spatial and velocity focusing of cold caesium atoms.

Although Gorceix's group published several papers using pulsed magnetic forces, they had two main lens experiments, both using the same experimental apparatus. Gorceix's group also used pulsed magnetic forces for spin-polarization interferometry [31], spatial coherence monitoring [32], and Stern-Gerlach state selection [33]. Both of the main lens experiments worked upon the same principle: caesium atoms were loaded into a vapour cell MOT, underwent further cooling in an optical molasses stage, before being allowed to fall under gravity through a distance of approximately 1 m.

Their first experiment [34] focussed atoms in 1-D (along the direction of propagation) in either space or velocity. 10^8 Cs atoms were released from an optical molasses phase, at 6.5 μK, to fall under gravity to a probe 95 cm vertically below the MOT region, in a flight time of 440 ms. An optical pumping beam, $>85\%$ efficient and positioned 3 cm below the MOT, was used to pump the atomic population into a state with $F=4$, $m_F=+4$. Here a single current-carrying coil, located 9.5 cm below the MOT, was used as a lens. The coil had 150 turns with a radius of 2.6 cm and operated at a current between zero and 2.5 A. An impulse of duration 20 ms was applied 130 ms after release from the optical molasses phase. By varying the current, either spatial or velocity focusing could be achieved. The dropped cloud had an initial radius of approximately 0.5 mm. The velocity-spread focusing (in the vertical direction) was quoted as having a minimum of 3.7 mm/s and corresponding to an effective temperature of 220 nK. For 1-D spatial focusing, again in the vertical direction, the cloud had a minimum of 2.3 times its initial diameter. For their configuration, Gorceix *et al.* predicted that the minimum spatial compression would be 2.2 times the initial extent.

The second experiment from Gorceix's group [35] loaded approximately 8×10^7 caesium atoms into a MOT, before an optical molasses stage cooled the atom cloud to 4 μK. The cloud was then dropped to fall under gravity, having an initial radius of 1.2 mm. Pulsed magnetic lenses were formed with two coils: a 5 cm-diameter, 50-turn circular coil located 9.5 cm below the MOT (coil 1); and a 7 cm-diameter, 260-turn circular coil located 24 cm below the MOT (coil 2). Both coil axes were oriented in the vertical direction. A horizontally-propagating optical pumping beam was situated 2 cm below the MOT to optically pump the atoms into an extreme WFS state. A vertical 10 μT orientation field was present. There was an aperture (a neck in the

vacuum chamber) extending between 6.5 cm and 7.5 cm below the MOT. This aperture allowed approximately 60 % of the atoms to pass though. Coil 2 was used to investigate 1-D (along the vertical (axial) direction) and 2-D focusing (in the radial direction) with the atoms in WFS states with $F = 4, m_F = +4$. Although coil 2 is a multi-turn single current loop, whose axial magnetic field curvature is negative, Gorceix's group utilised non-adiabatic following [36] to enable atoms initially in WFS states to be focussed in the axial direction. This non-adiabatic following was instigated by making the direction of the pulsed magnetic field from coil 2 anti-parallel to the orientation field. There is the danger with this method that (during the pulse switch-on) atoms could lose their orientation as the resultant magnetic field passes through zero. From an initial cloud width of 1.2 mm, truncated in its expansion by an aperture, the cloud was spatially focussed in 1-D to 1.0 mm (0.48 ms magnetic pulse duration); spatially focussed in 2-D to 1.0 mm (10 ms pulse duration); and velocity focussed in 2-D to 0.6 cm s^{-1} (6.2 ms pulse duration). Currents within the focusing coils ranged between zero and ±10 A. Then, in a following experiment, coil 1 and coil 2 were used in an alternate-gradient method to focus first in the axial direction and then in the radial direction. From an initial $1.2 \times 1.2 \times 1.2$ mm cloud, the size of the 3-D focussed cloud was $1.2 \times 1.2 \times 8.0$ mm, from a predicted unfocussed final size of $6.3 \times 6.3 \times 6.3$ mm.

The reader should note, to this date, no group has published experimental work showing a reduction of cold atom cloud size in all three dimensions (relative to the unfocussed final cloud size) using a single magnetic impulse.

1.4
The Aims of this Project

The aims of this project are:

1. To design, commission, and build an experiment to investigate the pulsed magnetic lensing of launched cold atoms.
2. To design and build a pulsed magnetic lens capable of focusing in 3-dimensions using a single impulse.
3. To investigate the focussed atom clouds:
    a. How does the cloud size at the apex of flight vary with the duration of the lens pulse?
    b. How does the relationship between the angular frequency of the lens in the x, y and z-directions (ω_x, ω_y, ω_z) affect the focussed clouds?
    c. What is the transfer efficiency between the initial launched cloud and the final focussed cloud?

1.5
Thesis Outline

Chapter 1 discussed the history of pulsed magnetic lenses with cold atoms, before discussing possible applications and outlining the aims of this project. Chapter 2 will detail the experimental set-up, along with relevant theoretical considerations, for building an experiment to launch cold atoms into a remote vacuum chamber vertically above a magneto-optical trap. Chapter 3 relates basic magnetic lens theory and Chapter 4 discusses numerical simulations of launched cold atoms subject to a single magnetic impulse during flight. Chapter 5 then considers the magnetic lens built for experimentation, based on the findings of the numerical simulations in Chapter 4. Chapter 6 presents the experimental results, then analyses and discusses the data obtained. Chapter 7 draws conclusions and discusses future work. The references for each chapter can be found at the end of each chapter.

[1] S Chu, *The manipulation of neutral particles*, Rev. Mod. Phys. **70** 685 (1998) and
C N Cohen-Tannoudji, *Manipulating Atoms with Photons*, Rev. Mod. Phys. **70** 707 (1998) and
W D Phillips, *Laser cooling and trapping of neutral atoms*, Rev. Mod. Phys. **70** 721 (1998)

[2] C S Adams and E Riis, *Laser cooling and trapping of neutral atoms,* Prog. Quantum Electron. **21** 1 (1997)

[3] E A Hinds and I G Hughes, *Magnetic atom optics: mirrors, guides, traps, and chips for atoms*, J. Phys. D: Appl. Phys. **32** R119 (1999)

[4] C S Adams, M Sigel and J Mlynek, *Atom Optics*, Phys. Rep. **240** 143 (1994)

[5] R Grimm, M Weidemüller, and Y B Ovchinnikov, *Optical Dipole Traps for Neutral Atoms*, Adv. Atom. Mol. Opt. Phys 42, 95 (2000).

[6] R Folman, P Krüger, D Cassettari, B Hessmo, T Maier and J Schmiedmayer, *Controlling Cold Atoms using Nanofabricated Surfaces: Atom Chips*, Phys. Rev. Lett. **84** 4749 (2000)

[7] C V Saba, P A Barton, M G Boshier, I G Hughes, P Rosenbusch, B E Sauer and E A Hinds, *Reconstruction of a Cold Atom Cloud by Magnetic Focusing*, Phys. Rev. Lett. **82** 468 (1999)

[8] P Rosenbusch, B V Hall, I G Hughes, C V Saba and E A Hinds, *Manipulation of cold atoms by an adaptable magnetic reflector*, Appl. Phys. B **70** 709 (2000)

[9] W G Kaenders, F Lison, I Müller, A Richter, R Wynands and D Meschede, *Refractive components for magnetic atom optics*, Phys. Rev. A **54** 5067 (1996)

[10] É Marechal, S Guibal, J-L Bossennec, R Barbe, J-C Keller and O Gorceix, *Longitudinal focusing of an atomic cloud using pulsed magnetic forces*, Phys. Rev. A **59** 4636 (1999)

[11] J Denschlag, D Cassettari and J Schmeidmayer, Guiding *Neutral Atoms with a Wire*, Phys. Rev. Lett. **82** 2014 (1999)

[12] M Key, I G Hughes, W Rooijakkers, B E Sauer, E A Hinds, D J Richardson and P G Kazansky, *Propagation of Cold Atoms along a Miniature Magnetic Guide*, Phys. Rev. Lett. **84** 1371 (2000)

[13] J A Richmond, B P Cantwell, S N Chormaic, D C Lau and A M Akulshin, *Magnetic guide for neutral atoms*, Phys. Rev. A **65** 033422 (2002)

[14] M Greiner, I Bloch, T W Hänsch and T Esslinger, *Magnetic transport of trapped cold atoms over a large distance*, Phys. Rev. A **63** 031401 (2001)

[15] L A Coulton and A T Barker, *The effect of low-frequency pulsed magnetic fields on chick embryonic growth*, Phys. Med. Biol. **36** 369 (1991)

[16] A W Thomas, M Kavaliers, F S Prato, K-P Ossenkopp, *Antinociceptive effects of a pulsed magnetic field in the land snail, Cepaea nemoralis*, Neurosci. Lett. **222** 107 (1997)

[17] R C Youngquist, C Immer, J E Lane, J C Simpson, *Dynamics of a finite liquid oxygen column in a pulsed magnetic field*, IEEE T. Magn. **39** 2068 (2003)

[18] D Müller, D Z Anderson, R J Grow, P D D Schwindt and E A Cornell, *Guiding Neutral Atoms Around Curves with Lithograhically Patterned Current-Carrying Wires*, Phys. Rev. Lett. **83** 5194 (1999)

[19] H Ito, T Nakata, S Sakaki, M Ohtsu, K I Lee and W Jhe, *Laser Spectroscopy of Atoms Guided by Evanescent Waves in Micron-Sized Hollow Optical Fibers*, Phys. Rev. Lett. **76** 4500 (1996)

[20] A S Arnold and E Riis, *Bose-Einstein condensates in 'giant' toroidal magnetic traps*, J. Mod. Opt. **49** 959 (2002)

[21] A S Arnold, C S Garvie and E Riis, *A condensate storage ring*, arXiv:cond-mat/0506142 v1 6th June (2005)

[22] J A Sauer, M D Barrett and M S Chapman, *Storage Ring for Neutral Atoms*, Phys. Rev. Lett. **87** 270401 (2001)

[23] D Mechede and H Metcalf, *Atomic nanofabrication: atomic deposition and lithography by laser and magnetic forces*, J. Phys. D: Appl. Phys. **36** R17 (2003)

[24] K Szymaniec, H J Davies and C S Adams, *An atomic fountain guided by a far-off resonance laser beam*, Europhys. Lett. **45** 450 (1999)

[25] H J Lewandowski, D M Harber, D L Whitaker, E A Cornell, *Simplified system for creating a Bose-Einstein condensate*, J. Low Temp. Phys. **132** 309 (2003)

[26] E A Cornell, C Monroe and C E Wieman, *Multiply Loaded, ac Magnetic Trap for Neutral Atoms*, Phys. Rev. Lett. **67** 2439 (1991)

[27] C Monroe, *Experiments with Optically and Magnetically Trapped Cesium Atoms*, Ph.D. thesis, University of Colorado, Boulder, Colorado (1992)

[28] A S Arnold, M J Pritchard, D A Smith, I G Hughes, Double-impulse magnetic focusing of launched cold atoms, (in preparation)

[29] H Ammann and N Christensen, *Delta Kick Cooling: A New Method for Cooling Atoms*, Phys. Rev. Lett. **78** 11 (1997)

[30] S H Myrskog, J K Fox, H S Moon, J B Kim and A M Steinberg, *Modified "δ-kick cooling" using magnetic field gradients*, Phys. Rev. A **61** 053412 (2000)

[31] É Maréchal, R Long, J-L Bossennec, R Barbé, J-C Keller and O Gorceix, *Cold-cesium-atom spin-polarization interferometry*, Phys. Rev. A **60** 3197 (1999)

[32] É Maréchal, R Long, T Miossec, J-L Bossennec, R Barbé, J-C Keller and O Gorceix, *Atomic spatial coherence monitoring and engineering with magnetic fields*, Phys. Rev. A **62** 053603 (2000)

[33] É Maréchal, S Guibal, J-L Bossennec, M-P Gorza, R Barbé, J-C Keller and O Gorceix, *Longitudinal Stern-Gerlach effect for slow cesium atoms*, Eur. Phys. J. D **2** 195 (1998) and

O Gorceix É Maréchal, J-L Bossennec, S Guibal,, R Barbé and J-C Keller, *Magnetic compression of a falling atom cloud*, C. R. Acad. Sci. Paris, Série II *b*, **327** 133 (1999)

[34] É Marechal, S Guibal, J-L Bossennec, R Barbe, J-C Keller and O Gorceix, *Longitudinal focusing of an atomic cloud using pulsed magnetic forces*, Phys. Rev. A **59** 4636 (1999)

[35] T Miossec, R Barbe, J-C Keller and O Gorceix, *Pulsed magnetic lenses for producing intense and bright cold atom beams*, Optics Comm. **209** 349 (2002)

[36] O Gorceix, private communication

Chapter 2

Experimental Theory and Set-up

2.1
Laser Cooling and Trapping

2.1.1 Experimental Overview

This project began in October 2001, at which point there was only an empty optical bench and some 780 nm mirrors in the laboratory. Since that time, all the experimental apparatus has been built, designed or commissioned by the author of this thesis.

2.1.2 Rubidium-85

^{85}Rb and its D_2-line

Rubidium is used for laser cooling and trapping because it is easily produced (using alkali metal dispensers [1, 2, 3], paramagnetic (making it suitable for magnetic trapping or lensing), and relatively cheap lasers for cooling can be built using readily-available commercial diode lasers.

^{85}Rb is the most abundant isotope of rubidium and its D_2-line offers good scope for laser cooling for two reasons. Firstly, the relatively large hyperfine splitting in the $5P_{3/2}$ state allows the cooling cycle to operate on a closed transition far enough away from other transitions so as to allow large laser detunings (e.g. for optical molasses (2.2.17)) without significant probability of other transitions occurring. Secondly, the D_2-line operates at 780 nm (384 THz), a wavelength available from inexpensive commercial laser diodes, making rubidium a relatively cheap element for laser cooling.

Figure 2.1 shows the relevant energy level diagram for laser cooling ^{85}Rb on the D_2-line.

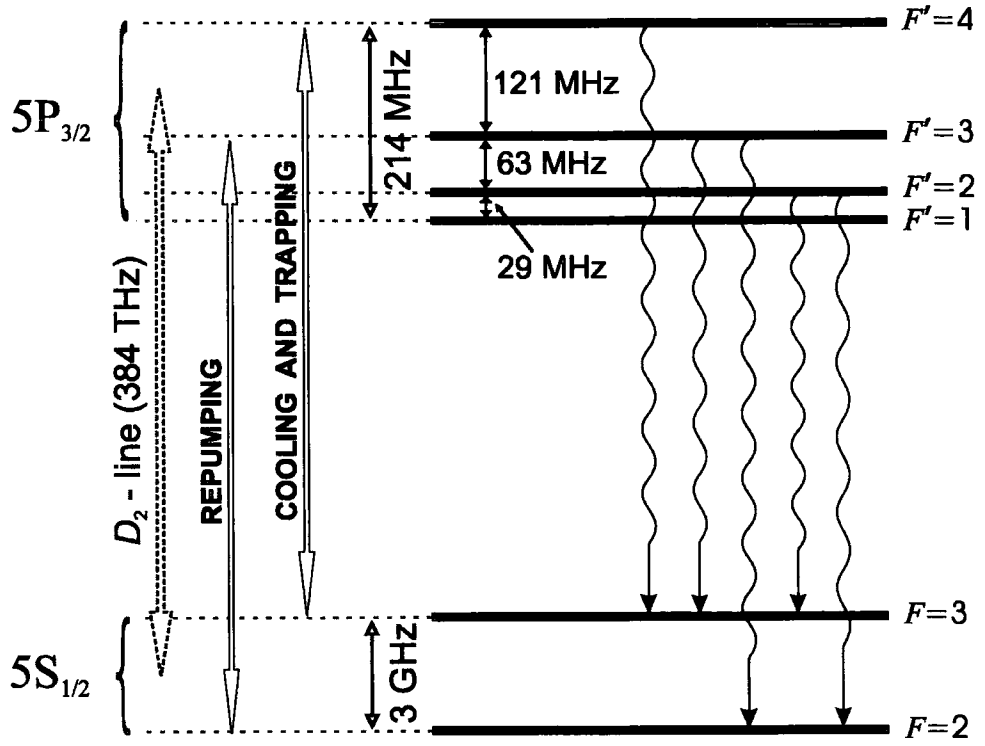

Figure 2.1. Relevant Energy Level Diagram for Laser Cooling of ^{85}Rb on the D_2-line. Cooling is operated on the closed $5S_{1/2}\ F=3$ to $5P_{3/2}\ F'=4$ transition. Also shown are the possible excited state $(5P_{3/2})$ decay channels. Although the cooling transition is closed, there is a probability of excitation to other $5P_{3/2}$ hyperfine levels, and hence decay to the lower ground-state and out of the cooling cycle. Therefore, a repumping laser (section 2.1.6) is present to return the atomic state into the cooling cycle. Energy level splittings taken from [4, 5].

3.1.2 Doppler Cooling Theory in 1-D

The following is a description of one-dimensional Doppler cooling, of two-level atoms, in the low intensity limit, where there is no need to consider the Stark shift of energy levels.

Scattering Force on an Atom

The steady-state scattering rate, (or the rate of absorption followed by spontaneous emission), of monochromatic electromagnetic radiation by a two-level atom is given by [6]:

$$R(\omega_L, I, \mathbf{v}) = \frac{\Gamma}{2} \frac{I/I_{SAT}}{1 + I/I_{SAT} + 4\left(\frac{\omega_L - \omega_0 - \mathbf{k}\cdot\mathbf{v}}{\Gamma}\right)^2} \tag{2.1}$$

where ω_0 is the angular frequency of the atomic transition in the rest frame of the atom, ω_L and I are the frequency and intensity of the incident radiation respectively, I_{SAT} is the saturation intensity of the transition, Γ is the inverse lifetime of the excited state, $\mathbf{k}$ is the wavevector of the radiation, $\mathbf{v}$ is the velocity of the atom (in the frame ω_L is measured) and $-\mathbf{k}\cdot\mathbf{v}$ is the first-order Doppler shift.

The parameter Δ can be used to denote the (angular) detuning from resonance of the radiation such that, $\Delta = \omega_L - \omega_0$. If $\omega_L > \omega_0$ then Δ is positive and the radiation is denoted as 'blue-detuned'. Conversely, if $\omega_L < \omega_0$ then Δ is negative and the radiation is termed 'red-detuned'.

Each quantum of absorbed radiation imparts a momentum $\hbar\mathbf{k}$ to an atom and the momentum change due to spontaneous emission time-averages to zero. Therefore, the time-averaged force on an atom is,

$$\langle \mathbf{F} \rangle = \hbar\mathbf{k}R\,. \tag{2.2}$$

Counter-propagating Laser Beams for Doppler Cooling

Now consider the case where there are two counter-propagating laser beams, both with frequency ω_L and intensity I. The time-averaged force on an atom in the laser beams would be,

$$\langle \mathbf{F} \rangle = \frac{\Gamma\hbar\mathbf{k}}{2}\left(\frac{I/I_{SAT}}{1 + 2I/I_{SAT} + 4\left(\frac{\Delta - \mathbf{k}\cdot\mathbf{v}}{\Gamma}\right)^2} - \frac{I/I_{SAT}}{1 + 2I/I_{SAT} + 4\left(\frac{\Delta + \mathbf{k}\cdot\mathbf{v}}{\Gamma}\right)^2} \right). \tag{2.3}$$

If $\Delta < 0$, then the force is in the direction opposed to an atom's motion. It is under this principle that Doppler Cooling operates. The velocity of an atom is damped towards zero, since the forces from the two laser beams are equal and opposite for $\mathbf{v} = 0$. The laser beams are analogous to a viscous medium and are often termed Optical Molasses.

The Doppler Limit

Although the time-averaged momentum change due to spontaneous emission is zero, each emission event does result in a discrete momentum change. As an atom's velocity approaches zero, the cooling mechanism is balanced by the random walk in momentum space caused by discrete momentum kicks from spontaneous emission and absorption. The cooling limit of this process, the Doppler Temperature, is, [6]

$$T_{Doppler} = -\frac{\hbar\Gamma^2}{8k_B\Delta}\left(1+\frac{2I}{I_{SAT}}+\left(\frac{2\Delta}{\Gamma}\right)^2\right) \tag{2.4}$$

which has a minimum in the low intensity limit ($2I \ll I_{SAT}$) of,

$$T_{Doppler\ Limit} = \frac{\hbar\Gamma}{2k_B}. \tag{2.5}$$

As can be seen, in the low intensity limit, the temperature of an ensemble of atoms depends only on the natural linewidth of the transition being used for cooling. For ^{85}Rb, the Doppler Limit is 143 μK [7].

2.1.4 Magneto-optical Trap Theory in 1-D

The magneto-optical trap (MOT) was first realised in 1987 by Raab *et al.* [8], based on the ideas of J. Dalibard [8]. For a 3-dimensional MOT, three equal-intensity pairs of counter-propagating laser beams are required, along with a magnetic field that increases in magnitude from the centre of the trap. The key thing to note is that the MOT, unlike Optical Molasses, confines atoms in position space as well as velocity space. The workings of the 3-dimensional MOT in the laboratory will be discussed in section 2.1.5, whereas below is a discussion of the MOT in 1D.

The Magneto-optical Trap in 1D

The simplest atomic dipole transition on which the magneto-optical trap operates is a $F = 0$ to $F' = 1$ transition, where F is the total atomic angular momentum. Figure 2.2 displays this atomic state configuration along with two counter-propagating laser beams in a region of linear magnetic field, which is zero at the centre of the trap.

The laser beams have right-hand circular polarisation, (defined by the rotation of the electromagnetic radiation's electric field vector about the wave-vector of the radiation), and are frequency detuned below (red-detuned from) the atomic resonance

of the considered states. Since the magnetic field direction points into the centre of the trap, the beam propagating to the right causes σ^- transitions in the left-hand side

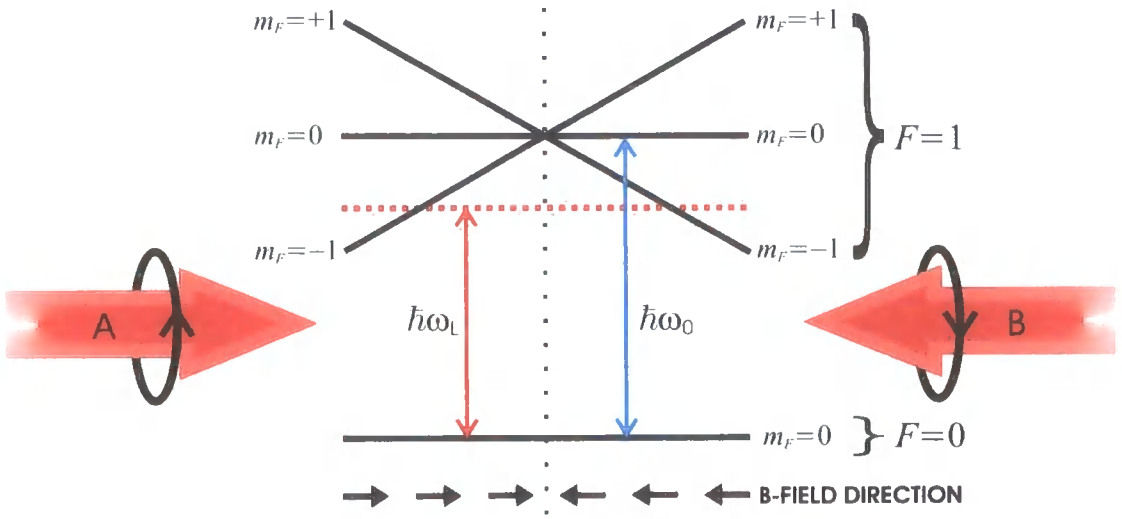

Figure 2.2. Diagram of the simplest transition on which the magneto-optical trap can operate: the $F=0$ to $F'=1$ transition. Both beam A and beam B are right-hand circularly polarised, of equal intensity and frequency, and counter-propagate each other. The ground state of the atomic system, $F=0$, has one magnetic sub-level, $m_F=0$. The excited state has three magnetic sublevels, $m_{F'}=0,\pm1$, which experience differential Zeeman splitting in the applied linear magnetic field that is zero at the centre of the trap. It must be noted that the Zeeman splitting is dependent on the magnitude of the magnetic field, but not on the direction of the field. The laser beam polarisation and the magnetic field direction are such that a beam causes σ^- transitions in the side of the trap it enters, and σ^+ transitions in the side of the trap it exits, i.e. beam A causes σ^- transitions in the left of the trap and σ^+ transitions in the right. The energy level separation between the $F=0, m_F=0$ and the $F'=1, m_{F'}=0$ sublevels is $\hbar\omega_0$, and the frequency of the laser beams is red-detuned such that $\omega_L<\omega_0$ – this dictates two things: that a zero velocity atom experiences more absorption away from the centre of the trap such that it is pushed towards the centre of the trap; and an atom with finite velocity absorbs more from the beam opposing its motion (if that beam is driving σ^- transitions). In this way, the force on the atoms in the MOT can be characterised by a term proportional to the velocity and a term proportional to the position (relative to the centre of the trap).

of the trap and σ^+ transitions in the right hand side of the trap. Conversely, the beam propagating to the left causes σ^- transitions in the right-hand side of the trap and σ^+ in the left hand side of the trap. The symmetry of the situation dictates that a beam

causes σ^- transitions in the side that it enters the trap and σ^+ transitions in the side that it exits.

The ground state has one magnetic sub-level, whereas the excited state has three. The excited state sub-levels experience differential Zeeman splitting in non-zero magnetic field; this is one of the main features that make this configuration of laser beams and magnetic field into a trap. If the ground state is considered to be at zero energy, then the excited states have energy [9],

$$E = \hbar\omega_0 + \mu_B g_{F'} m_{F'} B \tag{2.6}$$

where ω_0 is the angular frequency of resonance between $F = 0, m_F = 0$ and $F' = 1, m_{F'} = 0$; $g_{F'}$ is the Landé Factor; $m_{F'}$ is the magnetic quantum number of the excited state; and B is the magnitude of the magnetic field. The term proportional to B is the Zeeman splitting, where here B is a linear function of the distance from the centre of the trap. As can be seen in Figure 2.2, this Zeeman splitting causes a zero velocity atom in the $m_{F'} = -1$ sublevel to be closer to resonance with the laser frequency the further from the MOT the atom is situated.

The laser beams act to give Doppler cooling (section 2.1.3) such that the force on the atoms is proportional to the velocity. However, the addition of the magnetic field also gives a force term that is proportional to the position of the atom, such that the total force on an atom approximates to $-\alpha v_x - \beta x$ [10], where β is proportional to the gradient of the magnetic field, and α is a function of the intensity and frequency of the laser beams.

The configuration presented above is the simplest. However, the MOT works for higher values of F. The important factor is that $F' > F$ so that no ground state magnetic sub-level is uncoupled from either laser beam.

2.1.5 Magneto-optical Trap in the Laboratory

The MOT in 3-D

Section 2.1.4 outlined the 1-D operation of the MOT. However, the 3-D version in the laboratory is not as simple since atoms are often multi-level (rather than two-level as in Section 2.1.4), and the light field and magnetic field form a complicated mixture of polarisation and intensity gradients. Lindquist *et al.* [11] (^{133}Cs) and Wallace *et al.* [12] (^{85}Rb and ^{87}Rb) wrote excellent papers exploring the effects of laser beam size, intensity, detuning, and magnetic field gradient in experimental MOTs and compared their results to theoretical expectations. In summary, they found that the larger the laser beam intensity, the greater the number of trapped atoms; that, for a given laser intensity, the greater the beam diameter the greater the number of trapped atoms; and that the laser frequency and magnetic field gradient both had optimum values. It is for this reason that this experiment uses large vacuum view-ports and large optics to accommodate large beams so that a large number of atoms can be collected. The larger the number of atoms, the larger the available fluorescence signal, and hence the easier an atom cloud is to detect – this could be particularly important when imaging a cloud 20 cm above a MOT after 204 ms of ballistic expansion.

For the production of a 3-D MOT, one needs lasers at the correct frequencies; an array of optics for manipulation of laser beam properties; a vacuum chamber in which to situate the MOT; a magnetic quadrupole field; and a source of, in this case, rubidium. The following sub-sections discuss the implementation of these requirements; the characterisation of the MOT; imaging of cold atom clouds; temperature measurements; and finally optical molasses, which is a form of sub-Doppler cooling.

2.1.6 The Lasers

For the magneto-optical trap in this experiment, two lasers were required – a trap laser and a repumping laser. The trap laser was used to cool the rubidium atoms, and, since rubidium has two ground states, a repumping laser was required to return the atomic state into the cooling cycle, if it had decayed into the other (lower) ground state.

The lasers used in this experiment were extended-cavity diode lasers [13,14], of which there were two types: a unit utilising a Sanyo DL-7140-201 Laser Diode (the repumping laser), and a more compact, evolved version of that unit operating with a Sharp GH0781JA2C Laser Diode (the trap laser). Both were built in the Littrow

configuration, where the 0^{th} order from a diffraction grating is used as the output beam, and the 1^{st} order is fed back directly into the laser diode [13]. An extended cavity is used to reduce the linewidth of the diode laser.

The trap laser and the repumping laser were both locked to a linewidth of <1 MHz (in 250 ms) using polarisation spectroscopy [15].

The Repumping Laser

Figure 2.3 displays a photograph of the repumping ECDL. The beam emanating from a Sanyo DL-7140-201 Laser Diode is collimated by a 4.5 mm-focal-length aspheric lens, producing a beam of 0.7×1.4 mm $1/e^2$ radius. The ECDL emits at a wavelength of 780 nm with a typical output power of 18 mW, at a current of 46 mA through the laser diode. The beam passes onto an 1800 lines/mm reflection

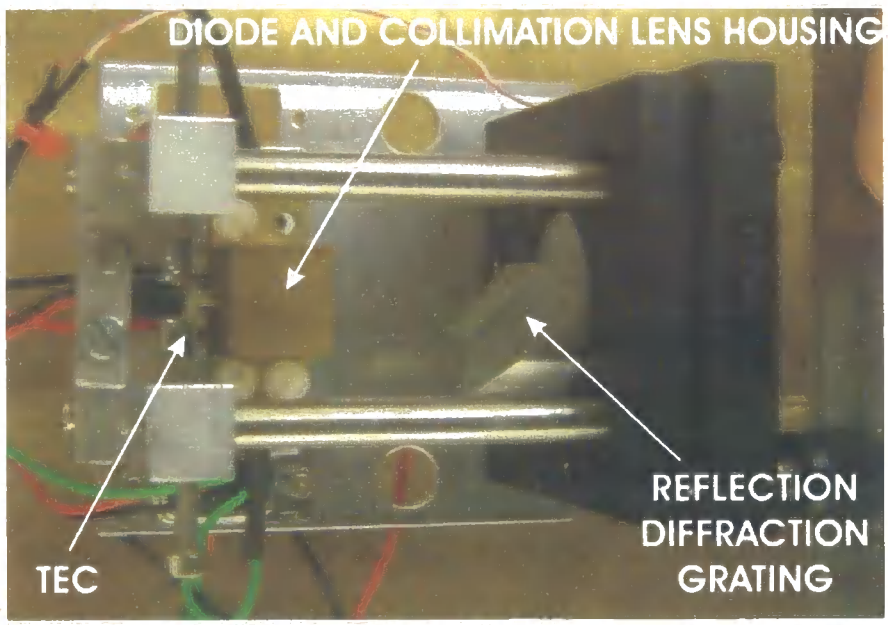

Figure 2.3. The Repumping Laser. The light from the Sanyo DL-7140-201 laser diode is collimated using a 4.5mm focal length lens and projected onto a 1800 lines/mm reflection diffraction grating, with the 0^{th} order being used as the output beam at ~90 ° to the incident beam. The 1^{st} order is retro-reflected into the laser diode. No other orders are present. A Thorlabs AE0203D08 PZT (positioned in the mirror mount) is used for fine positioning of the grating, and for frequency stabilisation (see below). The laser diode is cooled to, and stabilised at, a temperature such that it emits at the desired wavelength (~ 780 nm) using a Marlow Industries DT3-2.5 thermoelectric cooler and a 100 kΩ thermistor in conjunction with a Wavelength Electronics MPT-2500 Temperature Controller. The length of the extended cavity is approximately 30 mm.

diffraction grating, which is mounted on a Thorlabs KC1/M mirror mount. The distance between the grating and the back of the laser diode forms an extended cavity of approximately 30 mm. The temperature of the laser diode is stabilised using a Wavelength Electronics MPT-2500 Temperature Controller, a Marlow Industries DT3-2.5 Thermoelectric Cooler and a 100 kΩ bead thermistor.

The current through the laser diode is controlled via a Thorlabs LD1255 Constant Current Driver. The laser frequency can be scanned using a Thorlabs AE0203D08 Piezoelectric Transducer (PZT) mounted such that it can change the length of the cavity (by translating the part of the mirror mount holding the diffraction grating) and thus the output frequency. The frequency scanning range of the laser is limited by mode-hops rather than the maximum possible cavity length change available with the PZT.

Using the diffraction grating, the 1^{st} order is fed back into the laser diode and the 0^{th} order is used as the output beam, all in a horizontal plane. The ratio of the 0^{th} order to 1^{st} order is approximately 4:1, with a loss of 15 ± 2 % of the incident light. No other orders are present.

To reduce mechanical vibration, the cavity is mounted on a brass base-plate, which is glued to a lead-lined foam layer that rests upon the optical bench.

The Trap Laser

The trap laser operates in the same way as the repumping laser. However, the trap laser has a more recent, compact design intended to give better frequency stability and to have a smaller footprint on the optical bench. There are two main differences between the trap laser and the repumping laser – the diffraction grating and the laser diode. The trap laser uses a diode with a greater laser power output (for a given input current) – a Sharp GH0781JA2C. The ECDL has an output of 48 mW at 100mA input current. Instead of a reflection diffraction grating, the trap uses a holographic diffraction grating, which diffracts a smaller percentage of the total light back into the laser diode and has lower loss. The cavity is housed in a closed aluminium box, with an AR-coated window for laser beam output. Figure 2.4 show photographs of the trap laser.

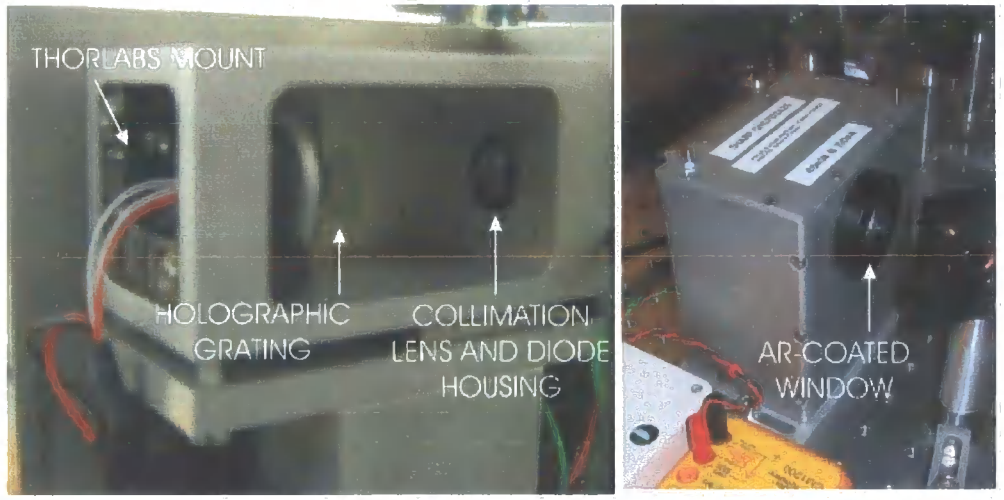

Figure 2.4. The Trap Laser. (Left) Picture of the extended cavity of the trap laser. Light from a Sharp GH0781JA2C laser diode is collimated using a 4.5 mm-focal-length lens and projected onto a 1800 lines/mm holographic diffraction grating, with the 0^{th} order being used as the output beam at ~90° to the incident beam. The 1^{st} order is retro-reflected into the laser diode. No other orders are present. Two Thorlabs AE0203D04 PZTs are used for fine positioning of the grating, and for frequency stabilisation (see below). The temperature of the cavity was stabilised (for length stability) with a Marlow Industries DT12-2.5 thermoelectric cooler and a 100kΩ thermistor (housed close to the diode) in conjunction with an MPT-2500 Temperature Controller. The length of the extended cavity is approximately 30 mm. The cavity is housed in an aluminium box with an AR-coated window for laser beam output.

Laser Locking Scheme: Polarisation Spectroscopy

Both lasers for this experiment were locked using a polarisation spectroscopy signal. Polarisation spectroscopy has been extensively studied in the laboratories in Durham, as described by Pearman *et al.* [15]. The main thrust of this method is a probe beam's frequency-dependent polarisation rotation due to a pump-beam-induced anisotropy within a medium. It is a modulation-free, relatively inexpensive spectroscopic technique whose signal requires little electronic manipulation to enable the locking of a laser.

Figure 2.5 shows an experimental schematic for polarisation spectroscopy.

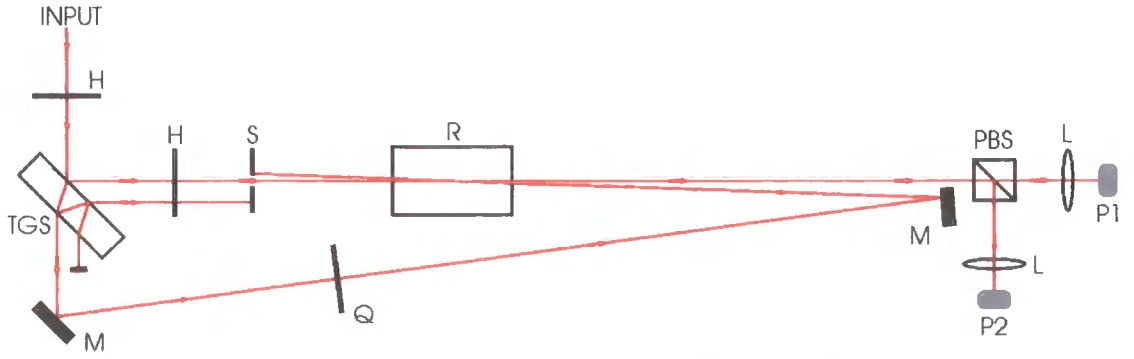

Figure 2.5. Schematic for polarisation spectroscopy. The linearly polarised input light (INPUT) passes through a half-wave plate (H) which controls the reflection and transmission of the light by the thick glass slide (TGS). The reflected light is utilised as a probe beam that passes through a 5 cm-long, room temperature Rubidium vapour cell (R) onto a polarising beam splitter (PBS). The horizontally polarised component of the probe is transmitted to photodiode 1 (P1) and the vertically polarised component is reflected onto photodiode 2 (P2). Both photodiodes are BPX65 models with an active area 1 mm^2, so lenses L are used to focus the light onto the photodiodes. The light transmitted by the thick glass slide forms the pump beam. It is directed, using mirrors (M), such that it (almost) counter-propagates the probe beam. The quarter-wave plate (Q) is present to produce a circularly polarised pump beam. An iris (S) is used to block any unwanted beams. Typically, the probe power is approximately 20 μW and the pump 250 μW.

A probe beam, with linear polarisation at 45 ° to the horizontal, is passed through a 5 cm-long Rubidium cell onto a polarising beam splitter (PBS), which separates the horizontal and vertical polarisation components of the probe. Each component is focused onto a photodiode circuit, which produces a voltage linearly proportional to the incident intensity. In the absence of a pump beam, the difference between the voltage signals from the photodiodes is zero, since the two polarisation components are of equal intensity.

The addition of a circularly polarised, (almost) counter-propagating pump beam, introduces a frequency dependent anisotropy to the medium in the cell. The atomic population becomes pumped such that the mean value of the magnetic quantum number $\langle m_F \rangle \neq 0$.

The linearly polarised probe can be considered to consist of equal parts of left-handed and right-handed circularly polarised light. Each of these two circular components has a different probability for absorption by the anisotropic population. In fact, the transition strength for transitions from the $m_F = 3$ sub-level to the $m_{F'} = 4$ sub-level is twenty-eight times larger than the transition strength for transitions from the

$m_F = 3$ to the $m_{F'} = 2$ sub-level [16]. The absorption coefficient and the refractive index are not independent, they are related by the Kramers–Kronig dispersion relation [17]. So the differential absorption between the left and right-handed polarisation results in a change in polarisation of the probe. The rotation of the probe polarisation manifests itself as an increase in the signal on one photodiode and a decrease in the signal on the other photodiode. Thus, the difference between the voltages from the two photodiode circuits is proportional to twice the small angle through which the polarisation is rotated [15]. This is the advantage of 45 °-polarisation spectroscopy over that done using crossed polarisers [18, 17], whose signal changes by the square of the rotation angle, giving a smaller peak-to-peak signal for small angles.

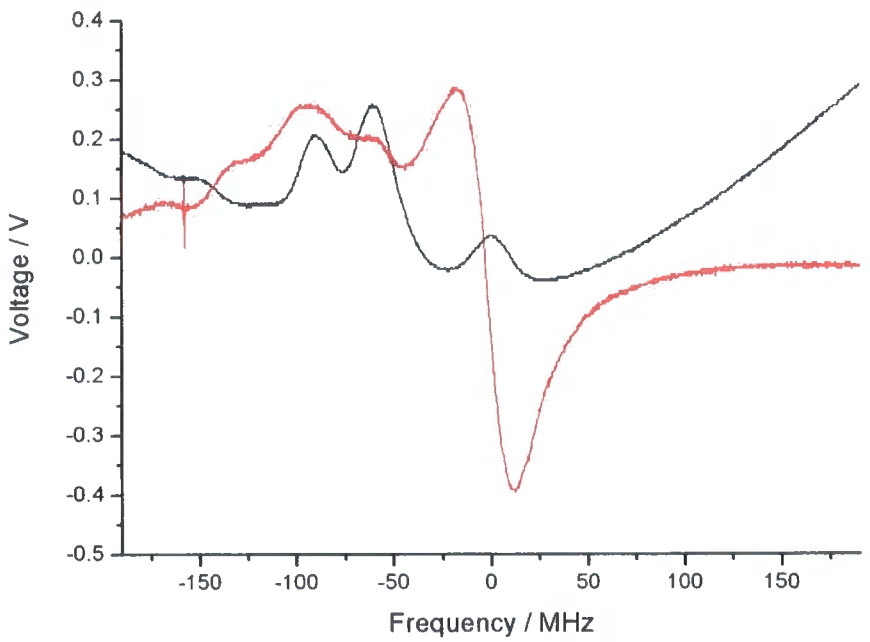

Figure 2.6. Polarisation spectroscopy signal (red) and saturated absorption/hyperfine pumping [19] signal (black) of the ^{85}Rb $5S_{1/2}$ $F = 3$ to $5P_{3/2}$ $F' = 2,3$ and 4 transition. The frequency is referenced relative to the $5S_{1/2}$ F=3 to $5P_{3/2}$ $F' = 4$ transition. The saturated absorption/hyperfine pumping signal (black) shows (from right to left) the $F = 3$ to $F' = 4$ saturation feature, the $F = 3$ to $F' = 3,4$ crossover feature, the $F = 3$ to $F' = 2,4$ crossover feature and the $F = 3$ to $F' = 3$ saturation/hyperfine pumping feature. The polarisation spectroscopy signal shows only one zero-crossing within a 400MHz range about the $5S_{1/2}$ F=3 to $5P_{3/2}$ $F' = 4$ transition, which is the trap transition for the magneto-optical trap. This provides an excellent signal for locking a laser.

Figure 2.6 shows a polarisation spectroscopy signal for the trap laser, along with a Doppler-broadened saturated absorption/hyperfine pumping [19] spectrum for

frequency reference, for the ^{85}Rb $5S_{1/2}$ $F=3$ to $5P_{3/2}$ $F'=2,3$ and 4 transition, obtained from the experimental set-up shown in Figure 2.5. To obtain the polarisation spectroscopy signal, the voltages from the photodiodes are subtracted using a differential amplifier; the absorption spectrum is the sum of the signals from the two photodiodes. The main features of the polarisation spectroscopy signal are: the single zero-crossing for over 200 MHz each side of the ^{85}Rb $5S_{1/2}$ $F=3$ to $5P_{3/2}$ $F'=4$ transitions; and the linear region around this transition of over 40 MHz and a peak-to-peak value of over 0.5 V.

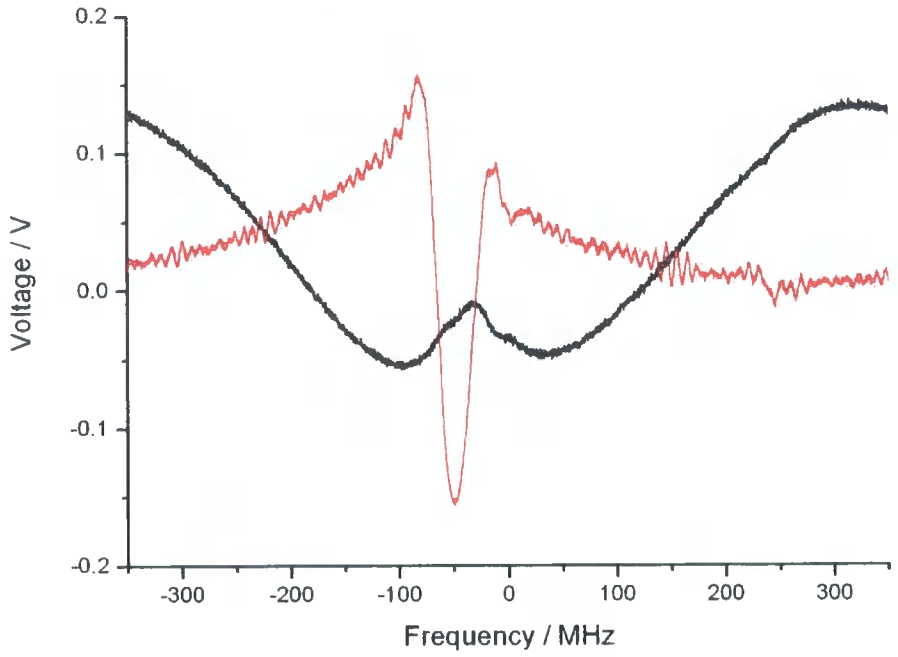

Figure 2.7. A polarisation spectroscopy signal (red) and saturated absorption/hyperfine pumping [19] signal (black) of the ^{85}Rb $5S_{1/2}$ F=2 to $5P_{3/2}$ $F'=1,2$ and 3 transition. The frequency is referenced relative to the $5S_{1/2}$ F=2 to $5P_{3/2}$ $F'=3$ transition, which is the frequency of interest for repumping in the magneto-optical trap. The repumping laser is locked to the zero-voltage point occurring on the sharp slope that passes through zero and decreases with frequency. An acousto-optic modulator is used to shift the repumping laser's frequency from the locking frequency to the desired frequency (sections 2.1.7 and 2.1.8).

Figure 2.7 shows a polarisation spectroscopy signal for the repumping laser, (along with a Doppler-broadened saturated absorption/hyperfine pumping [19] spectrum for frequency reference), for the ^{85}Rb $5S_{1/2}$ $F=2$ to $5P_{3/2}$ $F'=1,2$ and 3 transitions, obtained from the experimental set-up shown in Figure 2.5. This polarisation

spectroscopy signal is comparable to that for the trap laser, but in this case the main zero-crossing does not occur upon the closed transition. Instead, the largest peak-to-peak crossing arises around the cross-over feature that occurs half-way between the $5S_{1/2}\ F=2$ to $5P_{3/2}\ F'=2$ transition and the $5S_{1/2}\ F=2$ to $5P_{3/2}\ F'=3$ transition. The zero-point of the signal is dependent on the intensity balance between the two photodiode signals. In practice, manipulating the angle of the Rb vapour cell relative to the probe beam enables one to adjust the zero-point as required.

To enable the lasers to be locked to the polarisation spectroscopy signal, a small amount of electronic manipulation was required. Figure 2.8 shows a circuit diagram of the electronic circuit used for locking.

The locking circuit consists of three main components: an integrator, a low-pass filter, and a bias box. The latter is present to provide an offset voltage to the piezoelectric transducer (PZT) of the laser. This offset is required to place the laser at a particular frequency: the frequency corresponding to the zero-point of the polarisation spectroscopy signal. The integrator acts to keep the laser at that frequency. The low-pass filter prevents the resonance frequency of the PZT being fed to the PZT, and was set with a frequency roll-off of approximately 44 Hz, less than a tenth of the first resonance frequency of the PZT. The loss in amplitude of high-frequency signal was not significant since there was more than sufficient gain available within the circuit.

Using the above method, both lasers were locked to a linewidth of <1 MHz (in 250 ms). These line-widths were measured from 250 ms-long oscilloscope traces of the difference between the two photodiode signals in the polarisation spectroscopy. A map of voltage to frequency was calibrated from the saturated absorption/hyperfine pumping spectrum.

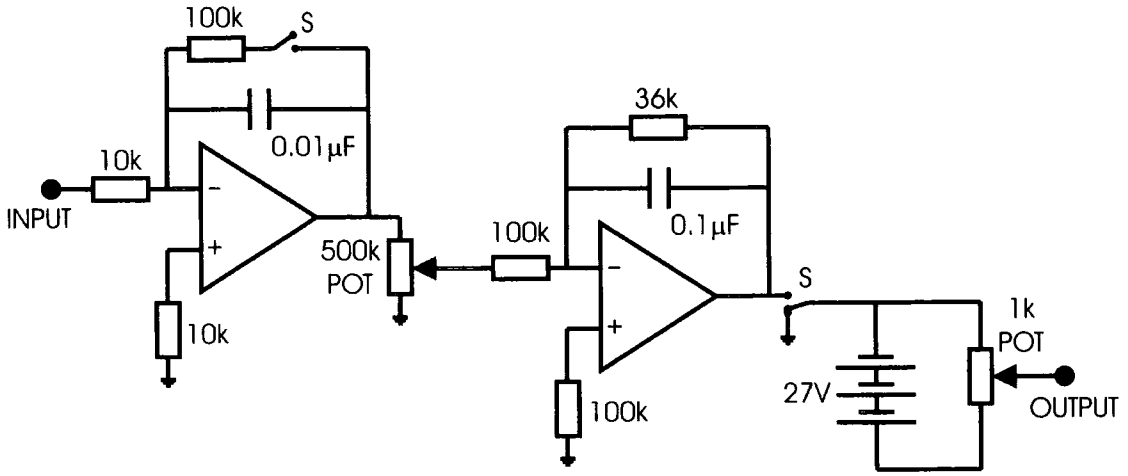

Figure 2.8. Laser Locking Circuit. Each operational amplifier is an AD548. All resistor values are in Ohms. The input (INPUT) for the circuit is the polarisation spectroscopy signal. The first op-amp acts as an integrator when the switch (S) is open and as an inverting amplifier when the switch is closed. A 500 kΩ potentiometer acts to vary the gain of the circuit. The second op-amp acts as a low-pass filter, which is present to prevent the resonance frequency of the PZT on the laser being fed to the PZT. The frequency roll-off of the filter was approximately 44 Hz, chosen as less than a tenth of the first-order resonance frequency of the PZT. The 27 V bias section of the circuit is constructed from three 9 V batteries. This bias section adds the required offset voltage to the PZT for the laser to produce the frequency to which it is to be locked (the preceding sections of the circuit then act to keep the laser at that frequency). The output (OUTPUT) of the circuit is fed directly to the PZT on the laser.

2.1.7 Optical Layout and Components

Optical Bench Plan View and Optical Components

An assortment of optics was used in this experiment: Table 2.1 displays the major optical components and their suppliers, (components being rated at 780 nm where applicable). The following section details the use of these components in the experiment.

Figure 2.9 shows a plan view of the optical set-up used in this experiment. The trap laser is locked using polarisation spectroscopy [15]. Approximately 600 μW of trap light is siphoned to pass twice (using a double-pass technique shown in section 2.1.8) through an acousto-optic modulator (AOM1) and into the polarisation spectroscopy set-up, which was detailed in section 2.1.6. The rest of the trap light is divided into

Optical Component	Supplier/Manufacturer
Dielectric Mirrors	LaserOptik
Lenses (Anti-Reflection Coated)	Comar
Polarising Beam Splitting Cubes	CVI and Comar
Half- and Quarter-wave-plates	CVI and Comar
Anamorphic Prisms	Comar
Optical Isolators	Linos Photonics
Opto-mechanics	Thorlabs and in-house
Acousto-optic crystals	Isle Optics

Table 2.1. Table of main optical components and suppliers.

half; each half is passed twice (using the double-pass arrangement in section 2.1.8) through a (separate) AOM (AOM2 and AOM3), then through (separate) expansion optics, to give each a $1/e^2$ beam radius of 15 mm. Each half is then split equally into three separate beams, giving six in total. The three beams from one half are sent to the bottom three MOT ports of the vacuum chamber; the three beams from the other half are sent to the top three MOT ports of the vacuum chamber (detailed in section 2.1.11). The use of two separate AOMs allows independent variation of the frequency of the upper and lower MOT beams, specifically for the moving molasses stage of the experiment, (detailed in section 2.2).

The 0^{th} order diffraction light from one of the trap AOMs (AOM3) was double-passed through another AOM (AOM4). The output light from AOM4 was used for optical pumping and imaging. Indeed, AOM4 effectively counteracts the effects of AOM1 in the polarisation spectroscopy arm by bringing the AOM4 output light to resonance with the $5S_{1/2}$ $F = 3$ to $5P_{3/2}$ $F' = 4$ transition.

The repumping laser was also locked using polarisation spectroscopy [15]. Repumping light was added to all six of the trap beams, ensuring that the repumping light was present over the whole cross-section of the trap beams. Since the lock-point of the repumping laser was approximately 80 MHz from the desired repumping frequency, a single-pass through an AOM (AOM5) was used to change the laser frequency to the required repumping frequency.

Details of the laser beams passed through the vacuum chamber can be found in section 2.1.11.

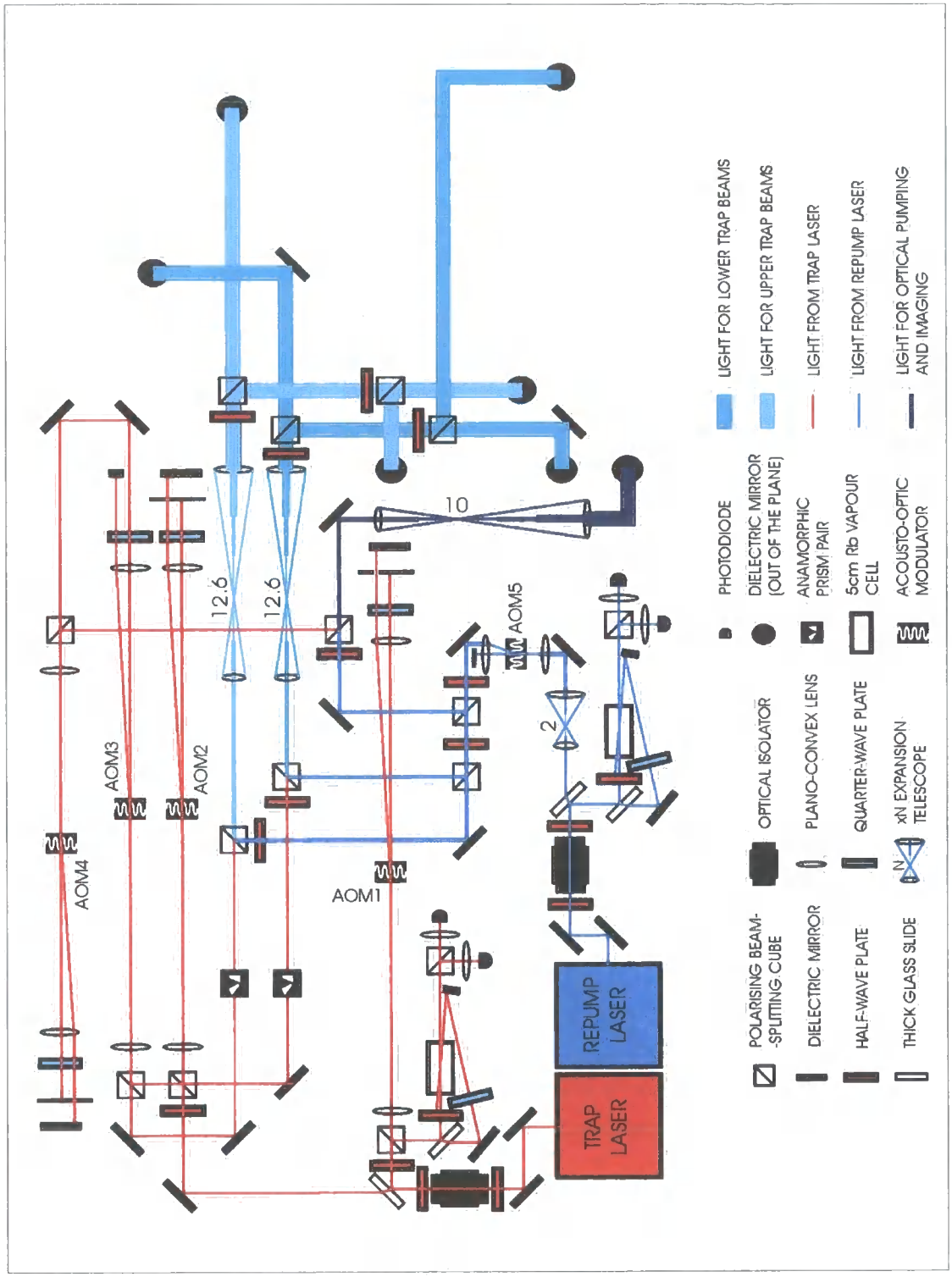

Figure 2.9. Optical Bench Plan View. A small portion of light was siphoned from a beam emanating from the Trap Laser, then double-passed through an Acousto-optic Modulator (AOM), before being used in polarisation spectroscopy. The remainder of the trap beam (~ 40 mW) is split in half. Each half is passed twice through a (separate) AOM, before being sent through expansion optics and then to the vacuum chamber. Light from the Repump Laser was added equally to the two arms of trap light, with the repumping frequency being locked using polarisation spectroscopy and set with a single pass through an AOM.

2.1.8 Radio-Frequency Electronics and Acousto-optic Modulators

Acousto-optic modulators (AOMs), and their accompanying radio-frequency (RF) electronics were used to change the frequency and intensity of laser beams to those required for different phases of the experiment. Detailed below are the optical set-up; the RF-electronics; and the relevant system efficiency and stability.

Optical Set-up for AOMs

Figure 2.10 shows the optical set-up used for the AOMs. This set-up enables the frequency of the input light to be increased by 120-180MHz (along with the RF electronics detailed below), and crucially this 'double-pass' arrangement produces no change in the direction of the output beam as the frequency is varied. An input lens (to the AOM) with a short focal length (< 20 cm) produces noticeably lower diffraction efficiency than a lens with higher focal length. For this reason, an input lens with a 50 cm focal length was used on the input of the AOM.

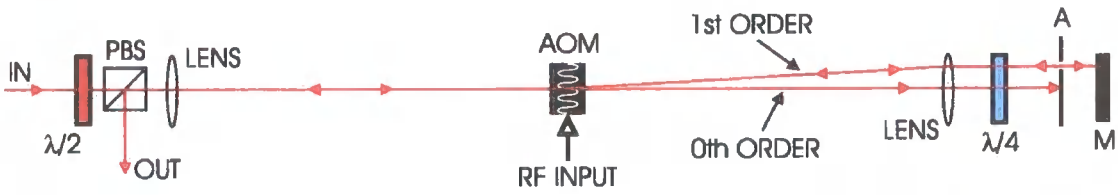

Figure 2.10. Optical Set-up for AOMs in a 'double-pass' arrangement. i.e. that the 1st-order diffracted light is passed through the same AOM twice before being output from the system. The polarisation of the light entering the system (IN) is set using the half-wave plate (λ/2) such that the maximum amount of light is transmitted by the polarisation beam splitting cube (PBS). A LENS (f = 50 cm) is used to focus the light into the AOM. The RF INPUT to the AOM causes a travelling wave within the AOM crystal, which causes Bragg diffraction of the laser beam. The 1st-order picks up a frequency shift equal to the frequency of the RF INPUT, whose power dictates the diffraction efficiency. Although other orders are present, the 1st-order and 0th-order are dominant when the optical alignment is optimised for this use. The 0th-order is blocked at the aperture A. The 1st-order is collimated by a second LENS (f=50 cm) and retro-reflected by a mirror (M). The 1st-order then passes back through the AOM, therefore being frequency shifted from the input light (IN) by twice the frequency of the RF INPUT. A quarter-wave plate (λ/4) is used to manipulate the polarisation such that the retro-reflected 1st-order is reflected by the PBS for further use in the experiment (OUT).

As a note, the above optical set-up was used for both Trap AOMs, the Polarisation Spectroscopy AOM, and the Imaging AOM. However, the Repumping AOM used

only a 'single pass' through the AOM since a frequency change of only approximately 80 MHz was required. Specific AOMs on the optical bench were detailed in section 2.1.7.

Using the above optical system and the below RF electronics the peak 'double pass' efficiency (i.e. the percentage value of the output divided by the total input) was 73 ± 1 %.

RF Electronics

Figure 2.11 shows a schematic of the RF electronics used for three (both Trap AOMs and the Polarisation Spectroscopy AOM) of the five AOM systems on this experiment. The other two AOM systems (the Repumping AOM and the Imaging AOM) both use an Isle Optics SD-100 RF driver to supply the acousto-optic crystal. All five acousto-optic crystals are Isle Optics LM080 crystals.

A National Instruments PCI-6713 Analogue Output card was used to control the frequency output of a Minicircuits ZOS-100 voltage controlled oscillator (VCO) via a voltage control box almost identical to that used by Littler *et al.* [20]. The intensity of the RF input to the AOM crystal was controlled using a Minicircuits ZX73-2500 voltage-variable attenuator (controlled by a line from the National Instruments PCI-6713). The RF power is amplified using a Minicircuits ZHL-3A RF amplifier before being passed into the AOM crystal.

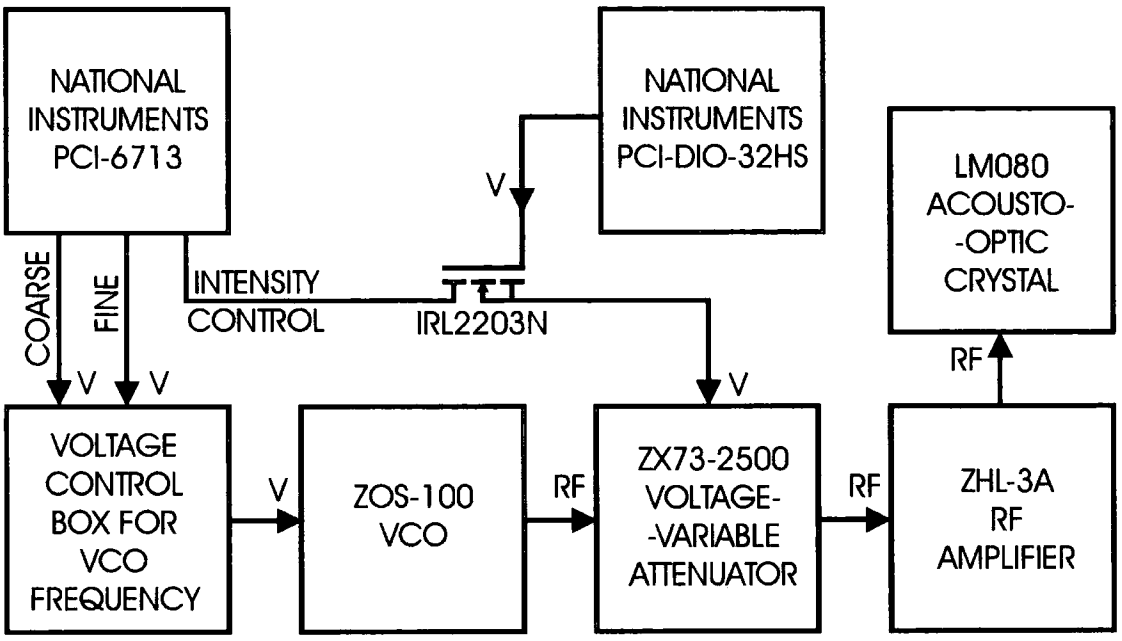

Figure 2.11. Schematic of the RF Electronics used to supply the acousto-optic crystals. V denotes a voltage input, RF denotes a radio-frequency input. A NATIONAL INSTRUMENTS PCI-6713 Analogue Card is used to provide a COARSE and a FINE voltage to a VOLTAGE CONTROL BOX, which is almost identical to that used by Littler *et al.* [20]. The output from the control box supplies a voltage controlled oscillator (Minicircuits ZOS-100 VCO), which produces an RF output dependent on the input voltage. The VCO output is passed into a Minicircuits ZX73-2500 VOLTAGE-VARIABLE ATTENUATOR, which can be used to attenuate the RF power to the LM080 ACOUSTO-OPTIC CRYSTAL, and hence control the intensity of the output light from the AOM optical system. This intensity was controlled in two ways: firstly an analogue voltage from the NATIONAL INSTRUMENTS PCI-6713, which was used for intensity ramps; and secondly a TTL on/off capability from a NATIONAL INSTRUMENTS PCI-DIO-32HS digital output card (via a IRL2203N FET) – this was done for ease in the programming of LabVIEW, which controlled the experiment (section 2.1.14). The RF output from the ZX73-2500 was amplified by a Minicircuits ZHL-3A RF AMPLIFIER before being passed to the LM080 ACOUSTO-OPTIC CRYSTAL through which the laser beams passed.

Control and Stability

The two most important AOM systems were those for the Trap beams, which formed the MOT, controlled optical molasses, and facilitated, crucially, the moving molasses phase of the experiment. Figure 2.12 shows the variation of frequency with supply voltage for the Upper and Lower Trap AOMs, which both used an RF system like that shown in Figure 2.11. As can be seen, the two AOMs are separated by almost 0.5 MHz at an input of 0.0 V despite being set identically at an input of 9.5 V. One must take into account any frequency difference for both the optical molasses stage

(section 2.1.17), where the AOMs will be detuned from a starting point of 80 MHz, and the moving molasses stage (section 2.2) since 0.5 MHz corresponds to a significant change in launch height.

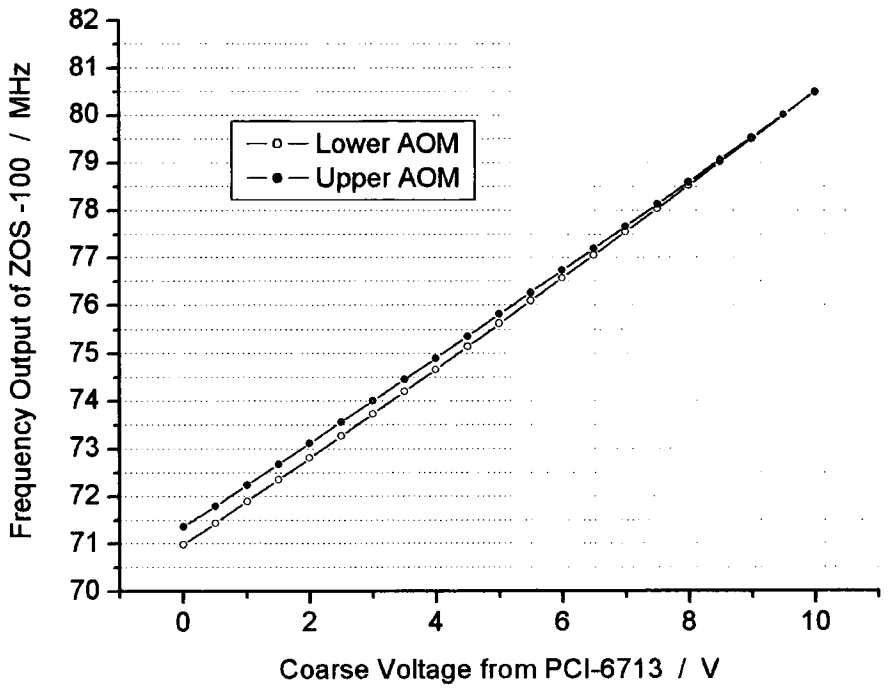

Figure 2.12. Graph of frequency output of Minicircuits ZOS-100 VCO against Coarse voltage output from the National Instruments PCI-6713 Analogue Card. Each voltage control box [20] was set so that the frequency output was 80.000 MHz at a Coarse voltage value of 9.5 V. As can be seen, the two AOMs are separated by almost 0.5 MHz at an input of 0.0 V despite being set identically at an input of 9.5 V. One must take into account any frequency difference for the moving molasses stage of the experiment (section 2.2).

Figure 2.13 shows two graphs depicting the frequency stability over time for the ZOS-100 VCOs supplying the two Trap AOMs. The stability is important when considering the launch height achieved by the moving molasses stage of the experiment (section 2.2). Over a period of 400 minutes, with laboratory air-conditioning operating at 19 °C, the frequency difference is typically less than 2 kHz when the difference is set to zero at zero minutes. As a guide, a 1 kHz drift in the difference approximates to a change in launch height of approximately 1 mm.

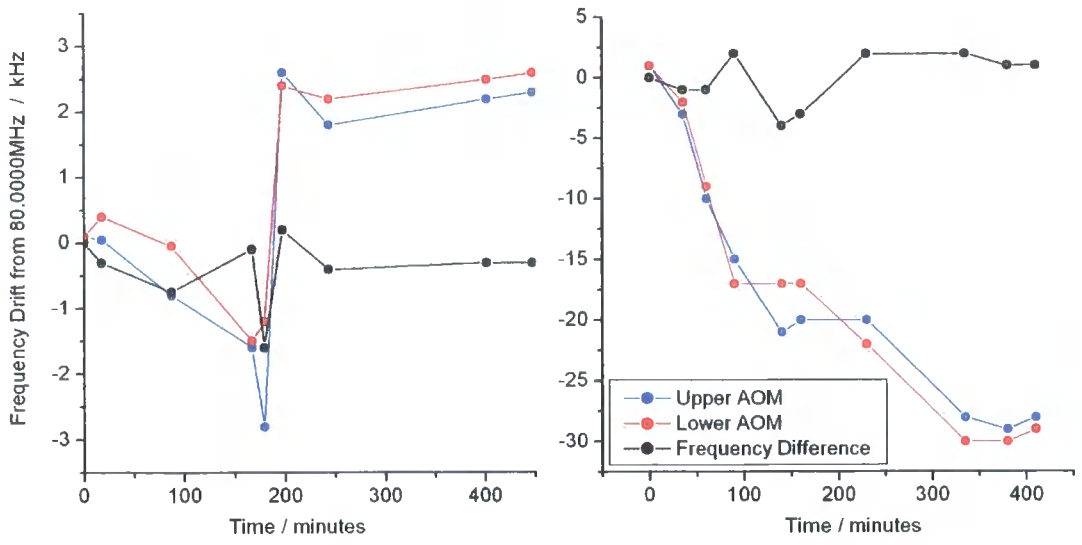

Figure 2.13. Graph of frequency stability over time for the ZOS-100 VCOs supplying the two Trap AOMs that are used for the moving molasses stage. (left) typical frequency drift over time with laboratory air-conditioning on at 19 °C. (right) frequency drift over time with the laboratory air-conditioning switched off at zero minutes. Both AOMs were set to 80.000 MHz at zero minutes. The most important factor is the frequency difference: 1 kHz corresponds to a change in height of approximately 1 mm for the moving molasses stage used in this experiment (section 2.2). When the air-conditioning is on, the frequency drift is typically less than 2 kHz over a period of 400 minutes. The important result from both graphs is that the fluctuations for both AOMs follow a common trend.

6.2.2 The Vacuum System

Vacuum System Schematic

Figure 2.14 shows a schematic of the vacuum system used in this experiment and Figure 2.15 shows a photograph of the same system. A turbomolecular pump, backed by a rotary vane pump, was attached to an all-metal valve that was connected to the T-piece during pumping and baking. The chamber is topped by a 2.6 x 2.6 x 8.3 cm, 0.5 cm-thick-quartz cell that emanates vertically from a twelve-way cross. The 12-way cross was specially commissioned (with Kurt J. Lesker Company) for this experiment; it has two vertical ports and four horizontal ports, constituting a six-way cross of three opposing pairs, each pair being mutually orthogonal to the other pairs.

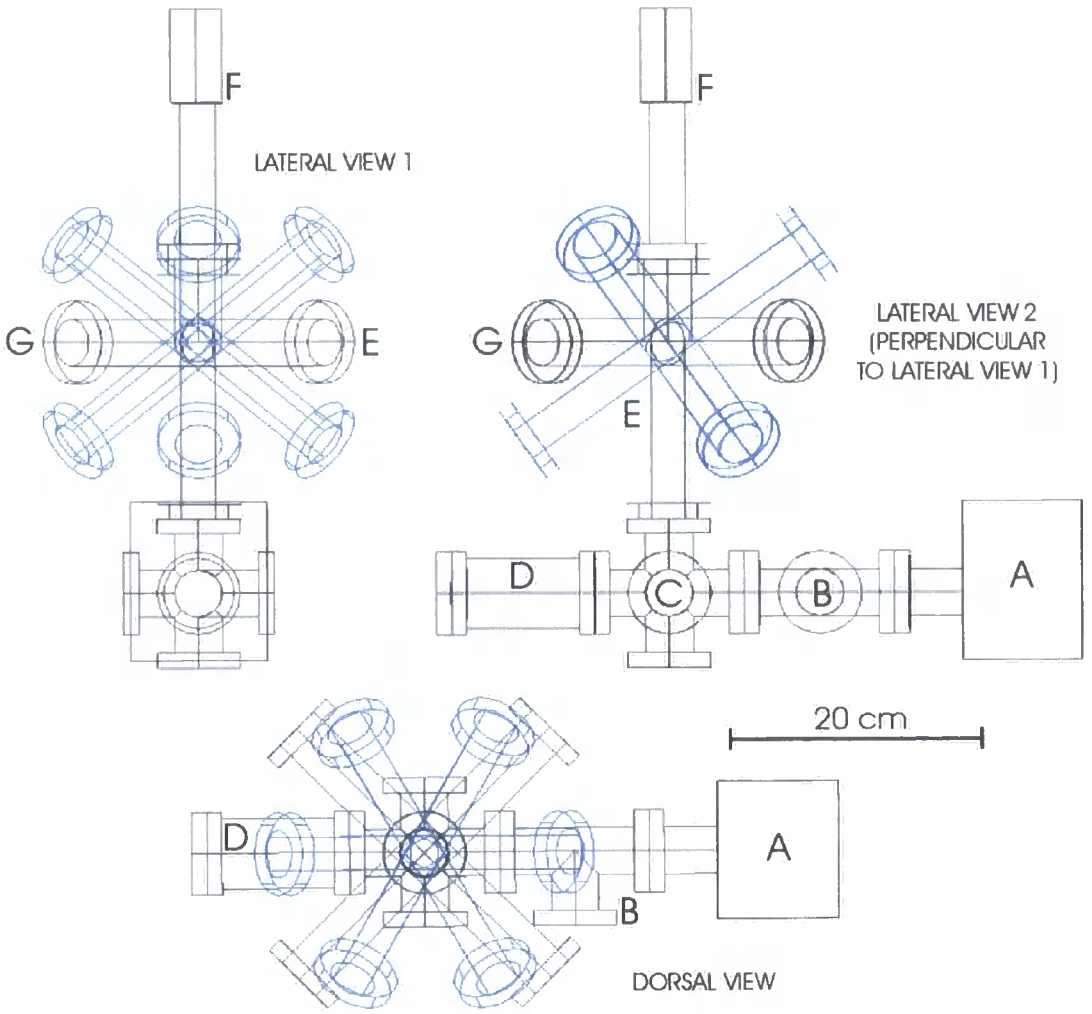

Figure 2.14. Vacuum System Schematic. The vacuum system is constructed from DN40 components made from non-magnetic stainless steel. The flange connections are 70 mm in diameter. A – Ion Pump [Varian Vaclon Plus 40 Diode Ion Pump]; B – T-piece that connects to an all-metal valve, which, during pumping and baking, connects to turbomolecular pump backed by a rotary vane pump; C – Six-way cross: the three non-connected flanges on the six-way cross held anti-reflection coated, quartz viewports; D – Ion Gauge [Varian UHV-24 Ionization Gauge] housed in a nipple; E – Twelve-way cross; F – Quartz cell (2.6 x 2.6 x 8.3 cm), which connects to the twelve-way cross on a glass-to-metal seal. The blue flanges denote the six magneto-optical trap laser beam ports, which are at such angles for the purposes of the Moving Molasses phase in the experiment (see section 2.2). Quartz viewports were attached to all but three of the flanges on the twelve-way cross. One of the horizontal ports on the twelve-way cross (G) housed a 10 A-max. 4-pin electrical feed-through that supplied current to a rubidium dispenser (the mounting of which is discussed below).

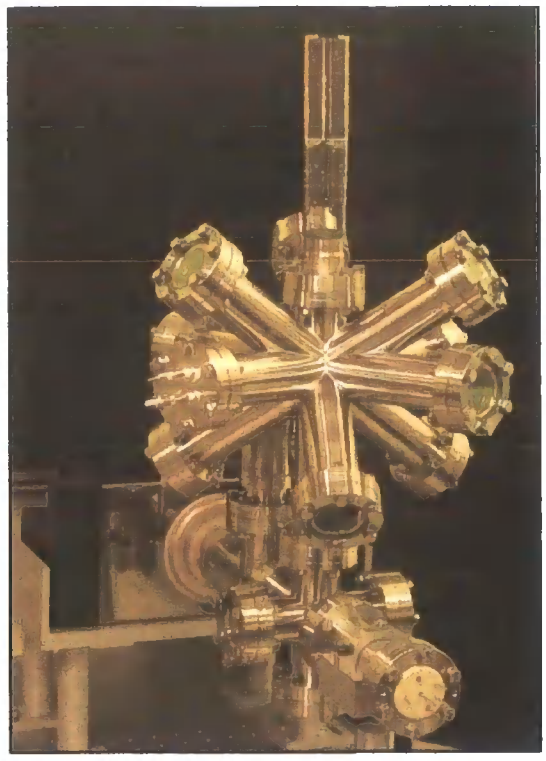

Figure 2.15. Photograph of the vacuum chamber detailed in the schematic in Figure 2.14. The main feature of the system is the specially commissioned 12-way cross, which has ports at specific angles for the purpose of a Moving Molasses phase in the experiment (see section 2.2).

The other six ports of the 12-way cross also form a six-way cross of three mutually orthogonal opposing pairs, but this second cross is rotated (relative to the first) such that all six ports have the same (acute) angle to the vertical, $\theta = \cos^{-1}\left(\frac{1}{\sqrt{3}}\right) = 54.7°$.

The purpose of the rotation of this second six-way cross is for the Moving Molasses stage of the experiment, which is detailed in section 2.2. One of the horizontal ports on the 12-way cross has a 10 A-max. 4-pin electrical feed-through to carry current to a rubidium dispenser (mounting details are described below) and nine quartz viewports attached to it. The 12-way cross sits on a 6-way cross that has quartz viewports to enable a vertical beam to be passed through the chamber, and, if the need arises, to detect atoms released from a magneto-optical trap situated at the centre of the 12-way cross (which is approximately 20 cm from the centre of the 6-way cross). An ion pump [Varian Vaclon Plus 40 Diode Ion Pump] and an ion gauge [Varian UHV-24 Ionization Gauge] are present for low pressure attainment and pressure measurement respectively.

Vacuum Preparation

The stainless steel and ceramic vacuum components used in this experiment required cleaning so as to remove any residues that could affect the speed at which low pressure was attained. A cleaning process utilising Decon90[1] (a vacuum compatible cleaning product), distilled water and a sonic bath is detailed below [21]. For components not compatible with Decon90, Neutracon[2] was used in its place.

i. Overnight soaking in a Decon90 solution (10 % Decon90, 90 % distilled water).
ii. Sonic bathe in a fresh 10 % Decon90, 90% distilled water solution for an hour.
iii. Overnight soaking in distilled water.
iv. Sonic bathe in fresh distilled water for an hour.
v. Heated with a heat gun to evaporate residue water.
vi. Wrapped in clean aluminium foil until needed for assembly.

Vacuum Assembly

UHV (Ultra-high Vacuum) technology was used as the basis for the vacuum chamber. Great care was taken not to get dirt or grease inside the chamber or around the inside of the flanges during assembly. Clean, plastic, powderless gloves were used to avoid finger grease contaminating the chamber, which would increase the time needed to attain low pressure. Gasket clips proved most useful for non-vertical flange connections.

Table of Vacuum Components

Table 2.2 shows a table of the components used in construction of the vacuum system.

[1] Decon90 made by Decon Laboratories Limited
[2] Neutracon is also manufactured by Decon Laboratories Limited

Section	Component
Main Structure	Ion Pump
	Twelve-way cross
	Six-way cross
	T-piece
	Nipple
	Electrical Feed-through
	Ion Gauge
	Quartz Cell
	Quartz Viewports
Rubidium Dispenser Mounting	Rubidium Dispenser
	Macor Ceramic
	Kapton Wire
	Barrel Connectors
	Stainless Steel Screws
	Aluminium
Cables	Ion Pump Cable
	Ion Gauge Cable
Copper Gaskets	20 Copper Gaskets

Table 2.2. Table of the components used for construction of the vacuum chamber in this experiment.

Vacuum Bake-out

After assembly, the vacuum chamber was evacuated using a turbomolecular pump [Pfeiffer TMU 065] backed by a rotary vane pump [Pfeiffer DUO 2,5A] to a pressure of 1 x 10^{-5} Torr. A Residual Gas Analyser[3] and a Helium line were used to check for any leaks. Then the whole of the vacuum chamber was baked in a purpose-built oven. The baking temperature was limited by the quartz viewports, which were rated with a maximum temperature of 200 °C. The vacuum chamber underwent two heating/cooling cycles.

The temperature inside the oven was increased at a rate of 1 °C/min from room temperature to 180 °C. This heating rate ensured an even temperature across the chamber, preventing cracks on the viewports, which were specified to have less than a 2 °C temperature gradient across them. The temperature was kept at 180 ± 2 °C for four days, and was measured by two thermocouples placed in the oven against the chamber.

[3] Stanford Research Systems RGA100

After four days the pressure inside the chamber was 1.0×10^{-6} Torr and the oven temperature was allowed to decrease to room temperature at a rate of 1 °C/min. However, the chamber cooled more slowly: an average rate of approximately 0.7 °C/min. At room temperature the pressure was 2.3×10^{-9} Torr.

At this point, the ion pump was turned on and the chamber valved-off using the all-metal valve. After two further days the pressure was 3.7×10^{-10} Torr.

The Rubidium dispenser inside the vacuum system needed to be degassed and it was decided that this would be done whilst the chamber was hot so that any contaminants released from the dispenser would be less likely to stick to the walls of the vacuum chamber, specifically the viewports. The ion pump was turned off and the turbo and rotary pumps re-started. The all-metal valve was re-opened, which gave a pressure of 1.0×10^{-5} Torr in the chamber.

The temperature was raised at a rate of 1 °C/min to 180 °C and maintained for three days at which point the pressure in the chamber was 9.6×10^{-7} Torr. The temperature was then raised, at 1 °C/min, to 200 °C.

The source of atoms for this experiment was a rubidium dispenser[4], which releases rubidium atoms through Ohmic heating when a sufficient current is passed through the dispenser. The Rubidium dispenser was degassed in accordance with the method used by Fortagh *et al.* [1], which incorporates small current increases towards a desired value without allowing the pressure to rise significantly above the background value. The increments of current were based on a dispenser test done at room temperature without letting the pressure rise by more than an order of magnitude. It took eleven hours to reach 5 Amps of current through the dispenser. The current was left at 5 A for five hours and the pressure in the chamber was then 7.1×10^{-6} Torr. Then the current was switched off.

The chamber was then cooled, as before, to room temperature, reaching a pressure of 3.9×10^{-9} Torr before the ion pump was switched on and the chamber valved-off from the turbo and rotary pumps. Within fifty hours the pressure was 1.9×10^{-10} Torr.[5] Figure 2.16 shows the final cooling curve.

The ultimate pressure of the chamber was 9.5×10^{-11} Torr.

---

[4] The rubidium dispenser is manufactured by SAES Getters Group.

[5] The ion gauge was not degassed before the chamber was valved-off, which probably hindered the speed at which the pressure decreased.

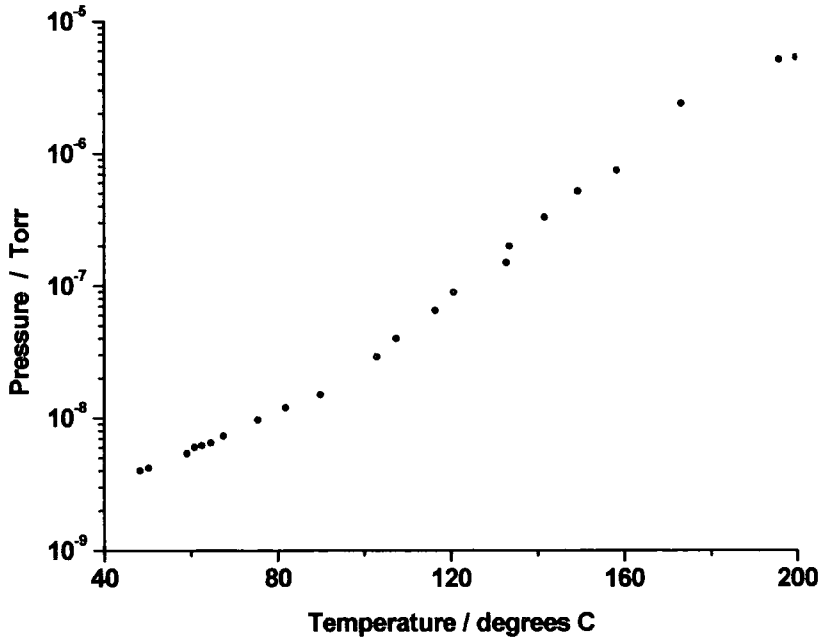

Figure 2.16. The final cooling curve for the vacuum system, (after baking for a second time). From an initial temperature of 200 °C and pressure 5 x 10^{-6} Torr, the chamber cooled to below 50 °C and to a pressure of 4 x 10^{-9} Torr, at which point the ion pump was turned on.

Rubidium Dispenser Mounting

Figure 2.17 shows a schematic of the mounting of a rubidium dispenser on a 10 A-max. 4-pin electrical feed-through and Figure 2.18 shows a photograph of the mounting. The rubidium dispenser operates by current induced heating: rubidium chlorate heated to evaporate rubidium vapour into the vacuum chamber. The dispenser is clamped, along with Kapton wire[6], by two pieces of Macor ceramic held by stainless steel screws that screw into a 35 mm diameter, 10 mm thick Macor ceramic disk. The Kapton wire is connected to the feed-through wires by BeCu barrel connectors. A piece of stainless steel wire was positioned such that it would prevent a direct line of sight between the dispenser and the centre of the 12-way cross, the site of the magneto-optical trap (MOT), to lower the probability that high velocity atoms would hit atoms trapped in the MOT.

[6] Kapton wire is manufactured by Caburn-MDC.

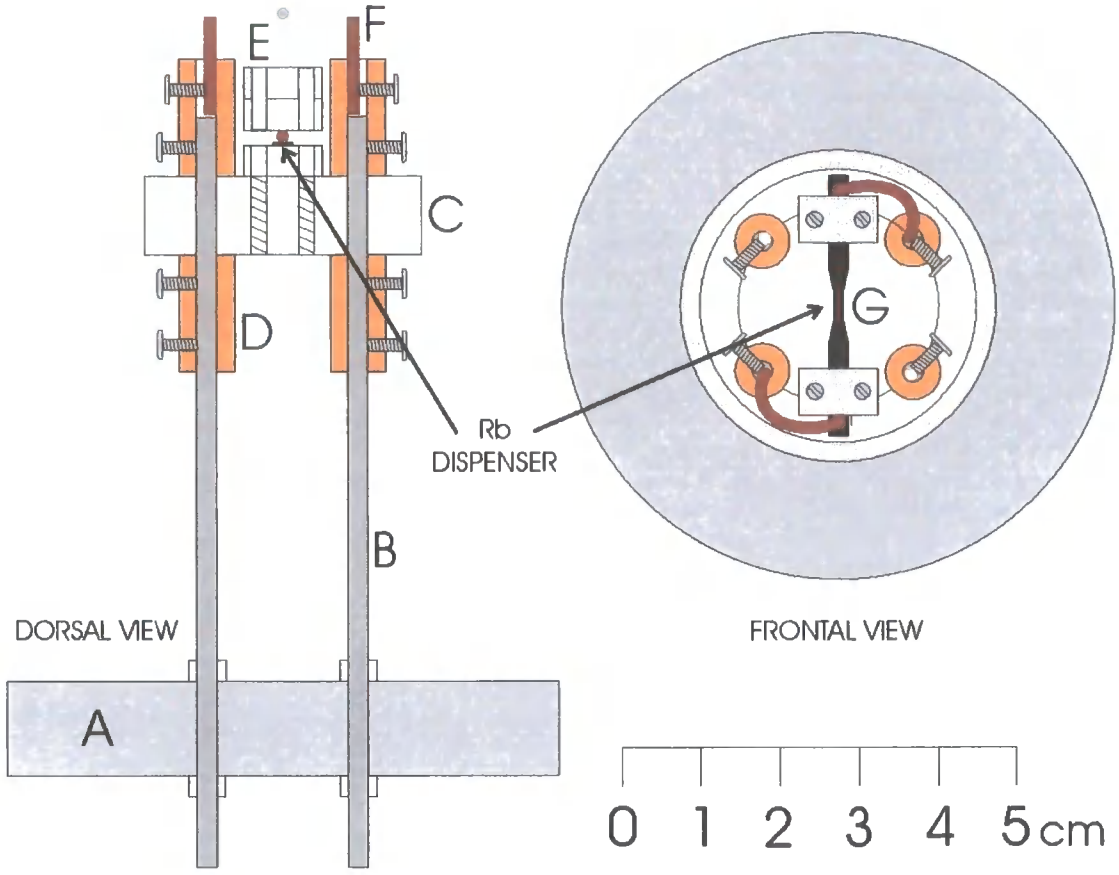

Figure 2.17. Schematic of the rubidium dispenser mounting and 10 A-max. 4-pin electrical feed-through. Through the CF70 Flange (A) pass the feed-through wires (B). A 35 mm diameter, 10 mm thick disk of Macor ceramic (C) slides onto the feed-through wires and is held by eight BeCu barrel connectors (D). A pair of 10 x 8 x 6 mm Macor ceramic pieces, topped by a similar piece of aluminium, clamps the rubidium dispenser and Kapton wire together (E). Stainless steel screws pass through M2 Clearance holes in the aluminium and ceramic pieces into M2 Tapped holes in the ceramic disk. Kapton wire (F) carries current from the feed-through wires to the dispenser. The two barrel connectors on top of the ceramic disk that do not carry current hold a piece of wire that passes directly over and parallel with the active region of the dispenser (G). The wire is not shown fully on the diagram on the right-hand side of the figure so as not to obscure the view of the dispenser, but can be seen clearly in Figure 2.18.

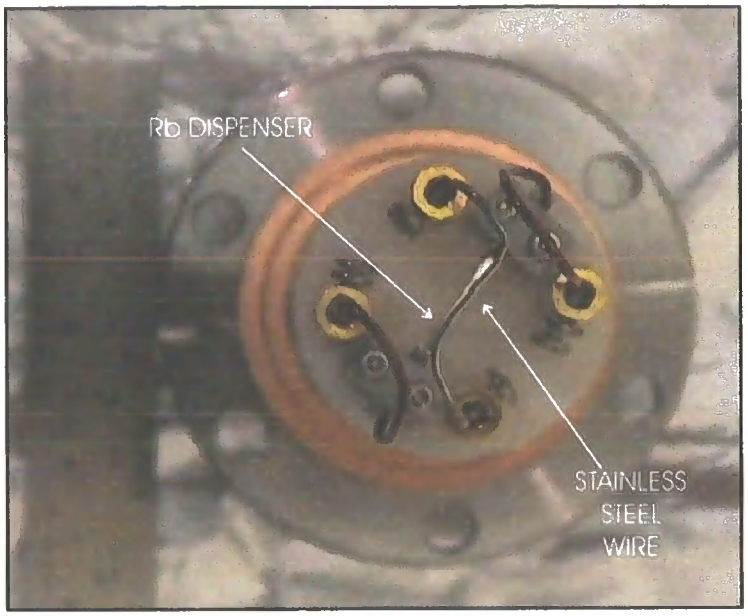

Figure 2.18. Photograph of the mounting of the rubidium dispenser, (frontal view). The barrel connectors and ceramic all sit on the Macor ceramic disk. The Kapton wire (brown) carries current from the feed-through to the dispenser, which is clamped between two ceramic plates at each end. The copper gasket below the ceramic disk was placed there to protect the knife-edge on the flange while the mounting was assembled. Over the top of the active region of the dispenser is a piece of stainless steel wire, which prevents direct line-of-sight between the dispenser and the centre of the 12-way cross, the place of the magneto-optical trap (MOT); this is to lower the probability of high velocity atoms from the dispenser hitting the cold atoms in the MOT.

2.1.10 Cancellation of Unwanted Magnetic Fields

There are two main sources of unwanted magnetic fields in this experiment - the Earth's magnetic field and the magnets on the ion pump. The cancellation of unwanted fields is important for two reasons: so that the MOT's magnetic centre and optical centre are co-incident, and so that there are minimal gradients that can affect atoms in freefall.

Mu-metal shield for the ion pump

The major source of unwanted magnetic field gradient in the region of the chamber was the magnets on the ion pump. This field was minimised using a mu-metal shield (from MSL Magnetic Shields), which surrounded the ion pump. The field was measured in two places (around the MOT region and around the quartz cell on top of

the vacuum chamber), both with and without the mu-metal shield. Without the shield, the fields measured were $B_{\mathrm{MOT}} = (0.35, 1.50, 0.70)$ Gauss and $B_{\mathrm{QUARTZ\,CELL}} = (0.20, 0.50, 0.70)$ Gauss. With the shield, the fields were $B_{\mathrm{MOT}} = (0.10, 0.10, 0.70)$ Gauss and $B_{\mathrm{QUARTZ\,CELL}} = (0.10, 0.10, 0.70)$ Gauss. Measurements were made to the nearest 0.05 Gauss. As can be seen, the shield eradicated the gradient seen in the x and y components (z being the vertical direction), but did not zero the field – this residual field is due to the Earth's magnetic field and any other magnetic bodies in the vicinity.

Cancellation of the Earth's Magnetic Field

Once the ion-pump's magnetic field had been minimised, the Earth's field dominated the remaining unwanted magnetic field. To cancel this field, three pairs of rectangular coils, were used (with current flowing in the same sense in each pair) [22]. Table 2.3 shows characteristics of the coils.

In reality, these coils were for ensuring the magnetic centre and the optical centre of the MOT were coincident, and not specifically to cancel the Earth's field. The coils were made to encompass a large volume so as to enclose the whole chamber, since atoms were to be transported through approximately 20 cm and unwanted magnetic gradients needed to be avoided.

	B_x	B_y	B_z (vertical)
Dimensions (cm)	50×78	50×103	80×105
Separation (cm)	103	84	60
No. of Turns	20	20	25
Typical Current (A)	0.7	2.0	1.7
Field Predicted with above current (G)	0.1	0.2	0.7

Table 2.3. Characteristics of the coils for cancelling the Earth's field. In reality, these coils are for ensuring the magnetic centre and the optical centre of the MOT are coincident.

2.1.11 Laser Beams through the Vacuum Chamber

Laser Beam Alignment and Properties

Figure 2.19 shows a schematic of the vacuum chamber discussed in section 2.1.9, along with the relevant laser beams for use in the experiment. The six MOT beams form three orthogonal, counter-propagating pairs. Consider that the six MOT beams are incident upon the centres of the faces of an imaginary cube, one beam per face: the vertical direction in the laboratory was the (1,1,1) direction [23], such that the acute angle of each MOT beam to the vertical was $\theta = \cos^{-1}\left(\frac{1}{\sqrt{3}}\right) = 54.7°$. Each MOT beam closely approximated a Gaussian profile, had a ($1/e^2$) radius of 15 mm, and 3 mW of trap light. Approximately 5 mW of repumping light was shared between the six MOT beams. The trap power difference between each beam was less than one part in fifty. Each of the six MOT beams passed through a quarter-wave plate set to give the correct circular polarisation for MOT operation.

Along with the MOT beams, there was one other laser beam through the chamber, a beam which was entirely vertical. This vertical beam doubles as both an optical pumping beam (OPB) and an imaging beam (IB) – their differing power requirements being met by the careful use of AOMs (see section 2.1.8). The OPB/IB was retro-reflected to minimise the trajectory disturbance of the launched atom cloud. The OPB/IB had a ($1/e^2$) radius of 12 mm. The OPB had an input power of 350μW, and the IB had an input power of 5.9 mW, the total power in each beam being double those values due to retro-reflection. 1mW of repumping light was added to the OPB/IB.

The beams could be switched on and off using computer control (section 2.1.14).

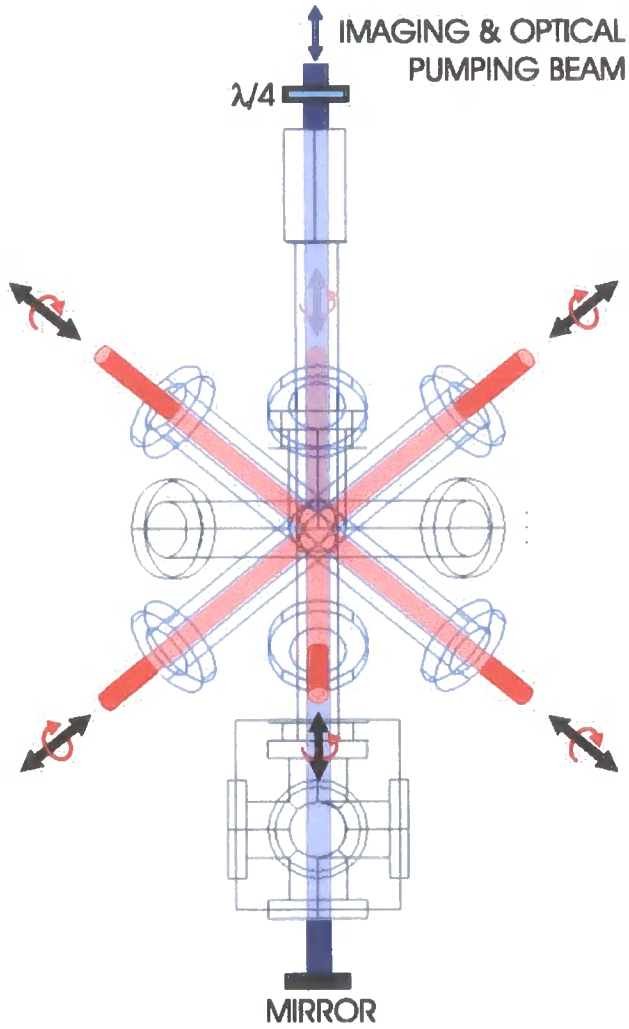

Figure 2.19. Schematic of the laser beams through the vacuum chamber. The six MOT beams, (three orthogonal, counter-propagating pairs), each have an acute angle to the vertical of 54.7 °. The Optical Pumping Beam (OPB) / Imaging Beam (IB) was a retro-reflected vertical beam, which allowed the atoms to be optically pumped and/or imaged during their ballistic flight. The OPB/IB was made circularly polarised with the use of a quarter-wave plate (λ/4). The six MOT beams also each passed through a (separate) quarter-wave plate (not shown) set to give the correct circular polarisation for MOT operation.

2.1.12 Magnetic Field for the Magneto-optical Trap

Magnetic Field Coils

The magnetic quadrupole field for the MOT was provided by two co-axial, current-carrying coils of equal radius. The coils carry current in the opposite sense to each other, their centres are separated by 18.0 ± 0.2 cm (the minimum separation given the

geometry of the vacuum chamber), and they have an inner radius of 3.8 cm. Each coil was constructed from 25 turns (in a 5×5 arrangement) of copper wire with a 3 mm-diameter circular cross-section and a 1 mm-diameter hollow bore. This hollow bore allows water-cooling of the coils. The copper wire was covered in heat-shrink to isolate electrically each turn of the coil. The coils were wrapped on a mechanical lathe on an aluminium former. Figure 2.20 shows a photograph of the MOT Coils mounted on the vacuum chamber.

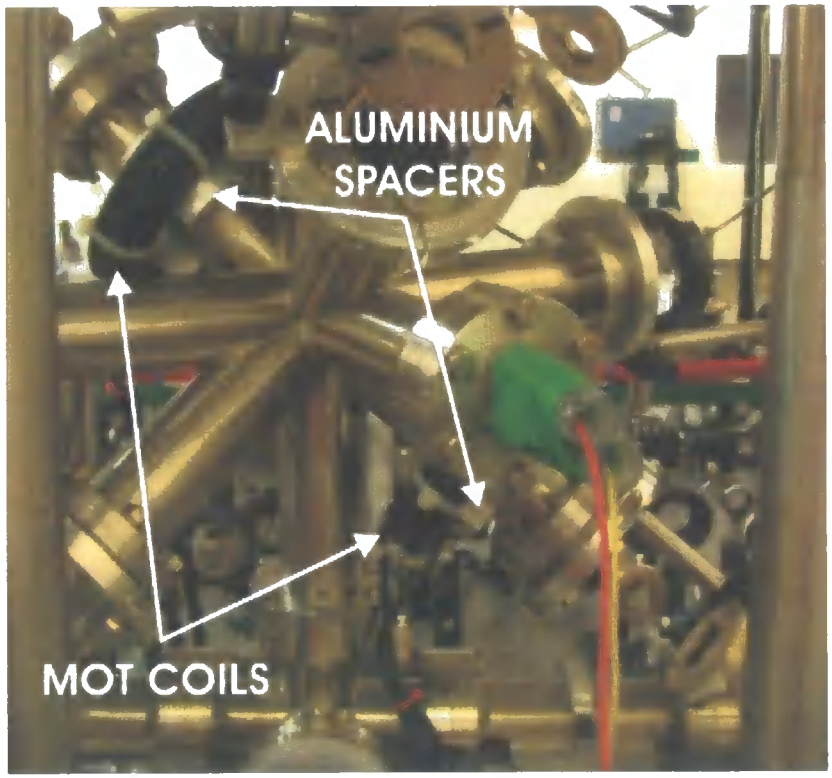

Figure 2.20. Photograph of the MOT coils mounted on the vacuum chamber. The MOT coils were wrapped on a mechanical lathe in an aluminium former. They are held together by large cable-ties and are secured into place by tight-fitting aluminium spacers, which are cut into segments to prevent Eddy currents upon coil switch-off.

The current for the coils was supplied by a Hewlett Packard 6260B DC Power Supply, which was in series with a water-cooled bank of three IRFP3703 FETs (each FET was quoted with $I_{D\max.} = 210$ A (the maximum allowed current through each FET) and $R_{DS} = 0.0028\ \Omega$ (the typical resistance of each FET when conducting fully)). The three FETs were in parallel and enabled the coils to be switched on and off (with a single TTL for the National Instruments PCI-DIO-32HS) for various experimental stages. In addition, a 203CNQ100R Schottky Rectifier diode was

placed in parallel with the MOT coils to prevent ringing upon switch-off. At typical currents, the coils took 5.2 ± 0.1 ms to switch-off to < 5 % of the operating current. This configuration for the MOT coils gave a magnetic field gradient of 0.182 ± 0.003 G cm^{-1} A^{-1}, (over a 2 cm distance through the centre of the two coil system), along the axis of the two coils, which is consistent with theoretical predictions. The MOT coils were typically operated at 50 A, which gave a magnetic field gradient of approximately 9 G cm^{-1} (see section 2.1.13).

2.1.13 MOT Characterisation

Typically several times 10^7 ^{85}Rb atoms were loaded into the MOT, with a (1/e) fill time of a few seconds, dependent on the current through the rubidium dispenser (~8.5 Amps). The maximum atom number was achieved with a detuning of $\Delta = -2\pi \times 13$ MHz from resonance with the closed $5S_{1/2}\ F = 3$ to $5P_{3/2}\ F' = 4$ transition, and a magnetic field gradient of 9 G cm^{-1}.

MOT Loading and Atom Number

For calculation of the atom number and fill-time, a photodiode was used to collect fluorescence from the MOT, as shown in Figure 2.21. In order to determine the

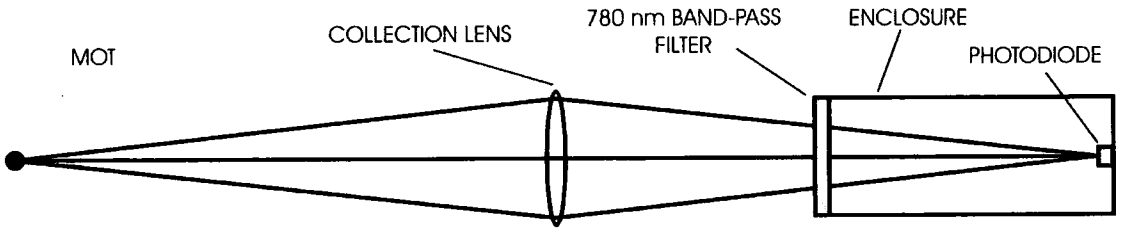

Figure 2.21. Collection of MOT fluorescence for atom number calculation. Fluorescence from the MOT was focused onto a 0.5 cm^2 photodiode using a convex 10 cm-focal-length, 50 mm-diameter lens, which was placed 20 cm from the MOT, and hence collects 1/256 of the MOT fluorescence. The collection lens was placed 20 cm from the MOT as this was the closest possible distance that was outside the vacuum chamber. The photodiode circuit was followed by an electronic gain circuit, giving a total transimpedance of $10^8\ \Omega$. A 780 nm band-pass filter, along with an enclosure, was used to keep any unwanted light from the photodiode. In addition, since the original circuit saturated once higher atom numbers were achieved, a 49%-transmission neutral density filter was placed before the band-pass filter, effectively halving the voltage output from the circuit for a given atom number.

current required for the Rb dispenser, fill curves were taken at various currents, initially at a detuning $\Delta = -2\pi \times 11$ MHz and a magnetic field gradient of 11 G cm^{-1}. These fill-curves are shown in Figure 2.22.

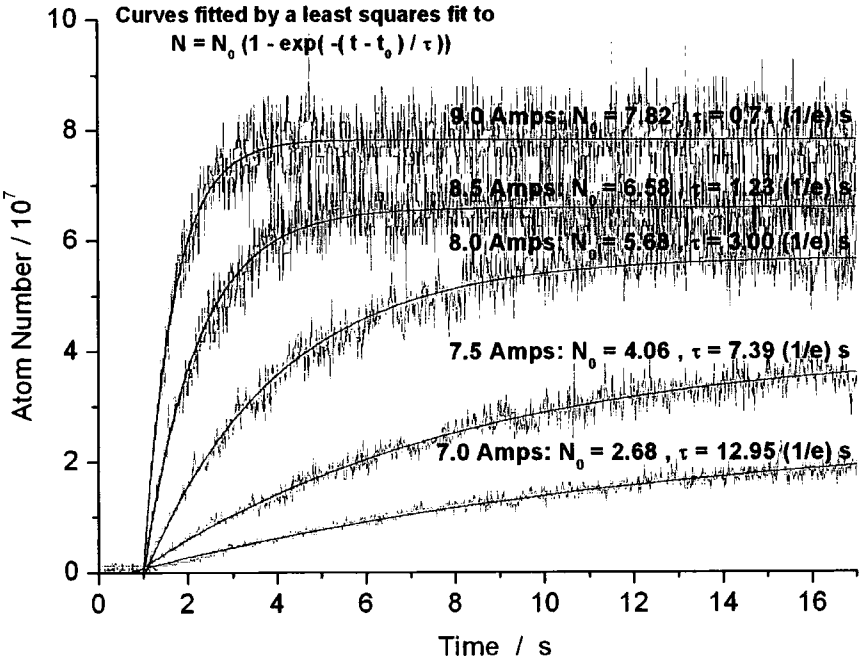

Figure 2.22. MOT fill-curves for a detuning of $\Delta = -2\pi \times 11$ MHz and a magnetic field gradient of 11 G cm^{-1}, i.e. atom number vs. time. The fill curves are taken using the photodiode in Figure 2.21, with the dispenser current ranging from 7.0 A to 9.0 A. The atom number was deduced using the calculation given in the main text. The grey lines are the raw data, and the black lines are least-square fits to that data.

The atom number was deduced using the following calculation.

The power P_{PD} incident on the photodiode in Figure 2.21 is proportional to the number of atoms N in the MOT. This power is related to the voltage output from the photodiode circuit V by,

$$P_{PD} = \frac{V}{SG} \tag{2.7}$$

where $S = 0.42 \pm 0.2$ A W^{-1} is the sensitivity of the photodiode and $G = 10^8\ \Omega$ is the total transimpedance of the photodiode circuit. The photodiode circuit consisted of two stages: firstly, a circuit that produced a voltage linearly proportional to the light incident on the photodiode, (with a gain of 10^4 on the voltage produced across the photodiode); and then a separate 10^4 gain stage. The sensitivity S of the photodiode was measured by shining a laser beam onto the photodiode (with electronics to

produce a voltage linearly proportional to incident light), and then calibrating the output voltage against the power of the laser beam measured by a Coherent FieldMate Power Meter.

The power P_{MOT} scattered by the atoms in the MOT is related to the number of atoms N by $P_{\mathrm{MOT}} = N\gamma E$, where γ is the scattering rate of the light per atom and $E = 2.6\times10^{-19}$ J is the energy per photon at 780 nm.

Therefore,

$$N = \frac{1}{\eta SGE\gamma}V, \tag{2.8}$$

where η is the collection efficiency of the optical system used to collect fluorescence, (Figure 2.21).

The optical system's efficiency η was a function of the transmission of the band-pass filter (67%); the transmission of the additional neutral density filter (49%); the transmission of the collection lens (90%), and the percentage of the light collected by the collection lens. Since the lens had a diameter of 50 mm and was located 20 cm from the MOT, the lens collected 1/256 of the light emitted from the MOT. Overall, $\eta = 0.0011$ (2 s.f.). It is assumed that no light scattered by the stainless-steel surface of the vacuum chamber reaches the photodiode.

The scattering rate γ is given (using the basic assumption of a two-level atom) by

$$\gamma = \frac{\Gamma}{2}\frac{I/I_{\mathrm{SAT}}}{1 + I/I_{\mathrm{SAT}} + 4\left(\frac{\Delta}{\Gamma}\right)^2}, \tag{2.9}$$

where $\Gamma = 2\pi\times5.9$ MHz [12, 24] is the inverse lifetime of the $5S_{1/2}$ to $5P_{3/2}$ transition in ^{85}Rb; I is the total intensity of the cooling laser beams at the centre of the MOT; I_{SAT} is the saturation intensity; and Δ is the detuning of the lasers from resonance with the cooling transition of $5S_{1/2}\ F=3$ to $5P_{3/2}\ F'=4$.

The MOT laser beams were discussed in section 2.1.11 and have a total peak intensity of approximately 50 W m^{-2}. For the calculations in this thesis, a value of $I_{\mathrm{SAT}} = 16$ W m^{-2} will be used, which is the saturation intensity of the stretched state transition of $5S_{1/2}\left|F=3, m_F=3\right\rangle$ to $5P_{3/2}\left|F'=4, m_{F'}=4\right\rangle$. However, there is some contention as to whether this is the correct value to use in the calculation of MOT atom number, since the MOT is a complicated system of light polarisations and

atomic states with many possible transitions. The saturation intensity calculated when one averages over all $5S_{1/2}\ F=3$ to $5P_{3/2}\ F'=4$ transitions is 38 W m^{-2} [21]. Townsend *et al.* [25] and Gabbanini *et al.* [26] discuss experimental correction factors to the saturation intensity, but these correction factors are specific to an experiment. Without actually inferring the saturation intensity through experiment, one must look at the theoretical effect of the saturation intensity on the scattering rate in equation (2.9), charted in Figure 2.23, (the intensity used in the experiment is between the two limits $I/I_{SAT} \ll 1$ and $I/I_{SAT} \gg 1$). The typical ^{85}Rb MOT operates approximately 2Γ from resonance with the cooling transition. As can be seen in Figure 2.23, for a detuning of 2Γ, the scattering rate for the average saturation intensity is approximately half the scattering rate for the saturation intensity of the stretched state. However, Townsend *et al.* [25] indicate that atoms in the MOT are

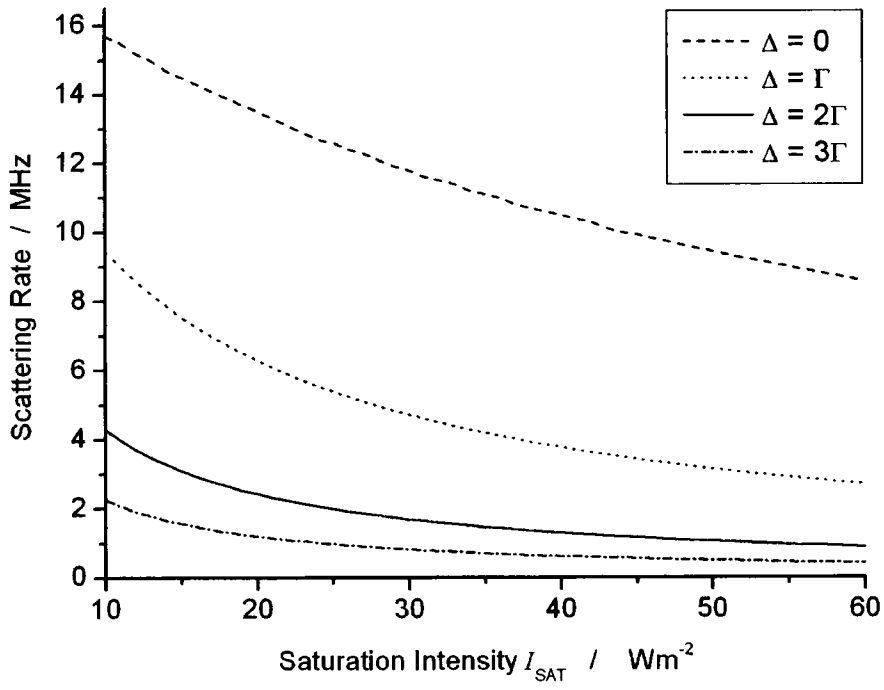

Figure 2.23. Variation of the scattering rate with the value of saturation intensity. The value for the saturation intensity used in all calculations in this thesis is that of the stretched state transition of $5S_{1/2}\left|F=3,m_F=3\right\rangle$ to $5P_{3/2}\left|F'=4,m_{F'}=4\right\rangle$, which is $I_{SAT}=16$ W m^{-2}. A value of $I=50$ W m^{-2} was used.

more likely to be in larger-valued m_F states since atoms will be pumped towards states of maximum interaction with the local light field – this would lower the

saturation intensity from the average value. Therefore, it seems that any calculation of MOT atom number with the stretched state saturation intensity $I_{SAT} = 16$ W m^{-2} will have an error of less than a factor of 2. The calculation of the exact MOT atom number is not important for this experiment.

Since γ is dependent on the as-yet undefined value of detuning Δ, it cannot be evaluated, hence,

$$N = \frac{8.3\times10^{13}}{\gamma} V . \qquad (2.10)$$

To maximise the atom number, the detuning Δ and MOT magnetic field gradient were varied independently. The results are shown in Figure 2.24, where a continuous current of 8.5 Amps was passed through the Rb dispenser. The maximum atom number was found at $\Delta = -2\pi \times 13$ MHz with a magnetic field gradient of 9 G cm^{-1}.

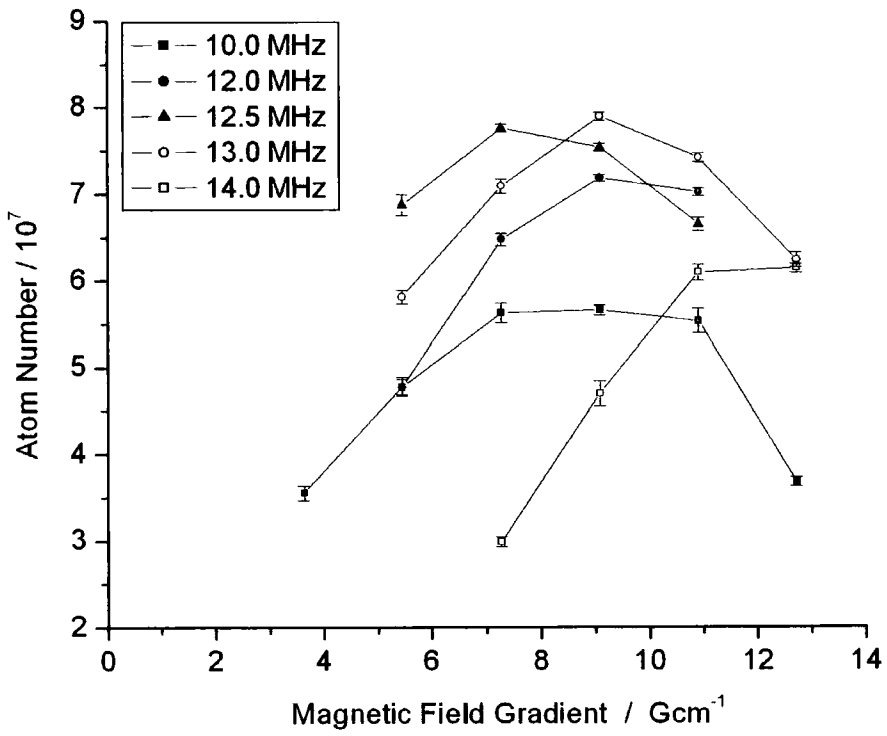

Figure 2.24. A graph of atom number against magnetic field gradient of the MOT (for various detunings from resonance with the $5S_{1/2}\ F = 3$ to $5P_{3/2}\ F' = 4$ cooling transition, i.e. from $\Delta/2\pi = -10$ MHz to -14 MHz). The peak atom number was found to be approximately at 9 Gcm^{-1} and $\Delta = -2\pi \times 13$ MHz. These data were taken at a continuous Rb dispenser current of 8.5 A. Each data point is the mean of three measurements, and the error bars are the standard error from those measurements.

Figure 2.25 shows a plot of both fill times and atom number against dispenser current. A fast fill time (a few seconds) allows quick repetition of the experiment, with Figure 2.26 showing that the fill time varies by only a few seconds with varying Δ and magnetic field gradient, i.e. that the dispenser current is more important for fast fill times than the detuning and magnetic field gradient, (over the presented range of values).

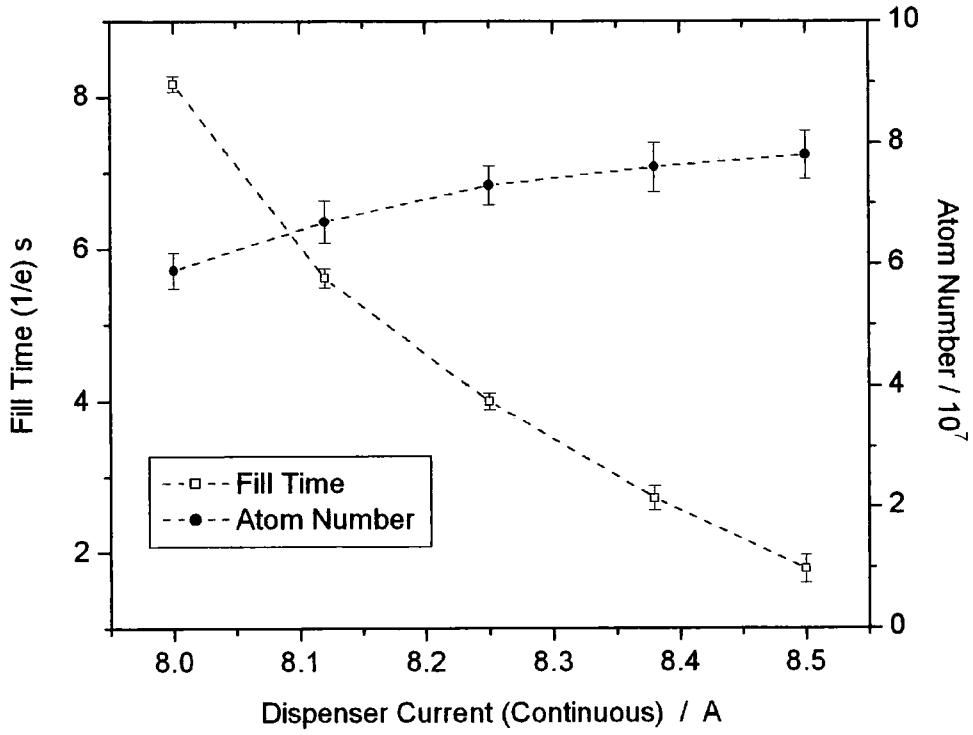

Figure 2.25. A graph showing how fill time and atom number vary with continuous dispenser current. As the current is increased, more Rb vapour is emitted from the dispenser into the vacuum chamber, consequently the atom number rises and the fill time falls. The dotted lines are present to acknowledge the trend of the data – they are not mathematical fits. The MOT magnetic field gradient was set at 9 G cm^{-1} with $\Delta = -2\pi \times 13$ MHz. Each data point is the mean of three measurements, and the error bars are the standard error from those measurements.

It should be noted here that the (continuous) current values for the rubidium dispenser in this experiment are significantly higher than continuous current values used in other work [1, 2]. Even at 8 A, the rubidium dispenser shows little signs of heating to the naked eye. It is thought that this is due to heat-sinking somewhere on the dispenser mount (section 2.1.9), possibly the BeCu barrel connectors that hold the current wires in place.

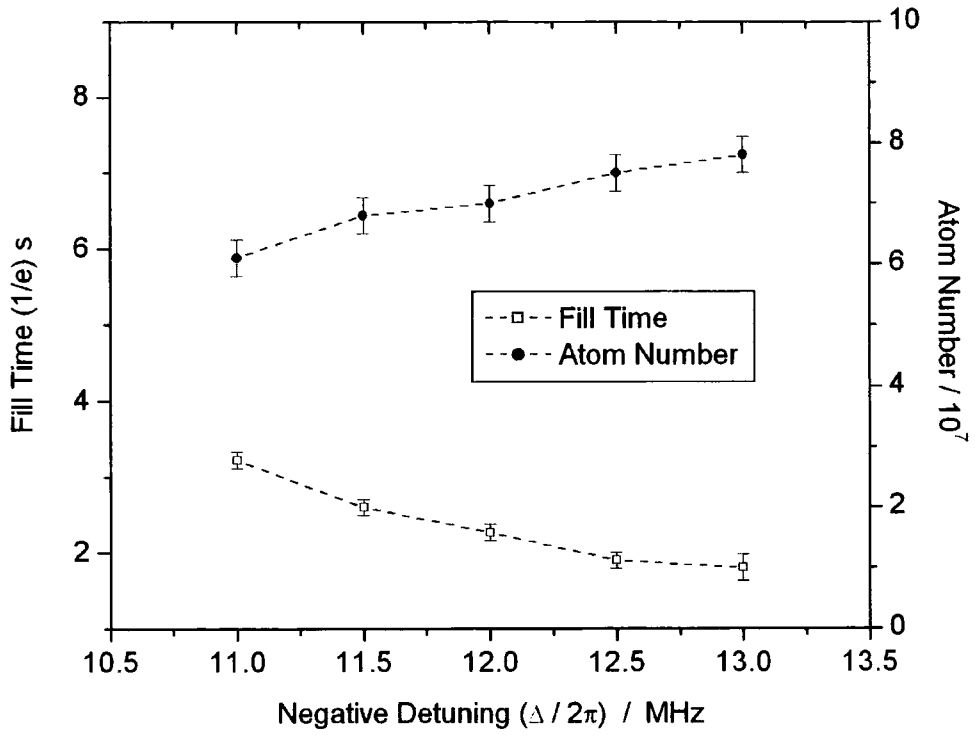

Figure 2.26. A graph showing how fill time and atom number vary with negative detuning from resonance with the $5S_{1/2}\ F = 3$ to $5P_{3/2}\ F' = 4$ cooling transition. For each negative detuning, the MOT magnetic field gradient was set to maximise the atom number, as in Figure 2.24. The Rb dispenser current was set at 8.5 A continuously. The dotted lines are present to acknowledge the trend of the data – they are not mathematical fits. Note that detuning has relatively little effect upon the fill time when compared to the effect of varying the current through the Rb dispenser, as seen in Figure 2.25.

2.1.14 Computer Control of the Experiment

The computer control of the experiment was done through the use of LabVIEW Version 7.1, which was installed on a computer using Windows XP Professional O/S with an Intel Pentium 4 CPU and 1Gb of RAM. Two National Instruments (NI) output cards were used: a PCI-6713 Analogue Card and a PCI-DIO-32HS Digital Card. The outputs from theses two cards were used to control the various electronic circuits that operated the experiment. All timing during output was done with the PCI-6713's on-board clock, which synchronised timing with the PCI-DIO-32HS via the RTSI (Real-Time Synchronization Interface) bus.

Figure 2.27 and Figure 2.28 show screen-shots of the LabVIEW front panel to illustrate the patterns required for an experiment such as this. These screen-shots show the voltage patterns sent to the NI cards by LabVIEW – all output patterns from the NI cards were measured, with a digital oscilloscope, to correspond to the input patterns.

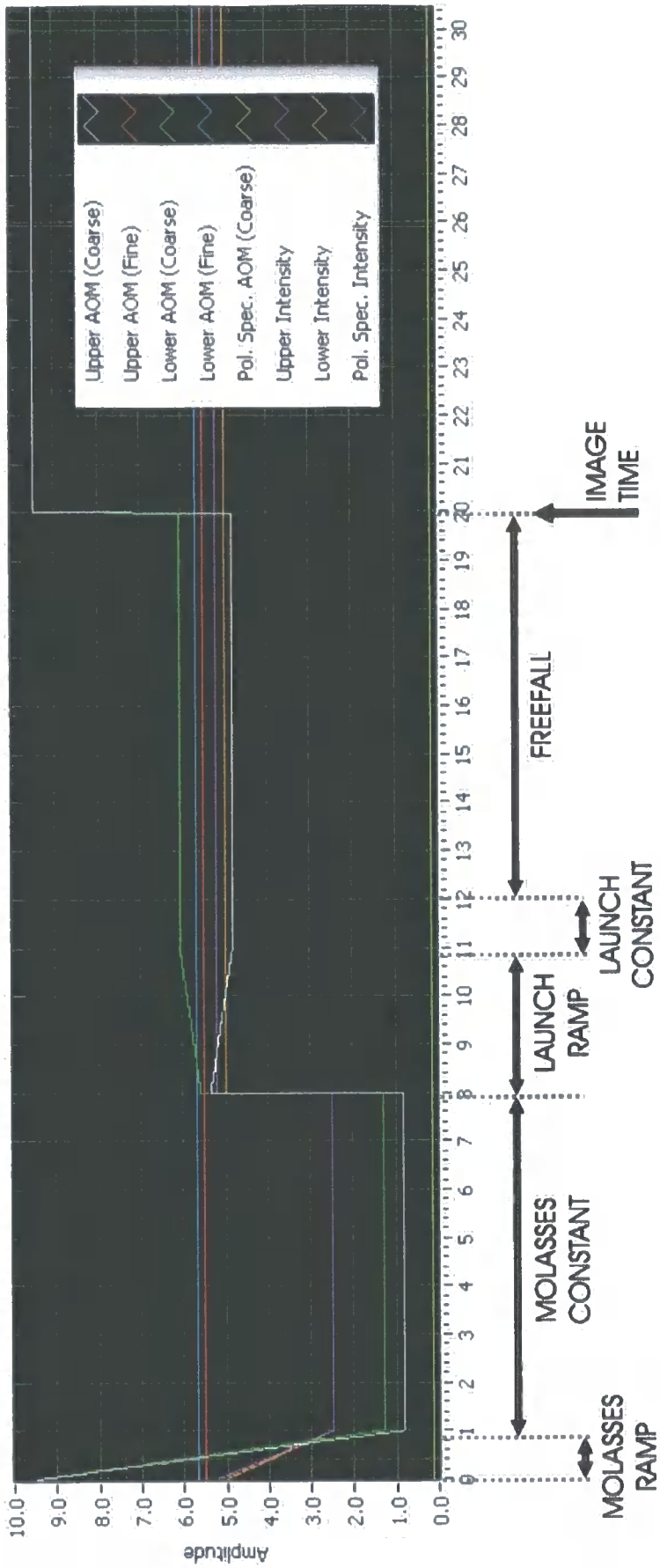

Figure 2.27. Screen-shot of LabVIEW front panel showing an illustration of the analogue lines for output to the National Instruments PCI-6713 Analogue Card. Upon running the LabVIEW program, the analogue patterns would be written to memory, before being output to the experiment. The analogue and digital patterns were configured to begin at the same time by the use of LabVIEW's in-built rendezvous.vi and a trigger from the digital card to the analogue card's PCI pin to begin the analogue output. Various experimental stages are labelled to give the reader a notion of the voltages changes required for each phase of the experiment. The *x*-axis is in units of milliseconds, but in reality, if atoms were launched through approximately 20 cm the image time would be at a time greater than 200 ms, not at 20 ms. The difference between the LAUNCH CONSTANT phase and the FREEFALL stage is that, although the analogue voltages remain the same, the digital card is used to switch the laser beams off in FREEFALL.

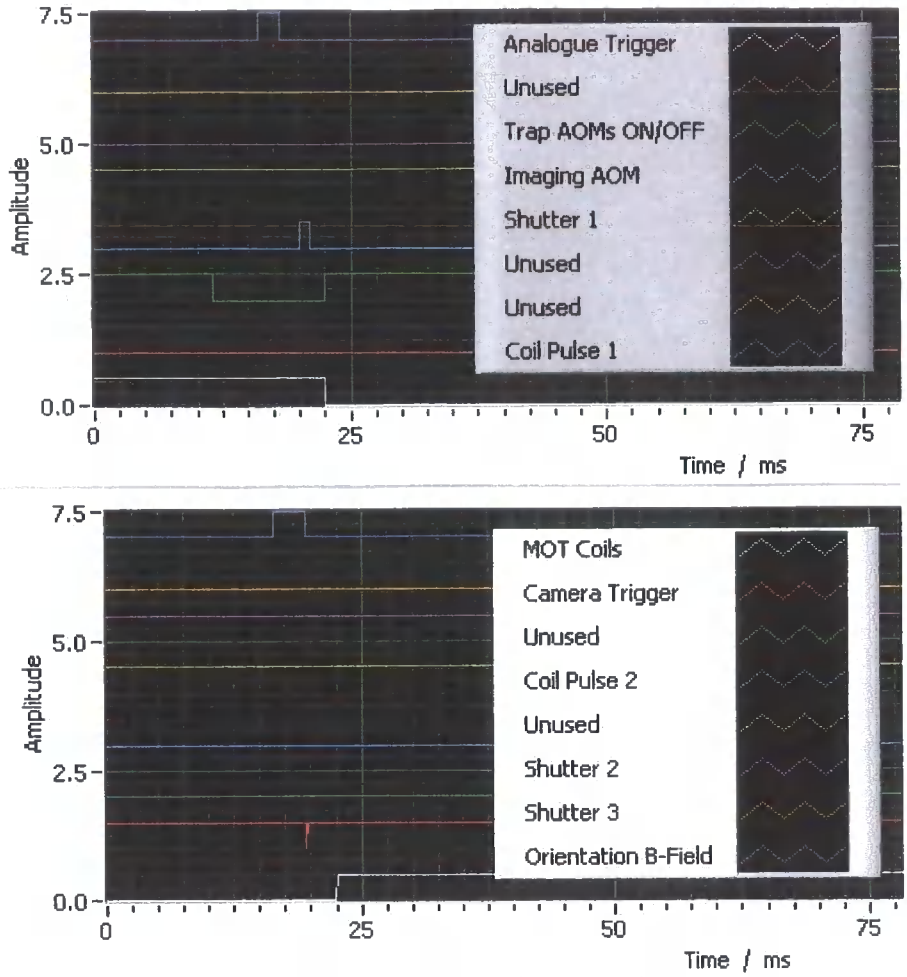

Figure 2.28. Screen-shot of the LabVIEW front panel showing an illustration of the digital lines for output to the National Instruments PCI-DIO-32HS Digital Input/Output card. Upon running the LabVIEW program, the digital patterns would be written to memory before being output to the experiment. The analogue and digital patterns were configured to begin at the same time by the use of LabVIEW's in-built rendezvous.vi and a trigger from the digital card (at zero milliseconds) to the analogue card's PCI pin to begin the analogue output, which is shown on the top of the above two panels in this figure (labelled Analogue Trigger).

2.1.15 Imaging in the MOT Chamber

CCD Camera and Calibration

All images of atom clouds were taken using a JAI CV-M50 IR CCD camera mounted with a Zenit Helios-44M-7 58mm SLR lens with the f-stop removed. The distance between the lens and the CCD chip dictated the image area. To take images in the MOT chamber, i.e. the region in which the MOT is formed, the camera was first mounted and focused on the MOT. The camera was then removed from the

experiment and a piece of fine graph paper brought into focus in-front of it. In this way, the number of millimetres per pixel in the horizontal and vertical directions could be calibrated.

The sensitivity of the CCD chip was calculated to be 0.053 ± 0.005 pixel counts per photon at 780 nm. To gain this calibration, a probe beam which did not saturate the CCD chip and that was smaller than the area of the CCD chip was impinged directly onto the chip. By measuring the power of the beam (using a Coherent FieldMate Power Meter) and counting the total number of pixel counts with and without the beam, the number of pixel counts per photon can be deduced. The camera specifications did not allow a quantum efficiency to be calculated.

Fluorescence Imaging, Image Capture and Fitting Cloud Widths

Fluorescence imaging [27] was facilitated by the imaging beam discussed in section 2.1.11. The front of the camera lens was situated 17.1 ± 0.1 cm from the MOT, and imaged the MOT chamber through an AR-coated quartz viewport. A trigger pulse was sent from the National Instruments PCI-DIO-32HS to the CCD camera to open the camera shutter to encompass the duration of the imaging light pulse from the imaging beam. Scattered light from the imaging beam was imaged onto the CCD.

Image capture into LabVIEW was through a National Instruments IMAQ PCI-1408 Image acquisition card. Using LabVIEW, the image could be manipulated for image clarity (by converting $n \times m$ pixels into singular super-pixels), and for fitting widths to the imaged atom clouds. To fit widths, the image was 'binned' in the horizontal direction (for fitting the vertical width) and 'binned' in the vertical direction (for fitting the horizontal width). The atom clouds were fitted, in LabVIEW, as Gaussian profiles of the form,

$$P(x) = A \exp\left(\frac{-(x - x_0)^2}{2\sigma_x^2} \right) + B \qquad (2.11)$$

where σ_x is the spatial standard deviation in the x-direction.

2.1.16 Making Temperature Measurements

Theory of Expansion of a Cold Atom Cloud

In 1-D, the initial (x_i) and final (x_f) position of an atom can be related by $x_f = x_i + v_x t$, where v_x is the velocity of the atom, and t is the expansion time. This allows the final position distribution of a cloud of atoms $P'(x_f,t)$ to be written as a convolution of the initial position distribution $P(x_i)$ and the velocity distribution $f(v_{x_i})$. If it is assumed that the initial position distribution $P(x_i)$ is Gaussian, that the velocity distribution $f(v_{x_i})$ is Maxwellian, and that the cloud has uniform temperature, then

$$P'(x_f,t) = \int_{-\infty}^{\infty} P(x_i)\, f(v_x)\, dx_i = \int_{-\infty}^{\infty} P(x_i)\, f\left(\frac{x_f - x_i}{t}\right) dx_i = P(x_i) \otimes f(v_x), \quad (2.12)$$

assuming [28],

$$P(x_i) = \frac{1}{\sigma_x \sqrt{2\pi}} \exp\left(\frac{-x_i^2}{2\sigma_x^2}\right), \quad (2.13)$$

and [29],

$$f(v_x) = \left(\frac{m}{2\pi k_B T_x}\right)^{\frac{1}{2}} \exp\left(\frac{-mv_x^2}{2k_B T_x}\right) = \left(\frac{m}{2\pi k_B T_x}\right)^{\frac{1}{2}} \exp\left(\frac{-m\left(x_f - x_i\right)^2}{2k_B T_x t^2}\right), \quad (2.14)$$

where T_x is the temperature of the cloud and m is the mass of a single atom.

The most important result of this convolution is that the standard deviation of the final position distribution is the root of the quadrature sum of the standard deviation of the initial position distribution and the standard deviation of the velocity distribution:

$$\sigma_{x_f}{}^2 = \sigma_{x_i}{}^2 + \frac{k_B T_x}{m} t^2 . \quad (2.15)$$

Therefore, one can obtain the temperature of a cloud from the gradient of a graph of $\sigma_{x_f}{}^2$ against t^2. By taking images of clouds at successive times and fitting Gaussian distributions to the images (as described in section 2.1.15), the temperature can be estimated.

2.1.17 Sub-Doppler Cooling

Theory

This section discusses sub-Doppler cooling in 3-D optical molasses. The lowest temperature attained in the molasses phase was 6.8 ± 0.4 μK, which was at a detuning $\Delta = -2\pi \times 28$ MHz, from the $5S_{1/2}$ $F = 3$ to $5P_{3/2}$ $F' = 4$ transition, and an intensity of approximately 13 W m^{-2} ($\sim 0.7 I_{SAT}$). Ultimately, the most important temperature for the experiment is that attained at the end of the moving molasses stage. However, since moving molasses is but molasses in a moving frame, minimisation of the temperature in the molasses phase is an excellent starting point.

The theoretical basis for 1-D sub-Doppler cooling was first presented by J. Dalibard and C. Cohen-Tannoudji [30] after experiments by Lett *et al.* showed that the Doppler limit could be breached in optical molasses [31]. It is extremely fortuitous that Doppler cooling is able to bring temperatures into the region where sub-Doppler processes can occur. Dalibard and Cohen-Tannoudji presented two forms of sub-Doppler cooling: firstly from two counter-propagating linearly polarised beams whose polarisations are orthogonal to each other ($\text{lin} \perp \text{lin}$); and secondly from two counter-propagating circularly polarised beams, both circularly polarised in the same sense with respect to their own propagation direction ($\sigma^+ - \sigma^-$). Both mechanisms cool by the use of polarisation gradients within the resultant light fields, and operate in the limit of low magnetic field. In the case of $\text{lin} \perp \text{lin}$, potential hills and potential valleys are formed. In the optimum scenario, an atom loses kinetic energy upon climbing to the peak of a potential hill before being optically pumped to a potential valley, thereby cooling. For cooling in the case of $\sigma^+ - \sigma^-$, the polarisation gradient causes an orientation in the ground-state population. This orientation produces a differential scattering rate between the two laser beams such that an atom scatters more from the beam into which it moves, thereby cooling.

The equilibrium temperature of both these cooling mechanisms, in the limit of low intensity and large detuning, is proportional to the magnitude of the dimensionless light-shift parameter $\frac{1}{2}\frac{\left(I/I_{SAT}\right)}{\left(|\Delta|/\Gamma\right)}$, where I is the total intensity of the cooling laser

beams, I_{SAT} is the saturation intensity, Δ is the (red) detuning from the cooling transition, and Γ is the inverse lifetime of the excited state.

In 3-D optical molasses, as in this experiment, both types of cooling will be present due to the complicated polarisation surface formed by six intersecting beams [32].

There is a limit to the effect of sub-Doppler cooling, since the above mechanisms still involve the interaction of atoms with the photons of the light field. The temperature limit, known as the recoil limit, is that associated with the recoil of an atom from a single photon:

$$\frac{1}{2}k_B T_{\text{recoil}} = \frac{1}{2m}(\hbar k)^2, \tag{2.16}$$

where T_{recoil} is the recoil limit, m is the mass of an atom, and k is the magnitude of the wave-vector of the electromagnetic radiation. In practice, the lowest attainable temperatures are limited by technical issues such as laser beam intensity imbalance, fringes within the interference patterns at beam intersections, alignment and non-uniform intensity. For this reason, this experiment was designed for the use of large beams, and AR-coated windows on the vacuum chamber to try to minimise deleterious effects.

Experiment

In practical terms, the equilibrium temperature of optical molasses was also found to be a linear function of the dimensionless light-shift parameter, [12, 33, 34,], provided the scattering force does not become so weak that there are insufficient scattering events to provide cooling. Indeed, this linearity was observed in this experiment and Figure 2.29 shows a plot of the cloud standard deviation against time for a detuning $\Delta = -2\pi \times 28$ MHz and a peak intensity of approximately 13 W m^{-2} ($\sim 0.7 I_{SAT}$), which gave a temperature of 6.8 ± 0.4 μK, the lowest temperature measured here. In this case, $I_{SAT} = 16$ W m^{-2} is the saturation intensity of the transition $5S_{1/2}\left|F=3, m_F=3\right\rangle$ to $5P_{3/2}\left|F'=4, m_{F'}=4\right\rangle$ (see section 2.1.13)), and $\Gamma = 2\pi \times 5.9$ MHz [12, 24] is the inverse lifetime of the $5P_{3/2}$ state in ^{85}Rb. The light-shift parameter is therefore 0.28, with the final detuning just over twice the detuning for the MOT and the final intensity approximately a quarter of that used for the MOT. Approximately 10^8 atoms were loaded into the MOT, followed by a 10 ms molasses

stage. The duration of the molasses stage is defined from the time at which the MOT coils begin to switch off to the point at which the laser light is switched off, (the MOT coils actually take 5.2 ± 0.1 ms to switch off to < 5 % of the maximum). At the beginning of the molasses stage, the atoms experience a 1 ms ramp to the final intensity and detuning. At lower light-shift parameters, the temperature was found to be unmeasurable since it became increasingly difficult to fit profiles to the clouds without extremely large error bars.

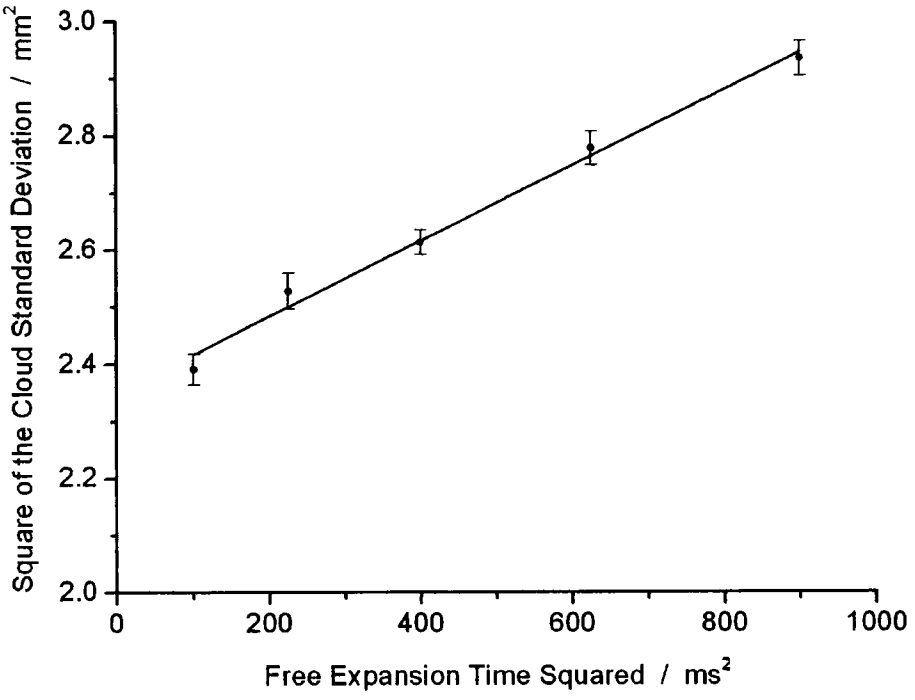

Figure 2.29. Plot of the square of the cloud standard deviation against the square of the expansion time for a detuning $\Delta = -2\pi \times 28$ MHz and an intensity of approximately 13 W m^{-2} ($\sim 0.7 I_{SAT}$), which gives a temperature fit of 6.8 ± 0.4 μK (shown by the black line). Approximately 10^8 atoms were loaded into the MOT, followed by a 10 ms molasses stage. At the beginning of the molasses stage, the atoms experience a 1 ms ramp to the final intensity and detuning. Each data point is the mean of three measurements, with the error bars given by the standard error of these measurements. Images were taken using the MOT laser beams.

2.2
Launching Cold Atoms

2.2.1 Moving Molasses Theory

Moving molasses is essentially optical molasses in a frame moving at a non-zero velocity relative to the lab frame. For this experiment, it is a technique used to transfer atoms from the MOT chamber to a remote chamber vertically above the MOT.

Laser Beam Configuration and Launch Height

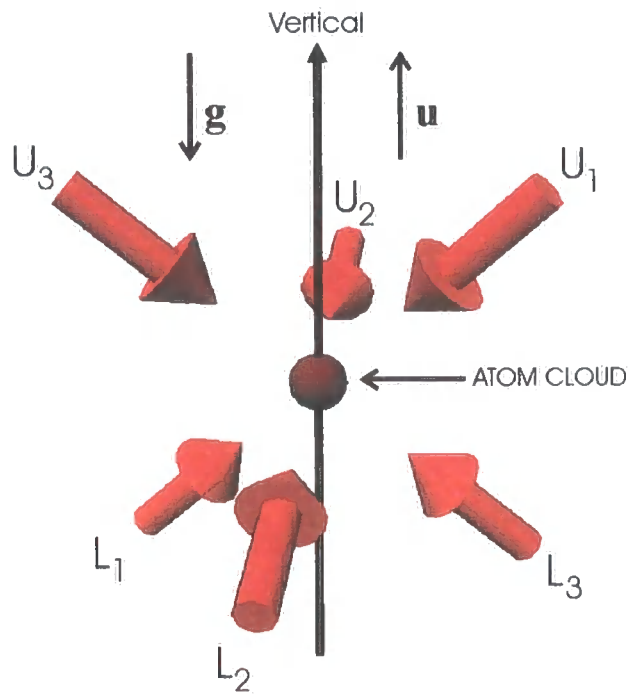

Figure 2.30. Diagram of the laser beam set-up for moving molasses. Before the moving molasses stage all six beams are at a central frequency ω. The beams are orientated such that beam U_N counter-propagates beam L_N, and the three pairs of beams are mutually orthogonal. All beams are of equal intensity, and initially all at the same frequency ω (after an optical molasses stage (section 2.1.17)). To launch the atoms, the upper beams (U_1, U_2, U_3) are tuned to a frequency $\omega - \delta_{angular}$ and the lower beams (L_1, L_2, L_3) to $\omega + \delta_{angular}$. This results in a vertical launch speed u given by $\delta_{angular} = \frac{ku}{\sqrt{3}}$, where k is the magnitude of each of the wavevectors of the beams at the central frequency ω. The $\sqrt{3}$ comes from the orientation of the beams relative to the launch direction.

Figure 2.30 shows a diagram of the laser beam set-up used for the moving molasses in this experiment. The beams form three mutually orthogonal, counter-propagating pairs, of equal intensity, and initially equal frequency ω (after an optical molasses stage (section 2.1.17)). The orientation of the beams is such that each beam has an acute angle to the vertical of $\theta = \cos^{-1}\left(\frac{1}{\sqrt{3}}\right) = 54.7°$. This configuration was chosen so that only two frequencies are needed for the launching process – one frequency for the upper beams and second frequency for the lower beams, a method now commonly employed in atomic fountains [23, 35]. Changing the upper beams to an (angular) frequency $\omega - \delta_{\text{angular}}$ and the lower beams to an (angular) frequency $\omega + \delta_{\text{angular}}$ gives a resultant force from the upper and lower beams that causes the atoms to move at a vertical (launch) speed u given by,

$$\delta_{\text{angular}} = \frac{ku}{\sqrt{3}}, \tag{2.17}$$

where $k = \frac{2\pi}{\lambda}$ is the magnitude of each of the wave-vectors of the beams, (consider the wavelength $\lambda = \frac{c}{\omega}$ as a convenient mean for the purposes of this explanation since $\delta_{\text{angular}} \ll \omega$)

The launch speed u is given by $u = \sqrt{2gh}$, (for atoms that come to rest at a height h, with g the acceleration due to gravity), and can thus be expressed as,

$$u = \frac{\sqrt{3}\lambda\delta_{angular}}{2\pi}, \tag{2.18}$$

and the launch height h as,

$$h = \frac{3\lambda^2\delta_{angular}^2}{8\pi^2 g}. \tag{2.19}$$

As such, the required linear detuning δ for a launch height h is given by,

$$\delta = \sqrt{\frac{2gh}{3\lambda^2}}. \tag{2.20}$$

Figure 2.31 shows a graph of δ against h. These linear frequencies are relevant for the acousto-optic modulators used to change laser frequencies in the experiment. For a launch height relevant to this experiment (between 20 cm and 30 cm), the required detuning is $1.5 \leq \delta \leq 1.8$ MHz.

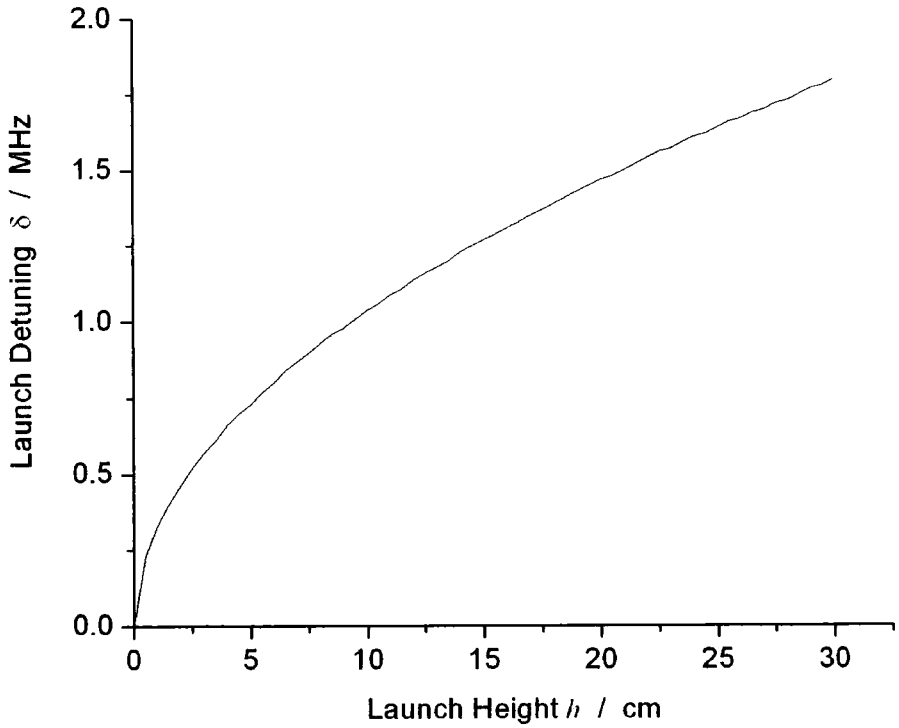

Figure 2.31. Graph of linear detuning δ for moving molasses against launch height h. For launch heights of consideration in this experiment (between 20 cm and 30 cm), the required launch detuning is between 1.5 MHz and 1.8 MHz.

2.2.2 Evolution of a Launched Cloud

The Evolution of the Standard Deviation with Time and Height

The evolution of an atom cloud in ballistic expansion was discussed in section 2.1.16, concluding with the equation:

$$\sigma_{x_f}{}^2 = \sigma_{x_i}{}^2 + \frac{k_B T_x}{m} t^2 \tag{2.21}$$

where σ_{x_f} is the final cloud standard deviation after a free-expansion time t, with σ_{x_i} the initial cloud standard deviation and T_x the temperature in the x-direction.

As expected from equation (2.21), for large times, the theoretical expansion of the standard deviation of the cloud is linear with time. Figure 2.32 shows the expansion of a cloud (of initial standard deviation 1 mm) launched to an apex 20.5 cm above its

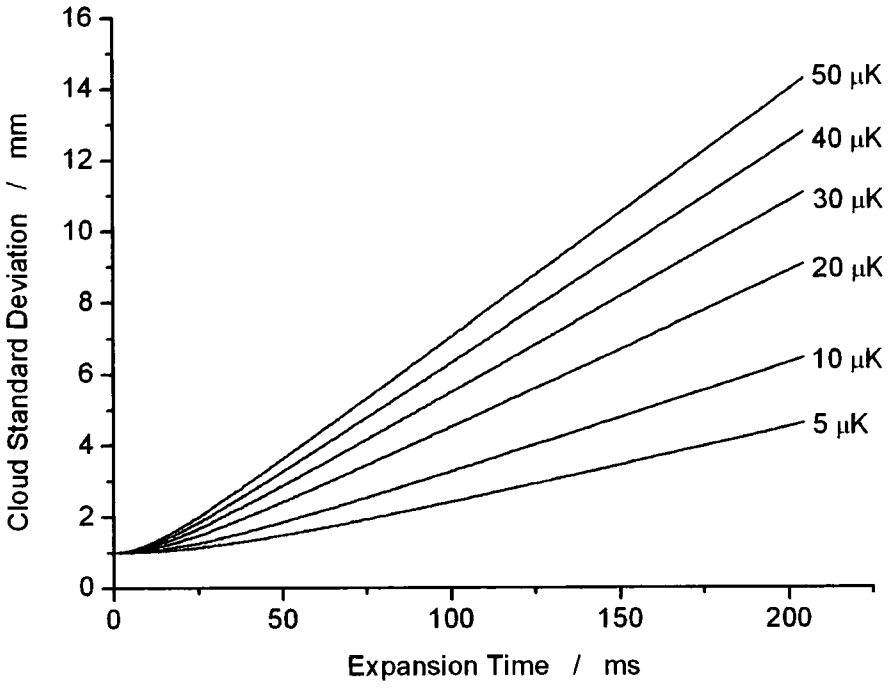

Figure 2.32. Evolution of the standard deviation of clouds (of initial standard deviation 1 mm) launched to an apex of 20.5 cm above its initial position. The temperature of the cloud is the dominant effect upon the final size - the final standard deviation varies between 4.6 mm (for 5 μK) and 14.2 mm (for 50 μK). The centre-of-mass of the cloud takes 204 ms to reach the apex. As dictated by equation (2.21), for large times, the standard deviation varies linearly with time.

initial position. The temperature of the cloud is the dominant effect upon the final size - the final cloud size varies between 4.6 mm (for 5 μK) and 14.2 mm (for 50 μK). However, the evolution of the standard deviation has a different relationship with height as the cloud rises to its apex. Since the centre-of-mass of the cloud decelerates to zero at the apex (from 2.01 m s^{-1} in this case), the cloud spends more time at higher heights, and hence the standard deviation increases more sharply nearer the apex. Figure 2.33 shows the evolution of the standard deviation with height for a cloud launched to reach an apex 20.5 cm above its initial position.

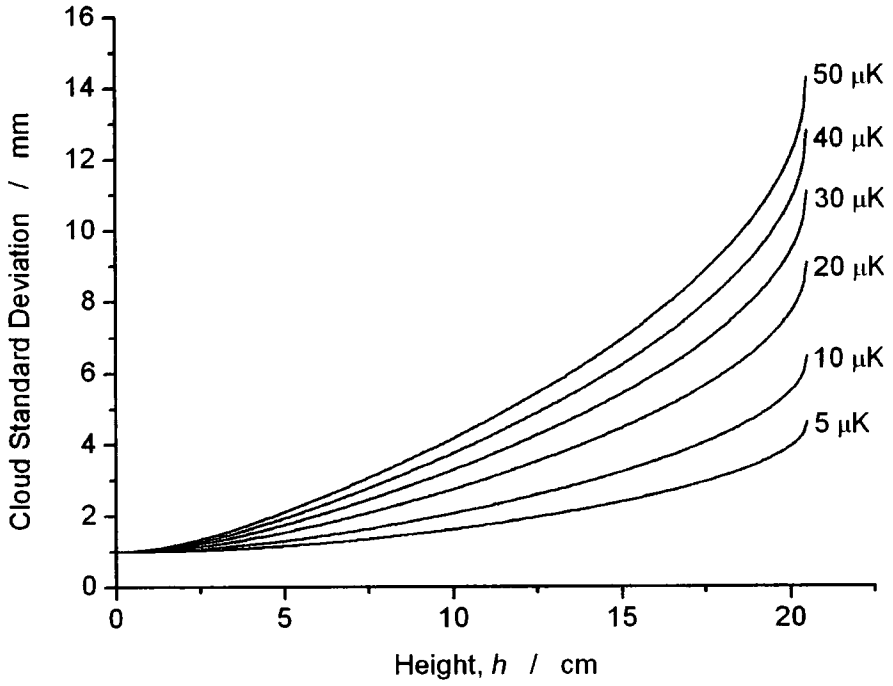

Figure 2.33. Evolution of the standard deviation of clouds (of initial standard deviation 1 mm) launched to an apex of 20.5 cm above its initial position. The temperature of the cloud is the dominant effect upon the final size - the final standard deviation varies between 4.6 mm (for 5 μK) and 14.2 mm (for 50 μK). The centre-of-mass of the cloud takes 204 ms to reach the apex. Since the centre-of-mass of the cloud decelerates to zero at the apex (from 2.01 m s^{-1} in this case), the cloud spends more time at higher heights, and hence the standard deviation increases more sharply nearer to the apex.

2.2.3 Moving Molasses and Imaging at the Apex of Flight: 15 mm ($1/e^2$) radius Laser Beams

Below are details of experimental moving molasses. The work of Münstermann *et al.* [23], conducted in the research group of G. Rempe, was used as a main reference since their beam configuration and set-up were very similar to the one presented here. As a note, the lowest published moving molasses temperature for rubidium was 1.85 μK achieved by Fertig and Gibble [35]. The set-up presented here was the first moving molasses set-up used on this experiment, and was realised to be incredibly inefficient (i.e. the number of atoms launched at the correct speed, as a percentage of the total atoms, was very low) upon performing experimentation at the apex of flight. After some preliminary experimentation, the moving molasses stage was then improved and is detailed in section 2.2.4.

Launch Speed and Launch Height

Figure 2.34 shows a theoretical graph of both the launch speed u and the time taken to reach the apex of flight t_{apex} against launch height h. The available image window in the quartz cell on top of the vacuum chamber gives an image height $19 < h < 27$ cm, and hence a required launch velocity of $1.9 < u < 2.3$ m s^{-1}. The time taken to reach the apex of flight is important for imaging the cloud at the apex, and this varies over a range of 38 ms for the available launch heights. The maximum image duration available is 2 ms with the JAI CV-M50 IR CCD camera and the IMAQ PCI-1408 (see section 2.1.15).

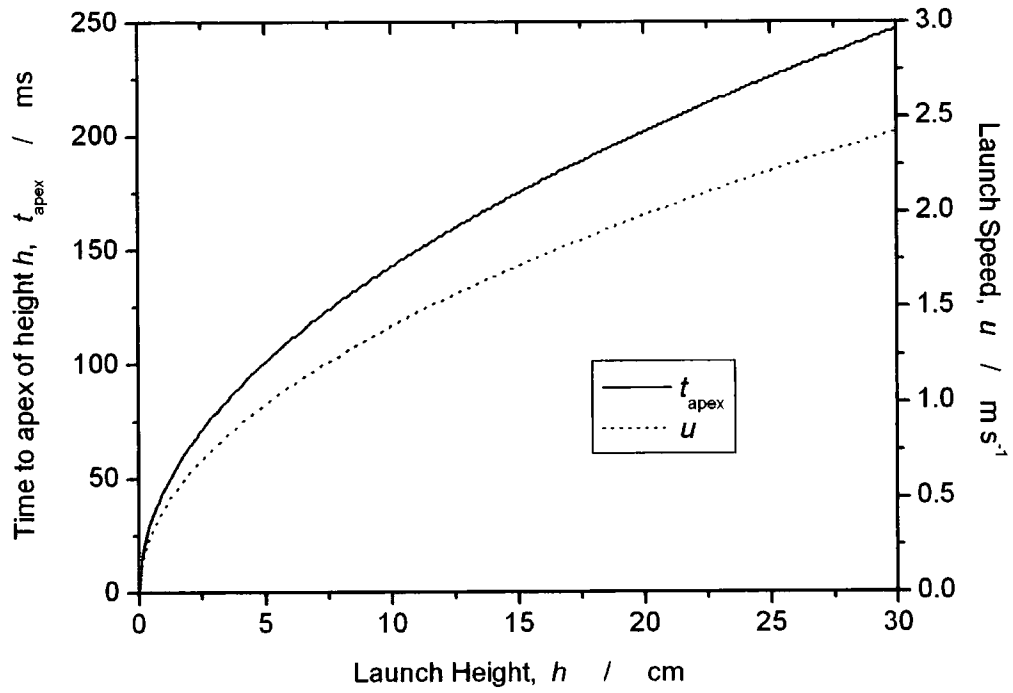

Figure 2.34. Graph of both the launch speed u, and the time taken to reach the apex of flight t_{apex}, against the launch height h.

A launch height of 20.5 cm was chosen since this was a height towards the bottom of the quartz cell where launched clouds would have higher densities (than at greater heights) and hence be easier to image. For a launch height of $h = 20.5$ cm, the time of flight to the apex is $t_{apex} = 204$ ms and the launch speed is $u = 2.01$ m s^{-1}. Therefore, the required launch detuning for the upper and lower beams (section 2.2.1) is $\delta = 1.48$ MHz, (δ being defined in section 2.2.1).

Figure 2.35 shows a raw Intensity Chart taken from the LabVIEW front panel of a sequence of images of the launching cloud in the MOT chamber, i.e. at the base of flight. The intensity and the central launching frequency were the same as those for the MOT, namely $\Delta = -2\pi \times 13$ MHz and $I \cong 3I_{SAT}$. To check that the cloud was launching vertically, the CCD camera was also positioned to look at the launch from a perpendicular viewpoint, but again in the horizontal plane – an intensity chart was attained that was practically identical to that shown in Figure 2.35.

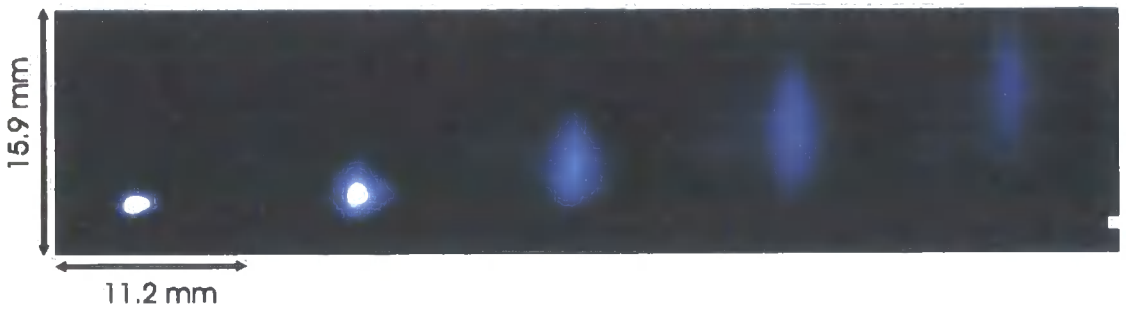

Figure 2.35. Intensity Chart from the LabVIEW front panel showing a sequence of images (separated by 1 ms) of a cloud in the process of launching. The images were taken in the MOT chamber as described in section 2.1.15. The CCD camera was also positioned to view the launch, again in the horizontal plane, but perpendicular to this viewpoint, to check that the cloud was launching vertically – the intensity chart obtained was almost identical to the one shown in this figure. The MOT was loaded with 10^8 atoms, followed by a 10 ms molasses phase (as described in section 2.1.17), then a 2 ms ramp to the required launch frequencies to reach a height of 20.5 cm. The image duration was 0.1 ms using the vertical imaging beam discussed in section 2.1.11. The intensity and the central launching frequency were the same as those for the MOT, namely $\Delta = -2\pi \times 13$ MHz and $I \cong 3I_{SAT}$.

The decrease in image intensity in Figure 2.35 was attributed to the atom cloud stretching during launch, i.e. that different parts of the cloud achieved (the theoretical) launch velocity at different times. The reader can see, in section 2.2.4, that this view was misguided and that a stretched cloud is indicative of a poor launch, i.e. that only a small percentage of atoms achieve the theoretical launch velocity, whilst the rest of the cloud is at some lower launch velocity – the reason the cloud stretches during launch. However, it was not until experimentation had been carried out in the upper chamber that these launching problems were highlighted.

In lieu of observing clouds launch (Figure 2.35), the CCD camera was moved to view the upper chamber, i.e. the quartz cell on top of the vacuum chamber, so that atoms could be detected there, and launched clouds' temperatures and widths characterised

and optimised. However, width characterisation proved very difficult with this set-up, as can be see in Figures 2.36 and 2.37.

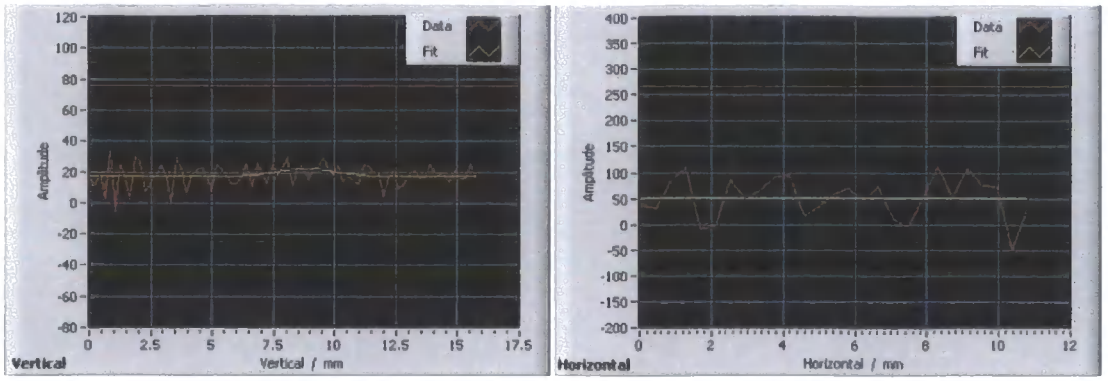

Figure 2.36. Typical 'binned' vertical (top) and horizontal (bottom) line profiles of a single image taken of the upper chamber with no atoms present (red). There is also a Gaussian fit (yellow), used to fit cloud widths, which has been left present to indicate the trend of the data. The *y*-axis Amplitude refers to the number of pixel counts. The mean base level is approximately 20 ± 5 pixel counts (mean of 5-shots) in the vertical direction and approximately 50 ± 10 pixel counts in the horizontal direction. Counts significantly above this indicate the presence of atoms. The image pulse duration was set at its maximum of 2ms (see section 2.1.15).

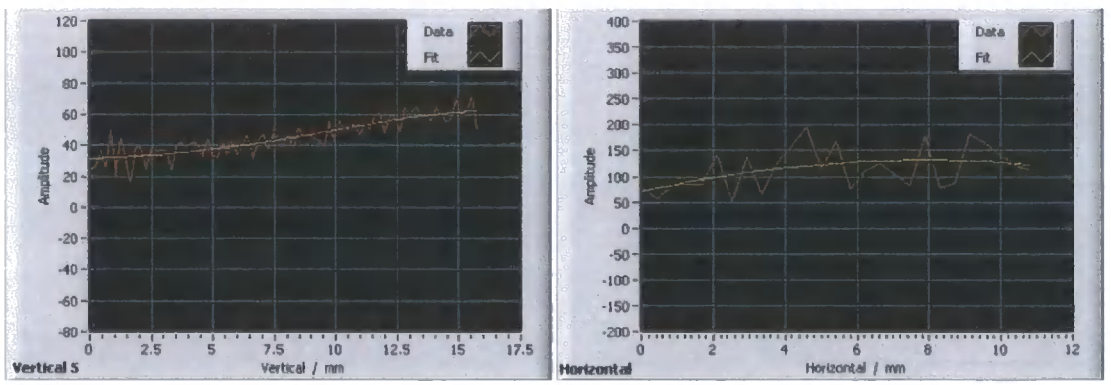

Figure 2.37. Typical 'binned' vertical (top) and horizontal (bottom) line profiles of a single image taken 202 ms after launch, in the upper chamber with no atoms present (red). There is also a Gaussian fit (yellow), used to fit cloud widths – as can bee seen, it is very difficult to fit widths to this data since a significant fraction of the profile is outside the image window, and, perhaps more significantly, the signal is low. The *y*-axis Amplitude refers to the number of pixel counts. The peak vertical pixel count is over 60 counts, which is significantly above the base of 20 ± 5 pixel counts. The peak horizontal pixel counts is over 150 counts, significantly above the base of 50 ± 10 pixel counts. These figures indicate the presence of atoms in the upper chamber since more counts indicate more photons, which indicates the presence of more light-scattering objects, i.e. atoms. The image pulse duration was set at its maximum of 2ms (see section 2.1.15).

Figure 2.36 shows the typical 'binned' horizontal and vertical profiles of an image, centred at a height 20.5 ± 0.2 cm above the MOT, taken with no atoms present. The data has undergone a 10-point average in both the horizontal and vertical directions. It was signal on-top of this background that indicated the presence of atoms, and hence Figure 2.37 shows a typical image taken in the presence of atoms, again with a 10-point average. The images themselves showed no observable difference; it was only in the 'binned' line profile that atoms could be detected. As can be seen, fitting cloud widths to the detected atom cloud was not possible due to the low signal and because a large fraction of the cloud lay outside the image window. The reader will see in section 2.2.4 that this low signal was indicative of an extremely inefficient moving molasses stage. Indeed, to observe (at a height of 20.5 cm) the line-profiles shown in Figure 2.37, the moving molasses had to be configured to launch to a height of 23.9 cm. This is because only a tiny fraction of the cloud was being launched at the correct speed, the rest experiencing a lower launch speed. By increasing the designated launch speed, the reduced launch speed experienced by the larger fraction of atoms was increased, and hence more atoms were observable at 20.5 cm. The tiny fraction launched at the correct speed was not detectable.

Since atoms were detected in the upper chamber, the pulsed magnetic lens was then set-up and used, as can be seen in chapter 6. However, after the moving molasses stage was improved (by changing the radius of the MOT laser beams (section 2.2.4)), the experiment worked far more efficiently.

2.2.4 Improved Moving Molasses and Imaging at the Apex of Flight: 10 mm ($1/e^2$) radius Laser Beams

Since the moving molasses stage presented in section 2.2.3 was extremely inefficient, efforts were made to improve matters by changing the MOT laser beams and studying the launch process. Details of an improved moving molasses stage are presented here, showing significant increase in efficiency and a far better diagnostic of the launching process.

Change of MOT Laser Beams

The optical telescopes for the trap beams (shown in section 2.1.7) were changed from $\times 12.6$ telescopes to $\times 8.0$ telescopes, i.e. the final lens in the telescope was changed

from a 315 mm-focal-length lens to a 200 mm-focal-length lens, with the input lens having a focal length of 25 mm. This made the peak intensity of the trap beams greater, which would provide a greater scattering force during the launch process. The former $1/e^2$ radius of the beams was approximately 15 mm, with the $1/e^2$ radius now being approximately 10 mm. This changed the peak intensity at the centre of the MOT from approximately 50 W m^{-2} ($\sim 3I_{SAT}$) to approximately 120 W m^{-2} ($\sim 8I_{SAT}$). The MOT atom number was then maximised as in section 2.1.13. The optimum parameters were found to be $\Delta = -2\pi \times 11$ MHz with a magnetic field gradient of 15 G cm^{-1}, giving a peak atom number of approximately 5×10^7 for the typical rubidium dispenser current of 8.5 A.

New Launching Experiments

After re-configuring the MOT laser beams, it was then important to investigate the launching process. The CCD camera was positioned to view the MOT chamber (as in section 2.1.15) and image clouds just as they launch. Two important parameters for launching are the central launch frequency (i.e. the overall detuning from the cooling transition from which the upper and lower trap beams are split for launching) and the intensity of the laser beams, since these dictate the scattering rate between the launch beams and the atoms. Afterall, it is the scattering force that causes the atoms to launch. Here, two other parameters are introduced: the ramp time R, which is the time taken to split the upper and lower trap frequencies from the central frequency to the launch frequencies; and the moving molasses constant time C, which is the time (after R) that the laser beams are held at the launch frequencies before being switched off. The parameters R and C are explained visually in Figure 2.38.

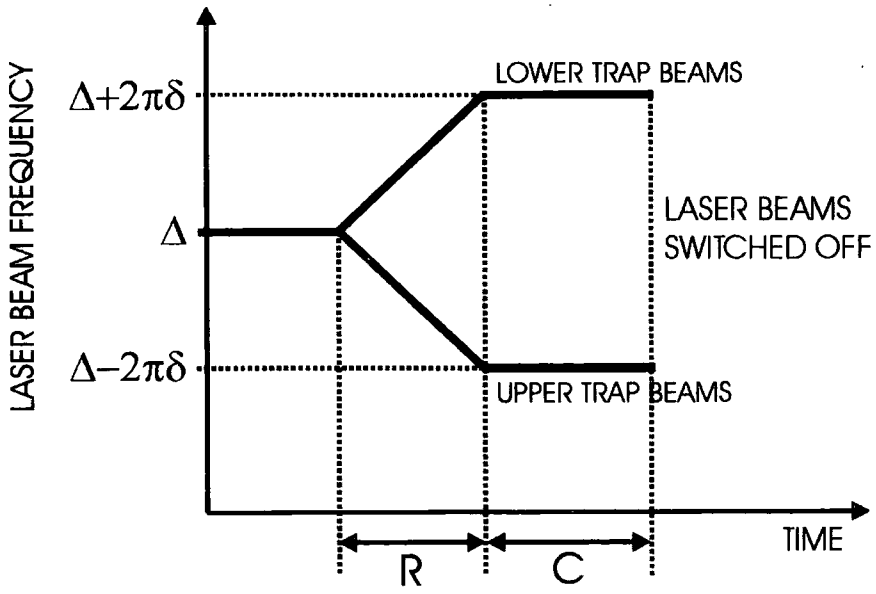

Figure 2.38. Visual representation of the parameters R (the ramp time) and C (the moving molasses constant time). From the central frequency Δ, the upper and lower trap beams are split to the required launch frequencies in a ramp time R. The lower beams are moved up in frequency to $\Delta + 2\pi\delta$ and the upper beams are decreased to $\Delta - 2\pi\delta$, where δ is the (linear) frequency required to achieve a specified launch height and is defined in section 2.2.1. The laser beams are held at the launch frequencies for a moving molasses constant time C, before being switched off.

With the laser beams' central launch frequency set at MOT detuning ($\Delta = -2\pi \times 11$ MHz) and the intensity held at MOT intensity (~ 120 W m^{-2}), the effect on the launch process of the parameters R and C were investigated. This is perhaps best represented pictorially, and hence Figure 2.39 shows sequences of pictures, after the launch beams are switched off, for varying values of R and C. Here the cloud is launched to reach a height of 20.5 cm, where a launch parameter $\delta = 1.48$ MHz is required. For $R = 0.5$ ms and $C = 0.5$ ms, the launch is extremely poor. In fact, only a very small fraction of the cloud is launched at the correct speed, whilst the rest of the cloud exists as a significant 'tail' on the launch. It is not until the case where $R = 1.0$ ms and $C = 0.5$ ms, that this tail has been significantly eradicated. The value of $R = 1.0$ ms, in this case, corresponds to a ramp rate of 1.48 MHz ms^{-1}. It is not only the ramp rate R that is important, the value of C (the moving molasses constant time) is also significant. The 3rd and 4th columns of Figure 2.39 show launches with identical values of R, but differing values of C. In the case of $C = 0.5$ ms, the cloud launches without a significant tail, but in the case of $C = 0.1$ ms a significant tail can still be observed. An important note is that not only can the

value of C be too small, it can also be too large. If C is such that the atoms have moved into a region of space where they begin to experience edge-effects from the lasers beams, the cloud can begin to veer from a vertical launch. It is not known if having laser beams that have been heavily spatially filtered eradicates this problem since we were not able to afford any loss in laser power, which this would require.

The launch speed of the far right column ($R = 2.0$ ms and $C = 2.0$ ms) is consistent with the predicted launch speed of 2.01 m s^{-1}, at 2.1 ± 0.1 m s^{-1}.

The data in Figure 2.39 was taken with $\Delta = -2\pi \times 11$ MHz and the intensity the same as in the MOT (~ 120 W m^{-2}). The minimum values for R and C, for an efficient launch (i.e. the absence of a 'tail' upon the launched cloud) were approximately 1.0 ms and 0.5 ms respectively. However, if the central detuning is decreased further to $\Delta = -2\pi \times 25$ MHz, the approximate minimum values are $R = 3.0$ ms and $C = 1.0$ ms, with this value of R corresponding to a ramp rate of 0.49 MHz ms^{-1}. Indeed, for $\Delta = -2\pi \times 39$ MHz, the value of R required is over 10 ms (corresponding to a ramp rate of less than 0.15 MHz ms^{-1}) and the cloud begins to experience effects from the edges of the extent laser beams (of finite extent). Consequently, it was decided to run the moving molasses stage at $\Delta = -2\pi \times 25$ MHz, $I = 120$ W m^{-2} (the intensity used for the MOT), $R = 3.0$ ms and $C = 1.0$ ms.

The CCD camera was then moved to view the upper chamber to see the effect of the improved moving molasses on the clouds detected there.

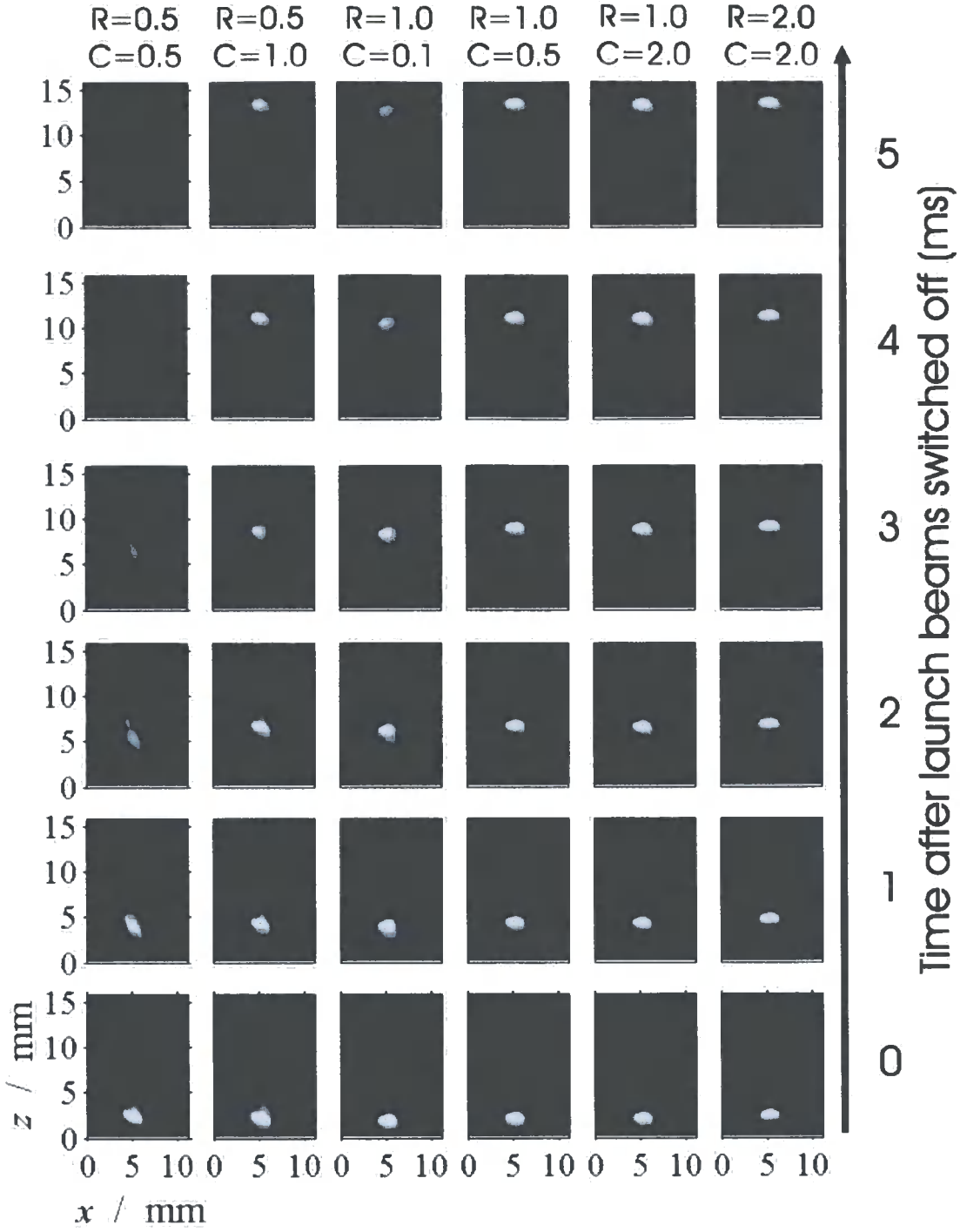

Figure 2.39. Columns of images showing the launch of 10^7 ^{85}Rb atoms, for varying values of the ramp time (R) and the moving molasses constant time (C), which are defined in the main text and are in units of milliseconds. The atoms were launched to come to rest (in theory) at an apex of 20.5 cm above the launch point. The bottom image in each column is taken at the time that the launch beams are turned off. Each subsequent image in a column is 1 ms after the previous image. Images were taken using the imaging beam discussed in section 2.1.11. For R = 0.5 ms and C = 0.5 ms, the launch is extremely inefficient. In this case, only a small fraction of the cloud is launched at the correct speed – the rest of the atoms contribute a significant 'tail' that is launched incorrectly. It is not until the case of R = 1.0 ms and C = 0.5 ms (and above) that the launched cloud becomes devoid of a significant tail of atoms. The central launch frequency and laser intensity for the launch process was the same as for the MOT, i.e. $\Delta = -2\pi \times 13$ MHz and $I \cong 3I_{SAT}$. At greater detunings or lower intensity, the values required for R and C were greater – this is discussed in the main text.

New Images at the Apex of Flight

Figure 2.40 shows an image, (along with the 'binned' horizontal and vertical profiles of the image), of a launched cloud in the quartz cell at the top of the vacuum chamber. The image is centred 20.5 ± 0.2 cm above the MOT, and was taken 204 ms after approximately 5×10^7 ^{85}Rb atoms were launched from a moving molasses stage with

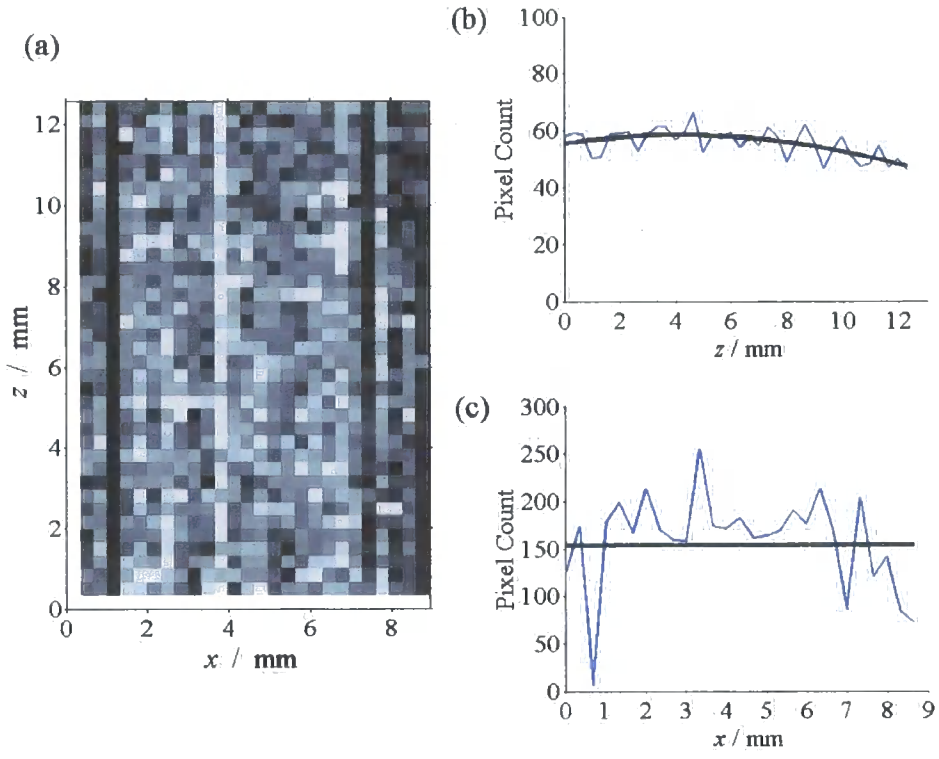

Figure 2.40. (a) Typical single-shot image of a launched cloud in the quartz cell. The image is centred at 20.5 ± 0.2 cm and was taken 204 ms after approximately 5×10^7 ^{85}Rb atoms were launched from a moving molasses stage with a central launch detuning of $\Delta = -2\pi \times 25$ MHz, $\delta = 1.50$ MHz, $I = 120$ W m^{-2} (the intensity used for the MOT) and with R = 3.0 ms and C = 1.0 ms. The image has been manipulated (for clarity) into 'super-pixels', i.e. each block of 10×20 raw pixels has been summed to give one value - a super-pixel. (b) and (c) show 'binned' vertical (z) and horizontal (x) profiles (respectively) of the image in (a). The profiles are a 20-point average in the vertical direction and a 10-point average in the horizontal direction. The peak count (for the binned profile of a 10×20 superpixelated image) is approximately 60 in the vertical direction and 150 in the horizontal direction, both approximately three times the background count shown in Figure 2.41.

a central launch detuning of $\Delta = -2\pi \times 25$ MHz, launch parameter $\delta = 1.50$ MHz[7], $I = 120$ W m^{-2} (the intensity used for the MOT), with R = 3.0 ms and C = 1.0 ms. Fluorescence imaging using the vertical imaging beam (section 2.1.11) was used to detect the atoms. In contrast, Figure 2.41 shows an image with no atoms present. Both images are calibrated to the same scale. In the case of the detected atoms, the signal (for the superpixelated image) is almost three times the background signal in both the horizontal and vertical directions. The shot-to-shot variation of the location of the peak in the atom cloud appears to be less than 4 mm, but this is difficult to judge since the cloud has such an ill-defined distribution.

The static molasses temperature for the above launch parameters, ($\Delta = -2\pi \times 25$ MHz, and $I = 120$ W m^{-2}) was measured to be 25 ± 2 μK, in the same way as in section 2.1.17. For a cloud with an initial standard deviation of 1.0 mm, this would give a standard deviation at the apex of 10.1 ± 0.4 mm, making the total cloud size significantly larger than the image window shown in Figure 2.40. Since the detected signal is so low, it is not possible to move the camera back to get both a larger viewing area and significant signal. Therefore it was not possible to measure the size of the cloud in this case.

[7] $\delta = 1.50$ MHz corresponds to a launch height of 21.0 cm. To put consistently the launched cloud (approximately) in the centre of the image, this increase from the theoretical value of $\delta = 1.48$ MHz was required. However, there is a 2 mm error in the measurement of the launch height plus a shot-to-shot variation in peak position of a few millimetres.

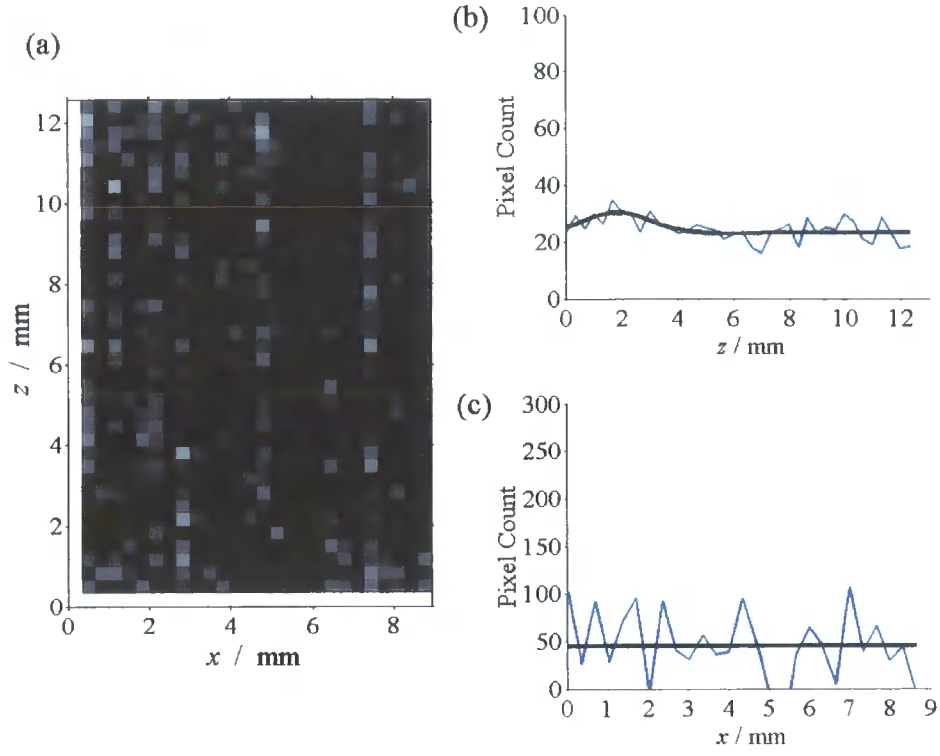

Figure 2.41 (a) Typical single-shot image of the quartz cell with no atoms. The image is centred at 20.5 ± 0.2 cm above the MOT region and has the same imaging parameters as the image in Figure 2.40, but no atoms were launched. The image has been manipulated into 'super-pixels', i.e. each block of 10×20 raw pixels has been summed to give one value - a super-pixel. (b) and (c) show 'binned' vertical and horizontal profiles (respectively) of the image in (a). The profiles are a 20-point average in the vertical direction and a 10-point average in the horizontal direction. The background count (for the binned profile of a 10×20 superpixelated image) is approximately 20 in the vertical direction and 50 in the horizontal direction.

For the purposes of pulsed magnetic lensing, it is extremely important that the unfocused cloud has an apex in the centre of the image. This is to ensure that any magnetic lens is used only to manipulate the size of the cloud and not the centre-of-mass velocity of the cloud. It is possible to turn the current through the rubidium dispenser to a higher value to observe a stronger signal. The dispenser current was increased from its normal operating current of 8.5 A to 10.0 A, which is the maximum safe operating current for the electrical feed-through on the vacuum chamber (this was used to carry current to the rubidium dispenser). The current was not maintained at

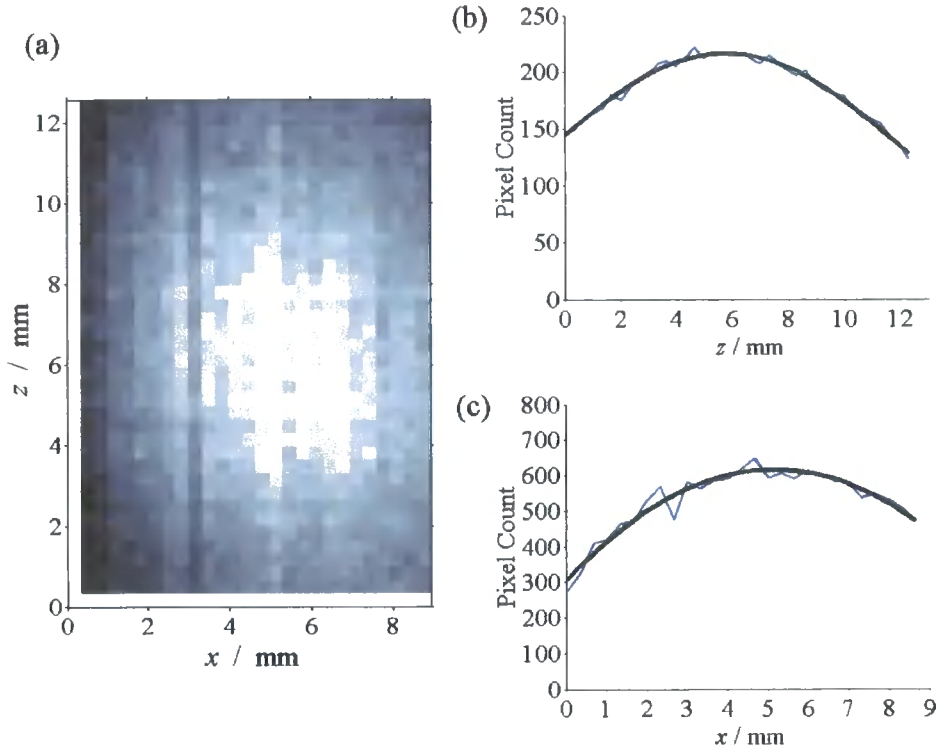

Figure 2.42. (a) Single-shot image of a launched cloud in the quartz cell. Here, the rubidium dispenser current was increased from its normal running value of 8.5 A to 10 A to increase the atom number and hence the signal of the launched cloud. This scenario was only a short-term solution since, at 10 A, this was the maximum current for the electrical feed-through on the vacuum chamber and because of the danger in damaging the dispenser at this stage of experimentation, either by releasing all the available rubidium, or from damaging the electrical connections inside the vacuum chamber. However, this was an extremely important piece of experimentation for the purposes of pulsed magnetic lensing. It was very important to know that the un-focused cloud had an apex at the centre of the image area, (images taken at later times, and earlier times registered the cloud lower in the image area), to ensure that any magnetic lens was only used to manipulate the size of the cloud and not the centre-of-mass velocity of the cloud. The image is centred at a height of 20.5 ± 0.2 cm above the MOT and was taken 204 ms after $> 10^8$ ^{85}Rb atoms were launched from a moving molasses stage with a central launch detuning of $\Delta = -2\pi \times 25$ MHz, $\delta = 1.50$ MHz, $I = 120$ W m^{-2} (the intensity used for the MOT) and with $R = 3.0$ ms and $C = 1.0$ ms. The image has been manipulated into 'super-pixels', i.e. each block of 10×20 raw pixels has been summed to give one value - a super-pixel. (b) and (c) show 'binned' vertical (z) and horizontal (x) profiles, respectively, of the image in (a). The profiles are a 20-point average in the vertical direction and a 10-point average in the horizontal direction. The peak count (for the binned profile of a 10×20 superpixelated image) is significantly larger than the background shown in Figure 2.40, but this required the rubidium dispenser to be operated at 10 A, which was untenable. The Gaussian fits to the profiles (black line plots on (b) and (c)) are discussed in the main text.

this value for more than a quarter of an hour because of the danger in damaging the dispenser at this stage of experimentation, either by releasing all the available rubidium, or from damaging the electrical connections inside the vacuum chamber (since the dispenser in this experiment did not seem to work as other research has found [1, 2] and the heat from the current must have been conducting to another heat sink, as discussed at the end of section 2.1.13). However, there was time to take images to ensure that the launched cloud appeared (approximately) in the centre of the image area. Figure 2.42 shows a single-shot image centred 20.5 ± 0.2 cm above the MOT, taken 204 ms after $>10^8$ ^{85}Rb atoms were launched from a moving molasses stage with a central launch detuning of $\Delta = -2\pi \times 25$ MHz, launch parameter $\delta = 1.50$ MHz, $I = 120$ W m^{-2} (the intensity used for the MOT), with R = 3.0 ms and C = 1.0 ms. This image has significantly more pixel counts than that shown in Figure 2.40, where the rubidium dispenser current was set to 8.5 A. To reiterate, it is important that the launched clouds reached an apex in the centre of the image (images taken at later and earlier times showed the cloud lower in the image) so that any magnetic lens acts only to modify the spatial extent of the cloud, and not to change the centre-of-mass velocity of the cloud. If the cloud (in the absence of a lens) did not have an apex in the centre of the image, the lens would have to be used to push the focused clouds (upwards or downwards) to appear in the centre of the image. By doing this, the cloud would have to spend more time in one half of the lens than the other, thus experiencing more magnetic aberration, since lenses are shown (in chapter 3) to vary more from the ideal at greater distances from the centre of the lens. We do not want to characterise a lens as both an acceleration device and a focusing device, only as a focusing device.

The 'binned' cloud profiles in Figure 2.42 (b) and (c) contain both data and theoretical fits of a Gaussian of the form,

$$P(x) = A \exp\left(\frac{-(x - x_0)^2}{2\sigma_x^2} \right) + B . \qquad (2.22)$$

However, as can be seen in Figure 2.42 (b) and (c), the profiles only contain a small fraction of the Gaussian profile, only the section around the peak. It would have been desirable to extract a temperature from the expanded cloud, but this was not possible

due to the uncertainty in the fit. However, the primary goal, of ensuring that the unfocused cloud's apex was in the centre of the image, was achieved.

Having improved the moving molasses efficiency, it was now important to use a pulsed magnetic lens upon the atoms, the results of which are shown in chapter 6.

Conclusions on the Improvement of the Moving Molasses Phase

The launch process in moving molasses can be flawed due to a scattering rate too low to accelerate the atoms to the correct speed. In this experiment, the scattering rate was increased by increasing the intensity of the laser beams, leading to a much more efficient moving molasses phase. Originally (for the inefficient moving molasses phase discussed in section 2.2.3) the work of Münstermann *et al.* [23] was followed since their experimental set-up was very similar to the set-up used here. However, that experiment only required a small number of atoms (<5) to be loaded into an optical cavity 25 cm above the MOT, and although quoting a molasses temperature of 5 μK, did not quote a launch temperature or specific launch parameters. By reference to the work of Clairon *et al.* [36], in which the first moving molasses fountain is described, it became apparent that it is first important to bring the atoms to the correct launch speed, and then to cool whilst they are in the moving frame. In the improved version of moving molasses in this experiment, the $1/e^2$ radius of the MOT laser beams is approximately 10 mm. In the required launch ramp time $R = 3.0$ ms and moving molasses constant time $C = 1.0$ ms, for the parameters used in this experiment, the centre-of-mass of the atom cloud moves approximately 5 mm if accelerated to a speed of 2.01 m s^{-1}. Indeed, the cloud has then moved through a significant fraction of the laser beams and can begin to experience edge effects. To avoid edge effects and allow more cooling after the correct launch velocity is attained, the solution would be much larger beams so that the intensity is approximately constant over a greater distance of cloud movement or a greater laser power to achieve launch speed sooner. Larger beams would require more power to give the same scattering rate, which would explain why Fertig and Gibble [35, 37] use six injection-locked slave lasers, one for each beam, and very large, smooth profiles to attain their extremely low rubidium moving molasses temperature of 1.85 μK. Perhaps the solution to power-limited moving molasses would be a beam configuration as found in the work by Clairon *et al.* [36], where the launch beams

propagate vertically. In this case, the moving molasses launch stage can last for a very long time, giving more time for cooling once launch speed is achieved. However, this configuration would limit the applications as a launch beam would propagate through the apex of flight.

[1] J Fortagh, A Grossmann, TW Hänsch, C Zimmermann, *Fast loading of a magneto-optical trap from a pulsed thermal source*, J. App. Phys. **84** 6499 (1998)

[2] U D Rapol, A Wasan, V Natarajan, *Loading of a Rb magneto-optical trap from a getter source*, Phys. Rev. A **64** 023402 (2001)

[3] K L Moore, T P Purdy, K W Murch, S Leslie, S Gupta and D M Stamper-Kurn, *Collimated, single-pass atom source from a pulsed alkali metal dispenser for laser cooling experiments*, arXiv:physics/0409011 v3 5th November (2004)

[4] U D Rapol, A Krishna and V Natarajan, *Precise measurement of hyperfine structure in the $5P_{3/2}$ state of ^{85}Rb*, Eur. Phys. J. D **23** 185 (2003)

[5] C V Saba, *Reconstruction of a cold atom cloud by magnetic focusing*, Ph.D. thesis, University of Sussex (1999)

[6] P D Lett, W D Phillips, S L Rolston, C E Tanner, R N Watts and C L Westbrook, *Optical molasses*, J. Opt. Soc. Am. B **6** 2084 (1989)

[7] H J Metcalf and P van der Straten, *Laser Cooling and Trapping*, p276, Springer-Verlag: New York (1999)

[8] E Raab, M Prentiss, A Cable, S Chu and D Pritchard, *Trapping of Neutral-Sodium Atoms with Radiation Pressure*, Phys. Rev. Lett. **59** 2631 (1987)

[9] G K Woodgate, *Elementary Atomic Structure*, 2nd Edition, p188, Oxford University Press (1980)

[10] C J Foot, *Atomic Physics*, p193, Oxford University Press (2005)

[11] K Lindquist, M Stephens and C Wieman, *Experimental and theoretical study of the vapour-cell Zeeman optical trap*, Phys. Rev. A **46** 4082 (1992)

[12] C D Wallace, T P Dinneen, K Y N Tan, A Kumarakrishnan, P L Gould and J Javanainen, *Measurements of temperature and spring constant in a magneto-optical trap*, J. Opt. Soc. Am. B **11** 703 (1994)

[13] A S Arnold, J S Wilson and M. G. Boshier, *A simple extended-cavity diode laser*, Rev. Sci. Inst. **69** 3 (1998)

[14] K B MacAdam, A Steinbach and C Wieman, *A narrow-band tuneable diode laser system with grating feedback, and a saturated absorption spectrometer for Cs and Rb*, Am. J. Phys. **60** 1098-1111 (1992)

[15] C P Pearman, C S Adams, S G Cox, P F Griffin, D A Smith and I G Hughes, *Polarization spectroscopy of a closed atomic transition: applications to laser frequency locking*, J. Phys. B: At. Mol. Opt. Phys. **35** 5141 (2002)

[16] H J Metcalf and P van der Straten, *Laser Cooling and Trapping*, ISBN 0-387-98728-2, Springer (1999)

[17] W Demtröder *Laser Spectroscopy*, 3rd Edition, Springer-Verlag: Berlin (2003)

[18] C Wieman and T W Hänsch, *Doppler-free laser polarization spectroscopy*, Phys. Rev. Lett. **36** 1170 (1976)

[19] D A Smith and I G Hughes, *The role of hyperfine pumping in multilevel systems exhibiting saturated absorption*, Am. J. Phys. **72** 631 April (2004)

[20] I C M Littler, J H Eschner and H-A Bachor, *Sub-kHz precision voltage-controlled-oscillator system or laser frequency control: An application in atom optics*, Rev. Sci. Instrum. **67** 3065 (1996)

[21] A S Arnold, *Preparation and Manipulation of an ^{87}Rb Bose-Einstein Condensate*, D.Phil Thesis, University of Sussex (1999)

[22] M Misakian, *Equations for the Magnetic Field Produced by One or More Rectangular Loops of Wire in the Same Plane*, J. Res. Natl. Inst. Stand. Technol. **105** 557 (2000)

[23] P Münstermann, T Fischer, P W H Pinkse and G Rempe, *Single slow atoms from an atomic fountain observed in a high-finesse optical cavity*, Optics Comm. **159** 63 (1999)

[24] C Gabbanini, S Gozzini and A Lucchesini, *Photoionization cross section measurement in a Rb vapour cell trap*, Optics Comm. **141** 25 (1997)

[25] C G Townsend, N H Edwards, C J Cooper, K P Zetie, C J Foot, A M Steane, P Szriftgiser, H Perrin and J Dalibard, *Phase-space density in the magneto-optical trap*, Phys. Rev. A **52** 1423 (1995)

[26] C Gabbanini, A Evangelista, S Gozzini, A Lucchesini, A Fioretti, J H Muller, M Colla and E Arimondo, *Scaling laws in magneto-optical traps*, Europhys. Lett. **37** 251 (1997)

[27] H J Lewandowski, D M Harber, D L Whitaker, E A Cornell, *Simplified system for creating a Bose-Einstein condensate*, J. Low Temp. Phys. **132** 309 (2003)

[28] E Kreyszig, *Advanced Engineering Mathematics*, 7th Edition, p1184, Wiley (1993)

[29] F Mandl, *Statistical Physics*, 2nd Edition, p190, Wiley (1988)

[30] J Dalibard and C Cohen-Tannoudji, *Laser cooling below the Doppler limit by polarization gradients: simple theoretical models*, J. Opt. Soc. Am. B **6** 2023 (1989)

[31] P D Lett, R N Watts, C I Westbrook, W D Phillips, P L Gould and H J Metcalf, *Observation of Atoms Laser Cooled below the Doppler Limit*, Phys. Rev. Lett. **61** 169 (1988)

[32] S A Hopkins, A V Durrant, *Parameters for polarization gradients in three-dimensional electromagnetic standing waves*, Phys. Rev. A **56** 4012 (1997)

[33] C Salomon, J Dalibard, W D Phillips, A Clairon, S Guellati, *Laser Cooling of Cesium Atoms below* 3 μK, Europhys. Lett. **12** 683 (1990)

[34] C Gerz, T W Hodapp, P Jessen, K M Jones, W D Phillips, C I Westbrook and K Mølmer, *The Temperature of Optical Molasses for Two Different Atomic Angular Momenta*, Europhys. Lett. **21** 661 (1993)

[35] C Fertig and K Gibble, *Laser Cooled ^{87}Rb Clock*, IEEE Trans. Instrum. Meas. **48** 520 (1999)

[36] A Clairon, C Salomon, S Guellati and W D Phillips, *Ramsey Resonance in a Zacharias Fountain*, Europhys. Lett. **16** 165 (1991)

[37] C Fertig, private communication.

Chapter 3

Theoretical Single Impulse Magnetic Focusing

3.1
Basic Pulsed Magnetic Lens Theory and Matrix Representation

3.1.1 Magnetic Dipole Interaction and Fields Required for Focusing

Paramagnetic atoms have a magnetic dipole moment dependent upon the total angular momentum of the atom [1]. Indeed, it is this magnetic dipole's interaction with external magnetic fields that forms the basis of the experiment presented in this thesis. The potential U experienced by an atom with magnetic moment $\boldsymbol{\mu}$ in a magnetic field $\mathbf{B}$ is [1],

$$U = -\boldsymbol{\mu} \bullet \mathbf{B} = -\mu_\xi B \tag{3.1}$$

where μ_ξ is the projection of the magnetic moment onto the magnetic field direction and B is the magnitude of the magnetic field. Therefore, the Stern-Gerlach force $\mathbf{F}$ experienced by the atom due to the magnetic field is,

$$\mathbf{F} = -\vec{\nabla} U = \vec{\nabla}\left(\mu_\xi B\right). \tag{3.2}$$

In this thesis, the weak-field-seeking (WFS) state $5^2S_{1/2}\left|F=3, m_F=3\right\rangle$ of ^{85}Rb will be considered for experimental focusing. This state has a constant magnetic moment even in magnetic fields large enough for F no longer to be a good quantum number. In this case, the projection μ_ξ of the magnetic moment onto the magnetic field direction can be written as the product of the magnetic quantum number m_F, the Landé g-factor g_F, and the Bohr Magneton μ_B, i.e. $\mu_\xi = -m_F g_F \mu_B$ [1], such that

$$\mathbf{F} = -m_F g_F \mu_B \vec{\nabla} B. \tag{3.3}$$

A weak-field-seeking (WFS) state is termed as such since it is attracted to minima in the magnetic field and has the criteria that $m_F g_F > 0$. In that case, if the magnetic-field gradient $\vec{\nabla} B$ is positive (negative), the force $\mathbf{F}$ is negative (positive).

One must now consider the potential U required to form a lens for the launched cold atoms in this experiment. As seen in Section 2.2.2, a cloud of atoms will, over time, evolve into a correlated state, where an atom's position in the cloud will be a linear function of the atom's velocity. To focus the cloud, the force $\mathbf{F}$ impinged upon the atoms must also be a linear function of position. Since the force $\mathbf{F}$ is a linear function

of the gradient of the magnetic field $\vec{\nabla}B$, the required magnetic field **B** must be harmonic in nature to form a perfect lens.

3.1.3 Matrix Representation and Liouville's Theorem

As with conventional ray-optics [2], an atom lens system can be represented in terms of matrices. Miossec *et al.* [3] detailed the derivation of these atom lens matrices, so it is sufficient to present here only the matrices themselves.

A two-dimensional vector can be used to represent the velocity and position of an atom, and an $\mathfrak{ABCD}$ system matrix to relate an initial vector to a final vector. For example, in 1-D, the initial position x_i and initial velocity v_{x_i} of an atom is related to the final position x_f and final velocity v_{x_f} by the equation,

$$\begin{pmatrix} x_f \\ v_{x_f} \end{pmatrix} = \begin{pmatrix} \mathfrak{A} & \mathfrak{B} \\ \mathfrak{C} & \mathfrak{D} \end{pmatrix} \begin{pmatrix} x_i \\ v_{x_i} \end{pmatrix} \tag{3.4}$$

In direct analogy to geometrical optics [2], $\mathfrak{A}$, $\mathfrak{B}$, $\mathfrak{C}$, and $\mathfrak{D}$ characterize the system. The condition $\mathfrak{B}=0$ represents the spatial image plane, hence $x_f = \mathfrak{A}x_i$, where $\mathfrak{A}$ denotes the spatial magnification in that image plane. $\mathfrak{D}$ gives the velocity magnification, with the condition that $\mathfrak{D}$ is the inverse of $\mathfrak{A}$. This spatial compression and concomitant velocity spread is a manifestation of Liouville's Theorem [4]. This theorem implies that phase-space density is conserved in a Hamiltonian system, a system without dissipation. The magnetic forces used in this experiment are conservative, and therefore this form of magnetic focusing is subject to Liouville's Theorem: high spatial compression of an atom cloud comes with a concomitant increase in the velocity spread (effective temperature) of the cloud.

For a lens system, this $\mathfrak{ABCD}$ system matrix can constitute several translation and lens matrices multiplied together. Equations (3.5), (3.6) and (3.7) show the matrices for a translation, a converging lens and a diverging lens respectively.

$$M_T \equiv \begin{pmatrix} 1 & t \\ 0 & 1 \end{pmatrix} \tag{3.5}$$

$$M_C \equiv \begin{pmatrix} \cos\omega\tau & \frac{1}{\omega}\sin\omega\tau \\ -\omega\sin\omega\tau & \cos\omega\tau \end{pmatrix} \tag{3.6}$$

$$M_D \equiv \begin{pmatrix} \cosh \omega\tau & \frac{1}{\omega}\sinh \omega\tau \\ \omega \sinh \omega\tau & \cosh \omega\tau \end{pmatrix} \tag{3.7}$$

The Translation matrix M_T does not affect the velocity component of the position-velocity vector, only the position component, with the spatial translation occurring for a time t. Both the converging lens and the diverging lens have duration τ and an angular frequency ω. The difference between the Converging Lens matrix M_C and the Diverging Lens matrix M_D is the switch from traditional trigonometric functions to hyperbolic functions. This switch can be considered as a change in the argument of the function from imaginary to real, or vice versa. Thus, to change from a converging to a diverging lens, one would merely have to multiply the angular frequency of the lens, ω, by the complex number i. A converging lens can be considered as a diverging lens with complex angular frequency.

This system-matrix approach predicts the image plane and smallest attainable cloud size for a purely harmonic lens. Although this method is a useful starting point, it does not include magnetic aberrations, and is hence limited in its predictions.

The rest of this thesis will consider, instead of x and v_x for individual atoms, the standard deviation of position and velocity for a cloud of atoms, σ_x and σ_{v_x} respectively. Therefore, the spatial standard deviation at a time t_f, σ_{x_f}, is related to the initial spatial standard deviation, σ_{x_i}, by

$$\sigma_{x_f}{}^2 = \left(\mathcal{A}\sigma_{x_i}\right)^2 + \left(\mathcal{B}\sigma_{v_{x_i}}\right)^2, \tag{3.8}$$

and the velocity standard deviation at t_f, $\sigma_{v_{x_f}}$, is related to the initial velocity standard deviation, $\sigma_{v_{x_i}}$, by

$$\sigma_{v_{x_f}}{}^2 = \left(\mathcal{C}\sigma_{x_i}\right)^2 + \left(\mathcal{D}\sigma_{v_{x_i}}\right)^2. \tag{3.9}$$

Although an image is predicted in the plane where $\mathcal{B}=0$, this is not necessarily the plane of highest spatial compression, as will be seen in chapter 4.

3.2
Current Carrying Coils for the Formation of Pulsed Magnetic Lenses

This section outlines the need for a harmonic magnetic field, and discusses the general field expansions of magnetic fields and their relevance to magnetic lenses, before going on to introduce the six strategies for focusing that will be considered theoretically in this thesis.

Harmonic Expansions

As discussed in Section 3.1, a purely harmonic magnetic field is required to form a perfect lens. However, such a field cannot be realised experimentally. This section will consider two ideal expansions of the 3-dimensional field magnitude: one for 1-dimensional focusing (axial or radial focusing) and another for 3-dimensional focusing (axial and radial focusing), denoted as appropriate,

$$B_{1D}(x,y,z) = B_0 + \frac{B_2}{2}\left(-\frac{x^2}{2} - \frac{y^2}{2} + (z-z_c)^2\right), \tag{3.10}$$

$$B_{3D}(x,y,z) = B_0 + B_1(z-z_c) + \frac{B_2}{2}\left(x^2 + y^2 + (z-z_c)^2\right). \tag{3.11}$$

The z-direction is the axial direction and will correspond to the launch direction of the experiment, where $\{0,0,z_c\}$ is the position of the centre of the lens. The directions x and y denote the Cartesian co-ordinates in the radial direction, i.e. the direction perpendicular to the launch direction. B_0, B_1 and B_2 are the bias field, the axial gradient of the field, and the curvature of the field, respectively. B_0 will have no effect upon the spatial or velocity distribution of an atom cloud, B_1 will act to change the centre-of-mass velocity of a cloud (in the axial direction), and B_2 is the significant term for lensing. As will be seen below, it is the higher order terms that appear in the expansion of real magnetic fields that cause aberrations in the lens characterised by B_2.

For a field characterised by equation (3.10), the field represents an axially converging (diverging) and a radially diverging (converging) lens if B_2 is positive (negative), (for

$m_F g_F > 0$ ($m_F g_F < 0$)). Lenses of the form of equation (3.10) can be used to focus atoms in both weak-field seeking (WFS) states, i.e. $m_F g_F > 0$, and atoms in strong-field-seeking (SFS) states, i.e. $m_F g_F < 0$. Indeed, with the correct application of two or more of these lenses, (with temporal separation), a 3-dimensional focus can be achieved. This Alternate Gradient method, which originated for use in particle accelerators [5], has been used to cool and slow polar molecules [6], and to focus launched caesium atoms [7,8], the latter of which is discussed in chapter 1. A theoretical study of the alternate gradient method for launched cold atoms can be found in Arnold *et al.* [9]. However, this thesis will concern its self only with the action of a single pulse on atoms in WFS states, specifically the $5^2S_{1/2}|F=3, m_F=3\rangle$ state of ^{85}Rb.

The 3-dimensional lens described by equation (3.11) can only be used to focus atoms in WFS states, not atoms in SFS states, a consequence of Wing's Theorem [10]. This theorem forbids focusing of atoms in SFS states due to the non-existence of magnetic field maxima in free space.

The subsequent sections discuss general field expansions for relevant magnetic fields then detail specific coil configurations and their associated fields.

General Field Expansions

The magnetic field at a point $\mathbf{x}$ relative to a current element $I\,d\mathbf{l}$ is given by the Biot-Savart law [11]:

$$d\mathbf{B} = \frac{\mu_0}{4\pi}\frac{(I\,d\mathbf{l}\times\mathbf{x})}{|\mathbf{x}|^3}. \tag{3.12}$$

The Biot-Savart law can determine the magnetic field produced by current carrying wires and the on-axis fields from current-carrying circular coils, the two mainstays of the magnetic lenses presented in this thesis. For the full 3-dimensional description of the magnetic field from a circular coil, the field must be expressed in terms of complete elliptic integrals [12,13].

The lenses in this thesis are constructed from circular coils and current bars, and produce magnetic fields that are approximately cylindrically symmetric. The use of Maxwell's Equations $\nabla\cdot\mathbf{B}=0$ and $\nabla\times\mathbf{B}=0$ [11], enables the deduction of the full 3-dimensional fourth-order magnetic field from the 1-dimensional fourth-order axial magnetic field given by equation (3.13),

$$B_z(r=0,z)=\sum_{i=0}^{4}\frac{B_i z^i}{i!}. \tag{3.13}$$

The full 3-dimensional fourth-order field is then,

$$\begin{aligned}\mathbf{B}(r,z)=\{B_r,B_z\}=\{0\,,B_0\}&\\ +B_1\left\{-\frac{r}{2},z\right\}&\\ +\frac{B_2}{2!}\left\{-rz\,,z^2-\frac{r^2}{2}\right\}&\\ +\frac{B_3}{3!}\left\{\frac{3r^3}{8}-\frac{3rz^2}{2},z^3-\frac{3r^2z}{2}\right\}&\\ +\frac{B_4}{4!}\left\{\frac{3r^3z}{2}-2rz^3\,,z^4-3r^2z^2+\frac{3r^4}{8}\right\},&\end{aligned} \tag{3.14}$$

with the third-dimensional component B_ϕ always equal to zero due to cylindrical symmetry. This 3-dimensional field then has a third-order magnitude of,

$$B(r,z)=B_0+B_1z+\frac{B_2}{2}z^2+\left(\frac{B_1^2}{8B_0}-\frac{B_2}{4}\right)r^2+\frac{B_3}{6}z^3+\left(\frac{B_1B_2}{4}-\frac{B_3}{4}-\frac{B_1^3}{8B_0^2}\right)r^2z\,. \tag{3.15}$$

Terms higher than third-order are somewhat cumbersome, but can be simplified if the system is axially symmetric, i.e. the expansion coefficients $B_{n=odd}=0$, to,

$$B(r,z)=B_0+\frac{B_2}{2}\left(z^2-\frac{r^2}{2}\right)+B_4\left(\frac{z^4}{24}+\frac{r^4}{64}\right)r^2+\left(\frac{B_2^2}{B_0}-B_4\right)r^2z^2\,. \tag{3.16}$$

The final term of equation (3.16) has been written in such a way as to highlight a particular factor, that of aberration. Clearly equation (3.16) does not represent a purely harmonic field, the ideal for a magnetic lens, with the terms higher than second-order representing aberration. Note that aberrations can be reduced significantly if a magnetic lens is constructed such that $B_2^2=B_0B_4$.

Introduction of Strategies

The sections immediately proceeding this will detail the fields from various coil configurations. However, it is useful to introduce these configurations, which shall be referred to as Strategies I-VI, for ease of reference and understanding, below and in chapter 4.

Figure 3.1 shows a diagram of six different strategies for the creation of single-impulse magnetic lenses. Considering atoms in weak-field-seeking states

($m_F g_F > 0$), Strategies I and II are for 2-dimensional (radial) focusing; Strategy III is for 1-dimensional (axial) focusing; Strategy IV can be used for 1-, 2- and 3-dimensional focusing; and Strategies V and VI are for 3-dimensional focusing.

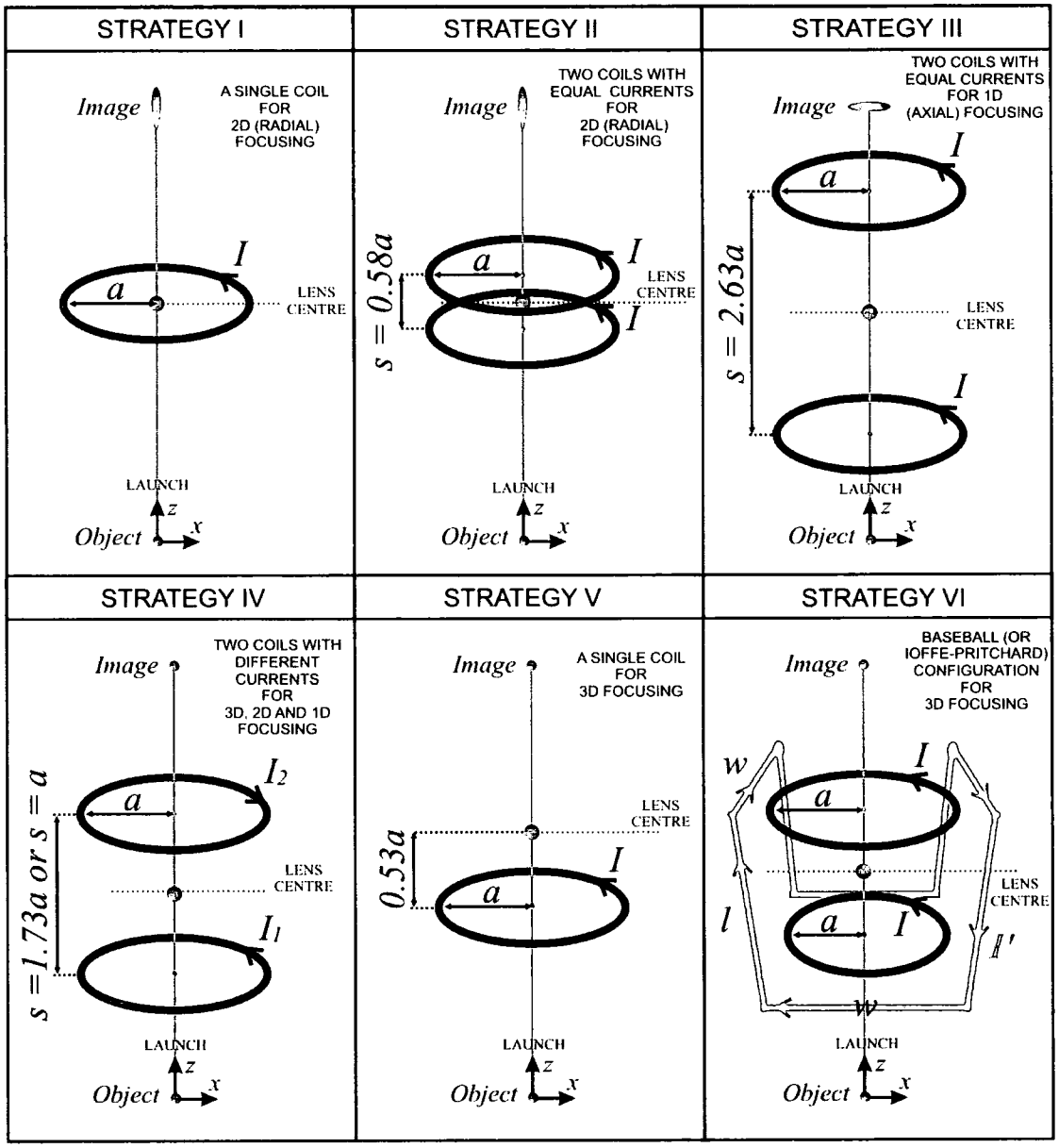

Figure 3.1. Schematics of Strategies I-VI. Strategy I utilizes the centre of a single coil; Strategies II and III use the geometric centre of a pair of coaxial coils (carrying equal currents in the same sense) with separations of $S = 0.58$ and $S = 2.63$ coil radii, respectively; Strategy IV uses the geometric centre of a pair of coaxial coils with unequal currents and a relative separation $S = \sqrt{3}$; Strategy V uses a single coil axially offset to $z/a = \pm\sqrt{2/7}$; Strategy VI uses the geometric centre of a Baseball coil with dimensions $w = l = 2a$ combined with a coaxial coil pair with $S = 1$.

All strategies except Strategy VI are cylindrically symmetric and are thus subject to equations (3.14) and (3.15) in section 3.1. However, only Strategies I-III acquiesce to equation (3.16), with Strategy VI being approximately axially symmetric. Strategies IV and V are not axially symmetric. Figure 3.2 displays the relevant magnetic field information for each strategy, which shall be referred in the discussion of each strategy.

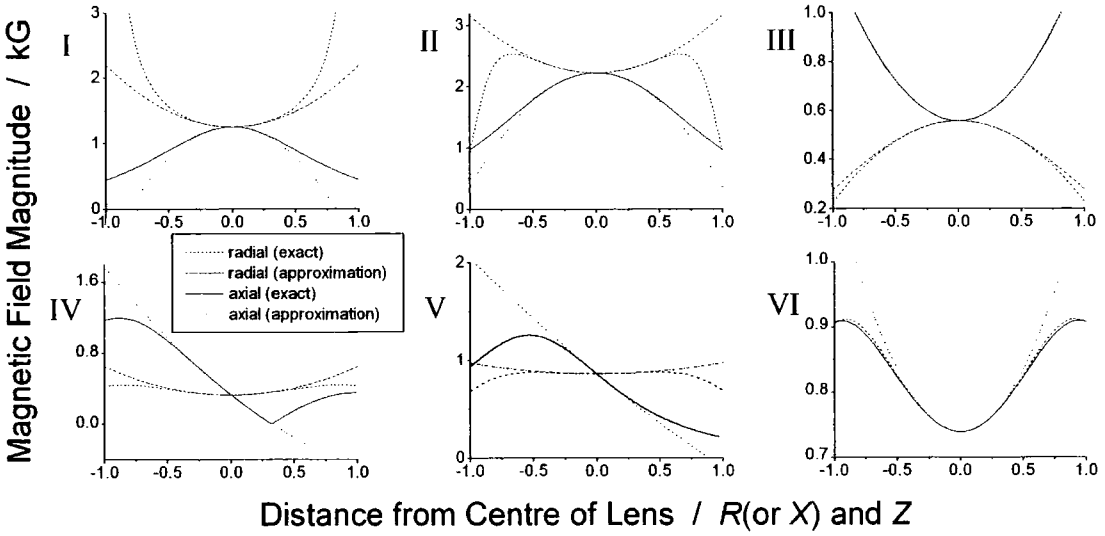

Figure 3.2. The relevant magnetic field information corresponding to Strategies I-VI shown in Figure 3.1. R, X and Z are the scaled coordinates of the radial, x, and axial directions respectively. The X coordinate is used for Strategy VI since this is a system without cylindrical symmetry. Along with the exact magnetic field information, parabolic approximations are given for comparison between the real and ideal. Note that the axial gradients present for Strategies IV and V would act to shift the centre of mass velocity of an atom cloud (equation (3.11)), but would not act to focus or defocus.

A Single Coil – Strategies I and V

Before discussing the case of a single coil in detail, it is first prudent to consider the general case of two coils of N turns with radius a, separation s, carrying currents I_1 and I_2, and then to simplify to a single coil in that formalism.

Let the currents be partitioned into symmetric and anti-symmetric components, $I_H = (I_1 + I_2)/2$ and $I_{AH} = (I_1 - I_2)/2$ respectively, where the subscript H is used to denote 'Helmholtz' configuration and the subscript AH to signify 'Anti-Helmholtz' configuration. The axial magnetic field can then be defined as,

$$B(0,z)=\left(\frac{(\eta_H+\eta_{AH})}{a\left(1+(z/a-S/2)^2\right)^{3/2}}+\frac{(\eta_H-\eta_{AH})}{a\left(1+(z/a+S/2)^2\right)^{3/2}}\right) \tag{3.17}$$

where $\eta=\mu_0 NI/2$, and the scaled separation $S=s/a$.

This axial magnetic field yields the Taylor expansion terms,

$$\begin{aligned} B_0&=\frac{2\eta_H}{a\left(1+S^2/4\right)^{3/2}} & B_1&=\frac{3\eta_{AH}S}{a^2\left(1+S^2/4\right)^{5/2}} \\ B_2&=\frac{6\eta_H\left(S^2-1\right)}{a^3\left(1+S^2/4\right)^{7/2}} & B_3&=\frac{15\eta_{AH}S\left(S^2-3\right)}{a^4\left(1+S^2/4\right)^{9/2}} \\ B_4&=\frac{45\eta_H\left(S^4-6S^2+2\right)}{a^5\left(1+S^2/4\right)^{11/2}} \end{aligned} \tag{3.18}$$

where the symmetric terms are in the left-hand column and the anti-symmetric terms in the right-hand column.

Therefore, considering a single coil with radius a and current NI_1, in equations (3.17) and (3.18), then $I_2=0$ and $S=0$. For Strategy I, as can be seen in Figure 3.2 I, the radial curvature is positive and the axial curvature is negative (and twice the magnitude of the radial curvature). Thus, atoms in WFS states would focus radially, but be defocused axially if this coil were to be used as a lens at the centre of the coil.

However, since the radial and axial components of the magnetic field have differing z-dependence, a single coil has two points at which the radial and axial curvatures are both positive and equal in magnitude: $z=\pm\sqrt{2/7}a$. A lens utilising one of these points, as in Strategy V, offers the possibility of an isotropic 3-dimensional focus. Figure 3.2 V shows that this configuration has an axial gradient that would act to shift the centre-of-mass velocity of the cloud in the z-direction.

A Pair of Co-axial Coils – Strategies II, III and IV

A pair of axially-displaced, co-axial coils can be utilised for radial (Strategy II), axial (Strategy III) or isotropic (Strategy IV) focusing.

If the two coils have equal current with the same sense, a radially converging (diverging) lens is produced for a separation s less (greater) than the coil radius a, i.e for $S<1$ ($S>1$), as in Strategy II (Strategy III). When $S=1$, i.e. the Helmholtz

condition for a uniform field, no lens is formed at the centre of the coil pair since the curvature is zero.

The optimum separation for the radially converging (and axially diverging) lens of Strategy II, is $S = 0.58$, by consideration of equation (3.16). The ideal lens is parabolic, so elimination of the third and fourth terms in equation (3.16) would optimise the lens. The third term is zero when $B_4 = 0$, which occurs if $S = \sqrt{3 \pm \sqrt{7}} = 0.595$ or 2.38. The fourth term is zero when $B_4 B_0 = B_2^{\,2}$, which occurs if $S = \sqrt{\frac{1}{3}\left(13 \pm \sqrt{145}\right)} = 0.565$ or 2.89. Taking the mean of the first solution in each case, since we are considering a radially converging lens, gives an optimum separation for Strategy II of $S = 0.58$. Figure 3.2 II shows that the axial curvature is negative and the radial curvature is positive for Strategy II.

Taking the mean of the second solution (from the minimisation of the third and fourth terms in equation (3.16)), gives the optimum separation for the axially converging (but radially diverging) lens of Strategy III, $S = 2.63$. Figure 3.2 III, shows that in this case the axial curvature is positive and the radial curvature is negative, the opposite way round to Strategy II.

Strategy IV offers the possibility of either an isotropic 3-dimensional lens, or a radial-only lens, or an axial-only lens. Equation (3.15), rather than equation (3.16), applies in this case, since Strategy IV is not axially symmetric. For an isotropic 3-dimensional lens, the condition $6B_0B_2 = B_1^{\,2}$ must be met. The relative currents in the two coils can the be linked using equation (3.18) such that,

$$\eta_{AH} = \pm\sqrt{8\eta_H^{\,2}\left(1 - \frac{1}{S^2}\right)}. \tag{3.19}$$

This relationship still allows one to vary the separation of the coils to reduce the third order terms, (i.e. the magnetic aberrations of the lens), present in equation (3.15). If $S = \sqrt{3}$, then $B_3 = 0$ and, for an isotropic 3-dimensional lens, the currents in the two coils (I_1 and I_2) must satisfy $I_1 = -2.528 I_2$. Figure 3.2 IV shows that for $I_1 \neq I_2$, although both the radial and axial curvatures are positive, there is also a significant axial gradient that would act to change the centre-of-mass velocity of the cloud in the axial direction.

Two more interesting cases arise for a pair of coils: that for a purely radial lens and that for a purely axial lens. The former is achieved by setting the separation of the two coils $S=1$, which would be the Helmholtz condition for a uniform field, if the currents in the two coils were identical in sense and magnitude. However, if η_H and η_{AH} are non-zero, then the axial curvature is zero and the radial curvature is given by $B_1^2/4B_0$, i.e. the lens is purely radial.

The purely axial lens is realised by setting $S=\sqrt{3}$ and ensuring $B_1^2=2B_0B_2$ (i.e. that the radial curvature is zero). Interestingly, this corresponds to the removal of all third order terms in the field expansion of equation (3.15).

Ioffe-Pritchard Configuration – Strategy VI

The so-called Ioffe-Pritchard (I-P) trap was first suggested by Pritchard [14] for trapping and cooling neutral atoms and is based on the Ioffe trap for plasma confinement discussed in Gott *et al.* [15]. Although this thesis discusses the use of an I-P configuration as a lens rather than a trap, the general principle of the magnetic field is the same.

For this experiment the interest lies in experimentally realisable I-P configurations, however it is prudent to discuss the idealised case: a pair of co-axial coils and four parallel, infinitely long current bars. The two coils, co-axial along the *z*-axis, have radius a, separation $s=Sa$, and carry current in the same sense. They 'plug' the field from the four current bars, which provide the radial confinement, i.e. the coils are present to provide the axial (*z*) confinement. The bars are arranged such that each bar passes through a different corner of a square, which is centred on and perpendicular to the *z*-axis, and of side length $w=Wa$. The bars are parallel to the *z*-axis and each bar carries equal current magnitude, but neighbouring bars carry currents in the opposite direction.

For small displacements from the *z*-axis, the ideal I-P can be considered to be radially symmetric, and the current bars to provide a magnetic field of $\{B_x,B_y,B_z\}=B_1'\{x,-y,0\}$. The prime on any B_n' is used to denote the field expansion coefficients from the bars, (and will be used to denote the field expansion coefficients of the Baseball Coil in the Baseball Lens discussed in chapter 5), to distinguish the coefficients from those used for circular coils. Here,

$B_1' = (4\mu_0 I')/(\pi w^2)$, where I' is the magnitude of the current in each bar. The shape of the magnetic field magnitude contours depends on the ratio of the coil current NI to the bar current I' and the geometry of the configuration.

For an isotropic ideal I-P configuration, the following relationship must hold,

$$\frac{I'}{NI'} = 3\pi W^2 \sqrt{\frac{S^2-1}{\left((S^2/2)+2\right)^5}}. \tag{3.20}$$

There are several experimentally realisable I-P configurations, including the Baseball configuration [16], the QUIC configuration [17] and even mm-scale I-P traps [18]. This thesis will use the Baseball configuration for Strategy VI, (as can be seen in Figure 3.1 VI), since the QUIC trap is asymmetric and the mm-scale trap is too small for the consideration of a launched cold atom cloud.

A cuboidal baseball coil of geometry $w \times w \times l$, as shown in Figure 3.1 VI (along with two bias coils), has both an axial and radial curvature. However, the coil cannot be made isotropic by variation of w and l alone – bias coils are required to achieve isotropy. The bias coils carry equal current I in the same sense, (a necessity for isotropy). The magnitude of the magnetic field then has a third-order Taylor expansion of,

$$B = B_{0R} + \left(\frac{B_1'^2}{2B_{0R}} - \frac{B_{2R}}{4}\right)\left(x^2+y^2\right) + \frac{B_{2R}}{2}z^2 + \left(B_3' - \frac{B_{2R}B_1'}{2B_{0R}}\right)\left(y^2-x^2\right)z, \tag{3.21}$$

with $B_{0R} = B_0 + B_0'$ and $B_{2R} = B_2 + B_2'$ the resultant bias field and curvature respectively. As noted above, the dashed terms denote those from the baseball coil and the undashed terms those from the bias coils. Of note is the relationship between B_0 and B_0' for the formation of B_{0R} for an isotropic lens.

The expansion terms for the bias coils, B_n, were given above in equation (3.18). The expansion terms B_n' are,

$$
\begin{aligned}
B_0' &= \frac{\frac{4\mu_0 I'}{\pi} W^2}{a\left(L^2+W^2\right)\left(L^2+2W^2\right)^{1/2}} \\
B_1' &= \frac{\frac{4\mu_0 I'}{\pi}\left(L^5+3L^3W^2+4LW^4\right)}{a^2W^2\left(L^2+W^2\right)^2\left(L^2+2W^2\right)^{1/2}} \\
B_2' &= \frac{\frac{32\mu_0 I'}{\pi}\left(6L^6W^2+18L^4W^4+11L^2W^6-5W^8\right)}{a^3\left(L^2+W^2\right)^3\left(L^2+2W^2\right)^{5/2}} \\
B_3' &= \frac{\frac{48\mu_0 I'}{\pi}\left(-5L^7W^2-10L^5W^4+11L^3W^6+24LW^8\right)}{a^4\left(L^2+W^2\right)^4\left(L^2+2W^2\right)^{5/2}}
\end{aligned}
, \qquad (3.22)
$$

where $W = w/a$ and $L = l/a$.

The condition for an isotropic lens is that the axial curvature is equal to the radial curvature, i.e. that,

$$B_1'^2 = \frac{3}{2} B_{0R} B_{2R} . \qquad (3.23)$$

If one extracts the currents from each of the expansion coefficients, in effect making the coefficients per unit of current, then,

$$B_1'^2 = \frac{3}{2}\left(\frac{NIB_0}{I'} + B_0'\right)\left(\frac{NIB_2}{I'} + B_2'\right). \qquad (3.24)$$

This way, the isotropic condition can be related to the ratio of the currents in the baseball coil and the bias coils.

The simplest isotropic baseball lens to use for calculations is cubic, i.e. $W = L$, with circular Helmholtz coils ($S = 1, B_2 = 0$). If $W = L = 2$ for the purposes of calculation, i.e. that the baseball coil has the same diameter as the bias coils, then $NI/I' = 0.154$.

Figure 3.2 shows distinctly that both the axial and radial curvatures are positive for the baseball configuration discussed.

3.3
Definition of Departure from Harmonicity

Comparison to the Ideal

The Departure from Harmonicity will be used to define the variation of a magnetic field from the ideal harmonic case. Section 3.2 detailed six strategies for magnetic lenses. This section will discuss the closeness to which these lenses approximate the ideal. The Departure from Harmonicity, $\epsilon[R,Z]$, is defined as,

$$\epsilon[R,Z]=\frac{|\mathbf{a}_F-\mathbf{a}_H|}{|\mathbf{a}_H-\mathbf{a}_0|} \tag{3.25}$$

where R and Z refer to the normalised radial and axial cylindrical co-ordinates, $\mathbf{a}_F$ is the acceleration from the full Biot-Savart description of the lens in question, $\mathbf{a}_H$ is the 2[nd]-order Taylor expansion of the full Biot-Savart description, and $\mathbf{a}_0$ is the acceleration due to any 1[st]-order term in that Taylor expansion.

This measure provides a good visual description of lens quality, as can be seen in Figure 3.3. Here, the Departure from Harmonicity is plotted for the six lens strategies discussed in section 3.2. Each strategy is discussed in detail below.

Strategies I and II are for 2-D (radial) focusing, Strategy III is for 1-D (axial) focusing. For strategies I, II and III the Departure from Harmonicity averaged over a sphere of radius $0.25a$, where a is the radius of the coil, is 0.058, 0.007 and 0.009 respectively. The radially converging lens of strategy II, and the axially converging lens of strategy III are almost an order of magnitude more harmonic than the single-coil radially converging lens of strategy I.

Strategies IV, V and VI are for isotropic 3D focusing. The isotropic 3D lens of strategy IV rapidly becomes anharmonic as one moves axially away from the lens centre because of the axial magnetic field zero illustrated in figure 3.2 IV. In both strategies IV and V the lack of axial symmetry means that there are 1[st]-order terms in the field magnitude, resulting in a gradient which affects the centre-of-mass motion of the atomic cloud. The main problem with strategy V is that although both the axial and radial curvatures are equal at the lens centre, they vary rapidly with position, shown clearly by Figure 3.3 V. The lens-centre curvatures are also 8.4 times less than the axial curvature at the centre of a single coil, leading to longer

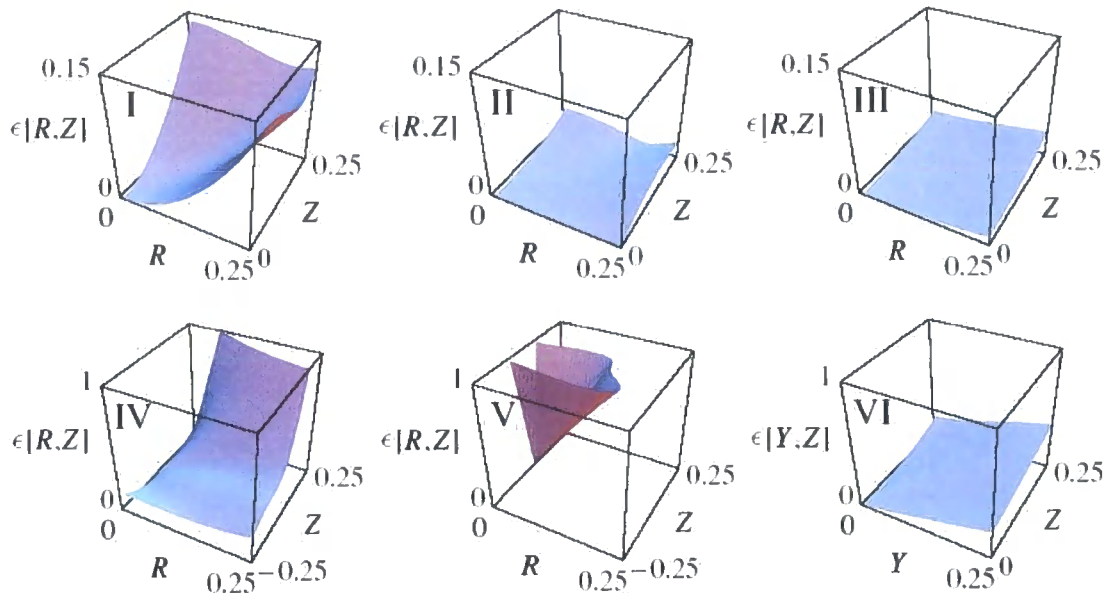

Figure 3.3. The Departure from Harmonicity $\epsilon[R,Z]$ for the six lens strategies presented in section 3.2. The labelling I-VI refers to the respective strategy. The bottom row of plots is for 3-D focusing, the top for focusing in a number of dimensions less than three. R and Z are the normalised radial and axial cylindrical co-ordinates, which are normalised to the radius of the coil in the lens, a. Averaged over a sphere of 0.25 times the coil radius, the Departures from Harmonicity for the six configurations are: 0.058, 0.007, 0.009, 0.385, 1.347 and 0.148, in order of strategy number. By observation of the above figure, one would expect the Strategies II and III to perform better than strategy I. Also, Strategy VI appears to have the best approximation to an ideal 3-D lens for 3-D focusing.

duration magnetic lensing impulses. The cloud of atoms therefore experiences the lens' axial anharmonicities for a greater period, again compromising the quality of the focus. For strategies IV, V and VI the departure from harmonicity averaged over a sphere of radius $0.25a$ is 0.385, 1.347 and 0.148 respectively. The Baseball Lens of strategy VI is thus significantly more harmonic than the two coil lens of strategy IV, which is in turn considerably better than the axially offset single-coil lens of strategy V.

[1] G K Woodgate, *Elementary Atomic Structure*, Second Edition, Oxford University Press (1980)

[2] G Brooker, *Modern Classical Optics*, chapter 7, Oxford University Press (2003)

[3] T Miossec, R Barbé, J-C Keller and O Gorceix, *Pulsed magnetic lenses for producing intense and bright cold atom beams*, Opt. Commun. **209** 349 (2002)

[4] F Mandl, *Statistical Physics*, Second Edition, p208, Wiley (1988)

[5] J D Lawson, *The Physics of Charged-particle Beams*, p76, Oxford University Press (1977)

[6] H L Bethlem, A J A van Roij, R T Jongma and G Meijer, *Alternate Gradient Focusing and Deceleration of a Molecular Beam*, Phys. Rev. Lett. **88** 13 (2002)

[7]E A Cornell, C Monroe and C E Wieman, *Multiply Loaded, ac Magnetic Trap for Neutral Atoms*, Phys. Rev. Lett. **67** 18 (1991)

[8] C Monroe, *Experiments with Optically and Magnetically Trapped Cesium Atoms*, Ph.D. Thesis, University of Colorado, Boulder, Colorado (1992)

[9] A S Arnold, M J Pritchard, D A Smith and I G Hughes, *Double-impulse magnetic focusing of launched cold atoms*, in preparation

[10] W H Wing, *On Neutral Particle Trapping in Quasistatic Electromagnetic Fields*, Prog. Quant. Electr. **8** 181 (1984)

[11] J D Jackson, *Classical Electrodynamics*, Third Edition, Wiley (1999)

[12] T Bergeman, G Erez and H J Metcalf, *Magnetostatic trapping fields for neutral atoms*, Phys. Rev. A **35** 4 (1987)

[13] W R Smythe, *Static and Dynamic Electricity*, Third Edition, New York: McGraw-Hill (1968)

[14] D E Pritchard, *Cooling Neutral Atoms in a Magnetic Trap for Precision Spectroscopy*, Phys. Rev. Lett. **51** 1336 (1983)

[15] Y V Gott, M S Ioffe and V G Tel'kovskii, Nucl. Fusion. Suppl. **3** 1045 (1962)

[16] U Ernst, A Marte, F Schreck, J Schuster and G Rempe, *Bose-Einstein Condensation in a pure Ioffe-Pritchard field configuration*, Europhys. Lett. **41** 1 (1998)

[17] T Esslinger, I Bloch, T W Hänsch, *Bose-Einstein condensation in a quadrupole-Ioffe-configuration trap*, Phys. Rev. A **58** 4 (1998)

[18] K L Moore, T P Purdy, K W Murch, K R Brown, K Dani, S Gupta, and D M Stamper-Kurn, *Bose-Einstein condensation in a mm-scale Ioffe-Pritchard trap*, cond-mat/0504010 (2005)

Chapter 4

Numerical Simulations of Single-Impulse Magnetic Focusing

4.1
Numerical Simulations

The results discussed in this chapter were published in the journal paper *Single-Impulse magnetic focusing of launched cold atoms*, Journal of Physics B: Atomic, Molecular and Optical Physics, Volume 37, pages 4435-4450, in 2004 [1]. This constitutes a numerical investigation of the limiting factors to the quality and size of the final image obtained in pulsed magnetic focusing experiments.

To date theoretical studies of pulsed magnetic focusing have used the assumption that the magnetic lens potential is harmonic. This chapter addresses the validity of this approximation, and the effects of magnetic aberrations. Attention is restricted to focusing strategies using a single-magnetic impulse. Focusing with more than one impulse (alternate gradient focusing) is considered in Arnold *et al.* [2]. Concentration is aimed towards producing a compact cloud in space, with numerical simulations being conducted using Wolfram Research Inc.'s *Mathematica*.

4.2
Matrices: A Good Starting Point

The use of matrices to model lenses was introduced in chapter 3, using the translation matrix M_T, converging lens matrix M_C, and the diverging lens matrix M_D:

$$M_T \equiv \begin{pmatrix} 1 & t \\ 0 & 1 \end{pmatrix} \tag{4.1}$$

$$M_C \equiv \begin{pmatrix} \cos\omega\tau & \frac{1}{\omega}\sin\omega\tau \\ -\omega\sin\omega\tau & \cos\omega\tau \end{pmatrix} \tag{4.2}$$

$$M_D \equiv \begin{pmatrix} \cosh\omega\tau & \frac{1}{\omega}\sinh\omega\tau \\ \omega\sinh\omega\tau & \cosh\omega\tau \end{pmatrix} \tag{4.3}$$

The total time of flight T can be written as the sum of the flight time before the lens t_1, the duration of the lens τ, and the flight time after the lens t_2, such that the system matrix M_{ABCD} (using a converging lens) becomes,

$$M_{\text{ABCD}} = \begin{pmatrix} 1 & t_2 \\ 0 & 1 \end{pmatrix} \begin{pmatrix} \cos\omega\tau & \frac{1}{\omega}\sin\omega\tau \\ -\omega\sin\omega\tau & \cos\omega\tau \end{pmatrix} \begin{pmatrix} 1 & t_1 \\ 0 & 1 \end{pmatrix}. \tag{4.4}$$

The 'thick' converging lens M_C can be written as a 'thin' lens M_{THIN} pre- and post-multiplied by a translation matrix with duration $\tau'/2$, where

$$\tau' = \frac{2}{\omega}\tan\left(\frac{\omega\tau}{2}\right). \tag{4.5}$$

This 'thin' lens M_{THIN} is given by,

$$M_{\text{THIN}} = \begin{pmatrix} 1 & 0 \\ C & 1 \end{pmatrix}, \tag{4.6}$$

where

$$C = -\omega\sin(\omega\tau), \tag{4.7}$$

which is the original $i = 2, j = 1$ element of the matrix M_C.

Therefore, the final system matrix M_{ABCD} (using a converging lens) is given by,

$$M_{\text{ABCD}} = \begin{pmatrix} 1 & t_2 + \frac{\tau'}{2} \\ 0 & 1 \end{pmatrix} \begin{pmatrix} 1 & 0 \\ -\omega\sin\omega\tau & 1 \end{pmatrix} \begin{pmatrix} 1 & t_1 + \frac{\tau'}{2} \\ 0 & 1 \end{pmatrix}. \tag{4.8}$$

The notation of primes is used to denote times in the 'thin' lens representation. This means that many of the simplicities of 'thin' lens optics can be used, even when dealing with the more accurate 'thick' lensing behaviour. The effective 'thin lens' duration of the pulse τ' differs from the actual pulse duration τ, but otherwise the treatments are identical. In the limit of a short, strong pulse $\omega\tau \to 0$, then $\tau' \to \tau$.

To consider the action of the diverging lens M_D, the transformation $\omega \to i\omega$ is made, and therefore $C \to C = \omega \sinh(\omega\tau)$ and $\tau' \to \tau' = \frac{2}{\omega}\tanh\left(\frac{\omega\tau}{2}\right)$.

The thin lens system has a total time $T' = t_1 + t_2 + \tau' = T - \tau + \tau'$, whereas the physical duration of the flight is $T = t_1 + t_2 + \tau$, and for a single-lens system the image condition (where the $\mathfrak{B}$ element in the $\mathfrak{ABCD}$ system matrix $M_{\mathfrak{ABCD}}$ is equal to zero), is,

$$CT' = \frac{1}{\lambda(\lambda - 1)} \tag{4.9}$$

where $\lambda = \frac{t_1'}{T'}$ and $t_1' = t_1 + \frac{\tau'}{2}$, i.e. λ is the fraction of the total time at which the thin lens occurs. The magnification of the image is given by $(\lambda - 1)/\lambda$.

Consider the experimental situation where the total time is fixed at $T = 212$ ms (equivalent to a launch height of 22 cm) and the maximum Amp-turns available is $NI = 10000$ Amp-turns. An analytic result for $\lambda(\omega, \tau)$ can be obtained, and is illustrated in Figure 4.1 for the case of a single-coil lens (Strategy I) of radius 5 cm ($\omega_r = \sqrt{\mu_B B_2 / 2m} = 69.6$ rad s^{-1}). The $\lambda(\omega, \tau)$ parameter is maximized (and the magnification $(\lambda - 1)/\lambda$ is minimized) when,

$$1 - \omega(T - \tau)\cot(\omega\tau) = 0, \tag{4.10}$$

which has the solution $\tau = 23.7$ ms and $\lambda = 0.929$. This corresponds to a reduction in the atomic cloud size by a factor of -13.1. This is achieved when the pulse duration τ is from time $t = T - \tau$ to $t = T$, i.e. the lens pulse ends at the time of focus. For a lens placed later in time, the magnetic pulse would not have finished at the predicted focal time T, resulting in an increase in cloud size at time T.

The above analysis would seem to suggest that the optimum strategy for achieving the smallest cloud size would be to construct a lens with a short, strong pulse $\omega\tau \to 0$,

and use the latest possible pulse time $\lambda \to 1$. However, experimental constraints and lens aberrations alter the above conclusion.

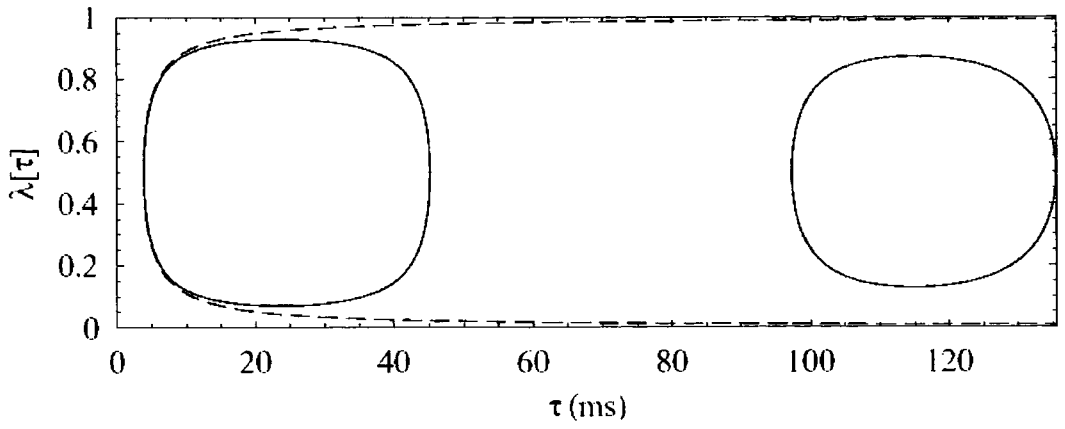

Figure 4.1. By fixing the strength of a 5 cm single coil (strategy I) radially converging lens at $\omega_r = 69.6$ rad s^{-1} and the total experimental focusing time $T = 212$ ms, the lens pulse width, τ, can be varied to find the focusing parameter $\lambda(\tau)$ through equation (4.9). The impulse τ has a minimum of 3.9 ms at $\lambda = 1/2$ and λ is symmetric about this point. Two focusing 'islands' can be seen for 3.9 ms $\leq \tau \leq$ 45 ms and 97 ms $\leq \tau \leq$ 135 ms, where the latter corresponds to lens durations of more than one half-cycle of the harmonic potential. Also shown (dashed) is the result obtained if one makes the strong, short pulse approximation $\omega\tau \to 0$, leading to the simplification $\sin(\omega\tau) \approx \omega\tau$ in equation (4.7) - resulting, unsurprisingly, in a divergence for large pulse durations.

4.3
What about Real Magnetic Fields?

The $\mathcal{ABCD}$ matrix formalism outlined above is a useful starting point for studying pulsed magnetic focusing. However, this formalism ignores magnetic aberrations arising due to the departure of the real potential from an ideal parabolic spatial dependence (as discussed in chapter 3). For a non-parabolic potential the change in position and velocity which occur during lensing must be calculated numerically. The numerical simulations test the 'perfect' atomic lens approximations. The cloud and its motion are treated classically, and for the atomic densities encountered in the expanding cloud, the collision rate is negligible. The atoms travel on ballistic trajectories, except when a magnetic impulse is applied, in which case the full Stern–Gerlach force is included in the numerical integration. For the sake of definiteness the focusing of ^{85}Rb atoms was investigated in an atomic fountain launched vertically through a height of 22 cm (which corresponds to a flight time of 212 ms), a height which is of experimental interest. The atoms come to rest at the apex of their trajectories where they could be used for further experiments or loaded into a dipole trap. The effects of gravity were included, but these effects on the quality of focus were found to be negligible for the parameters used in these simulations.

The approach adopted was a numerical simulation, in which the trajectories of typically 500 atoms were followed. The initial velocity and position probability distributions are isotropically Gaussian for each Cartesian direction. The standard deviation of position was chosen to be a value typical of experiments at 0.4 mm [3], and the velocity distribution corresponding to a typical launch temperature obtained with Rb in moving molasses, namely $T = 20\ \mu$K. These simulations facilitate the calculation of statistically relevant quantities, such as the standard deviation of the time-dependent size of the atomic cloud. In all the simulations the maximum current value in any coil was limited to 10 000 A.

4.4
Axial (1-dimensional) and Radial (2-dimensional) Focusing

To illustrate the methodology the focusing properties of a single, circular, current carrying coil (strategy I) were investigated. Figure 4.2 (a) shows the evolution of the horizontal (x) component of a launched cloud of 500 atoms subject to a radially converging lens. The impulse is applied half-way in time, and the length of the impulse is chosen to reverse the transverse velocity, as can be seen from the change in sign of the gradient after $t = 106$ ms. For this case, the $\mathfrak{ABCD}$ matrix predicts a radial focus with magnification -1, which is in excellent agreement with the numerical simulation using a parabolic lens (Figure 4.2 (a)). The vertical line at $t = 212$ ms corresponds to the imaging time. For real coils (of radii 5 cm and 3 cm), it is seen that the focussed cloud image is significantly larger than the initial cloud. The aberration worsens as the coil radius decreases. Note that although focusing is seen in the radial direction, defocusing is seen in the axial direction due to the opposite sign of the magnetic field curvature.

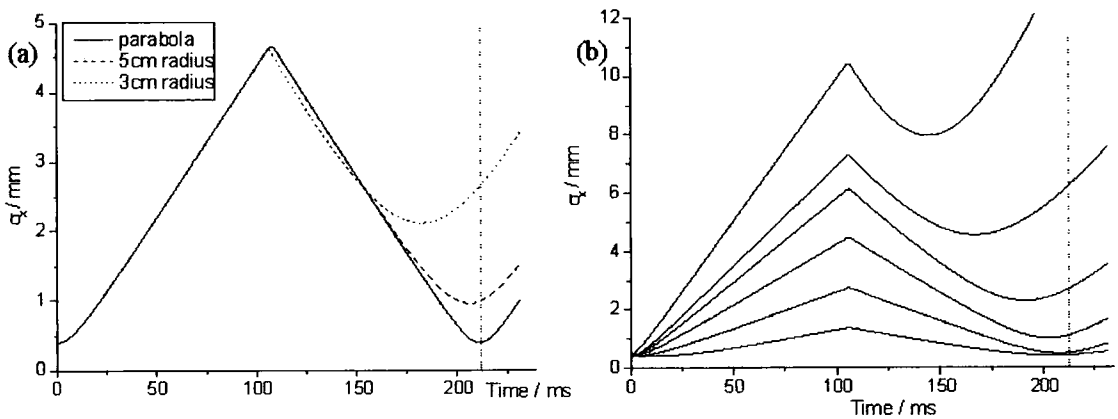

Figure 4.2. (a) Simulation of 500 atoms going through a 10 000 Amp-turn strategy I lens. The solid, dashed and dotted lines correspond to a parabolic approximation lens, a 5 cm radius lens, and a 3 cm radius lens, respectively. The duration and timing of the impulse is chosen using the $\mathfrak{ABCD}$ matrix formalism, bringing the atoms to a focus 22 cm above their launch height. (b) A shell plot of 1000 simulated atoms passing through a 3 cm radius strategy I lens. The distances from the coil centre are 0–10% of the coil radius, 10–20%, through to 50–60%. Atoms further from the centre are not focussed as well, and the focusing occurs at earlier times. Both of these factors degrade the image quality and size.

Figure 4.2 (b) contains an analysis of the cloud in terms of shells of different radii measured from the centre of the coil; atoms further from the centre are not focussed as tightly, and also focus earlier in time. As the ratio between cloud extent and coil radius decreases, the departure of the field from the parabolic approximation becomes less significant. Therefore one method to reduce the aberrations experienced by the atoms is to increase the coil radius, or decrease the atomic cloud temperature.

The minimum cloud size can be obtained by investigating the effect of the λ parameter. As discussed in section 4.2, a thin parabolic lens produces the smallest cloud size when $\lambda \to 1$, i.e. the pulse is applied as late in time as possible. This is a manifestation of Liouville's Theorem [4] - a more compact spatial extent can be generated at the expense of a larger velocity spread.

Figure 4.3 (a) shows simulations of radial focusing. The radial cloud expansion factor, σ_x/σ_{x_0}, is plotted as a function of the imaging parameter λ. It can be seen that the smallest cloud size for a parabolic lens occurs when one waits as long as possible before focusing, i.e. λ is as close as possible to 1 (limited by the solution of equation (4.10)). This means that the magnetic impulse ends at the desired focusing time. For parabolic fits to the 3 and 5 cm radius single coils (strategy I) the maximum values of λ are 0.968 and 0.929, corresponding to negative magnifications, $M = (1-\lambda)/\lambda$, of 1/30.1 and 1/13.1 respectively.

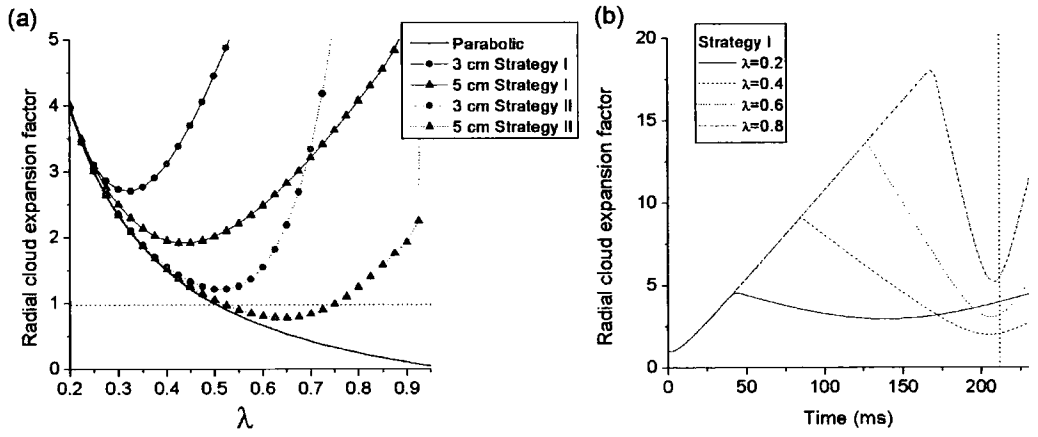

Figure 4.3. (a) The radial expansion factor, at $T = 212$ ms, for radially converging lenses is plotted against λ. The solid line without symbols shows the parabolic lens solution, the dotted lines with symbols show the result of atoms passing through strategy I (II) lenses. Circular (square) symbols are used for the 3 cm (5 cm) radius lenses. The strategy II lens is more parabolic, allowing a smaller radial cloud size to be achieved: a cloud image 0.75 times the original size occurs for $\lambda = 0.65$ using a 5 cm lens. (b) For a 5 cm strategy I lens, the radial expansion factor is plotted against time for λ values of 0.2, 0.4, 0.6 and 0.8.

Along with the parabolic case, Figure 4.3 (a) shows numerical simulations for 500 atoms passing through 3 and 5 cm radius coils, for both strategies I (single coil) and II (two coils). As expected the 5 cm lens better approximates a parabola. Compared to the $\mathcal{ABCD}$ matrix result there is a marked difference in the behaviour of the minimum radially-focussed cloud-size for fields from real coils – the value of λ at which the $\mathcal{ABCD}$ minimum is obtained is dominated by aberrations in the magnetic field. The $\mathcal{ABCD}$ matrix approach does not provide an adequate description of pulsed magnetic focusing when one considers the entire atomic cloud.

In Figure 4.3 (b) the radial expansion factor of a 5 cm single coil (strategy I) is plotted against time for values of λ varying from 0.2 to 0.8.

The easiest way to reduce aberrations appears to be the use of a very large coil radius. Unfortunately the curvature of the field decreases with the cube of the coil radius, which necessitates longer pulse durations for larger radius coils. This increase in pulse duration reduces the maximum value of λ that can be used and therefore also limits the minimum cloud size. The aberrations can only be further reduced by increasing the current-turns, something which has experimental limitations.

The aberrations associated with a real coil dramatically affect the strategy for achieving a radially compact cloud. The impulse has to be applied significantly earlier than an $\mathcal{ABCD}$ matrix analysis would suggest. However, for experimentally-realistic parameters it is seen that it is possible to achieve a final radial cloud size that is smaller than the initial size. Strategy II (two coils of radius a carrying the same current I, separated by $S = 0.58$), clearly has a better performance than strategy I (single coil), as seen in Figure 4.3 (a). Most importantly, in the 5 cm case, the radial extent of the final cloud is 0.75 times the original radial extent of the cloud.

Strategy III produces an axially converging/radially diverging lens with a high level of harmonicity comparable to that of strategy II. The results for axial focusing are omitted here as they will be revisited in the context of alternate-gradient focusing in Arnold *et al.* [2].

4.5
3-dimensional Focusing

Isotropic 3D focusing can be achieved using two coils with differing currents (strategy IV). For realistic experimental parameters, the numerical simulations showed that the aberrations in the lens smeared out any focusing. However, for unrealistically large lens radii and large currents (e.g. 15 cm and 200 000 Amp-turns) it is possible to achieve 3D focusing.

As discussed in chapter 3, a single coil (of radius a) can be made to have isotropic curvature (strategy V). At $z = \pm\sqrt{2/7}a$, the axial and radial curvatures are equal, and the gradient of the field is non-zero. A numerical simulation was performed for a launched cloud, with an impulse applied when the cloud's centre of mass reached a distance $z = \pm\sqrt{2/7}a$ from the centre of a single coil. Due to the large departure from harmonicity for the experimentally realistic parameters used, aberrations dominated and focusing was not observed.

The baseball lens (strategy VI) yielded the best isotropic 3D lens. Figure 4.4 (a) shows the temporal evolution of the volume expansion factor, $\sigma_x\sigma_y\sigma_z/\sigma_{x_0}\sigma_{y_0}\sigma_{z_0}$, for a launched cloud subject to a focusing pulse from a Baseball Lens. Five different values of λ are depicted, from 0.3 to 0.7 in steps of 0.1. The bias coils have radii of $a = 5$ cm, separation $S = 1$, and current $NI = 1541$ A; the baseball has sides of length $W = L = 2$ and carries a 10 000 A current.

The minimum cloud size is obtained when $\lambda = 0.3$, and represents a 31.9 increase in cloud volume at the focal time, $T = 212$ ms. This is to be contrasted with the 13 000 increase in cloud volume if no magnetic lens were used. It is interesting to note that for the parameters we have simulated, the results of a 'pure' Ioffe–Pritchard lens ($W = 2$, $L \to \infty$ and $S = 2$) are almost identical to the Baseball Lens. Surprisingly the Baseball Lens performs better, and produces smaller cloud sizes at the focus.

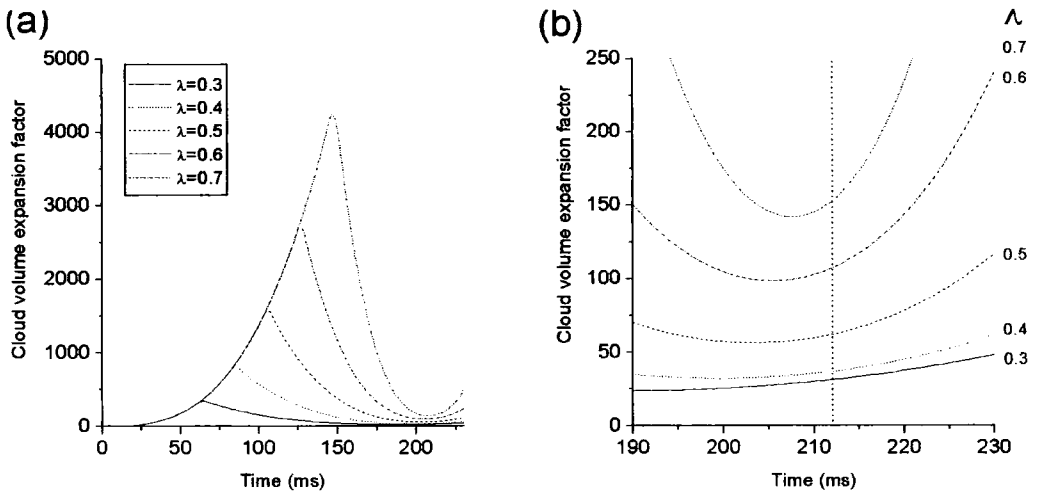

Figure 4.4. (a) A simulation of 500 atoms sent through an isotropic baseball coil lens (strategy VI). The ratio of the cloud volume to the initial volume is plotted as a function of time for values of λ ranging from 0.3 to 0.7. (b) A close-up of the simulations near the $t = T$ imaging time (vertical line). Pulse durations range from 10 to 12 ms, being symmetric about $\lambda = 0.5$.

4.6
Conclusions and Choice of Lens for Experimentation

A comparison of the limiting focal size of a launched cold cloud of weak-field seeking atoms has been made between various single-impulse magnetic lenses. The $\mathcal{ABCD}$ matrix formalism is convenient for giving an estimate as to the parameters needed for magnetic focusing, but does not contain the departure of the potential experienced by atoms from a perfect parabolic dependence for fields produced by real coils (and bars). It is important to consider these aberrations as they drastically alter the results.

It was demonstrated with strategy II that a radially focusing lens formed from two coils with relative separation $S = 0.58$ provided much tighter focusing than the single-coil lens of strategy I. Amongst the isotropic 3D lenses (strategies IV–VI) the Baseball Lens (strategy VI) was superior to the two coil lens (strategy IV), which was in turn considerably better than the axially offset single-coil lens (strategy V). Of the single-impulse lenses, the Baseball Lens offers the best possibilities for isotropically focusing a cloud of weak-field-seeking atoms in 3D. For this reason, and since a 3-dimensional focus with a single magnetic impulse is yet to be realised, a Baseball Lens will be built for the experimentation presented in this thesis.

[1] M J Pritchard, A S Arnold, D A Smith and I G Hughes, *Single-impulse magnetic focusing of launched cold atoms*, J. Phys. B: At. Mol. Opt. Phys. **37** 4435 (2004)

[2] A S Arnold, M J Pritchard, D A Smith and I G Hughes, *Double-impulse magnetic focusing of launched cold atoms*, (in preparation)

[3] E A Hinds and I G Hughes, *Magnetic atom optics: mirrors, guides, traps, and chips for atoms*, J. Phys. D: Appl. Phys. **32** R119 (1999)

[4] F Mandl, *Statistical Physics*, Second Edition, p208, Wiley (1988)

Chapter 5

The Baseball Lens: Design and Testing

5.1
Current Pulse Test Circuit

A current pulse is required to create the magnetic field for the pulsed magnetic lens. The original plan was to use charged capacitors to supply the current, but it quickly became apparent that this would not suffice since any switching device would have to throttle the output to square the capacitor discharge – a square pulse is the ideal as it provides the greatest impulse in the shortest time (for a given peak). The power source used in this experiment was lead-acid batteries (in the end three Volvo Truck batteries in series), switched by an integrated-gate bipolar transistor (IGBT). The switching of IGBTs for large-current pulses is extremely important and is discussed in section 5.2. Below are detailed the general circuit for forming current pulses, an experiment to choose the diameter of wire from which to construct the baseball, and finally an 850 A high, approximately-square current pulse attained with three truck batteries.

The Main Test Circuit and Initial Supply for $V_{Gate\text{-}Emitter}$

Figure 5.1 shows a diagram of the general circuit used to provide current for the pulsed magnetic lenses used in this thesis. A lead-acid battery is used to supply a current pulse through a load (i.e. a magnetic lens), with the current switched by an integrated-gate bipolar transistor (IGBT). A solenoid switch (for manual on/off) and fuses are present as safety precautions – IGBT gates blow open when damaged and one does not want a lead-acid battery essentially short-circuited indefinitely. A diode is placed across the load to prevent ringing upon switch-off.

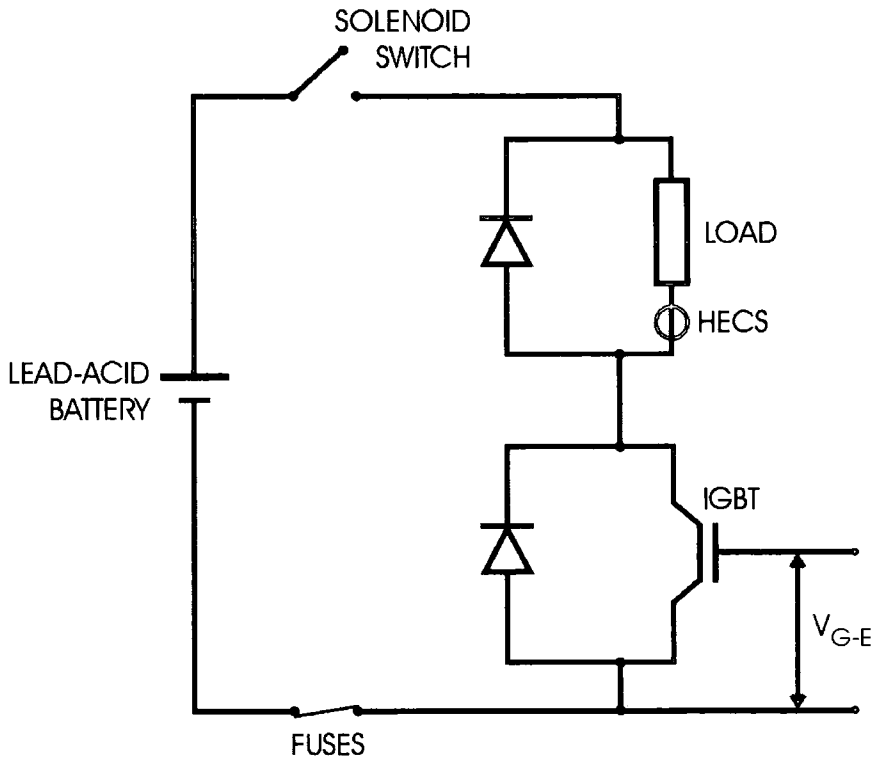

Figure 5.1. Diagram of the general circuit used to form current pulses. A solenoid switch, for manual on/off, and fuses are present as safety precautions. Upon application of sufficient Gate-Emitter voltage (V_{G-E}) to the IGBT, the circuit closes and current flows through the load. The current (and voltage for the circuit) is provided by the lead-acid battery. The current through the load is measured non-invasively by a Hall-effect current sensor (HECS). A diode is usually present in an IGBT unit to prevent damage to the IGBT Gate (shown across the IGBT). A diode is also present across the load to prevent ringing upon switch-off.

Wire Diameter Choice for Construction of Baseball

It was important to choose the diameter of wire for construction of the baseball lens. Copper wire (Polyester 200 Grade 2 C101 purchased from F. D. Sims Ltd., rated at 101% I.A.C.S.) of solid circular cross-section with varying diameter (1 mm, 2 mm and 3 mm) was used as the load in the pulse test circuit of Figure 5.1, a 10 m length of wire used in each case. A 12V, 495 A-max. car battery was used as the power source, along with a Mitsubishi CM200DY-24H IGBT for switching the current pulse on and off. The gate pulse (V_{G-E}) was supplied by a Philips PM5715 Pulse Generator that has a manual single-shot button. The results of this test are shown in Figure 5.2. A Honeywell CSNK591 HECS was used to measure the current through the load. The use of 3 mm diameter wire produced a current pulse of over 250 A, five times larger

than the peak of the 1 mm diameter wire, and over one and a half times the peak for 2 mm diameter wire. 3 mm diameter wire is the approximate limit of wire diameter for forming a baseball as required here – 3 mm diameter wire is difficult enough to form. Therefore, wire of diameter 3 mm was used for construction of the Baseball Lens.

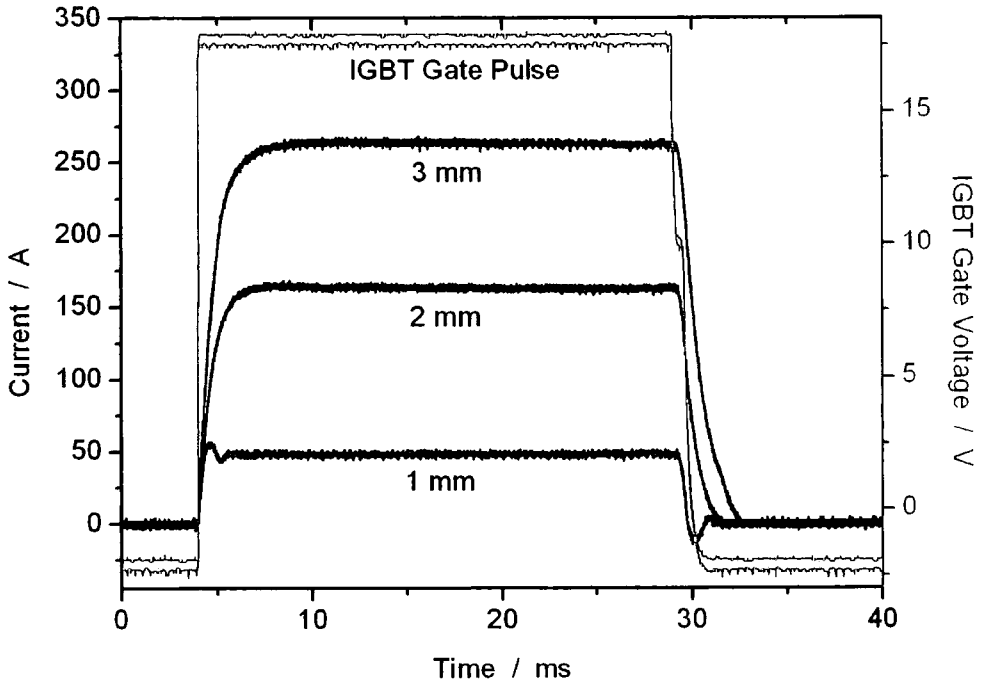

Figure 5.2. Current through the load of the current pulse test circuit for varying load wire diameters (1 mm, 2 mm, and 3 mm). The wire is of solid circular cross-section, and in each case a length of 10 m of wire was used as a load. Also shown is the IGBT Gate Pulse (the Gate-Emitter voltage for the IGBT) that closed the circuit and allowed current to flow (more details of $V_{G\text{-}E}$ are given in section 5.2). The gate pulse was supplied by a Philips PM5715 Pulse Generator that has a manual single-shot button. Wire diameters > 3 mm were not tested since they would be very difficult to form into a baseball coil. However, the above graph shows clearly that more current will be attained using 3 mm diameter wire – over five times more current than the 1 mm diameter wire and over one and a half times the 2 mm diameter. For lens construction in this thesis, 3 mm diameter wire was used.

Initial Tests with Three 12V 1150A-max. Truck Batteries

The next step in circuit testing was to replace the car battery with three 12V 1150 A-max. Volvo Truck batteries (in series). Three batteries were chosen as this suited our monetary budget. The same circuit as in Figure 5.1 was used, with a Mitsubishi CM1400DU-24NF IGBT, 4×30 A fuses (in parallel), and a 10 m length of solid core copper wire (diameter 3 mm) as the load. The gate pulse ($V_{G\text{-}E}$) was supplied by a

Philips PM5715 Pulse Generator. The IBGT Gate-Emitter voltage is discussed in detail in section 5.2. A current pulse with a peak of approximately 850 A was observed. The results of this test are shown in Figure 5.3. This was done using a 10 m length of copper wire as the load, which would be more than sufficient to make a 9-turn baseball of diameter 10 cm – giving a baseball with over 7500 Amp-turns. Details of the construction of the Baseball Lens can be found in section 5.3. The next step in circuit design was to control the current pulse with a TTL line from the National Instruments PCI-DIO-32HS.

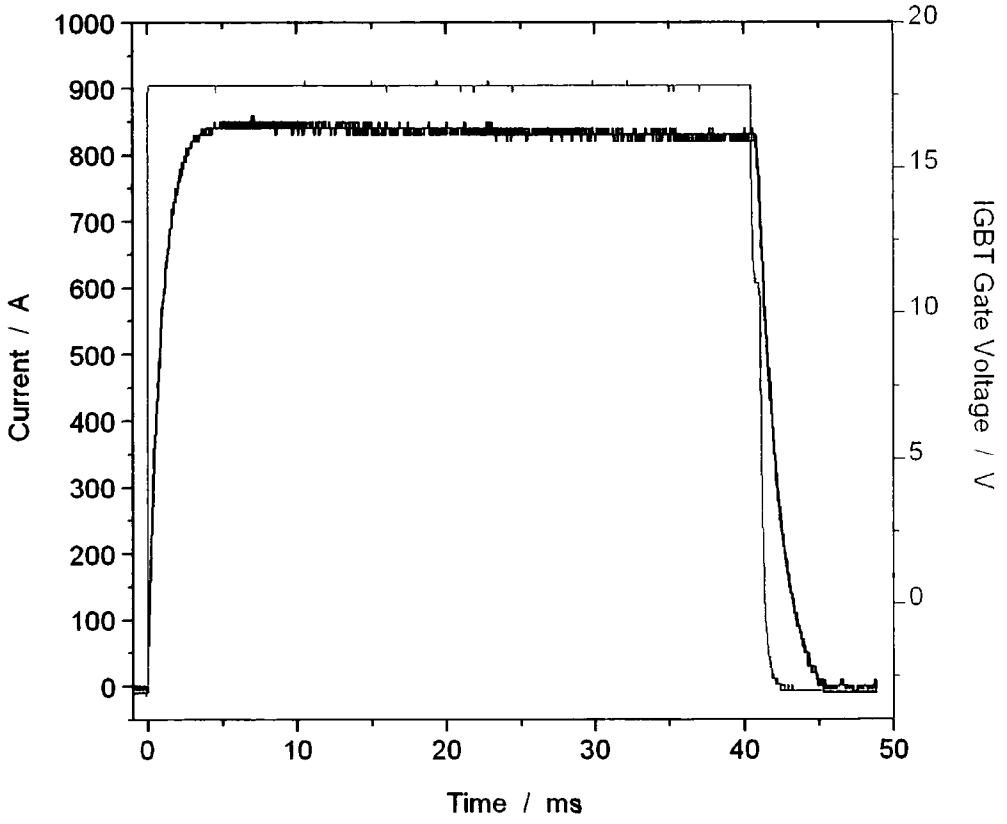

Figure 5.3. Current pulse from three 12V 1150 A-max. Volvo Truck batteries (in series) through a load of a 10 m length of solid core 3 mm-diameter copper wire. The gate pulse (V_{G-E}) was supplied by a Philips PM5715 Pulse Generator. A peak of approximately 850 A was measured passing through the load by a Honeywell CSNK591 HECS.

5.2
Supply of the Gate-Emitter Voltage to IGBTs for Large Current Pulses

So What's So Difficult About Making Large Current Pulses?

When using an IGBT to produce large-current pulses, great care must be taken in the supply of the Gate-Emitter voltage ($V_{G\text{-}E}$) to prevent severe damage to the IGBT. The commonly accepted power-FET industry stance is that an IGBT must be turned on and off as quickly as possible to avoid damage, i.e. the rise and fall time of $V_{G\text{-}E}$ must be made as short as possible [1]. This is not the case with very large-current pulses (supplied from a constant voltage power source). Although a very fast rise time for $V_{G\text{-}E}$ should not damage an IGBT, since there is no current flowing, the fall time is far more critical.

To ensure that the IGBT used in this experiment was switched correctly, an Isahaya Electronics VLA502-01 Driver for IGBT Modules was aquired. Isahaya Electronics made IGBT drivers solely for Mitbubishi, their products being Mitsubishi branded, before becoming an independent manufacturer. The gate drivers are "designed to convert logic level control signals into optimal IGBT gate drive," [2] and "simplify gate drive design by minimising the number of components required," [2], which is ideal for our purposes. However, upon using the VLA502 to re-create the 850 A current pulse shown in Figure 5.3, the IGBT blew open upon switch-off. Initially, it was thought that this was due to the IGBT not being switched off fast enough [1], but it transpired that the IGBT was actually being turned off too quickly. Comparison of the $V_{G\text{-}E}$ supplied by the Philips PM5715 Pulse Generator used to create the 850 A current pulse in Figure 5.3 with the $V_{G\text{-}E}$ from the VLA502 showed that the PM5715 voltage went from its maximum through zero in approximately 100 μs, but the VLA502 voltage went from its maximum through zero in < 5 μs. This is an empirical fact found from our experiment. We could not afford to damage any more (expensive) IGBTs to test comprehensively the minimum (or maximum) switch-off rates. In any case, inspection of the damaged IGBT showed burnt sections in its circuitry indicating excess power dissipation. It is possible that, having switched off too quickly, the diodes in the circuit had not had time to switch on and too much power had to be dissipated within gate of the IGBT, hence causing damage, but this is conjecture. A thorough analysis of the switching characteristics of IGBTs with large

currents is a large project in itself, whilst this project concerns itself with the pulsed magnetic focusing of cold atoms. Not wanting to spend any more time on an already lengthy process of trying to understand the switching process, attention was returned to the Phillips PM5715 Pulse Generator as the source for the Gate-Emitter voltage. The PM5715 Pulse Generator was not considered initially as a permanent source for $V_{G\text{-}E}$ because the external TTL trigger was broken. After fixing the broken trigger, it was then possible to switch the large current pulses using a TTL line from the National Instrument PCI-DIO-32HS.

It was very fortunate that the Philips PM5715 Pulse Generator was able to switch the IGBT correctly. Efforts were made to re-create the pulse generator signals, with success for an unloaded IGBT. However, with a loaded IGBT, the fall time was still too fast. The pulse generator is a complicated analogue circuit that was difficult to emulate.

5.3
Baseball Lens Construction

The Baseball lens was constructed from enamel coated, 3 mm-diameter cylindrical cross-section, copper wire (Polyester 200 Grade 2 C101 purchased from F. D. Sims Ltd., rated at 101% I.A.C.S.). The lens is constructed from two components: a baseball coil and a pair of circular bias coils. The baseball coil has nine turns in a 3x3 arrangement, each turn fixed relative to the others using Araldite 2011 epoxy. Each bias coil has two turns stacked radially.

Baseball Coil Construction

Figure 5.4 shows a schematic of the cubic baseball coil, which has a diameter of 10 cm. The baseball coil has nine turns in a 3x3 arrangement, chosen to provide sufficient Amp-turns for the experiment, but without making the baseball coil too large.

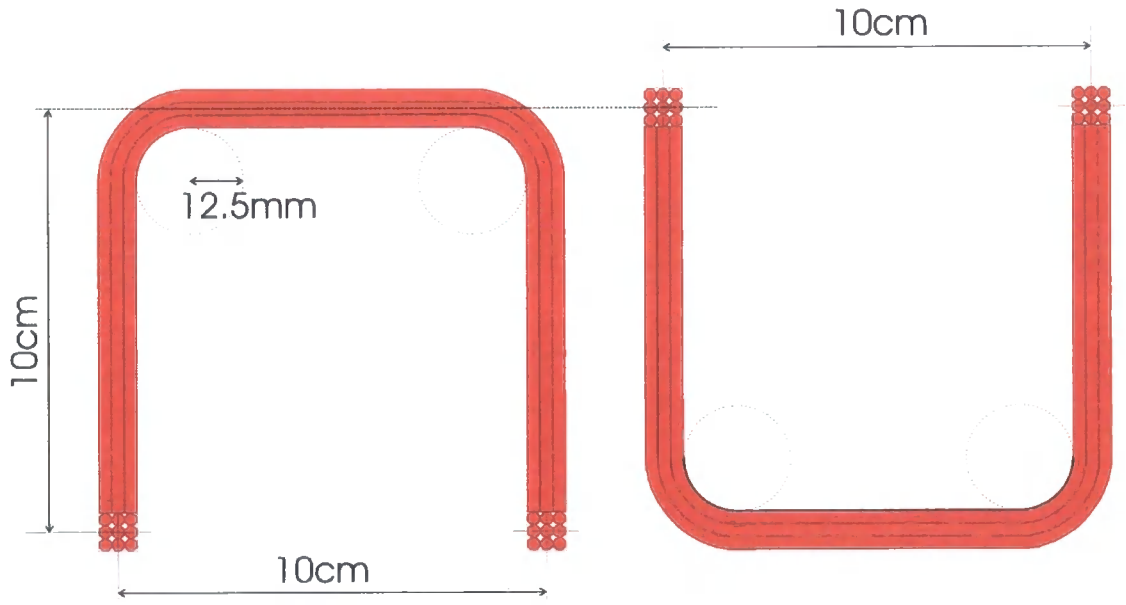

Figure 5.4. Schematic of the Baseball Coil. The coil is cubic in form with a diameter of 10 cm, measured from the central turn of the 3x3 arrangement. The inner radius of curvature is 12.5 mm, since a design with a smaller radius of curvature would be difficult to realise in practice due to the rigidity of the 3 mm diameter copper wire.

Construction of the baseball proceeded with the use of an aluminium former. The former consisted of two interlocking U-shapes, which were designed to separate upon completion of the baseball coil. A thin layer of vacuum grease coated the former, before sections of 125 μm Mylar film were used to cover the parts of the former on

which the coil was wrapped. A thin layer of vacuum grease was then added onto the Mylar. The grease and Mylar preparation was used to prevent epoxy both from sticking the coil to the former and from gluing the two halves of the former together. Enamel-coated C101 copper wire, with circular cross-section of diameter 3 mm, was used to construct the coil. The first two turns were wrapped and then glued together using Araldite 2011 epoxy, the wire being held firmly in place by clamps attached to the former. The epoxy was then left to set for 24 hours. Each subsequent turn was added, then glued and left for 24 hours before the start of the next. This slow wrapping process was necessary for two reasons. Firstly, the solid, thick copper wire had sufficient spring so as to move out of place if not clamped firmly, making the

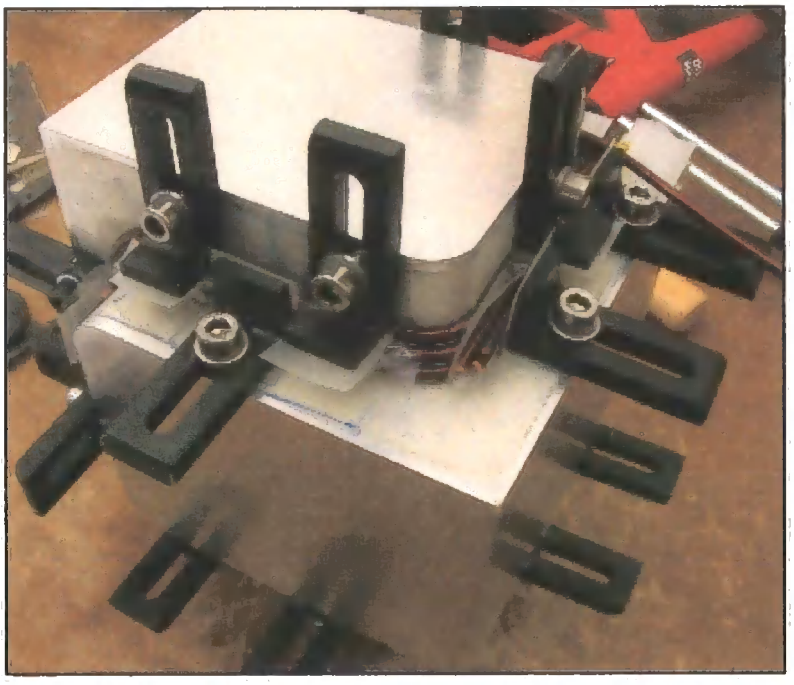

Figure 5.5. Baseball Coil during construction upon the aluminium former. Metal clamps and extra pieces of copper wire were used to hold the turns in place whilst the epoxy set. Note the use of Mylar film to prevent the Baseball Coil being glued to the assembly structure.

addition of more than one turn very difficult. Secondly, the thick wire required careful hammering at times (to bend the wire neatly around corners), which required the previous turns to be set in place by epoxy so as not to dislodge them. Figure 5.5 shows the coil during the process of construction.

Once all nine turns had been added to the baseball coil, another layer of epoxy was added to ensure rigidity. Figure 5.6 shows a photograph of the completed coil.

Figure 5.6. Photograph of the completed Baseball Coil. After the ninth turn was completed and set, the whole coil was coated in epoxy to provide extra rigidity.

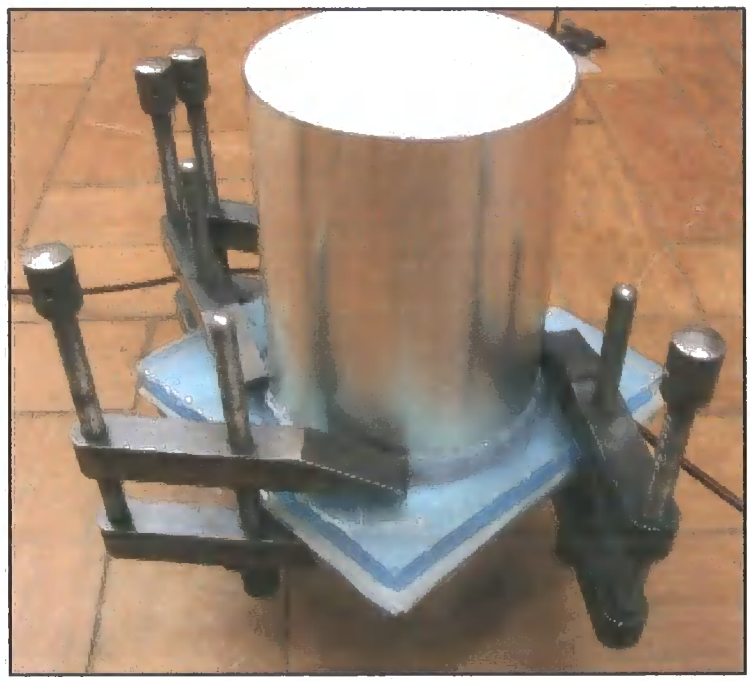

Figure 5.7. Photograph of bias coil construction. Each bias coil was wrapped around the aluminium cylinder, coated in epoxy and then clamped between two Perspex formers. Each coil had two turns stacked radially. Mylar film was used to prevent the coil gluing to the former.

Bias Coil Construction

Both bias coils were constructed with the use of a 9.1 cm diameter aluminium cylinder, along with two 10 mm thick Perspex rings, as shown in Figure 5.7. A thin

layer of vacuum grease was applied to the inside of the Perspex rings, then a layer of 125 μm Mylar, before a further thin layer of grease (as with the baseball coil, this was to prevent the coil gluing to the former). For each coil, two turns of enamel-coated C101 copper wire, with circular cross-section of diameter 3 mm were stacked radially, interlaced with Araldite 2011 epoxy. The Perspex rings were then clamped together, to hold the coil in place such that the epoxy could set.

The bias coil pair was then positioned and glued (using Araldite Precision epoxy) in a Helmholtz configuration using a Perspex mount, as shown in Figure 5.8.

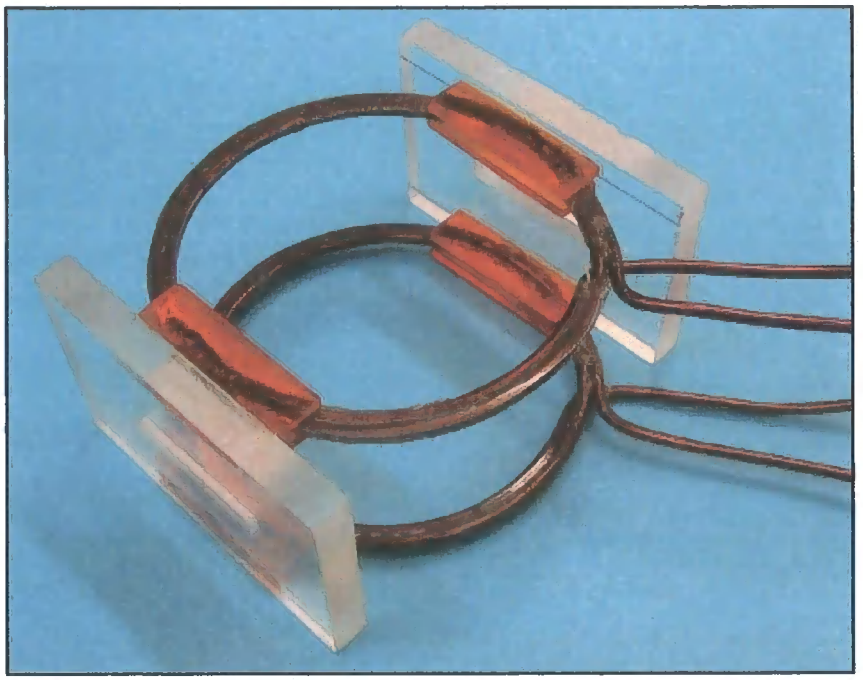

Figure 5.8. Photograph of the completed bias coil pair in Helmholtz configuration, i.e. the coils are separated by their radius. The coils are held in place by Perspex mounts. Note the slots in the clear Perspex mounting sections: these were to mount the completed Baseball Lens around the chamber.

The Finished Lens

Figure 5.9 shows a photograph of the completed Baseball Lens: the bias coil pair was glued into the baseball coil, using Araldite 2011 epoxy, such that their centres were coincident.

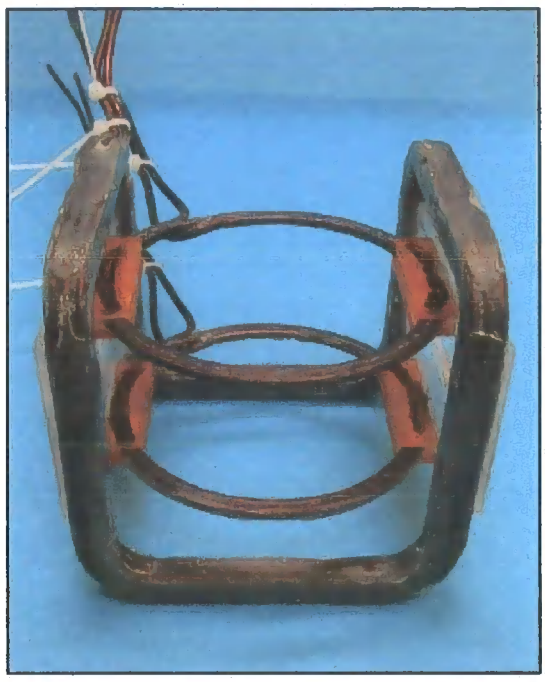

Figure 5.9. Photograph of the completed Baseball Lens. The Bias Coil pair was set within the Baseball Coil, using Araldite 2011 epoxy, to form the completed Baseball Lens. The white flecks that can be seen on the coil are places where excess epoxy was filed gently away.

5.4
Baseball Characterisation

The magnetic fields from the two components of the Baseball Lens, (the bias coils and the baseball coil), were measured with a 10 A test current passing through the coils. Using the following expansion for the magnitude of the magnetic field, as in chapter 3,

$$B = B_0' + B_0 + \left(\frac{B_1'^2}{2(B_0' + B_0)} - \frac{(B_2' + B_2)}{4} \right)(x^2 + y^2) + \frac{(B_2' + B_2)}{2} z^2 + \left(B_3' - \frac{B_1'(B_2' + B_2)}{2(B_0' + B_0)} \right)(y^2 - x^2) z \tag{5.1}$$

the coefficients B_i' and B_i were deduced and are shown in Table 5.1 along with their theoretical counterparts. The following sections describe the characterisation process after presenting the theoretically expected values.

Coefficient		Measured	Theoretical	
B_0'		415 ± 4	$(42 \pm 2) \times 10$	$\mathrm{mG\,A^{-1}}$
B_1'	B_{1x}'	14.9 ± 0.1	16.6 ± 0.7	$\mathrm{Gm^{-1}\,A^{-1}}$
	B_{1y}'	15.5 ± 0.2		$\mathrm{Gm^{-1}\,A^{-1}}$
B_2'		0.26 ± 0.02	0.28 ± 0.01	$\mathrm{kG\,m^{-2}\,A^{-1}}$
B_3'	B_{3x}'	2 ± 6	1.39 ± 0.06	$\mathrm{kG\,m^{-3}\,A^{-1}}$
	B_{3y}'	28 ± 6		
B_4'		-3 ± 1	-	$\mathrm{MG\,m^{-4}\,A^{-1}}$
B_0		Central 2cm 0.3596 ± 0.0002	0.37 ± 0.02	$\mathrm{G\,A^{-1}}$
B_2		Central 2cm -25 ± 7	0 ± 24	$\mathrm{G\,m^{-2}\,A^{-1}}$

Table 5.1. Values of Expansion Coefficients, theoretical and experimental.

Theoretical Expectations

Using the equations in chapter 3 for the baseball coil expansion coefficients, with $W = L = 2$, $a = 5.0 \pm 0.2$ cm, i.e.,

$$
\begin{aligned}
B_0' &= \frac{\frac{4\mu_0 I'}{\pi} W^2}{a\left(L^2+W^2\right)\left(L^2+2W^2\right)^{1/2}} \\
B_1' &= \frac{\frac{4\mu_0 I'}{\pi}\left(L^5+3L^3W^2+4LW^4\right)}{a^2W^2\left(L^2+W^2\right)^2\left(L^2+2W^2\right)^{1/2}} \\
B_2' &= \frac{\frac{32\mu_0 I'}{\pi}\left(6L^6W^2+18L^4W^4+11L^2W^6-5W^8\right)}{a^3\left(L^2+W^2\right)^3\left(L^2+2W^2\right)^{5/2}} \\
B_3' &= \frac{\frac{48\mu_0 I'}{\pi}\left(-5L^7W^2-10L^5W^4+11L^3W^6+24LW^8\right)}{a^4\left(L^2+W^2\right)^4\left(L^2+2W^2\right)^{5/2}}
\end{aligned}
\tag{5.2}
$$

the theoretically expected values for the B-field expansion coefficients for the baseball coil are,

$$
\begin{aligned}
B_0' &= (42\pm 2)\times 10 \text{ mG A}^{-1} \\
B_1' &= 16.6\pm 0.7 \text{ G m}^{-1}\text{ A}^{-1} \\
B_2' &= 0.26\pm 0.01 \text{ kG m}^{-2}\text{ A}^{-1} \\
B_3' &= 1.39\pm 0.06 \text{ kG m}^{-3}\text{ A}^{-1}
\end{aligned}
\tag{5.3}
$$

and the coefficients for the bias coils are, with $a = 4.9\pm 0.2$ cm and $s = 4.9\pm 0.2$ cm,

$$
\begin{aligned}
B_0 &= 0.37\pm 0.02 \text{ kG A}^{-1} \\
B_2 &= 0\pm 24 \text{ kG m}^{-2}\text{ A}^{-1}
\end{aligned}
\tag{5.4}
$$

Characterisation with a Test Current

Since the baseball and bias coils are designed to run at hundreds of Amps for only tens of milliseconds, they do not need water-cooling for their intended use. Consequently, the magnetic field must be characterised at a low (~10 A) continuous current that does not require water-cooling.

Using a Bell 640 Incremental Gauss Meter with a Bell HTG4-0608 transverse probe (1.8mm diameter circular active area), along with an x-y vernier-scaled translation stage, the magnetic field for both the baseball and the bias coils was characterised along the three principal axes of the lens.

The Baseball Coil

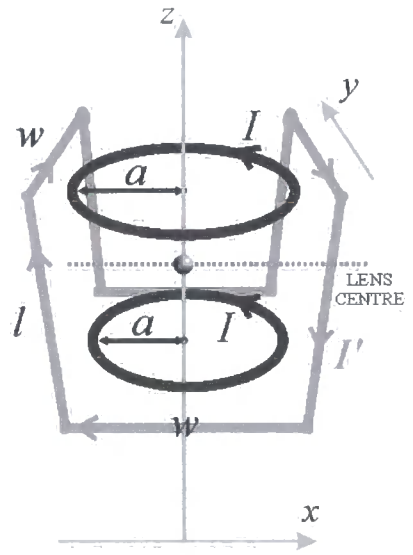

Figure 5.10. Schematic of whole Baseball Lens showing principle directions. The z-direction is along the axis of the baseball coil and the bias coil pair. The baseball coil dimensions are $w \times w \times l$ and the bias coils have radius a, separated by a to form a Helmholtz pair.

After preliminary experiments showed that $B'_{x,y}(z)$, $B'_{y,z}(x)$ and $B'_{x,z}(y)$ were approximately constant in the central region of the lens, careful measurements of $B'_x(x)$, $B'_y(y)$, and $B'_z(z)$ were made to deduce the magnetic field expansion coefficients B'_i, where $B'_{i=even}$ are deduced from $B'_z(z)$ and $B'_{i=odd}$ from $B'_x(x)$ and $B'_y(y)$. Figure 5.10 shows a schematic of the baseball coil along with the principle directions x, y and z.

Figure 5.11 shows a plot of $B'_z(z)$ over the central 20 mm of the lens along a line close to the axis $(0,\ 0,\ z)$, for $I' = 10.0 \pm 0.1$ A through the baseball coil. A 4th-order expansion $B'_z(z) = \sum_0^4 B'_i \frac{z^i}{i!}$ with $B'_{i=odd} = 0$ was used with a χ^2 minimisation to model the measured fields. The expansion coefficients were deduced to be,

$$\begin{aligned} B'_0 &= 415 \pm 4 \text{ mG A}^{-1}, \\ B'_2 &= 0.26 \pm 0.02 \text{ kG m}^{-2} \text{ A}^{-1}, \\ B'_4 &= -3 \pm 1 \text{ MG m}^{-4} \text{ A}^{-1}, \end{aligned} \tag{5.5}$$

where the errors were garnered from the $\chi^2 + 1$ contour. As a note, the 4th-order model produced a 12% change in B'_2 from a 2nd order model, but a 6th-order model

produced a change of <0.1% in B_2' from the 4th-order model, so the 4th-order was deemed sufficient.

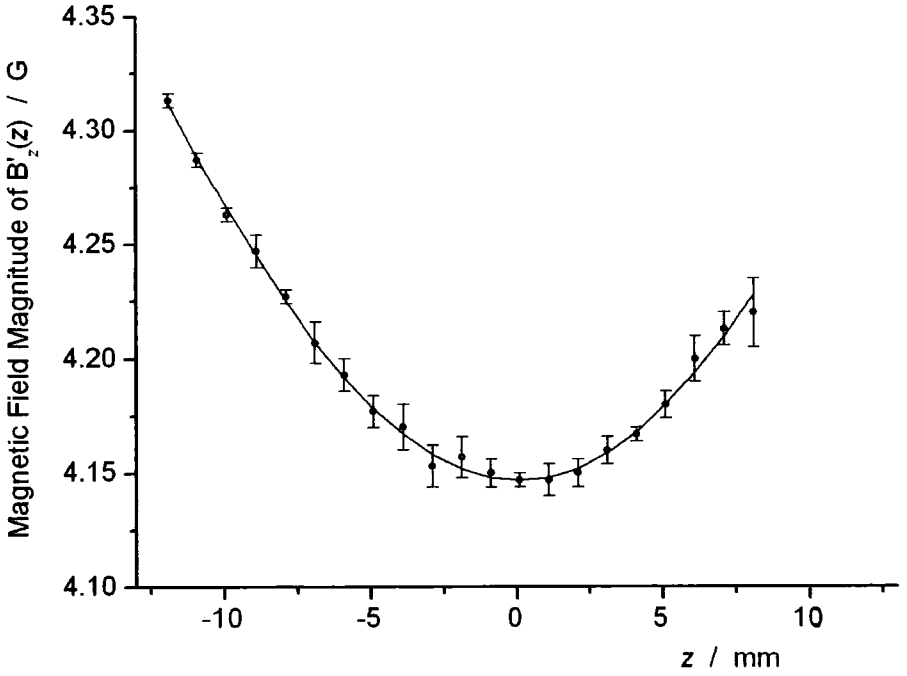

Figure 5.11. Graph of $B_z'(z)$ against z, where the z-direction is along the axis of the baseball coil. The solid black line represents a 4th-order fit to the data where the coefficients were deduced to as $B_0' = 415 \pm 4$ mG A^{-1}, $B_2' = 0.26 \pm 0.02$ kG m^{-2} A^{-1}, and $B_4' = -3 \pm 1$ MG m^{-4} A^{-1}. The magnetic field was measured using a Bell 640 Incremental Gauss Meter with a Bell HTG4-0608 transverse probe (1.8mm diameter circular active area), along with a vernier-scaled translation stage. A test current of 10.0 ± 0.1 A was passed through the baseball coil. Each data point is the mean value of three measurements, with the error bars given by the standard error of these measurements.

Figure 5.12 (a) and (b) show plots of $B_x'(x)$ and $B_y'(y)$ respectively, each with the expansion $B_x'(x) = B_{1x}'x + B_3'\frac{x^3}{3!}$ fitted to the data. As in the case of $B_z'(z)$, a χ^2 minimisation was used to fit to the data, with errors taken from the χ^2+1 contour, such that:

$$\begin{aligned} B_{1x}' &= 14.9 \pm 0.1 \text{ G m}^{-1} \text{ A}^{-1} \\ B_{1y}' &= 15.5 \pm 0.2 \text{ G m}^{-1} \text{ A}^{-1} \\ B_{3x}' &= 2 \pm 6 \text{ kG m}^{-3} \text{ A}^{-1} \\ B_{3y}' &= 28 \pm 6 \text{ kG m}^{-3} \text{ A}^{-1}. \end{aligned} \tag{5.6}$$

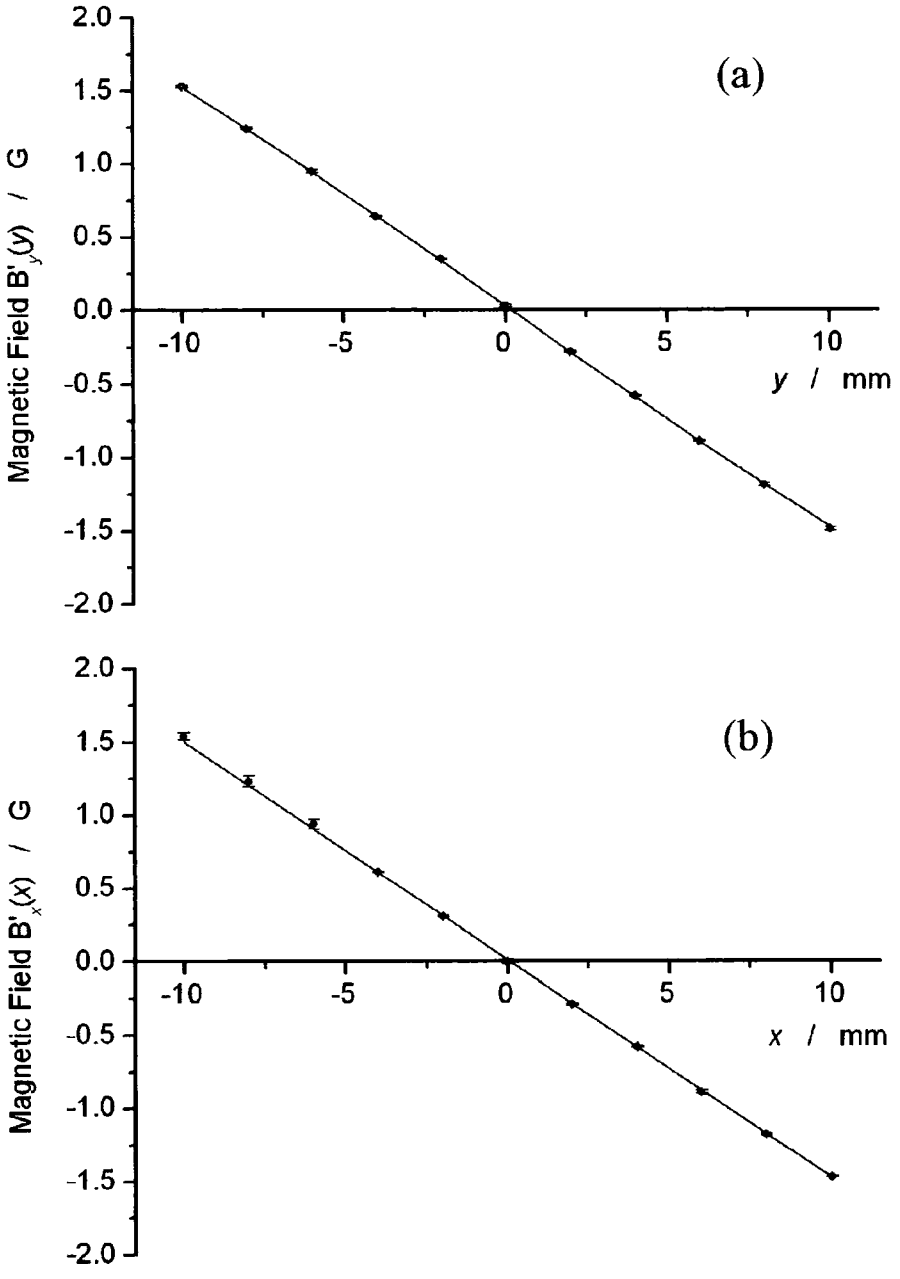

Figure 5.12. (a) shows $B'_x(x)$ against x, and (b) shows $B'_y(y)$ against y for the baseball coil. 3rd-order fits were used to deduce the expansion coefficients as $B'_{1x} = 14.9 \pm 0.1$ G m^{-1} A^{-1}, $B'_{1y} = 15.5 \pm 0.2$ G m^{-1} A^{-1}, $B'_{3x} = 2 \pm 6$ kG m^{-3} A^{-1}, and $B'_{3y} = 28 \pm 6$ kG m^{-3} A^{-1}. The magnetic field was measured using a Bell 640 Incremental Gauss Meter with a Bell HTG4-0608 transverse probe (1.8mm diameter circular active area), along with a vernier-scaled translation stage. A test current of 10.0 ± 0.1 A was passed through the baseball coil. Each data point is the mean value of three measurements, with the error bars given by the standard error of these measurements.

The Bias Coils

Since, for a pair of Helmholtz coils, the magnitude of the magnetic field is dominated by $B_z(z)$, careful measurements of $B_z(z)$ were made along a line close to the axis (0, 0, z) in-between the two coils. Figure 5.13 shows the variation of $B_z(z)$ with z over the central 2 cm of the bias coil pair. The measurement here is limited by the discrete measurement limit of the Bell 640 Incremental Gauss Meter used to measure the magnetic field. This discrete limit was 0.01 G, but each data point is the mean of three measurements. A current of 10.0 ± 0.1 A was passed through the bias coils. The field magnitude was approximately constant, within 0.02 G over the central 2 cm, but did appear to exhibit a slight negative curvature. A 2nd-order fit produced expansion coefficient values of $B_0 = 0.3596 \pm 0.0002$ G A^{-1} and $B_2 = -25 \pm 7$ G m^{-2} A^{-1}.

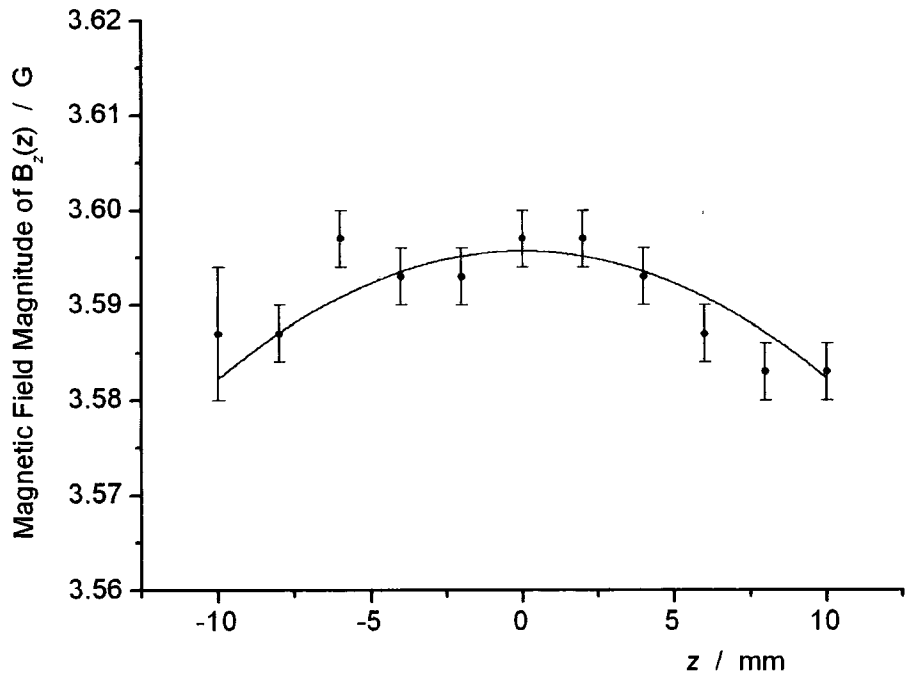

Figure 5.13. Plot of the magnitude of the axial magnetic field $B_z(z)$ against the axial direction z, over the central 2 cm of the bias coil pair. The measurement here is limited by the discrete measurement limit of the Bell 640 Incremental Gauss Meter used to measure the magnetic field. This discrete limit was 0.01 G. Each data point is the mean value of three measurements, with the error bars given by the standard error of these measurements. A 2nd-order fit (black line) gave expansion coefficient values of $B_0 = 0.3596 \pm 0.0002$ G A^{-1} and $B_2 = -25 \pm 7$ G m^{-2} A^{-1}.

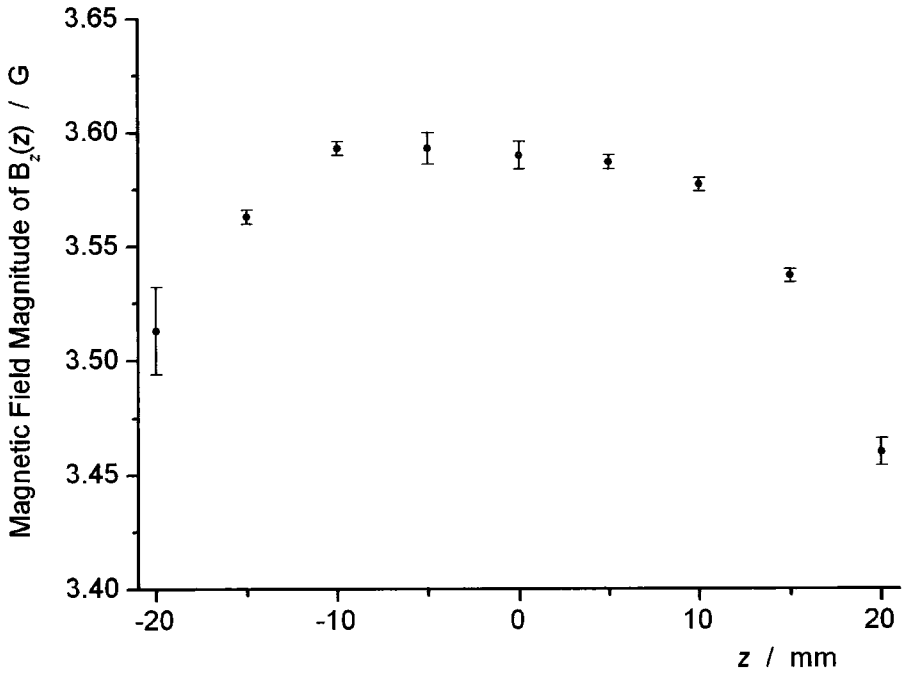

Figure 5.14. Plot of the magnitude of the axial magnetic field $B_z(z)$ against the axial direction z, over the central 4 cm of the bias coil pair. Each data point is the mean value of three measurements, with the error bars given by the standard error of these measurements. An approximately constant region is observable in the centre of the bias coil pair. However, the magnetic field magnitude begins to decrease further from the centre.

Further from the centre of the bias coil pair, the magnetic field decreased more sharply. Figure 5.14 shows the variation of $B_z(z)$ with z over the central 4 cm of the bias coil pair. This variation is over 0.1 G. Observation of Figure 5.14 shows that the field is approximately constant over the central 2 cm, compared with the variation over the central 4 cm.

5.5
Baseball Lens Operation and Conditions for an Isotropic Lens

Overview

Four configurations of the Baseball Lens were used in this experiment, i.e. four ratios between the axial and radial curvature of the Baseball Lens. First, three truck batteries were used to create a pulse through only the baseball coil to observe the maximum current available. Then, the bias coils were added, along with a tuning resistor, R_{TUNE}, to regulate the percentage of the total current that passed through the bias coils, and hence the relationship between the axial and radial curvature.

Figure 5.15 shows a diagram of the final circuit used to supply the current pulse to the Baseball Lens. The current was supplied by three 12 V 1150 A-max. Volvo Truck Batteries connected in series. A Mitsubishi CM1400DU-24NF Integrated Gate Bipolar Transistor (IGBT), connected in series with the load (the baseball coil, the bias coils and the tuning resistor R_{TUNE}), was used to pulse the current on and off by application of a voltage, V_{G-E}, to the IGBT gate, discussed in section 5.2. Safety features were present in the circuit to prevent a short-circuit of the batteries, and hence a potential explosion. The total current through the whole load (and therefore the current through the baseball coil), and the current through the tuning resistor R_{TUNE} were measured using two Honeywell CSNK591 Hall Effect Current Sensors (HECS). The rest of this section looks at the four lens configurations used in the experiment and the condition for an isotropic lens.

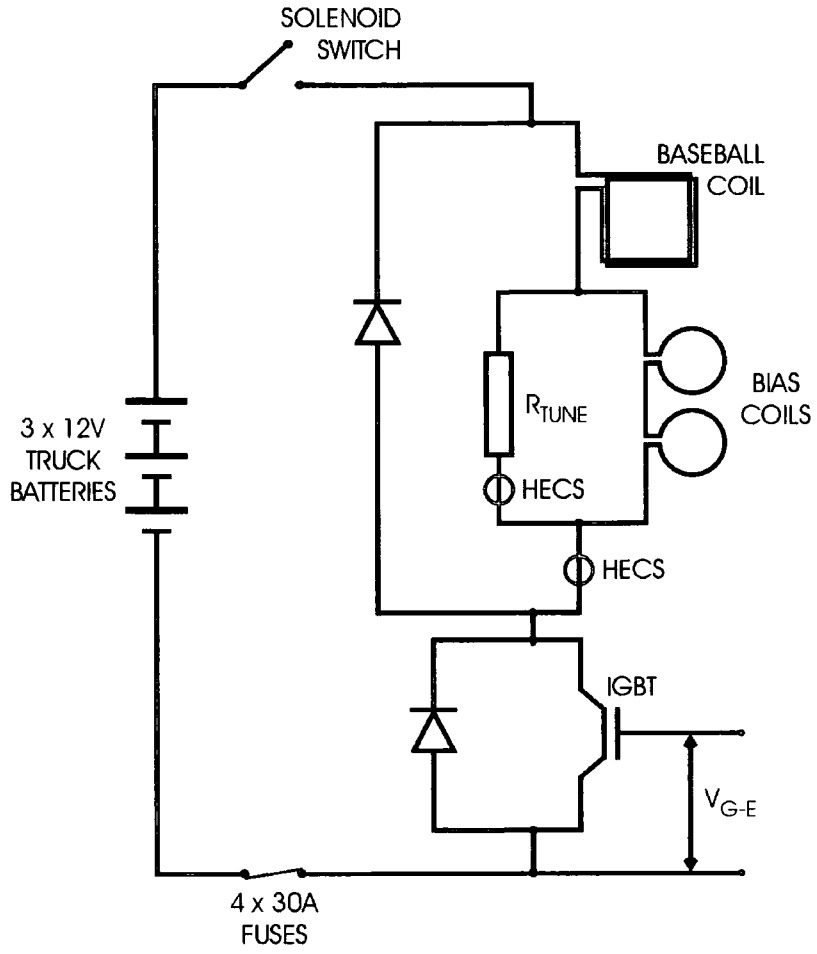

Figure 5.15. Circuit diagram of the electronics for the current pulse through the Baseball Lens. The power was provided by three 12 V 1150 A max. Volvo Truck batteries connected in series. As a primary safety measure, four 30 A fuses (in parallel) were present to prevent the truck batteries being short-circuited, in the case that the IGBT were to blow open. A 12 V solenoid switch, closed before pulsing, operated as a manual safety switch. At $V_{G\text{-}E} = 0$ V, the IGBT gate is closed and no current flows. When a pulse of > 15 V is applied to the IGBT gate, i.e. $V_{G\text{-}E} > 15$ V, the IGBT gate opens and current flows. The reverse-biased diode across the IGBT is inherent within the IGBT module, for protection of the IGBT. The reverse-biased diode (International Rectifier Schottky Rectifier 240NQ045) in parallel with the load (the baseball coil, the bias coils and the tuning resistor R_{TUNE}) is present to prevent oscillatory currents in the lens after switch-off. The tuning resistor R_{TUNE} is present to regulate the percentage of the total current that flows through the baseball coil. Two Honeywell CSNK591 HECS are present to measure the total current through the whole load and the current through R_{TUNE}.

Notes on R_{BIAS} and R_{TUNE}

R_{BIAS} and R_{TUNE} are both made from enamel coated, 3 mm-diameter cylindrical cross-section, copper wire (Polyester 200 Grade 2 C101 purchased from F. D. Sims Ltd., rated at 101% I.A.C.S.), as used for the baseball coil. The wire was measured to have approximately $10\ \mathrm{m\Omega\ m^{-1}}$. A length of approximately 60 cm was used for the construction of the bias coils (each coil having two turns (stacked radially) with a mean radius of $a = 4.9 \pm 0.2$ cm. To vary the fraction of the total current that passed through the bias coils, R_{TUNE} was placed in parallel to R_{BIAS} and made from a suitable length of wire for the fraction of current required.

In chapter 3 section 3.2, the ratio of the current-turns of the baseball coil and the current turns of each of the bias coils, for a cubic isotropic Baseball Lens, was given as $NI/I' = 0.154$. Therefore the ratio between the current-turns of the baseball coil and the current-turns of *both* the bias coils in this condition is $N_{BB}I'/2NI = 3.245$, where $N_{BB} = 9$ is the number of turns of the baseball coil, I' is the current through the baseball coil, N is the number of turns on a single bias coil, and I is the current through the bias coils.

If the current through the resistor R_{TUNE} (in Figure 5.15) is denoted I_{TUNE}, then,

$$\frac{9I'}{2NI} = \frac{9\left(I + I_{\mathrm{TUNE}}\right)}{2NI} = 3.245. \tag{5.7}$$

Since the ratio of I_{TUNE} to I is the same as the ratio of R_{BIAS} to R_{TUNE} then,

$$\frac{R_{\mathrm{BIAS}}}{R_{\mathrm{TUNE}}} = 0.721N - 1. \tag{5.8}$$

The minimum value of the number of turns N on each of the bias coils, where the ratio of R_{BIAS} to R_{TUNE} is positive, is $N = 2$. Therefore the bias coils were constructed with two turns on each coil, since this minimised the inductance of the bias coils, and would hence minimise their effect upon the rise-time of the current pulse.

The Four Configurations of the Baseball Lens

Figure 5.16 shows a graph of the current through the baseball coil (only) with a 20 ms long IGBT gate pulse, using the circuit shown in Figure 5.15 without the bias coils or R_{TUNE}. The mean peak current was measured to be 947 ± 5 A, giving a baseball coil with $947 \times 9 = 8523$ Amp-turns.

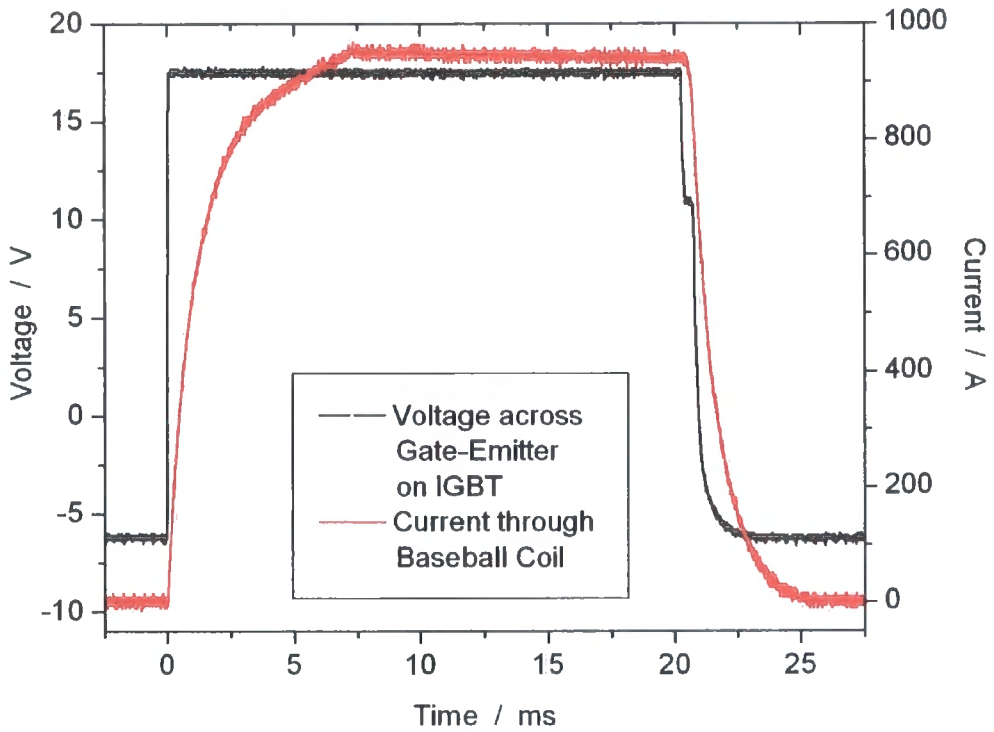

Figure 5.16. Graph showing the current through the baseball coil (only), with a 20 ms long IGBT gate-pulse, using the circuit in Figure 5.15 without the bias coils or R_{TUNE}. The mean peak current is 947 ± 5 A. The non-square rise and fall are due to the inductance of the circuit - the baseball coil and its leads were measured to have an inductance of $31.6 \pm 0.1\,\mu$H. In this case, $\omega_z = 40 \pm 2$ Hz and $\omega_x = 50 \pm 2$ Hz.

A peak current of 947 ± 5 A would give angular frequencies of $\omega_z = 40 \pm 2$ Hz and $\omega_x = 50 \pm 2$ Hz, using the characterisation data in section 5.1, with

$$B = B_{0R} + \left(\frac{B_1'^2}{2B_{0R}} - \frac{B_{2R}}{4} \right)\left(x^2 + y^2\right) + \frac{B_{2R}}{2} z^2 + \left(B_3' - \frac{B_{2R} B_1'}{2B_{0R}} \right)\left(y^2 - x^2\right) z , \qquad (5.9)$$

that,

$$\omega_z^{\,2} = \mu_B (B_2' + B_2)/m , \qquad (5.10)$$

and that,

$$\omega_x^{\,2} = \frac{2\mu_B}{m}\left(\frac{B_1'^2}{2(B_0' + B_0)} - \frac{(B_2' + B_2)}{4}\right), \tag{5.11}$$

where μ_B is the Bohr magneton and m is the mass, in this case, of a ^{85}Rb atom. The errors on the calculation on the values of ω are dominated by the errors on the expansion coefficients B_n, with the error on the measured current having little effect.

To make the lens isotropic, the radial curvature ω_x must be decreased with the addition of a bias field from the bias coils.

One can calculate the percentage of the total current that is required to pass through the bias coils to make the lens isotropic, i.e. by use of the coefficients found in section 5.1 and equation (5.9) above. Along with the baseball coil only case, three more

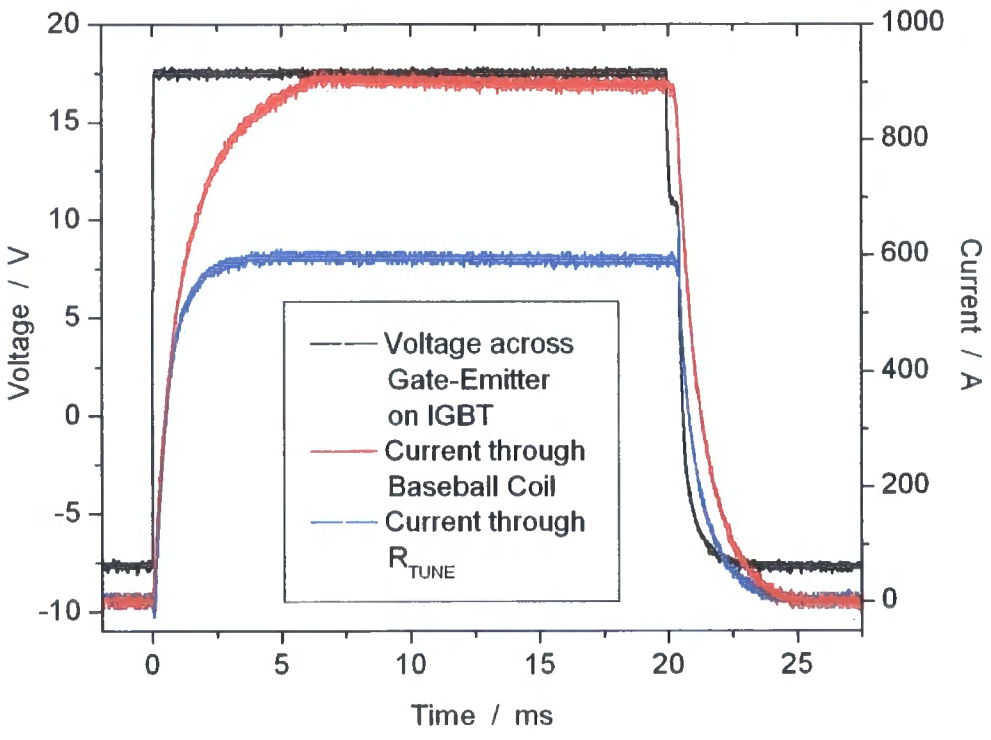

Figure 5.17. Graph showing the current through the Lens, with a 20 ms long IGBT gate-pulse, using the circuit in Figure 5.15 with $R_{TUNE} = R_{BIAS}/2$. The mean peak current in the baseball coil is 898 ± 4 A, and 304 ± 2 A in the bias coils. The non-square rise and fall are due to the inductance of the circuit - the baseball coil and its leads were measured to have an inductance of $31.6 \pm 0.1\,\mu$H and the bias coils to have an inductance of $1.8 \pm 0.1\,\mu$H. In this case, $\omega_z = 39 \pm 2$ Hz and $\omega_x = 41 \pm 2$ Hz.

cases are considered: the case where a third of the total current is passed through the bias coils; the case where half the total current is passed through the bias coils; and the case where the total current is passed through the bias coils.

Figure 5.17 shows the first of these cases, where two-thirds of the total current is measured to pass through R_{TUNE} and hence a third of the current passes through the bias coils. The mean peak current in the baseball coil is 898 ± 4 A, and 304 ± 2 A in the bias coils, giving $I/I' = 0.339$. In this case, $\omega_z = 39 \pm 2$ Hz and $\omega_x = 41 \pm 2$ Hz.

Figure 5.18 shows a graph depicting the third configuration of the Baseball Lens, where half of the total current is measured to pass through R_{TUNE} and hence half of the current passes through the bias coils. The mean peak current in the baseball coil is 872 ± 4 A, and 466 ± 3 A in the bias coils, giving $I/I' = 0.511$. In this case, $\omega_z = 39 \pm 1$ Hz and $\omega_x = 38 \pm 1$ Hz.

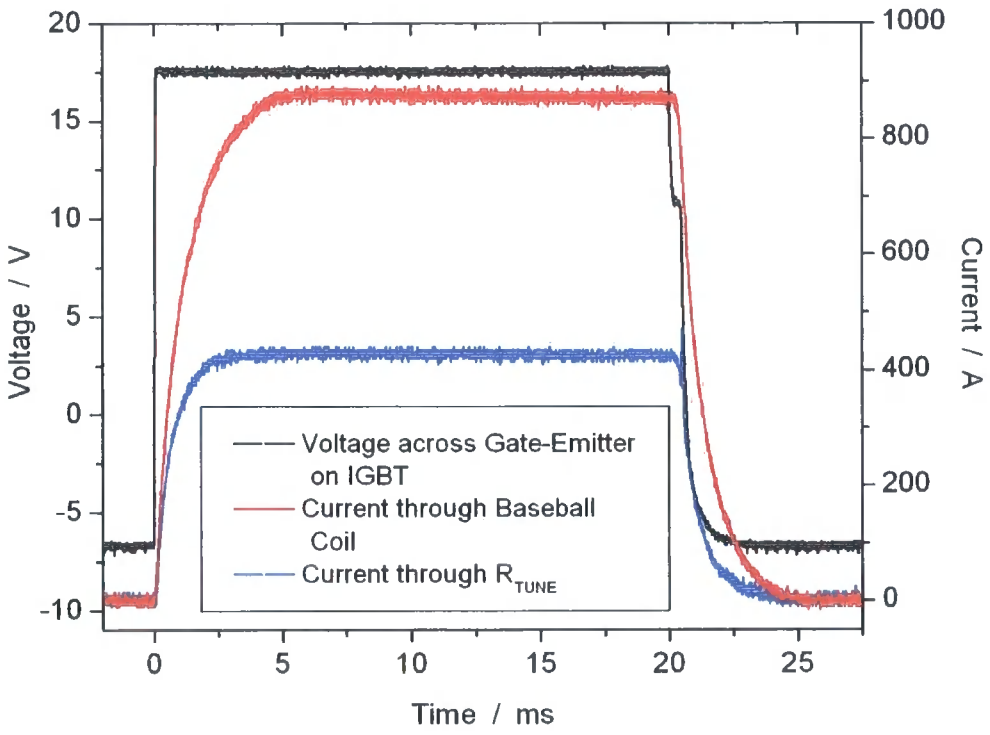

Figure 5.18. Graph showing the current through the Lens, with a 20 ms long IGBT gate-pulse, using the circuit in Figure 5.15 with $R_{\text{TUNE}} = R_{\text{BIAS}}$. The mean peak current in the baseball coil is 872 ± 4 A, and 446 ± 3 A in the bias coils. In this case, $\omega_z = 39 \pm 1$ Hz and $\omega_x = 38 \pm 1$ Hz.

Figure 5.19 shows a graph depicting the final configuration of the Baseball Lens. R_{TUNE} is removed from the circuit, so that all of the current passes through the bias coils, i.e. $I/I' = 1$. The mean peak current is 832 ± 4 A. In this case, $\omega_z = 38 \pm 1$ Hz and $\omega_x = 30 \pm 1$ Hz.

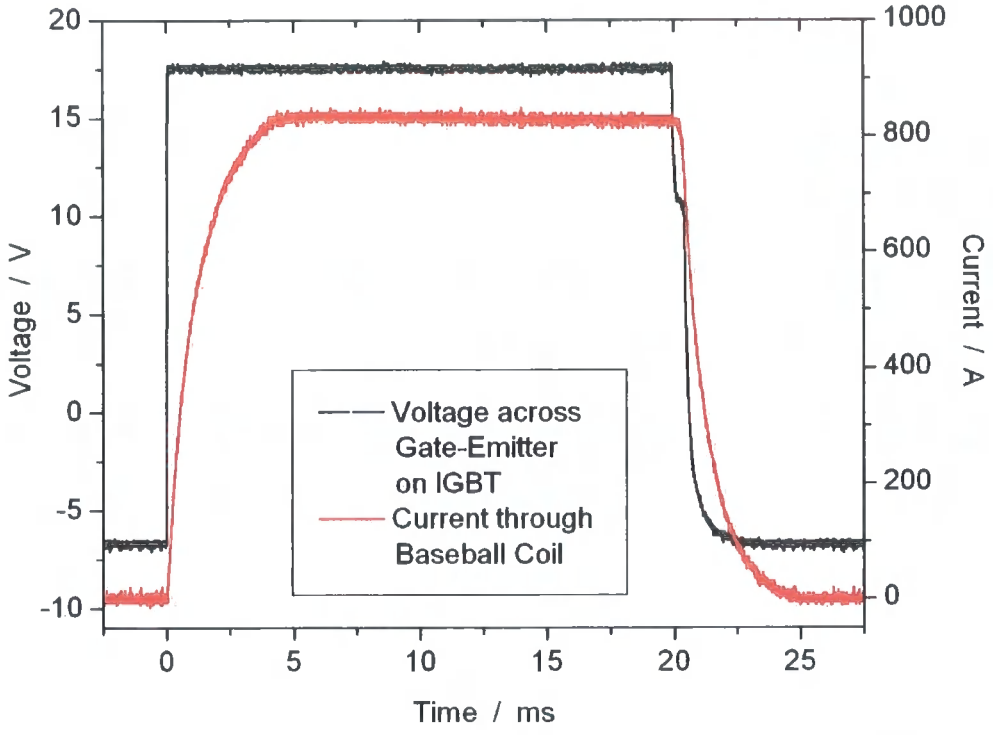

Figure 5.19. Graph showing the current through the Lens, with a 20 ms long IGBT gate-pulse, using the circuit in Figure 5.15 with R_{TUNE} removed, i.e. $R_{\text{TUNE}} \to \infty$ and all the current flows through the bias coils. The mean peak current in both the baseball coil and the bias coils is 832 ± 4 A. In this case, $\omega_z = 38 \pm 1$ Hz and $\omega_x = 30 \pm 1$ Hz.

Conclusions about the Four Baseball Lens Configurations

Table 5.2 tabulates the axial and radial angular frequencies for the four configurations of the Baseball Lens.

Configuration	ω_z	ω_x
Baseball coil only	40 ± 2	50 ± 2
$R_{\mathrm{TUNE}} = R_{\mathrm{BIAS}}/2$	39 ± 2	41 ± 2
$R_{\mathrm{TUNE}} = R_{\mathrm{BIAS}}$	39 ± 1	38 ± 1
R_{TUNE} removed	38 ± 1	30 ± 1

Table 5.2. The experimentally inferred angular frequencies of the four configurations of the Baseball Lens. For both the cases $R_{\mathrm{TUNE}} = R_{\mathrm{BIAS}}/2$ and $R_{\mathrm{TUNE}} = R_{\mathrm{BIAS}}$ the Baseball Lens should be approximately isotropic.

In the case of the baseball coil only, for a given pulse duration, an atom cloud should focus in the x-direction before the z-direction. For both cases $R_{\mathrm{TUNE}} = R_{\mathrm{BIAS}}/2$ and $R_{\mathrm{TUNE}} = R_{\mathrm{BIAS}}$ the x and z-directions should focus at approximately the same time. However, in the case that R_{TUNE} is removed, i.e. $R_{\mathrm{TUNE}} \to \infty$, a cloud should focus in the z-direction before the x-direction.

---

[1] private communication, John G Peck Ltd., UK suppliers and technical support for Mitsubishi Semiconductors Power Modules, and private communication with International Rectifier, power module manufacturers.

[2] Mitsubishi Electric Publication, *Using Hybrid Gate Drivers and Gate Drive Power Supplies*, Mitsubishi Semiconductors Power Modules MOS (September 2000)

Chapter 6

Experimental Spatial Focusing of a Launched Cold Atom Cloud

6.1
Preliminary Results using the Baseball Coil Only

6.1.1 First Pulsed Magnetic Action: Baseball Coil Only

The following section presents preliminary data using the Baseball Lens configured as only the baseball coil (i.e. no bias coils), along with the moving molasses stage detailed in section 2.2.3. The current through the baseball coil (during the magnetic impulse) was 947 ± 5 A, giving a baseball with a total of $947 \times 9 = (852 \pm 4) \times 10$ Amp-turns.

Approximately 7×10^7 ^{85}Rb atoms were loaded into the MOT ($\Delta = -2\pi \times 13$ MHz and a magnetic field gradient of approximately 9 G cm^{-1}), before undergoing a 10 ms long optical molasses stage at MOT detuning and intensity (to 24 ± 2 μK). Then the upper MOT beams were decreased in frequency and the lower MOT beams increased in frequency (relative to the central detuning $\Delta = -2\pi \times 13$ MHz) in 6 ms to bring the atoms to a launch speed to reach an apex of 20.5 cm. The beams were held at the final launch frequencies for 1 ms before being shut-off. 20 ms after the launch beams were extinguished an orientation magnetic-field of approximately 300 mG was applied for orientation of the atoms' magnetic dipoles. The orientation field was in the vertical direction. 5 ms after the orientation field was turned on, a 350 μW, retro-reflected, vertically propagating, optical pumping beam was turned on for 50 μs to pump the atoms into the weak-field-seeking $5^2S_{1/2}|F = 3, m_F = 3\rangle$ state. A JAI CV50-IR CCD camera and a 6 mW, retro-reflected, vertically propagating, imaging beam were used to take fluorescence images of the launched clouds at the apex of flight, 204 ms after launch. The image light pulse duration was 2 ms.

The centre of the Baseball Lens was located 16.5 ± 0.2 cm above the MOT. The unfocussed cloud came to rest in (approximately) the centre of the image (see section 2.2.3). For each pulsed magnetic lens duration τ, the lens turn-on time was adjusted to centre the focussed cloud in the image, which was taken 204 ms after launch. The area seen by the following images was $(x = 9.0\,\text{mm}) \times (z = 12.7\,\text{mm})$.

An image where no magnetic impulse occurred during the flight of the atom cloud is shown in Figure 6.1, along with 'binned' line profiles of the horizontal and vertical

directions. The z-direction is the vertical direction and is the direction in which the atoms were launched. This image is formed from two images: it is the difference between the image of an unfocused launched cloud and a background image taken in the presence of no atoms (other than background vapour). The other images presented below also have a background image subtracted from them. The images in the rest of this section are calibrated in the same way as the image in Figure 6.1.

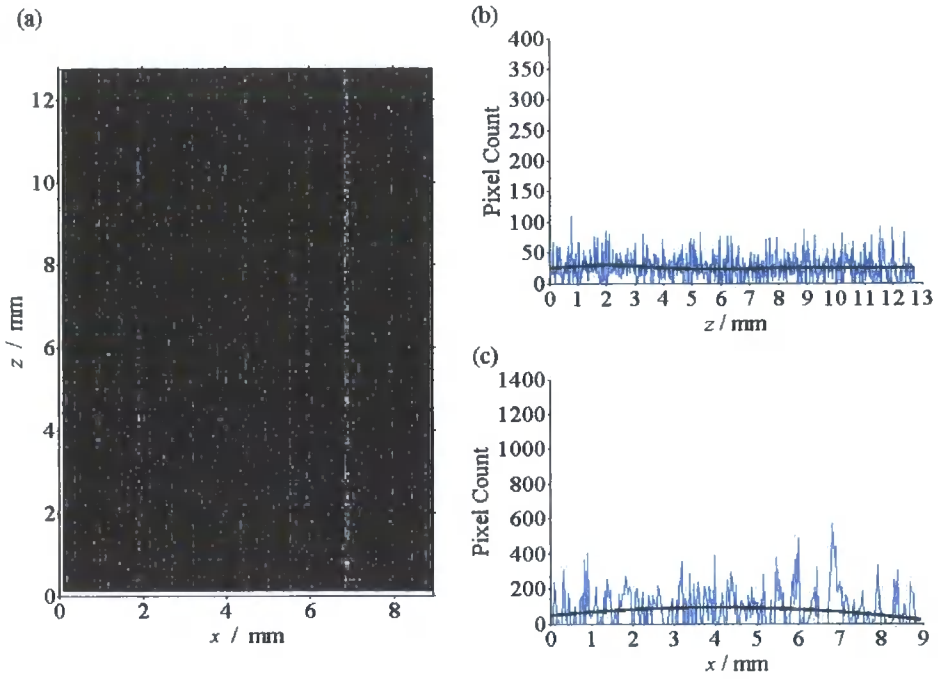

Figure 6.1. Image of the quartz cell on top of the vacuum chamber when no magnetic impulse acts on the atoms during their ballistic flight from the MOT chamber to the quartz cell. The image is centred at a height of 20.5 ± 0.2 cm above the MOT. (b) and (c) show 'binned' vertical and horizontal line profiles, respectively, of the image in (a). The image was super-pixelated into blocks of 2×5 pixels for display.

Three images of focussed clouds are shown below in Figures 6.2, 6.3 and 6.4 for varying magnetic pulse duration τ : Figure 6.2 $\tau = 18$ ms; Figure 6.3 $\tau = 32$ ms; and Figure 6.4 $\tau = 9$ ms.

Figure 6.2 shows a focused cloud when the magnetic lens is turned on for a pulse duration of $\tau = 18$ ms. The vertical profile is too wide to fit reliably, but the horizontal profile gives a standard deviation of 2.34 ± 0.09 mm (the mean of five measurements). When the pulse duration is increased to $\tau = 32$ ms (Figure 6.3), neither the vertical profile, nor the horizontal profile can be fitted (with sufficient

accuracy), showing that the horizontal cloud standard deviation σ_x has increased from the case where $\tau = 18$ ms.

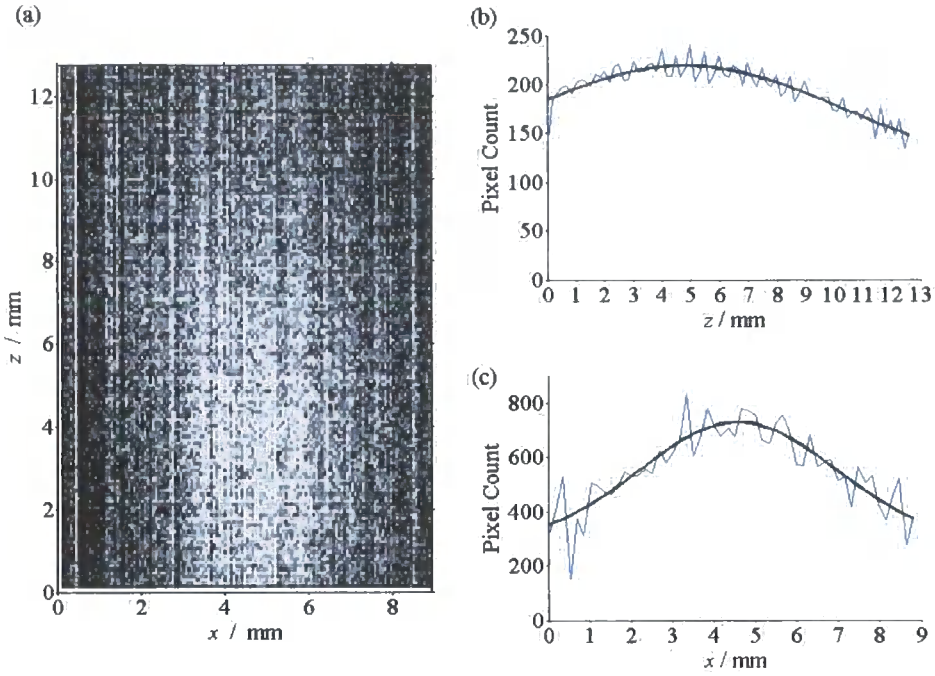

Figure 6.2. Image of a focussed cloud that has experienced a pulse duration of $\tau = 18$ ms, starting 104 ms after launch. The z-direction is the vertical direction. The horizontal width was fitted (black line) to be 2.34 ± 0.09 mm (the mean of five measurements) using the 'binned' horizontal profile (blue lines) in (c), but an insufficient fraction of the vertical profile was imaged to enable a reliable fit (black lines) to the 'binned' vertical profile (blue line) shown in (b). The image was super-pixelated into blocks of 2×5 pixels for display. The profiles have a ten point average in the horizontal direction and a 20 point average in the vertical direction.

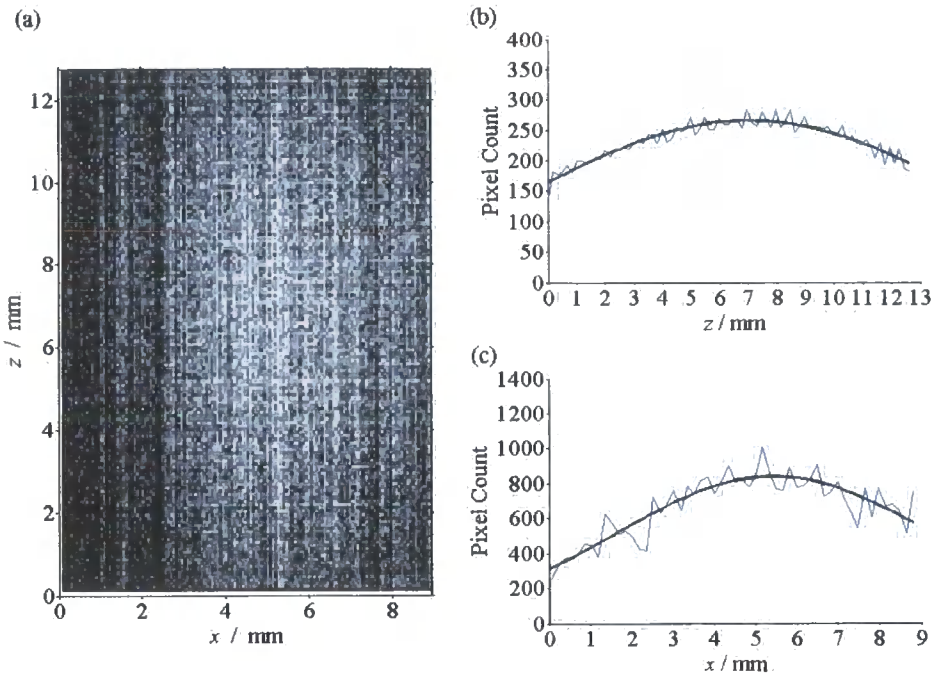

Figure 6.3. Image of a focussed cloud that has experienced a pulse duration of $\tau = 32$ ms, starting 98 ms after launch. The z-direction is the vertical direction. An insufficient fraction of the vertical (b) or the horizontal (c) 'binned' line profiles (blue lines) were present to fit reliable widths to the cloud. The image was super-pixelated into blocks of 2×5 pixels for display. The profiles have a ten point average in the horizontal direction and a 20 point average in the vertical direction.

If the magnetic pulse duration is decreased to the value of $\tau = 9$ ms (Figure 6.4), the result is dramatic in comparison to the cases where $\tau = 18$ ms and $\tau = 32$ ms. A tight horizontal focus with a standard deviation of 1.76 ± 0.04 mm (the mean of five measurements) is achieved at the apex of flight. An insufficient fraction of the vertical profile is present to fit reliably in the z-direction.

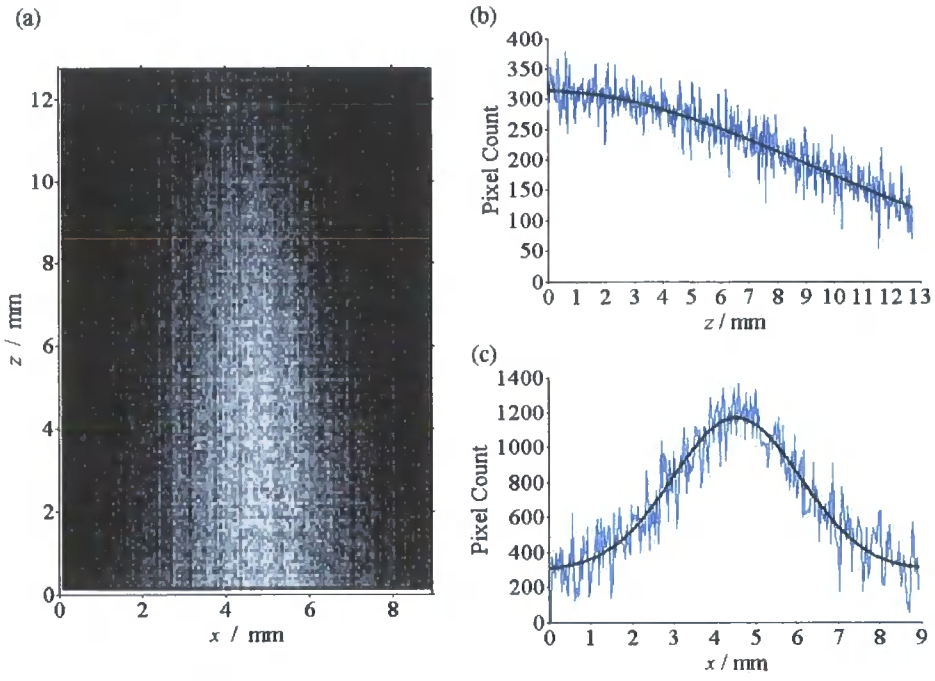

Figure 6.4. Image of a focussed cloud that has experienced a pulse duration of $\tau = 9$ ms, starting 107 ms after launch. The z-direction is the vertical direction. The horizontal width was fitted (black line) to be 1.76 ± 0.04 mm (the mean of five measurements) using the 'binned' horizontal profile (blue lines) in (c), but an insufficient fraction of the vertical profile was imaged to enable a reliable fit (black line) to the 'binned' vertical profile (blue line) shown in (b). The image was super-pixelated into blocks of 2×5 pixels for display. The 'binned' profiles are the profiles from the raw image.

Although the standard deviation in the z-direction cannot be fitted reliably, the change in the horizontal standard deviation σ_x with τ can be plotted, as shown in Figure 6.5. The smallest value of σ_x was 1.76 ± 0.04 mm (the mean of five measurements), which occurred at a pulse duration of $\tau = 9$ ms.

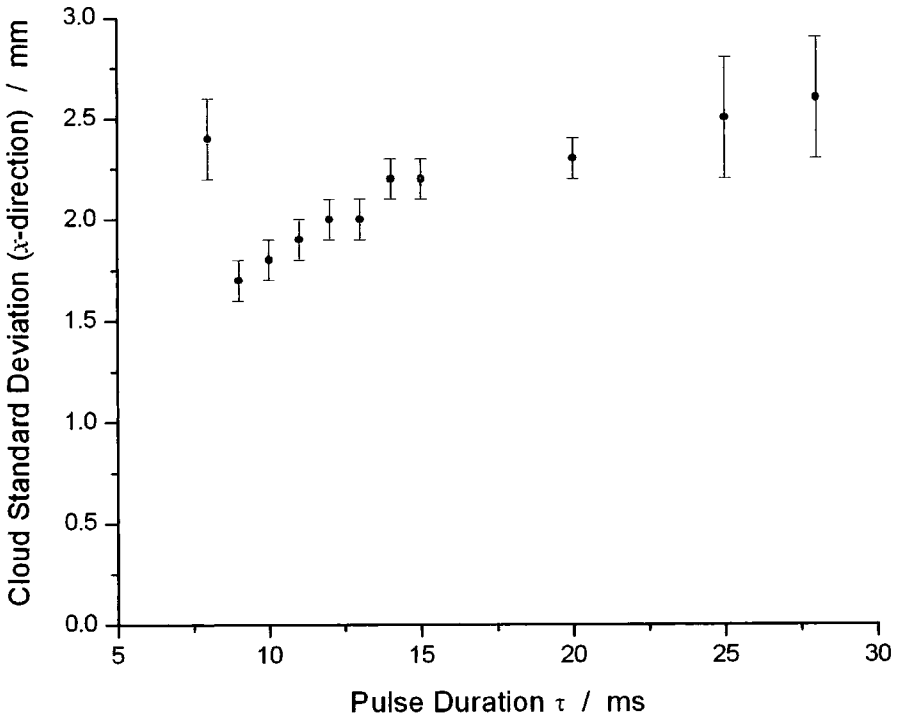

Figure 6.5. Plot of the cloud standard deviation in the x-direction σ_x against pulse duration τ. Each data point is the mean of five measurements and the error bars are the standard error of those measurements. The minimum horizontal standard deviation was 1.76 ± 0.04 mm, as shown in Figure 6.4.

6.1.2 Image Pulse Length and Measured Cloud Width

Figure 6.6 shows a graph of the measured cloud standard deviation, σ_x against the image light pulse length. These measurements were important to ensure that the observed clouds were not being heated by the imaging beam. The experiment was carried out as detailed above with a pulse duration $\tau = 10$ ms. The maximum available image duration was limited (by the JAI CV-M50 IR CCD Camera, in conjunction with the NI IMAQ 1408 PCI image acquisition card) to 2 ms. Each of the data points is the mean of five measurements and the error bars are the standard deviation of those measurements, (the standard deviation is used here, rather than the standard error, to illustrate the spread of values obtained). It can be seen that there is no discernable decrease in cloud size between 2.0 ms and 0.5 ms image pulse duration. The greater the image pulse length, the greater the number of scattered

photons within the image time, and hence the greater the signal available for detection with the CCD camera. Therefore, an image pulse duration of 2.0 ms was chosen for the experiment.

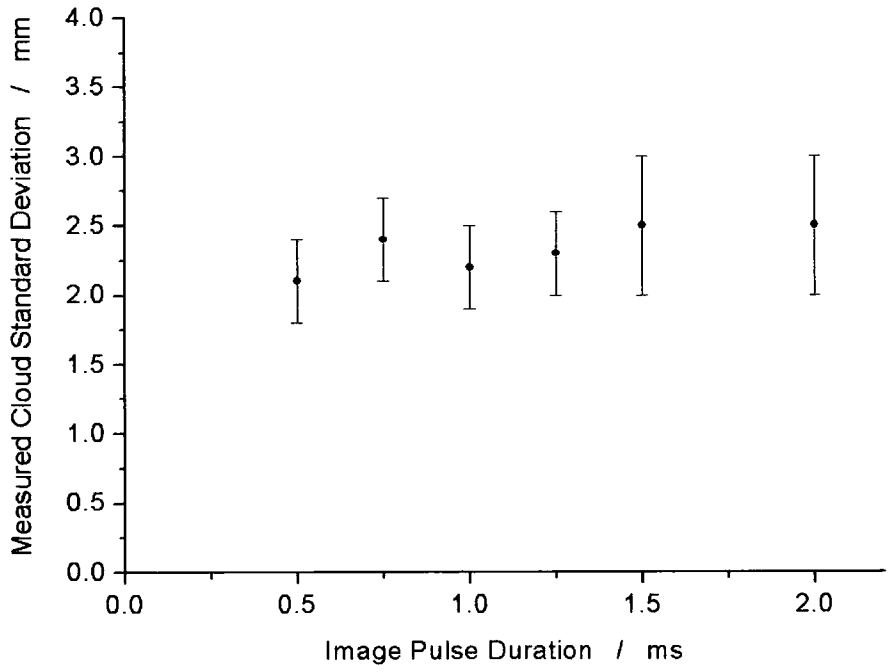

Figure 6.6. Graph of measured horizontal cloud standard deviation σ_x against image light pulse duration. Each data point is the average of five measurements, and the error bars are the standard deviation of those measurements. The experiment was conducted as described in section 6.1.1 with a magnetic pulse duration of $\tau = 10$ ms. There is no discernable decrease in the measured cloud size as the imaging pulse duration is decreased from 2.0 ms to 0.5 ms. Since the greater the imaging pulse duration, the greater the available signal for detection of atoms, an imaging pulse duration of 2.0 ms was chosen for further experiments.

6.1.3 Optical Pumping

Optical Pumping Set-up

For this experiment, it was required that the launched atoms were prepared in the weak-field-seeking (WFS) $5^2S_{1/2}|F=3, m_F=3\rangle$ state, as described in section 3.1, so that all the atoms were nominally focussed to the same point in space and time. If the atomic cloud had had a distribution of m_F values, then differing WFS states would focus at different positions and times, and strong-field-seeking (SFS) states would be

de-focussed, with the $m_F = 0$ state being unaffected, i.e. the production of a Stern-Gerlach experiment, such as the work by Maréchal *et al.* [1].

Initially, atoms in the launched cloud are in some distribution of m_F states, and to optically pump the atoms into the $5^2S_{1/2}|F=3, m_F=3\rangle$ state, the atoms must undergo a series of σ^+ transitions. Two things are required to achieve this population transfer: an orientation magnetic field to orient each atom's magnetic dipole, and relevant light that is circularly polarised with respect to that orientation field. The orientation field is provided by an increase in the current to the vertical Earth-Field Cancelling Coils (detailed in section 2.1.10), providing a field of approximately 300 mG, inline with work by Cognet *et al.* [2]. The light is provided by a laser beam retro-reflected vertically through the vacuum chamber, having passed through a quarter-wave plate before first entering the chamber. This optical pumping beam had a power of 350 μW (retro-reflected to give 700 μW) and a $1/e^2$ radius of approximately 12 mm, the beam cut at a diameter of just less than 20 mm (between 19.5 mm and 20 mm) for entry into the vacuum chamber. The optimisation of the wave-plate orientation and other optical pumping features is discussed below.

For experimental ease, it was chosen to optically pump on the $5S_{1/2}$ $F=3$ to $5P_{3/2}$ $F'=4$ transition.

Optimisation of Optical Pumping

Two aspects of the optical pumping set-up needed optimisation: the optical pumping duration and the orientation of the quarter-wave plate through which the optical pumping beam passed. The optimisation of the optical pumping duration is important to prevent excess heating of the launched clouds, and the quarter-wave plate orientation is important so that the light causes the correct optical transitions to pump the atoms into the weak-field seeking state of $5^2S_{1/2}|F=3, m_F=3\rangle$. Both aspects were optimised empirically.

The baseball coil was used, as described above in section 6.1.1, to optimise the optical pumping process, with a magnetic pulse duration of 20 ms. The magnetic pulse was turned on 105 ms after launch, with a current of 947 ± 5 A in the baseball coil. The peak pixel count of the image of the focussed cloud corresponded to a peak in atom density. The atoms in the launched cloud will have some distribution in m_F states. Without optical pumping, the WFS states would be focussed, the strong-field-seeking

(SFS) states would be defocused and the $m_F = 0$ states would be unperturbed by the magnetic impulse from the baseball coil. Only be pumping all the atoms into the $5^2S_{1/2}|F=3, m_F=3\rangle$ state, i.e. the extreme WFS state, can the cloud density, and hence the peak pixel count, be maximised, since different WFS states would be focussed at different times.

Figure 6.7 shows a plot of the orientation of the quarter-wave plate (shown in Figure 2.19 of chapter 2), (the orientation being defined as the angle of the fast-axis of the wave-plate relative to the (linear) light incident on the wave-plate). The wave-plate was set at the angle which gave the peak pixel count.

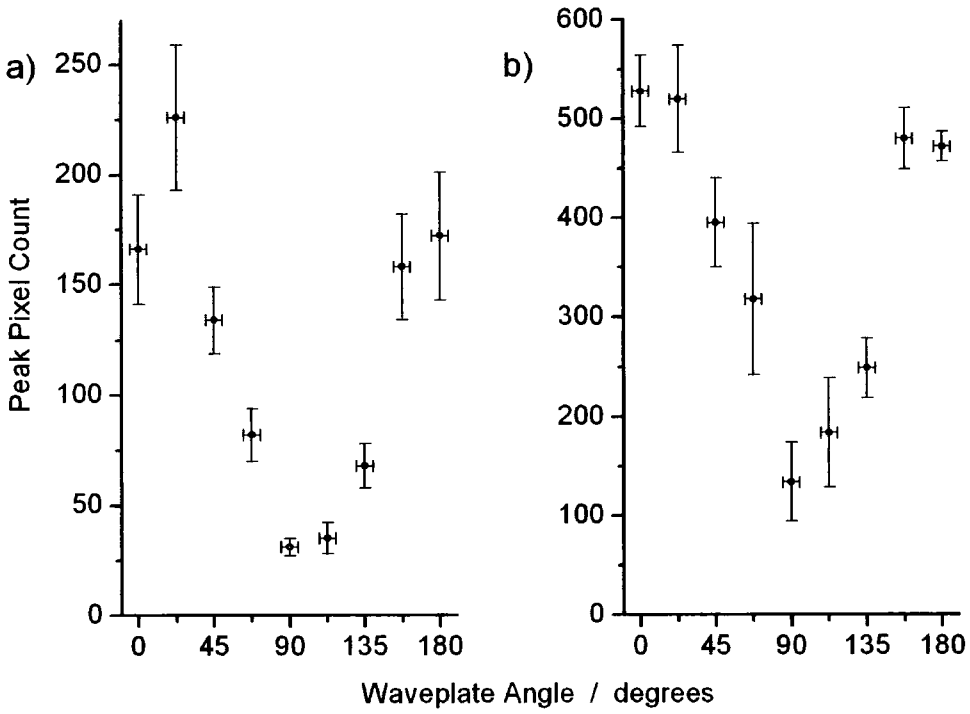

Figure 6.7. Optimisation of the orientation of the quarter-wave plate for optical pumping. Graph of Peak Pixel Count against angle of the fast axis of the quarter-wave plate used in the optical pumping beam. 0° and 90° degrees are (approximately) the points where the incident (linearly polarised) light is made circularly polarised. a) the peak pixel count from images of focussed clouds 'binned' to show the vertical profile. b) the peak pixel count from images of focussed clouds 'binned' to show the horizontal profile. All data points were taken under the same conditions, with only the orientation of the wave-plate altered. The experimental details are described in the main text. Each data point is the mean of three measurements and the error bars are the standard error of those measurements.

Figure 6.8 shows a graph of peak pixel count against the length of time that the atom cloud is exposed to the optical pumping beam, (the optical pumping pulse duration).

If the pulse is does not last for a sufficient time, the atomic population will not be pumped maximally into the $5^2S_{1/2}|F=3,m_F=3\rangle$ state. If the pulse lasts too long, the atom cloud will undergo radiative heating and the peak pixel count will decrease from its maximum value. The optimum optical pumping pulse duration was found to be approximately 50 μs.

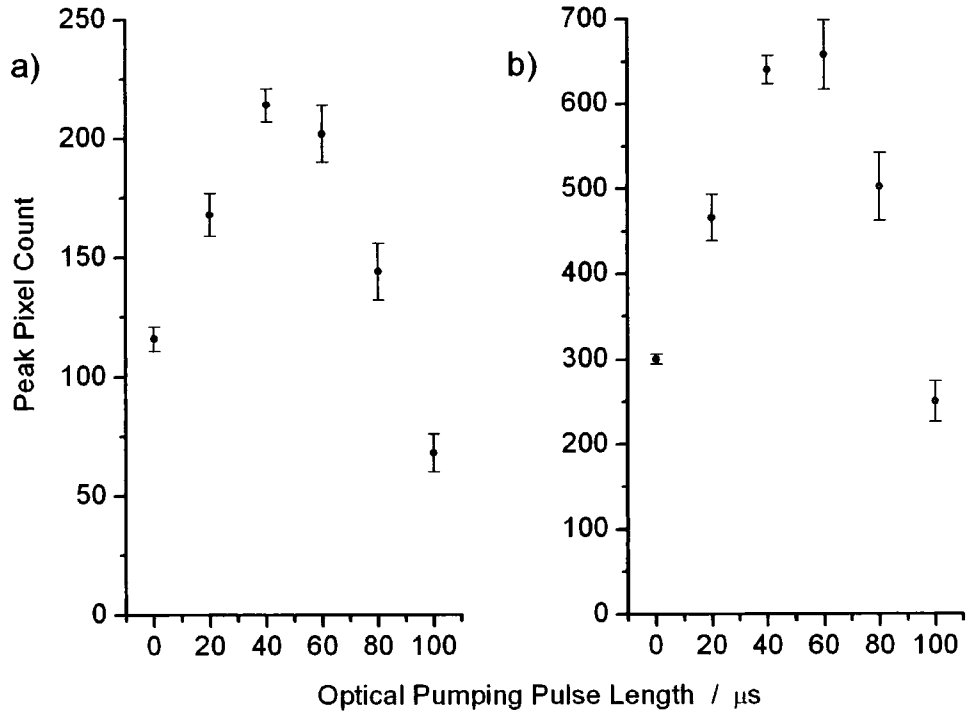

Figure 6.8. Graph of Peak Pixel Count against optical pumping pulse duration. a) and b) show the peak pixel count from the 'binned' vertical and horizontal profiles, respectively. The optical pumping light was derived from a 350 μW, vertically propagating, retro-reflected beam which is detailed in section 2.1.11. The optimum optical pulse duration was found to be approximately 50 μs.

6.2
Change in MOT Laser Beams – Improved Launching

After the preliminary experimentation detailed in section 6.1, the MOT laser beams were changed to improve the moving molasses stage. In the previous moving molasses (section 2.2.3) launch frequencies equivalent to a height of 23.9 cm were required to observe (unfocussed) atoms at a height of 20.5 cm, which indicated that the moving molasses phase of the experiment was not working as well as it might. After improvements to the moving molasses stage (section 2.2.4) the results in the following sections were obtained. As a note, the optimum configuration for optical pumping and the imaging pulse length were found to be the same as that realised in section 6.1.

6.3
Determination of the Initial Cloud Widths

For analysis of the focussed clouds, it was important to discern the initial cloud standard deviations, σ_{x_0} and σ_{z_0}. Approximately 6×10^7 ^{85}Rb atoms were collected in the MOT, before undergoing the launching process describe in section 2.2.4. A central launch detuning of $\Delta = -2\pi \times 25$ MHz and an intensity of approximately 120 W m^{-2} were used for the launch beams, with a moving molasses ramp time $R = 3.0$ ms and a moving molasses constant time of $C = 1.0$ ms. Figure 6.9 shows an image (of duration 0.5 ms) of an atom cloud just after the launch beams had been turned off (i.e. after the end of the constant moving molasses time C introduced

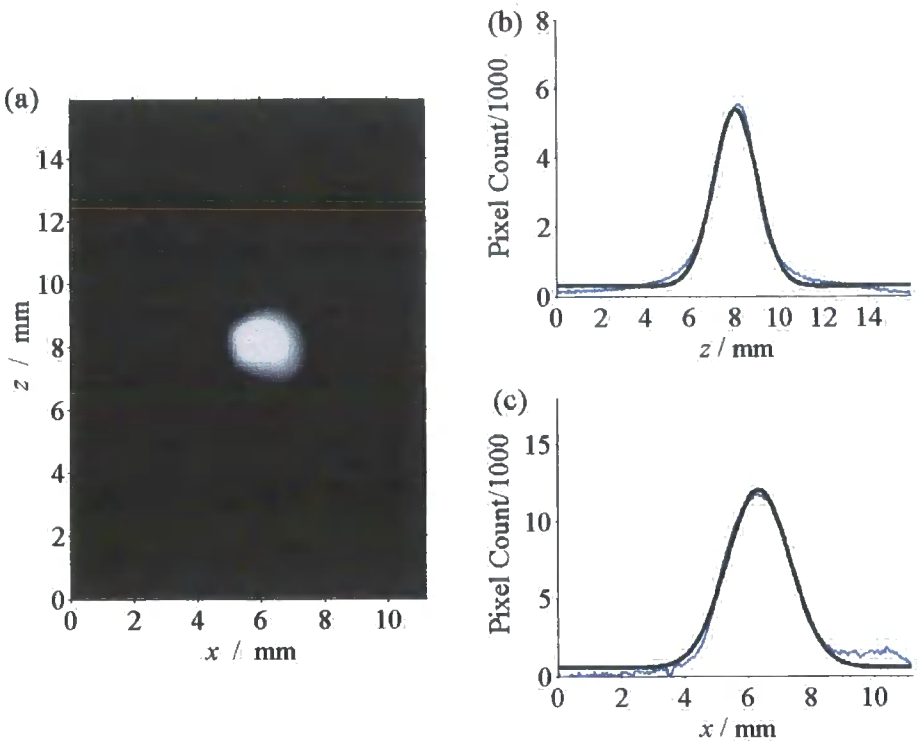

Figure 6.9. (a) Image of an atom cloud at the point the launch beams are switched off for the determination of σ_{x_0} and σ_{z_0}. The image was taken using the vertical imaging beam described in section 2.2.11 and had duration 0.5 ms. The mean of five measurements gave the initial cloud standard deviations of $\sigma_{x_0} = 1.01 \pm 0.01$ mm and $\sigma_{z_0} = 0.97 \pm 0.01$ mm. (b) and (c) show, respectively, the vertical and horizontal 'binned' profiles (blue line)), along with Gaussian fits (black line).

in section 2.2.4). The image was taken using the vertical imaging beam described in section 2.1.11. From a mean of five measurements, the initial cloud standard deviations were discerned to be $\sigma_{x_0} = 1.01 \pm 0.01$ mm and $\sigma_{z_0} = 0.97 \pm 0.01$ mm.

6.4
Results from the Four Configurations of the Baseball Lens

Images of focussed clouds and their widths are presented in this section for the four configurations of the Baseball Lens presented in chapter 5. Approximately 6×10^7 ^{85}Rb atoms were collected in the MOT, underwent a 10 ms optical molasses stage, before undergoing a moving molasses vertical launch at a speed of approximately 2 m s^{-1} to reach an apex approximately 20.5 cm above the MOT. Details of the launch process can be found in section 2.2.4. Here, a central launch detuning of $\Delta=-2\pi\times25$ MHz and an intensity of approximately 120 W m^{-2} were used for the moving molasses stage, with a moving molasses ramp time $R=3.0$ ms and a moving molasses constant time of $C=1.0$ ms. The static molasses temperature using the central detuning and intensity of the launch was 25 ± 2 μK. 20 ms after the launch beams were extinguished (at the end of the moving molasses constant time C), an orientation magnetic-field of approximately 300 mG was applied for orientation of the atoms' magnetic dipoles. The orientation field was in the vertical direction. 5 ms after the orientation field was turned on, a 350 μW, retro-reflected, vertically propagating, optical pumping beam was turned on for 50 μs to pump the atoms into the weak-field-seeking $5^2S_{1/2}\left|F=3,m_F=3\right\rangle$ state. A JAI CV50-IR CCD camera and a 6 mW, retro-reflected, vertically propagating, imaging beam were used to take fluorescence images of the launched clouds at the apex of flight, 204 ms after launch. The image light pulse duration was 2 ms in each case.

The centre of the Baseball Lens was located 16.5 ± 0.2 cm above the MOT. The unfocussed cloud came to rest in (approximately) the centre of the image. For each pulsed magnetic lens duration τ, the lens turn-on time was adjusted to centre the focussed clouds in the image, which was taken 204 ms after launch. The area seen in the following images is $(x=18.1\text{mm})\times(z=25.8\text{mm})$.

6.4.1 The Baseball Coil Only

Figure 6.10 shows a sequence of images for varying magnetic pulse duration τ, using the baseball coil only (i.e. no bias coils). The current through the baseball was measured to be 947 ± 5 A, giving a total of $947 \times 9 = (852 \pm 4) \times 10$ Amp-turns. The focussed cloud shape evolves as the pulse duration τ is increased, showing a marked increase in peak pixel count from the case where $\tau = 0$ (i.e. a freely expanding cloud).

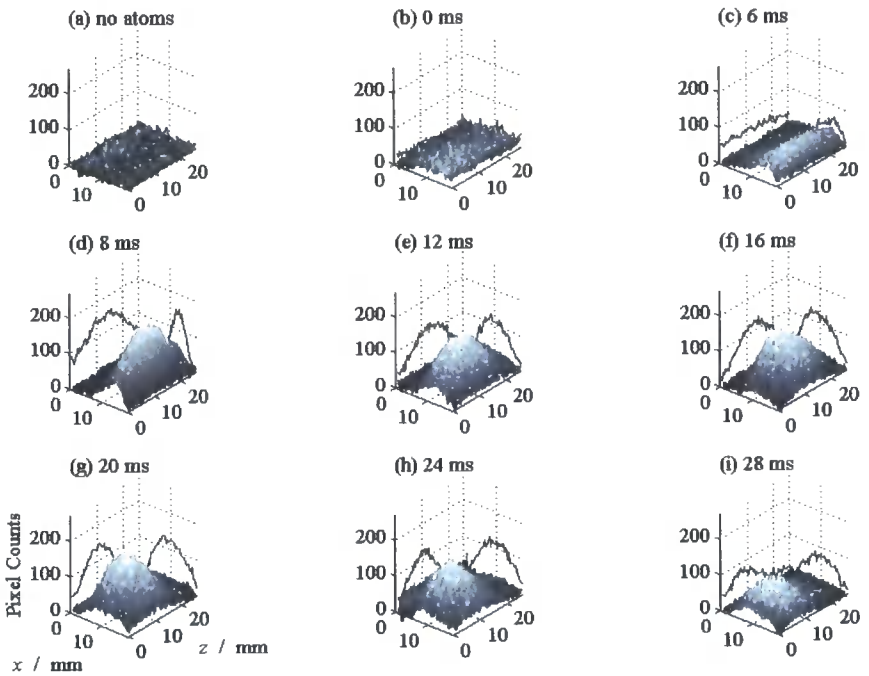

Figure 6.10. Varying pulse duration τ for the Baseball Coil only, i.e. no bias field. The centre of the lens was located 16.5 ± 0.2 cm vertically above the MOT (with the apex of flight of the centre of mass of the atom cloud was approximately 20.5 cm. (a) Image taken, but no atoms launched; (b) typical image of launched atoms, but with no lensing, i.e. $\tau = 0$; (c) - (i) the variation of τ from 6 ms to 28 ms (labelled). The z-direction is the vertical direction. The turn-on time of the lens was varied such that the cloud still reached the same apex. Each image displayed is a 6×12 ($x \times z$) super-pixelation of a raw image taken using a JAI CV50-IR CCD camera. For the baseball coil only, the angular frequencies were characterised to be $\omega_x = 50 \pm 2\ \mathrm{s}^{-1}$ and $\omega_z = 40 \pm 2\ \mathrm{s}^{-1}$, therefore the x-component of the cloud comes to a focus in the region between $\tau = 6$ and 12 ms, but the z-component has not focussed by this point. This tight radial focus means that the peak pixel count begins to reduce significantly for values of $\tau > 24$ ms, since the cloud rapidly becomes diffuse – as a consequence the ratio of signal to noise in the image makes it difficult to fit cloud widths in the z-direction, seen by the absence of data in Figure 6.11 for higher values of τ. Subsequently, it is difficult to ascertain the focus of the z-component for this lens configuration.

Figure 6.11 shows a plot of the standard deviation in the x and z-directions for the images shown in Figure 6.10 above (for the baseball coil only). The smallest measured standard deviation in the x-direction was 2.43 ± 0.07 mm ($\tau = 8$ ms), and the data indicate a minimum value of σ_x between $\tau = 6$ ms and $\tau = 12$ ms. The smallest measured standard deviation in the z-direction was 5.40 ± 0.06 mm ($\tau = 24$ ms). However, a low signal-to-noise ratio (due to the expansion of the cloud in the x-direction) meant that the standard deviation in the z-direction σ_z could not be ascertained for $\tau > 24$ ms. The initial cloud widths were measured to be $\sigma_{x_0} = 1.01 \pm 0.01$ mm and $\sigma_{z_0} = 0.97 \pm 0.01$ mm. The minimum value of σ_x at the apex of flight is 2.4 times the initial value.

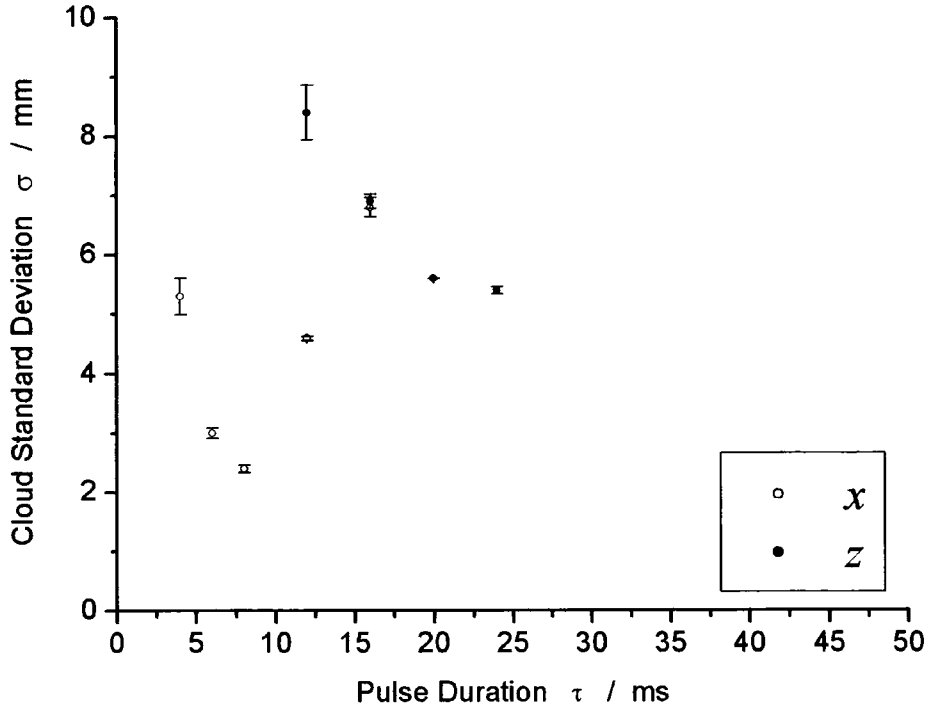

Figure 6.11. Variation of σ_x and σ_z with pulse duration τ for the baseball coil only. The smallest measured standard deviation in the x-direction was 2.43 ± 0.07 mm ($\tau = 8$ ms), and the data indicates a minimum value of σ_x between $\tau = 6$ ms and $\tau = 12$ ms. The smallest measured standard deviation in the z-direction was 5.40 ± 0.06 mm ($\tau = 24$ ms). However, a high signal-to-noise ratio (due to the expansion of the cloud in the x-direction) meant that the standard deviation in the z-direction σ_z cloud not be ascertained for $\tau > 24$ ms.

Figure 6.12 shows a plot of the volume of the cloud (calculated from the data in Figure 6.11) against the pulse duration τ. The volume is calculated as $\sigma_x^2 \sigma_z$. Since the actual volume is $\sigma_x \sigma_y \sigma_z$, an assumption is made that $\sigma_x = \sigma_y$, valid from the geometry and characterisation of the Baseball Lens. For some pulse durations it was not possible to ascertain both σ_x and σ_z due to the cloud being a significant fraction of the image size $(x = 18.1\text{mm}) \times (z = 25.8\text{mm})$. The maximum values available for measurement were $\sigma_x = 7$ mm and $\sigma_z = 9$ mm, chosen as the limits above which the Gaussian fitting done in LabVIEW became extremely erratic (due to an insufficient fraction of the Gaussian being present in the image). For values of τ where only one of the standard deviations was measured, the volume was calculated using the limit values ($\sigma_x = 7$ mm and $\sigma_z = 9$ mm) in place of the unmeasured standard deviation.

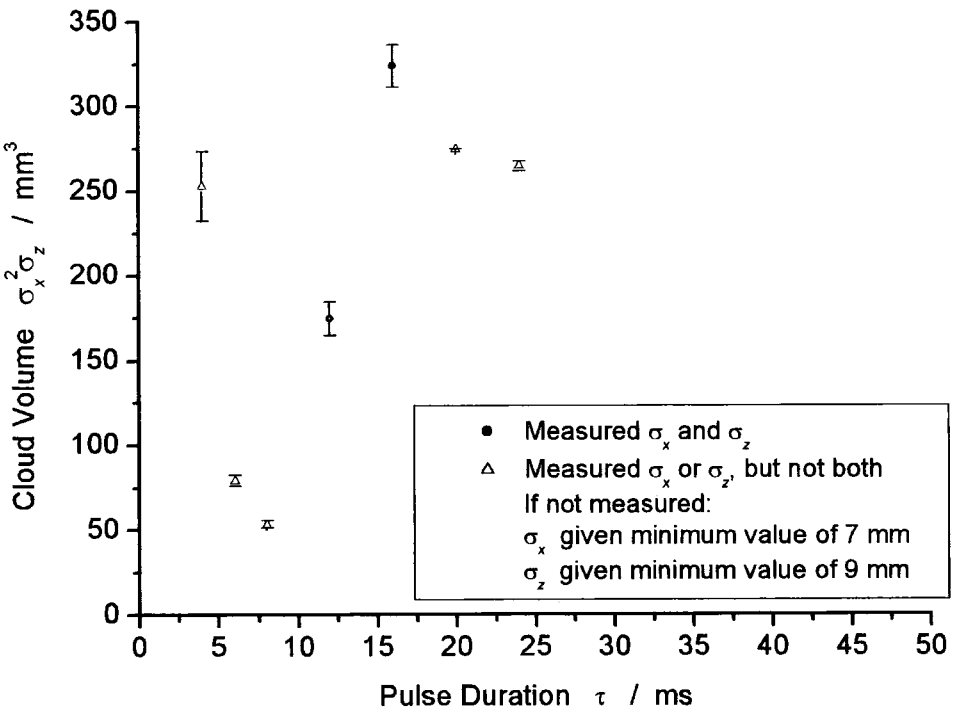

Figure 6.12. Variation of cloud volume $\sigma_x^2 \sigma_z$ with pulse duration τ. The volume is dominated by the variation of σ_x (shown in Figure 6.11). Due to the large difference between $\omega_x = 50 \pm 2\ \text{s}^{-1}$ and $\omega_z = 40 \pm 2\ \text{s}^{-1}$, there is little overlap between the measurement of σ_x and σ_z. For values of τ where only one of the standard deviations was measured, the volume was calculated using the measurement-limit values ($\sigma_x = 7$ mm and $\sigma_z = 9$ mm) in place of the unmeasured standard deviation.

The initial cloud widths were measured to be $\sigma_{x_0} = 1.01 \pm 0.01$ mm and $\sigma_{z_0} = 0.97 \pm 0.01$ mm, and hence the initial volume as $\sigma_{x_0}{}^2 \sigma_{z_0} = 0.99 \pm 0.02$ mm^3. The minimum (inferred) volume using the baseball coil only is approximately 50 mm^3. This compares well with the projected final volume of an unfocussed cloud of temperature 25 μK, approximately 1000 mm^3, representing a decrease in volume by a factor of 20.

6.4.2 R_{TUNE} Equal to Half R_{BIAS}

Figure 6.13 shows a sequence of images for varying magnetic pulse duration τ, using the Baseball Lens configuration of $R_{TUNE} = R_{BIAS} / 2$ (i.e. a third of the baseball coil current passed through the bias coils). The current through the baseball was 898 ± 4 A, and the current through the bias coils was 304 ± 2 A. The focussed cloud shape evolves as the pulse duration τ is increased, showing a marked increase in peak pixel count from the case where $\tau = 0$ (i.e. a freely expanding cloud).

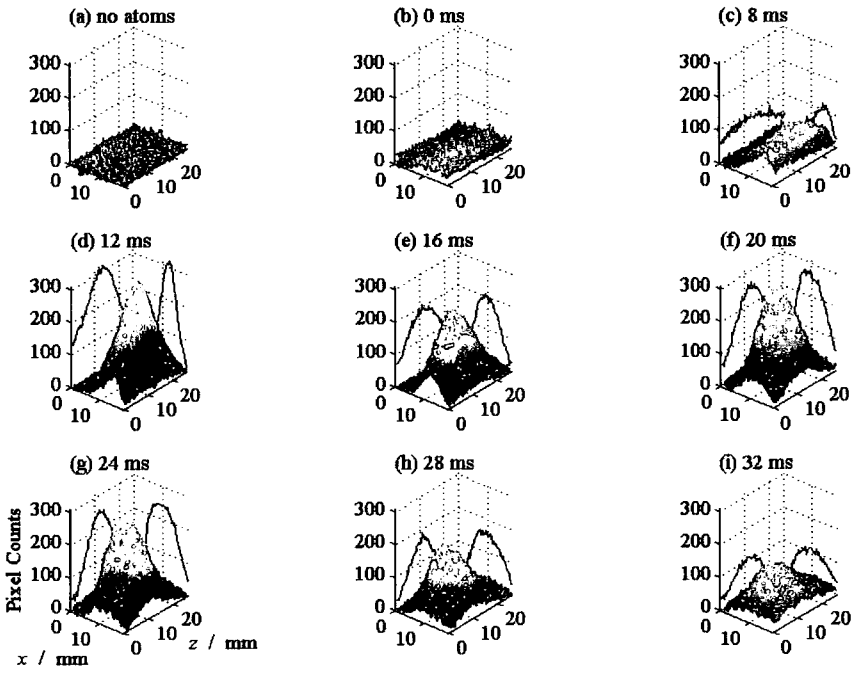

Figure 6.13. Varying pulse duration τ for the Baseball Lens with $R_{TUNE} = R_{BIAS}/2$. The centre of the lens was located 16.5 cm vertically above the MOT (with the apex of flight of the centre of mass of the atom cloud at 20.5 cm. (a) Image taken, but no atoms launched; (b) typical image of launched atoms, but with no lensing, i.e. $\tau = 0$; (c) - (i) the variation of τ from 8 ms to 32 ms (labelled). The turn-on time of the lens was varied such that the cloud still reached the same apex. Each image displayed is a 6×12 ($x \times z$) super-pixelation of a raw image taken using a JAI CV50-IR CCD. For this configuration, the angular frequencies were characterised to be $\omega_x = 41 \pm 2$ s^{-1} and $\omega_z = 39 \pm 2$ s^{-1}. The x-component of the cloud comes to a focus in the region between $\tau = 8$ and 16 ms, but the z-component has not focussed by this point. This tight radial focus means that the peak pixel count begins to reduce significantly for values of $\tau > 28$ ms, since the cloud rapidly becomes diffuse – as a consequence the ratio of signal to noise in the image makes it difficult to fit cloud widths in the z-direction, seen by the absence of data in Figure 6.14 for higher values of τ. Subsequently, it is difficult to ascertain the focus of the z-component for this lens configuration, as in the case of using only the baseball coil only.

Figure 6.14 shows a plot of the standard deviation in the x and z-directions for the images shown in Figure 6.13 above (for the configuration of $R_{\mathrm{TUNE}} = R_{\mathrm{BIAS}} / 2$). The smallest measured standard deviation in the x-direction was 2.73 ± 0.03 mm ($\tau = 12$ ms), and the data indicate a minimum value of σ_x between $\tau = 8$ ms and $\tau = 16$ ms. The smallest measured standard deviation in the z-direction was 4.83 ± 0.03 mm ($\tau = 36$ ms). However, a low signal-to-noise ratio (due to the expansion of the cloud in the x-direction) meant that the standard deviation in the z-direction σ_z could not be ascertained for $\tau > 36$ ms. The minimum value of σ_x at the apex of flight is 2.7 times the initial value.

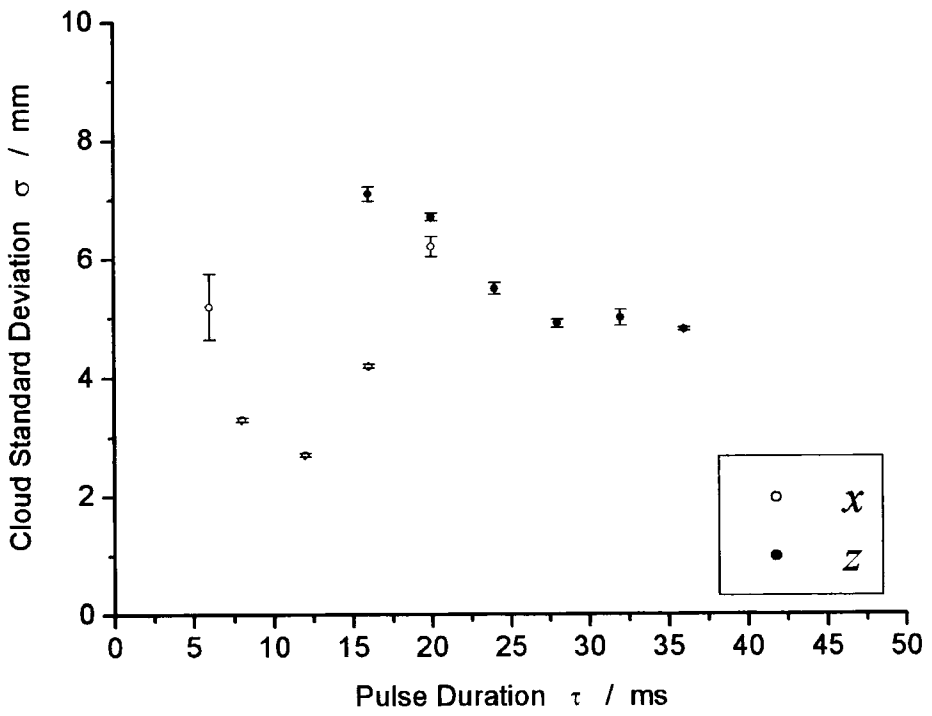

Figure 6.14. Variation of σ_x and σ_z with pulse duration τ for Baseball Lens with $R_{\mathrm{TUNE}} = R_{\mathrm{BIAS}}/2$. The smallest measured standard deviation in the x-direction was 2.73 ± 0.03 mm ($\tau = 12$ ms), and the data indicates a minimum value of σ_x between $\tau = 8$ ms and $\tau = 16$ ms. The smallest measured standard deviation in the z-direction was 4.83 ± 0.03 mm ($\tau = 36$ ms). However, a high signal-to-noise ratio (due to the expansion of the cloud in the x-direction) meant that the standard deviation in the z-direction σ_z not be ascertained for $\tau > 36$ ms.

Figure 6.15 shows a plot of the volume of the cloud (calculated from the data in Figure 6.14) against the pulse duration τ, using the lens configuration of $R_{\mathrm{TUNE}} = R_{\mathrm{BIAS}} / 2$.

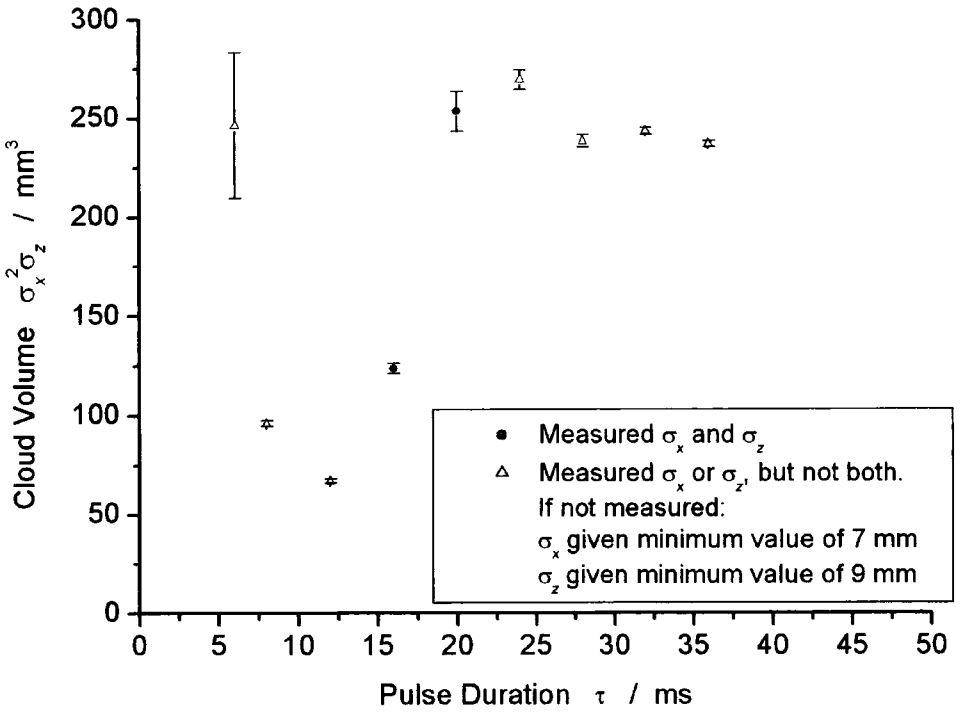

Figure 6.15. Variation of cloud volume $\sigma_x^2\sigma_z$ with pulse duration τ for the Baseball Lens with $R_{\mathrm{TUNE}} = R_{\mathrm{BIAS}}/2$. The volume is dominated by the variation of σ_x (shown in Figure 6.14). For values of τ where only one of the standard deviations was measured, the volume was calculated using the measurement-limit values ($\sigma_x = 7$ mm and $\sigma_z = 9$ mm) in place of the unmeasured standard deviation.

The initial volume $\sigma_{x_0}^2\sigma_{z_0} = 0.99 \pm 0.02$ mm^3. The minimum (inferred) volume of a focussed cloud using the lens configuration of $R_{\mathrm{TUNE}} = R_{\mathrm{BIAS}} / 2$ is approximately 70 mm^3. This compares well with the projected final volume of an unfocussed cloud of temperature 25 μK, approximately 1000 mm^3, representing a decrease in volume by a factor of 14.

6.4.3 R_{TUNE} Equal to R_{BIAS}

Figure 6.16 shows a sequence of images for varying magnetic pulse duration τ, using the Baseball Lens configuration with $R_{TUNE} = R_{BIAS}$ (i.e. half the current through the baseball coil passes through the bias coils). The current through the baseball was 872 ± 4 A, and the current through the bias coils was 446 ± 3 A. The focused cloud shape evolves as the pulse duration τ is increased, showing a marked increase in peak pixel count from the case where $\tau = 0$.

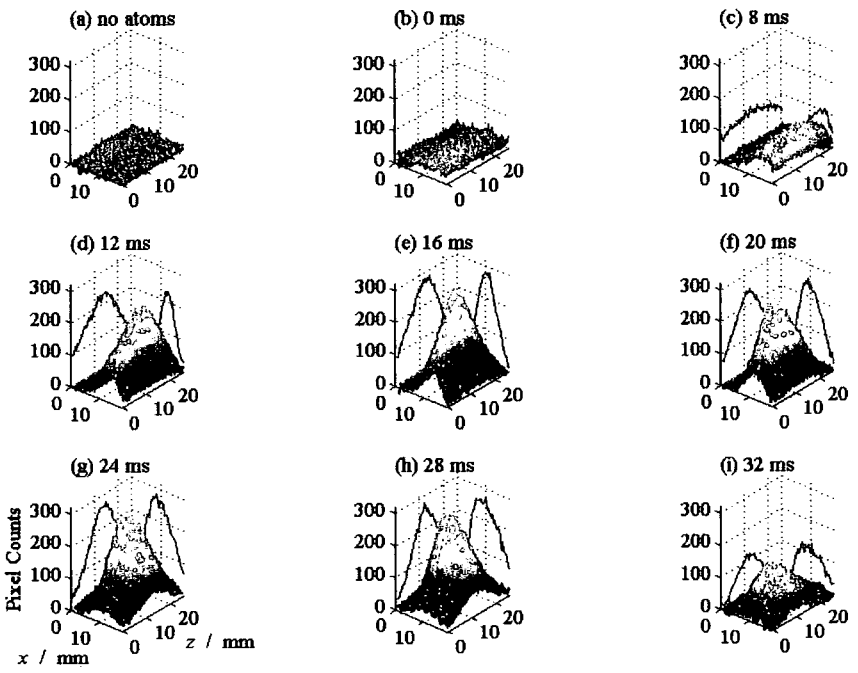

Figure 6.16. Varying pulse duration τ for the Baseball Lens with $R_{TUNE} = R_{BIAS}$. The centre of the lens was located 16.5 cm vertically above the MOT (with the apex of flight of the centre of mass of the atom cloud at 20.5 cm. (a) Image taken, but no atoms launched; (b) typical image of launched atoms, but with no lensing, i.e. $\tau = 0$; (c) - (i) the variation of τ from 8 ms to 32 ms (labelled). The turn-on time of the lens was varied such that the cloud still reached the same apex. Each image displayed is a 6×12 ($x \times z$) super-pixelation of a raw image taken using a JAI CV50-IR CCD. For this configuration of the Baseball Lens, the angular frequencies were characterised to be $\omega_x = 38 \pm 1$ s^{-1} and $\omega_z = 39 \pm 1$ s^{-1}, therefore the x-component of the cloud comes to a focus in the region between $\tau = 12$ and 16 ms, but the z-component has not focussed by this point. The z-component actually comes to focus between $\tau = 36$ and 40 ms.

Figure 6.17 shows a plot of the standard deviation in the x and z-directions for the images shown in Figure 6.16 above (for the lens configuration $R_{TUNE} = R_{BIAS}$). The

smallest measured standard deviation in the x-direction was 2.77 ± 0.03 mm ($\tau = 12$ ms), and the data indicate a minimum value of σ_x between $\tau = 8$ ms and $\tau = 16$ ms. The smallest measured standard deviation in the z-direction was 4.57 ± 0.03 mm ($\tau = 36$ ms), and the data indicate a minimum value of σ_z between $\tau = 36$ ms and $\tau = 40$ ms. The initial cloud widths were measured to be $\sigma_{x_0} = 1.01 \pm 0.01$ mm and $\sigma_{z_0} = 0.97 \pm 0.01$ mm, representing focussed cloud sizes of 2.7 and 4.7 times the initial sizes in the horizontal and vertical directions respectively.

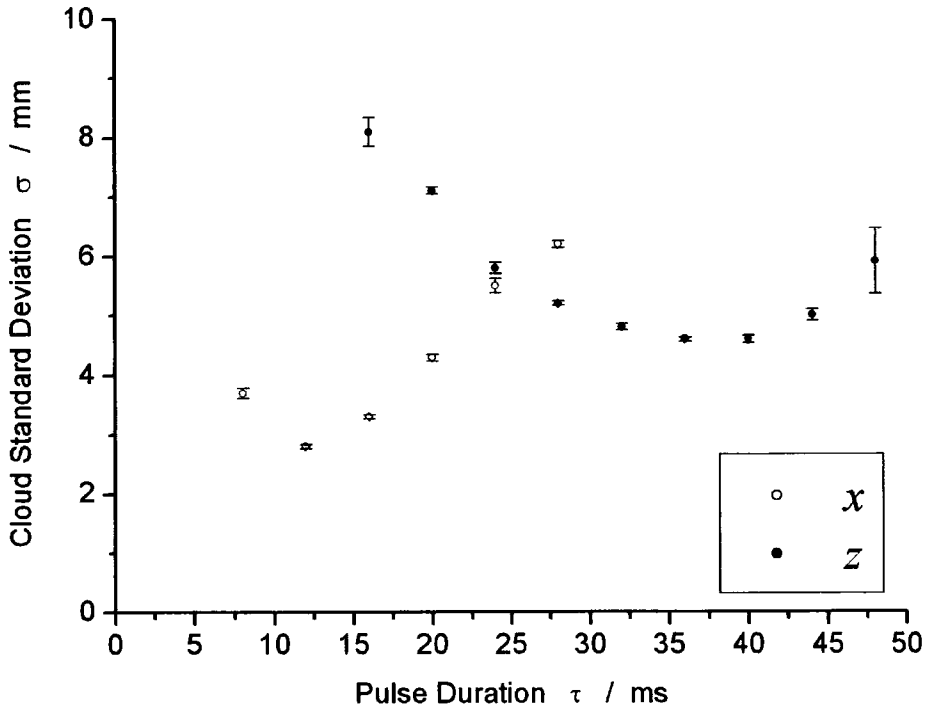

Figure 6.17. Variation of σ_x and σ_z with pulse duration τ for Baseball Lens with $R_{\text{TUNE}} = R_{\text{BIAS}}$. The smallest measured standard deviation in the x-direction was 2.77 ± 0.03 mm ($\tau = 12$ ms), and the data indicates a minimum value of σ_x between $\tau = 8$ ms and $\tau = 16$ ms. The smallest measured standard deviation in the z-direction was 4.57 ± 0.03 mm ($\tau = 36$ ms), and the data indicates a minimum value of σ_z between $\tau = 36$ ms and $\tau = 40$ ms.

Figure 6.18 shows a plot of the volume of the cloud (calculated from the data in Figure 6.17) against the pulse duration τ.

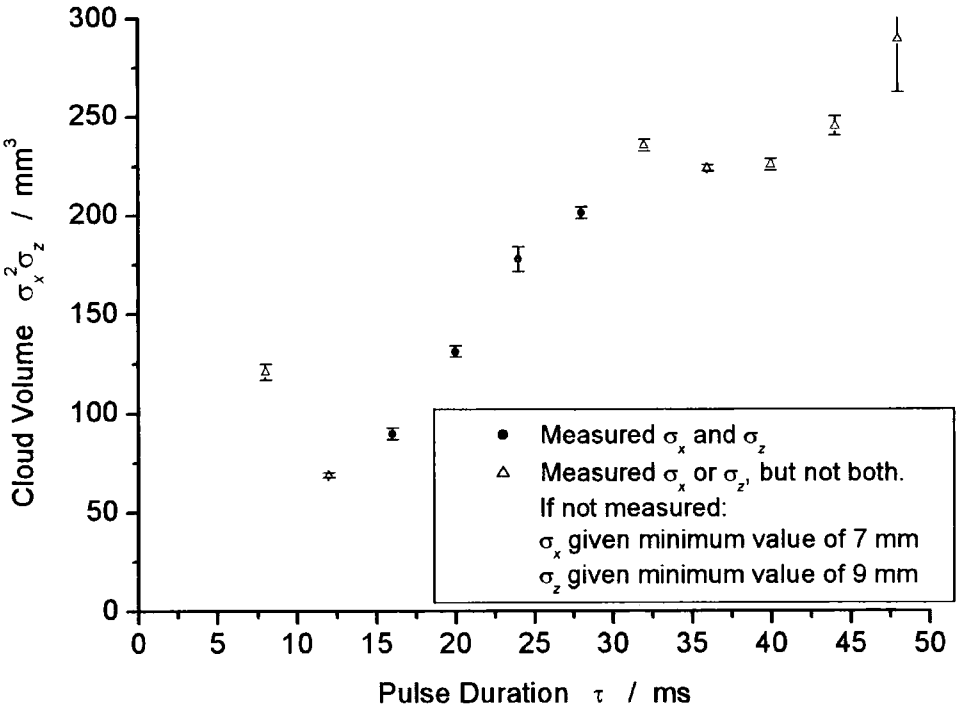

Figure 6.18. Variation of cloud volume $\sigma_x^2\sigma_z$ with pulse duration τ for the Baseball Lens with $R_{\mathrm{TUNE}} = R_{\mathrm{BIAS}}$. The volume is dominated by the variation of σ_x (shown in Figure 6.17). For values of τ where only one of the standard deviations was measured, the volume was calculated using the measurement- limit values ($\sigma_x = 7$ mm and $\sigma_z = 9$ mm) in place of the unmeasured standard deviation.

The initial volume $\sigma_{x_0}^2\sigma_{z_0} = 0.99 \pm 0.02$ mm^3. The minimum (inferred) volume using the lens configuration of $R_{\mathrm{TUNE}} = R_{\mathrm{BIAS}}$ is approximately 70 mm^3. This compares well with the projected final volume of an unfocussed cloud of temperature 25 μK, approximately 1000 mm^3, representing a decrease in volume by a factor of 14.

6.4.4 R_{TUNE} Removed

Figure 6.19 shows a sequence of images for varying magnetic pulse duration τ, using the Baseball Lens configuration of R_{TUNE} Removed (i.e. all the current through the baseball coil passes through the bias coils). The current through the Baseball Lens was measured to be 832 ± 4 A. The focussed cloud shape evolves as the pulse duration τ is increased, showing a marked increase in peak pixel count from the case where $\tau = 0$.

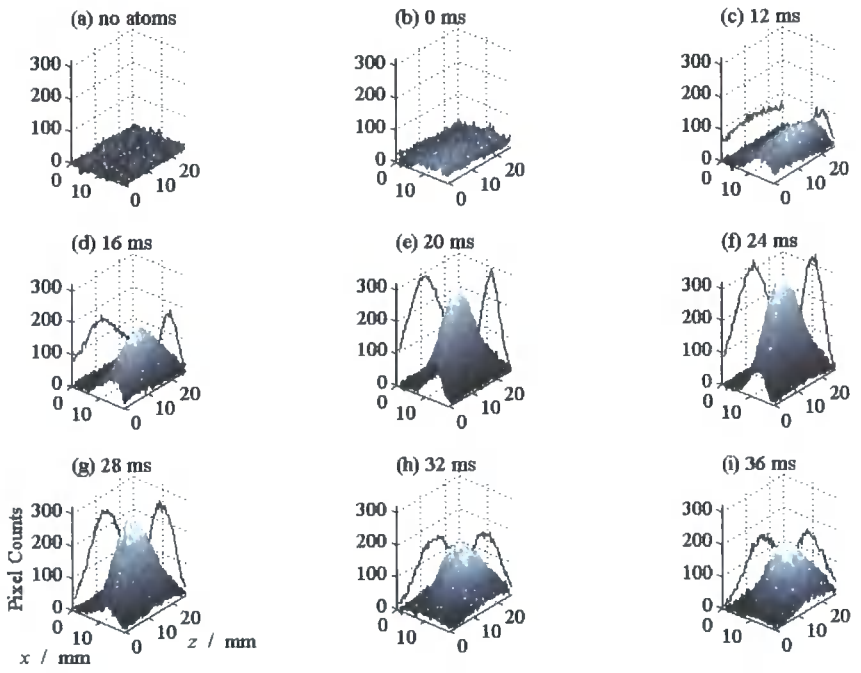

Figure 6.19. Varying pulse duration τ for the Baseball Lens with R_{TUNE} removed. The centre of the lens was located 16.5 cm vertically above the MOT (with the apex of flight of the centre of mass of the atom cloud at 20.5 cm. (a) Image taken, but no atoms launched; (b) typical image of launched atoms, but with no lensing, i.e. $\tau = 0$; (c) - (i) the variation of τ from 12 ms to 36 ms (labelled). The turn-on time of the lens was varied such that the cloud still reached the same apex. Each image displayed is a 6×12 $(x \times z)$ super-pixelation of a raw image taken using a JAI CV50-IR CCD. For this configuration of the Baseball Lens, the angular frequencies were characterised to be $\omega_x = 30 \pm 1\,s^{-1}$ and $\omega_z = 38 \pm 1\,s^{-1}$. The x-component of the cloud comes to a focus in the region between $\tau = 16$ and 20 ms, but the z-component has not focussed by this point. The z-component actually comes to focus between $\tau = 28$ and 32 ms.

Figure 6.20 shows a plot of the standard deviation in the x and z-directions for the images shown in Figure 6.19 above (for the lens configuration R_{TUNE} Removed). The

smallest measured standard deviation in the x-direction was 2.83 ± 0.03 mm ($\tau = 16$ ms), and the data indicate a minimum value of σ_x between $\tau = 16$ ms and $\tau = 20$ ms. The smallest measured standard deviation in the z-direction was 6.17 ± 0.07 mm ($\tau = 28$ ms), and the data indicate a minimum value of σ_z between $\tau = 28$ ms and $\tau = 32$ ms. The initial cloud widths were measured to be $\sigma_{x_0} = 1.01 \pm 0.01$ mm and $\sigma_{z_0} = 0.97 \pm 0.01$ mm, representing focussed cloud sizes of 2.8 and 6.4 times the initial sizes in the horizontal and vertical directions respectively.

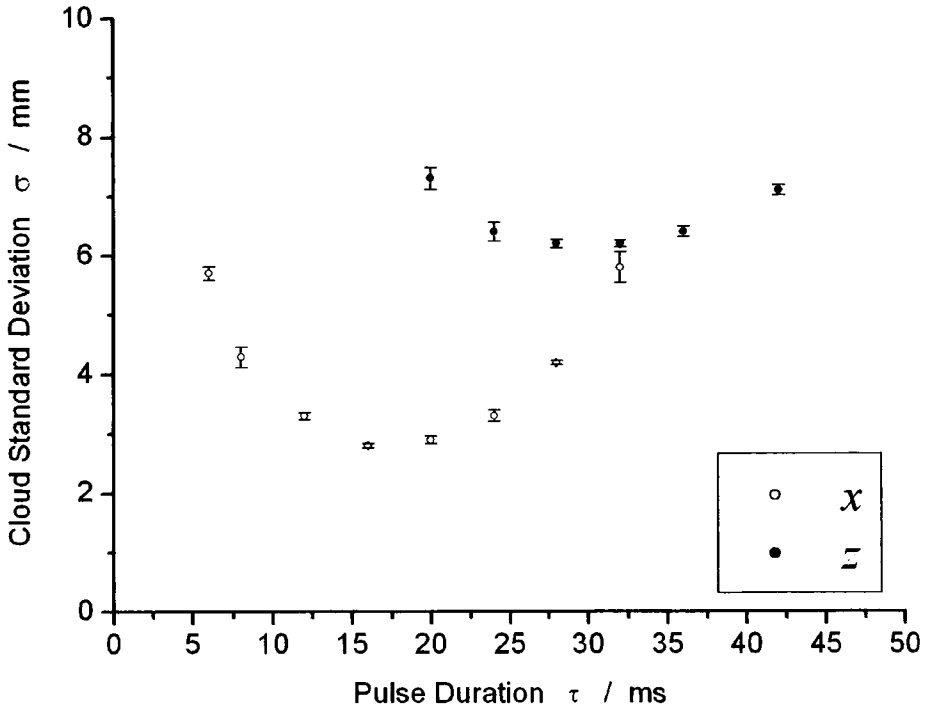

Figure 6.20. Variation of σ_x and σ_z with pulse duration τ for the Baseball Lens with R_{TUNE} removed. The smallest measured standard deviation in the x-direction was 2.83 ± 0.03 mm ($\tau = 16$ ms), and the data indicates a minimum value of σ_x between $\tau = 16$ ms and $\tau = 20$ ms. The smallest measured standard deviation in the z-direction was 6.17 ± 0.07 mm ($\tau = 28$ ms), and the data indicates a minimum value of σ_x between $\tau = 28$ ms and $\tau = 32$ ms. Although the minimum in σ_x and the minimum in σ_z do not occur at for the same pulse duration τ, this figure clearly shows 3-dimensional focusing with a single magnetic impulse.

Figure 6.21 shows a plot of the volume of the cloud (calculated from the data in Figure 6.20) against the pulse duration τ.

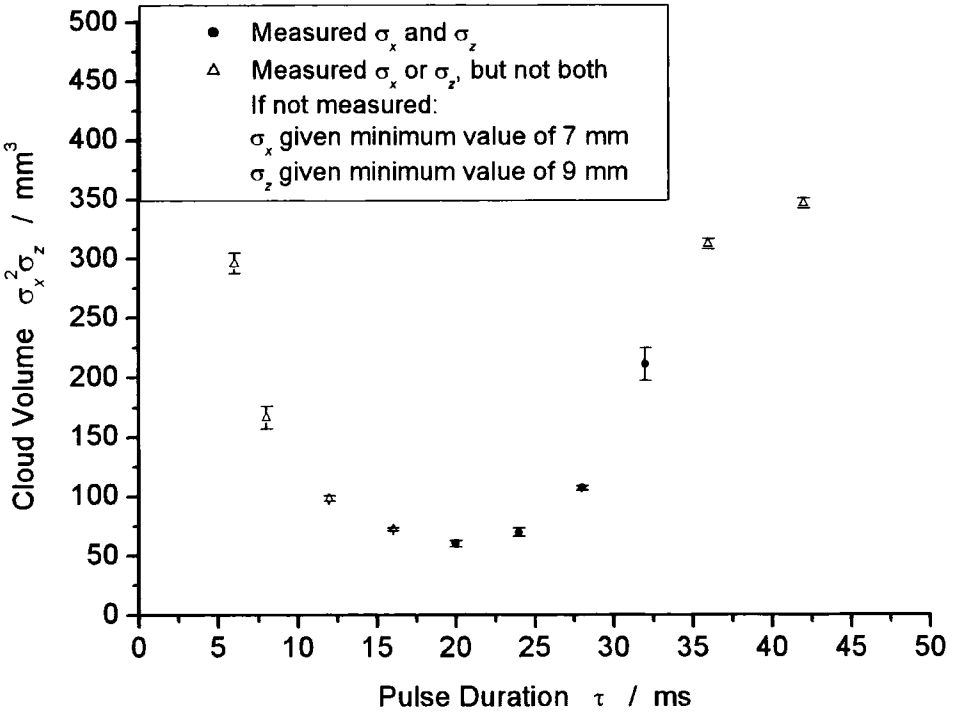

Figure 6.21. Variation of cloud volume $\sigma_x{}^2\sigma_z$ with pulse duration τ for the Baseball Lens with R_{TUNE} removed. For values of τ where only one of the standard deviations was measured, the volume was calculated using the measurement-limit values ($\sigma_x = 7$ mm and $\sigma_z = 9$ mm) in place of the unmeasured standard deviation. The measured minimum volume using the lens configuration with R_{TUNE} removed is approximately $\sigma_x{}^2\,\sigma_z = 60 \pm 3$ mm^3.

The initial volume $\sigma_{x_0}{}^2\,\sigma_{z_0} = 0.99 \pm 0.02$ mm^3. The measured minimum volume using the lens configuration with R_{TUNE} removed was $\sigma_x{}^2\,\sigma_z = 60 \pm 3$ mm^3. This measured volume compares very favourably with the projected final volume of an unfocussed cloud of temperature 25 μK, approximately 1000 mm^3, representing a decrease in volume by a factor of 17.

6.4.5 The Trends of the Results

The following trends are observed in the data:

- 3-dimensional magnetic focusing with a single magnetic impulse has been observed, most notably in the lens configuration with R_{TUNE} removed, as shown in Figure 6.20.
- As the radial angular frequency was decreased (by increasing the current in the bias coils), the value of τ required to produce a minimum in σ_x increased.
- The minimum (measured) volume of a focussed cloud was 60 ± 3 mm^3, which should be compared to the initial measured volume of 0.99 ± 0.02 mm^3, where the volume is given by $\sigma_x^{\,2}\,\sigma_z$.
- The minimum measured value of the standard deviation in the *x*-direction σ_x, of a focussed cloud, was 2.43 ± 0.07 mm. This was achieved with the Baseball Lens configuration utilising only the baseball coil with a pulse duration $\tau = 8$ ms. The initial cloud size in the *x*-direction was measured to be $\sigma_{x_0} = 1.01 \pm 0.01$ mm.
- The minimum measured value of the standard deviation in the *z*-direction σ_z, of a focussed cloud, was 4.57 ± 0.03 mm. This was achieved with the Baseball Lens configuration with $R_{\text{TUNE}} = R_{\text{BIAS}}$ and a pulse duration of $\tau = 36$ ms. The initial cloud size in the *z*-direction was measured to be $\sigma_{z_0} = 0.97 \pm 0.01$ mm.

6.5
$\mathcal{ABCD}$ - Matrix Analysis

The data presented in section 6.4 were analysed using an analytical matrix approach with the system matrix $M_{\mathcal{ABCD}}$ for a finite-duration harmonic lens, presented in section 4.2, i.e.,

$$M_{\mathcal{ABCD}} = \begin{pmatrix} \mathcal{A} & \mathcal{B} \\ \mathcal{C} & \mathcal{D} \end{pmatrix} = \begin{pmatrix} 1 & t_2 + \frac{\tau'}{2} \\ 0 & 1 \end{pmatrix} \begin{pmatrix} 1 & 0 \\ -\omega \sin \omega\tau & 1 \end{pmatrix} \begin{pmatrix} 1 & t_1 + \frac{\tau'}{2} \\ 0 & 1 \end{pmatrix},$$

where t_1 is the free expansion time before the lens, t_2 is the free expansion time after the lens, $\tau' = \frac{2}{\omega} \tan\left(\frac{\omega\tau}{2}\right)$, and τ is the physical duration of the lens of angular frequency ω.

The total physical time of flight is given by the launch height of 20.5 cm as $T = 204$ ms, with the lens located 16.5 cm above the MOT. In the experiment, the centre-of-mass of the atom cloud reaches the centre of the lens 114 ms after launch. In the analysis, the lens is centred (in time) at 114 ms.

The cloud spatial standard deviations from the experiment were measured at the apex of flight, 204 ms after launch. The theoretical final cloud spatial standard deviation σ_{x_f} in the matrix approach is given by,

$$\sigma_{x_f}{}^2 = \left(\mathcal{A}\sigma_{x_0}\right)^2 + \left(\mathcal{B}\sigma_{v_{x_0}}\right)^2,$$

where σ_{x_0} and $\sigma_{v_{x_0}}$ are the initial spatial standard deviation and the initial velocity standard deviation, respectively, in the x-direction. The equivalent is true for the z-direction. The initial spatial standard deviations were measured to be $\sigma_{x_0} = 1.01 \pm 0.01$ mm and $\sigma_{z_0} = 0.97 \pm 0.01$ mm. Using a temperature of 25 μK (the static optical molasses temperature of the launch parameters), gives a value for the initial velocity standard deviation $\sigma_{v_{x_0}} = 4.9$ cm s^{-1}.

Figure 6.22 shows a theoretical graph of the spatial standard deviation of a cloud against pulse duration τ for various values of angular frequency ω. Using the angular frequencies deduced for the four configurations of the Baseball Lens in section 5.5, the variation in cloud spatial standard deviation with the magnetic pulse duration τ can be compared to the experimental data. This section goes on to

compare the experimental data presented in section 6.4 to the predicted behaviour of the spatial standard deviation, as well as to fit values of the angular frequency ω to the data using the matrix approach.

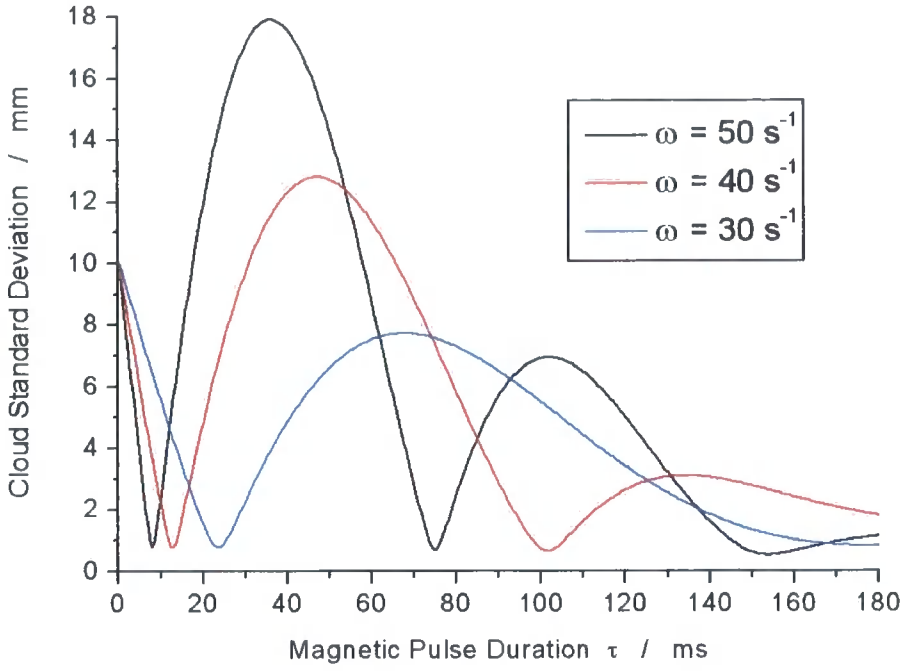

Figure 6.22. Graph of the theoretical variation of (position) standard deviation (at $T = 204$ ms) against pulse duration τ for various values of lens angular frequency ω. After 180 ms, the free expansion time after the lens $t_2 = 0$. This theory does not account for the centre of mass movement of the atom cloud in the z-direction. The centre of mass of the atom cloud is moving at approximately 1 m s^{-1}, and decelerating, in the region of the lens. Using a temperature of 25 μK gives the cloud standard deviation for $\tau = 0$ as 10 mm. In the case of $\omega = 50$ s^{-1}, the size of the cloud can be made to be significantly larger (whilst still using a converging lens) than the unfocussed cloud. For a given ω several maxima and minima can be observed, which correspond to oscillations within the (harmonic) magnetic potential formed by the lens.

6.5.1 Horizontal Cloud Size: Predicted and Fitted

Figure 6.23 shows the experimental data for the change in cloud standard deviation in the x-direction with pulse duration τ using the Baseball Lens configured as only the baseball coil. The matrix theory prediction using the characterised angular frequency $\omega_x = 50$ s^{-1} is plotted against the experimental data, along with a χ^2 fit to the data using the matrix theory. Only allowing the angular frequency ω to vary for the fit

gave a value of $\omega_x = 50$ s^{-1}. Gaining an error on this fit was compromised by a large reduced χ^2 value. However, observation of Figure 6.23 shows that the experimental data is in good agreement with the matrix prediction. Also allowing the initial temperature of the cloud to vary produced a fit of 40 μK and $\omega_x = 48$ s^{-1}.

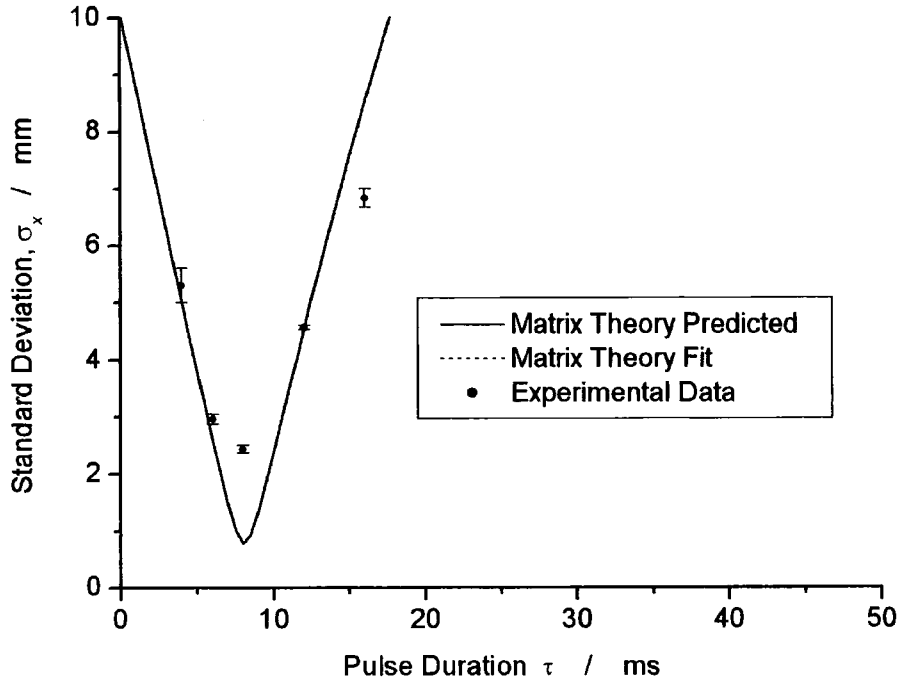

Figure 6.23. Matrix theory prediction and fit to the experimental standard deviation in the x-direction when using the baseball coil only. The matrix theory prediction using the characterised angular frequency $\omega_x = 50$ s^{-1} is plotted against the experimental data, along with a χ^2 fit to the data using the matrix theory. Only allowing the angular frequency ω to vary for the fit gave a value of $\omega_x = 50$ s^{-1}.

Figures 6.24, 6.25 and 6.26 show the same plots as in Figure 6.23, but for the other three configurations of the Baseball Lens. For the configuration $R_{\text{TUNE}} = R_{\text{BIAS}} / 2$, the predicted angular frequency is $\omega_x = 41$ s^{-1} and the fitted angular frequency is $\omega_x = 44$ s^{-1}. With $R_{\text{TUNE}} = R_{\text{BIAS}}$, the predicted angular frequency is $\omega_x = 38$ s^{-1} and the fitted angular frequency is $\omega_x = 39$ s^{-1}. Finally, the lens configuration where R_{TUNE} is removed was characterised to have an angular frequency of $\omega_x = 30$ s^{-1} and the χ^2 fit gave an angular frequency of $\omega_x = 30$ s^{-1}. In each case, allowing the temperature to vary produced little change in the fitted angular frequency.

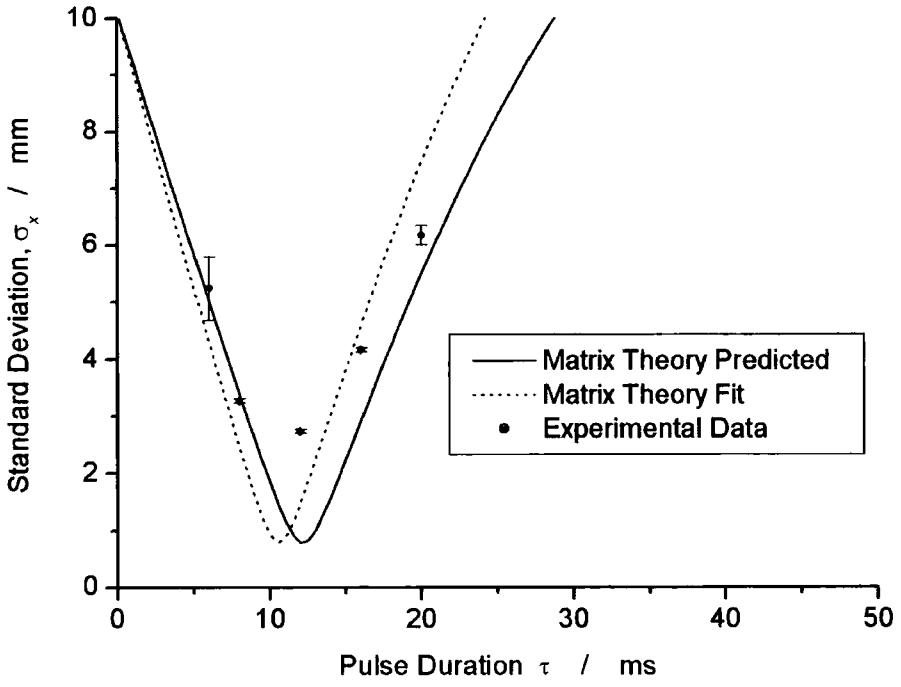

Figure 6.24. Matrix theory prediction and fit to the experimental standard deviation in the x-direction when using the Baseball Lens configured with $R_{\text{TUNE}} = R_{\text{BIAS}} / 2$. The matrix theory prediction using the characterised angular frequency $\omega_x = 41\,\text{s}^{-1}$ is plotted against the experimental data, along with a χ^2 fit to the data using the matrix theory. Only allowing the angular frequency ω to vary for the fit gave a value of $\omega_x = 44\ \text{s}^{-1}$.

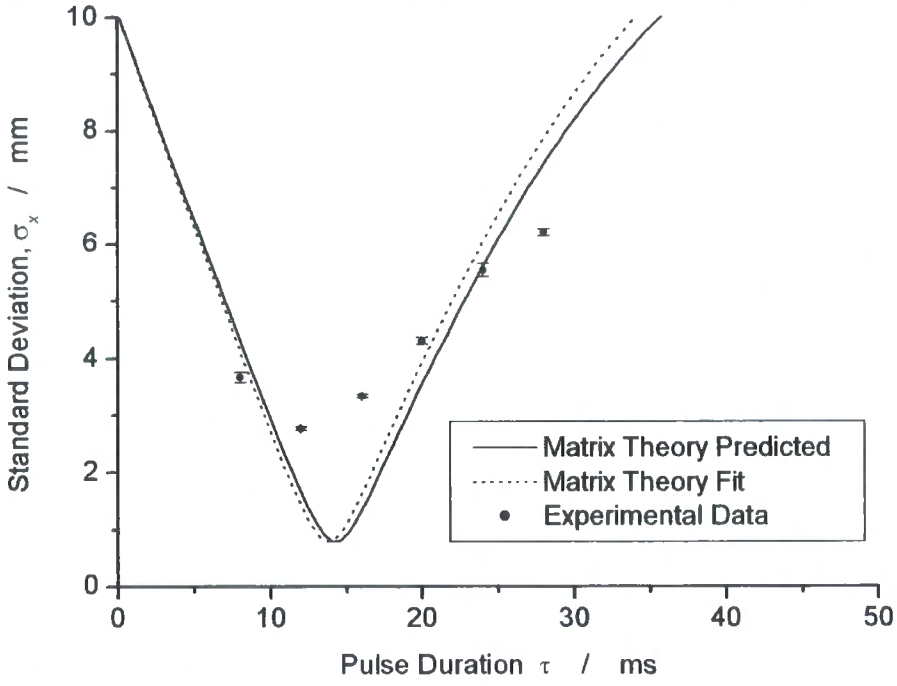

Figure 6.25. Matrix theory prediction and fit to the experimental standard deviation in the x-direction when using the Baseball Lens configured with $R_{\text{TUNE}} = R_{\text{BIAS}}$. The matrix theory prediction using the characterised angular frequency $\omega_x = 38\ \text{s}^{-1}$ is plotted against the experimental data, along with a χ^2 fit to the data using the matrix theory. Only allowing the angular frequency ω to vary for the fit gave a value of $\omega_x = 39\ \text{s}^{-1}$.

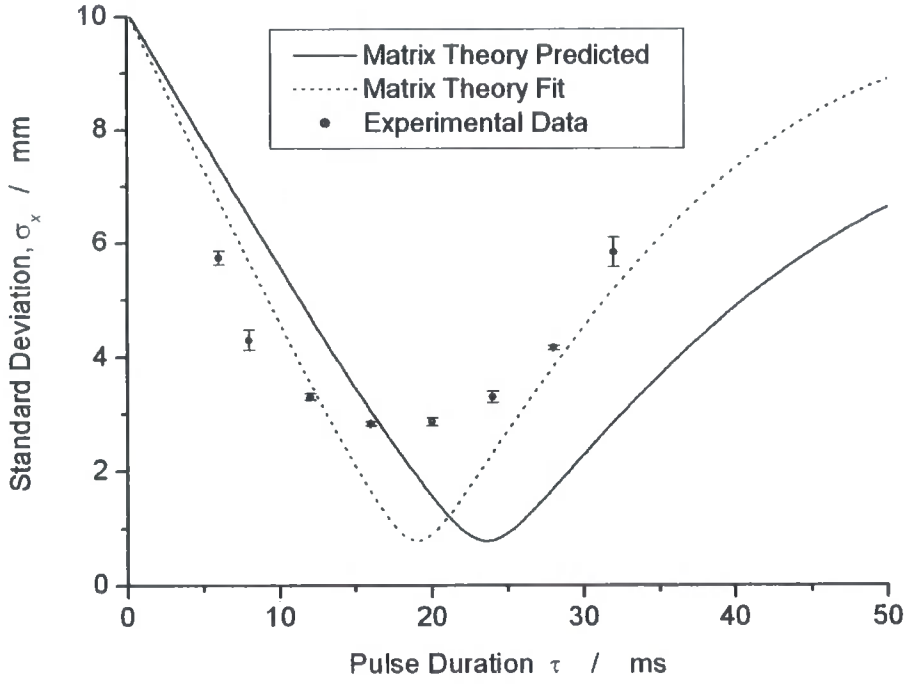

Figure 6.26. Matrix theory prediction and fit to the experimental standard deviation in the x-direction when using the Baseball Lens configured with R_{TUNE} removed. The matrix theory prediction using the characterised angular frequency $\omega_x = 30\ \text{s}^{-1}$ is plotted against the experimental data, along with a χ^2 fit to the data using the matrix theory. Only allowing the angular frequency ω to vary for the fit gave a value of $\omega_x = 33\ \text{s}^{-1}$.

In summary, Table 6.1 displays the predicted and fitted values of the angular frequency ω_x for the four configurations of the Baseball Lens using the $\mathfrak{ABCD}$-matrix approach.

Configuration	Predicted	Fitted
Baseball coil only	50	50
$R_{\text{TUNE}} = R_{\text{BIAS}}/2$	41	44
$R_{\text{TUNE}} = R_{\text{BIAS}}$	38	39
R_{TUNE} removed	30	33

Table 6.1. The predicted and fitted values of the angular frequencies ω_x using an $\mathfrak{ABCD}$-matrix analysis.

6.5.2 Vertical Cloud size

The matrix theory did not account for the variation of the cloud size σ_z with pulse duration τ. In the vertical direction, the minimum cloud size occurred at significantly larger value of τ, and that minimum was significantly larger than that predicted by matrix theory. In section 6.6, the variation of the cloud size in the vertical direction is analysed with numerical simulations as described in chapter 4.

6.6
Numerical Simulations for Analysis

Although $\mathcal{ABCD}$-matrix analysis of the experimental data for the variation of the focussed cloud size proved fruitful for the horizontal (x) direction, it did not account for the behaviour of the focussed cloud in the vertical (z) direction. Therefore, numerical simulations of the experiment were performed, as described in chapter 4 and Pritchard *et al.* [3].

Simulations were performed, using Wolfram Research Inc.'s *Mathematica*, to plot the variation in the spatial standard deviation of a focussed cloud (at the apex of flight) against the pulsed magnetic lens duration τ. The $\mathcal{ABCD}$ matrix formalism uses an ideal parabolic potential. However, by modelling the Baseball Lens as current bars and coils, magnetic aberrations arising due to the departure of the real potential from the parabolic potential can be included. The cloud and its motion were treated classically, and for the atomic densities encountered in the expanding cloud, the collision rate is negligible. The atoms were simulated to travel on ballistic trajectories, except when the lens is turned on, in which case the full Stern–Gerlach force is included in the numerical integration.

The trajectories of 250 atoms were followed (for the following simulations, higher numbers of atoms took many hours to simulate). The initial spatial standard deviations were chosen to be those found in the experiment ($\sigma_{x_0} = 1.01 \pm 0.01$ mm and $\sigma_{z_0} = 0.97 \pm 0.01$ mm). The initial velocity distribution was defined by the static molasses temperature of the central launch detuning and launch intensity (25 ± 2 μK). The baseball coil was constructed from eight equal-length, straight, infinitesimally-thin conductors, which ignored the finite extent of the conductors in the 3×3 array of the real lens. The bias coils were modelled as single current loops, rather than the 2-turn coils in the experimental lens. However, these simulated constructs were instilled with the full $9 \times I'$ current-turns (for the experimental baseball coil) and the $2 \times I$ current-turns (for each bias coil) that were measured in section 5.5.

6.5.1 Horizontal Cloud Size: Numerical Simulations

Figure 6.27 show the experimental data and the matrix theory prediction for the Baseball Lens utilising the baseball coil only. Also shown is a numerical simulation

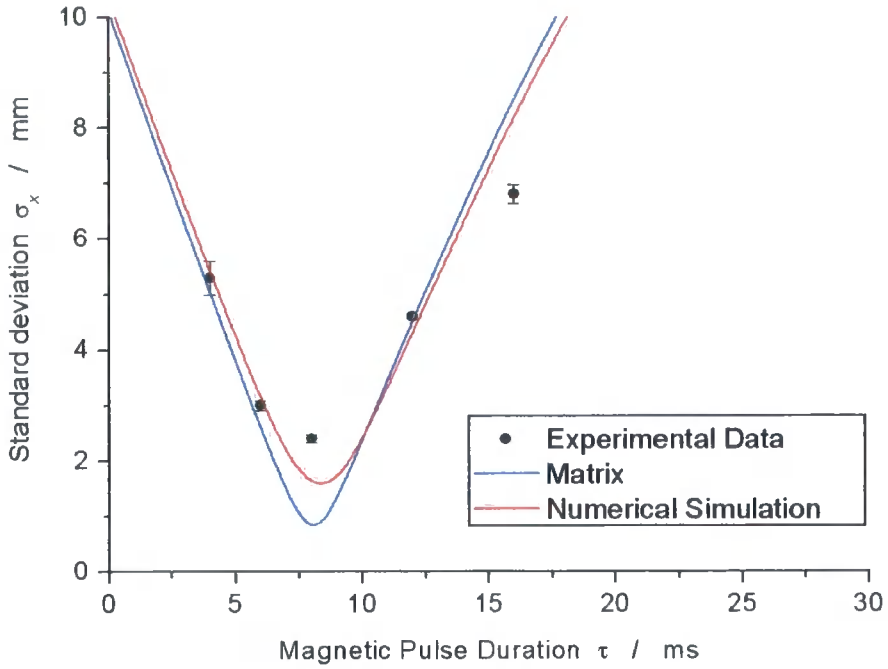

Figure 6.27. Numerical simulation of the variation of the standard deviation in the x-direction when using the baseball coil only. The matrix theory prediction using the characterised angular frequency $\omega_x = 50\,\mathrm{s}^{-1}$ is also plotted along with the experimental data. The numerical simulation (of an ideal Baseball Lens) shows that magnetic aberration has a significant effect upon the minimum obtainable cloud size. It is likely that the experimental lens has significantly more magnetic aberration than the ideal Baseball Lens due to construction imperfections.

of a launched cloud of 250 atoms subject to differing magnetic pulse duration τ. The matrix theory predicted a minimum cloud size significantly less than found in the experimental data. The numerical simulation (of an ideal Baseball Lens) shows that magnetic aberration has a significant effect upon the minimum obtainable cloud size. It is likely that the experimental lens has significantly more magnetic aberration than the ideal Baseball Lens due to construction imperfections.

For both the lens configurations of $R_{\mathrm{TUNE}} = R_{\mathrm{BIAS}} / 2$ and $R_{\mathrm{TUNE}} = R_{\mathrm{BIAS}}$, the numerical simulations make significant improvement in fitting the minimum cloud size over the

matrix analysis. The predictions of the numerical simulations for the configurations $R_{\mathrm{TUNE}} = R_{\mathrm{BIAS}} / 2$ and $R_{\mathrm{TUNE}} = R_{\mathrm{BIAS}}$ can be seen in Figures 6.28 and 6.29 respectively.

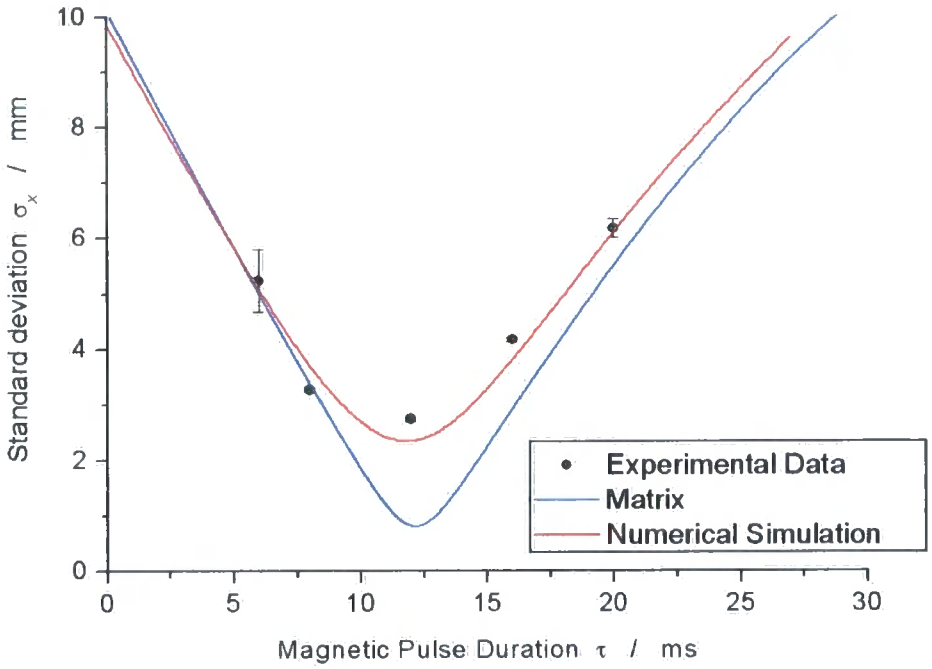

Figure 6.28. Numerical simulation of the variation of the standard deviation in the x-direction when using the Baseball lens in the configuration with $R_{\mathrm{TUNE}} = R_{\mathrm{BIAS}} / 2$. The matrix theory prediction using the characterised angular frequency $\omega_x = 41\,\mathrm{s}^{-1}$ is also plotted along with the experimental data. The numerical simulation (of an ideal Baseball Lens) shows that magnetic aberration has a significant effect upon the minimum obtainable cloud size in comparison to the ideal parabolic potential of the matrix analysis.

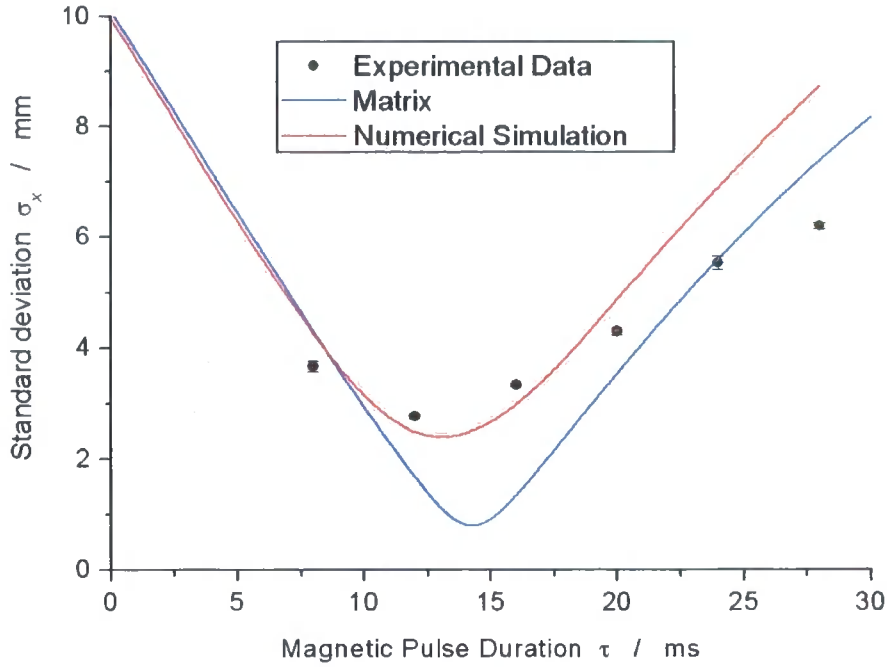

Figure 6.29. Numerical simulation of the variation of the standard deviation in the x-direction when using the lens in the configuration with $R_{\text{TUNE}} = R_{\text{BIAS}}$. The matrix theory prediction using the characterised angular frequency $\omega_x = 38\ \text{s}^{-1}$ is also plotted along with the experimental data. The numerical simulation (of an ideal Baseball Lens) shows that magnetic aberration has a significant effect upon the minimum obtainable cloud size in comparison to the ideal parabolic potential of the matrix analysis.

In the case of the lens configuration with R_{TUNE} removed, the matrix analysis predicted that the minimum value of the standard deviation should occur at a greater value of τ than the experimental data depicted. This could have been put down to the error bars upon the characterisation and the effects of building an experimental lens. However, the numerical simulation of the ideal Baseball lens in the configuration with R_{TUNE} removed provides not only a solution with a greater minimum standard deviation (an effect expected due to lens aberrations), but also a minimum in standard deviation that occurs at a lower value of τ. The numerical simulation is remarkably in-line with the experimental data in comparison to the matrix theory. Figure 6.30 shows the experimental data along with the numerical simulation and the matrix theory prediction.

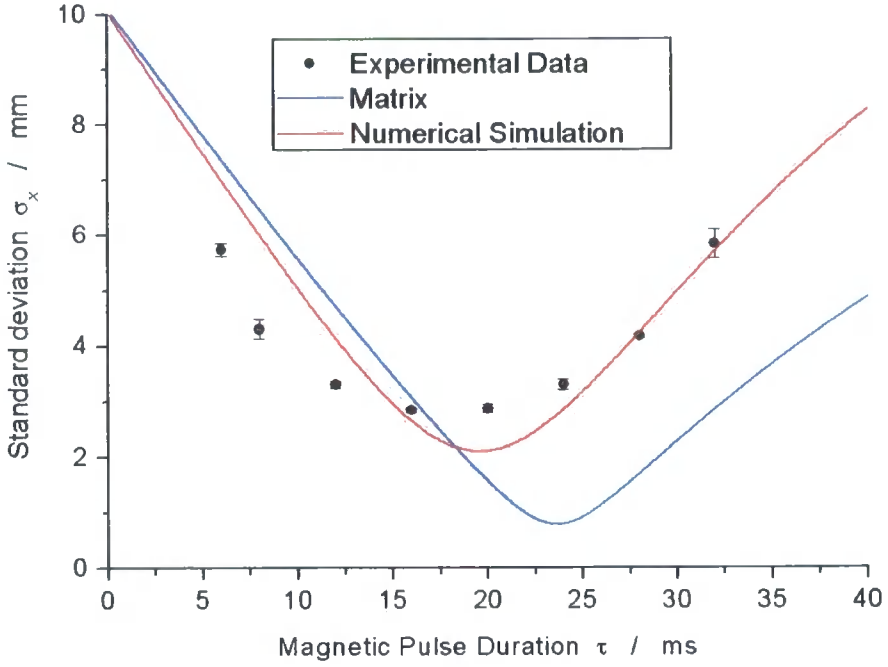

Figure 6.30. Numerical simulation of the variation of the standard deviation in the x-direction when using the lens in the configuration with R_{TUNE} removed. The matrix theory prediction using the characterised angular frequency $\omega_x = 30\,\text{s}^{-1}$ is also plotted along with the experimental data. The numerical simulation (of an ideal Baseball Lens) is more in-line with the experimental data than the matrix theory. The numerical simulation shows a minimum cloud size that is both greater and occurring at a lower value of τ, characteristics also shown by the experimental data.

6.5.2 Vertical Cloud size

In the vertical (z) direction, the minimum cloud size occurs at a significantly larger value of τ than that predicted by an $\mathcal{ABCD}$-matrix analysis. For that reason, numerical simulations (as described above) were performed to aid the analysis of the situation. However, numerical simulations of the ideal Baseball Lens including magnetic aberrations do not account fully for the experimentally observed relationship between the standard deviation in the vertical (z) direction and the pulse duration τ. Therefore, other factors were considered.

Figure 6.31 shows the experimental data obtained using the lens in the configuration with R_{TUNE} removed for the standard deviation in the vertical (z) direction, σ_z, as a

function of τ. Also shown is a numerical simulation using the ideal Baseball Lens and the curve predicted by matrix theory using the characterised angular frequency $\omega_z = 38\ s^{-1}$. As can be seen, neither of these attribute the shape nor the values obtained for σ_z. The axial curvature of the simulated ideal Baseball Lens is given by the axial curvature of the baseball coil. However, in the case of the experimental lens, there is an error in the separation S of the bias coils due to the physical construction. A change in S would change the axial curvature of the lens, and hence its focusing properties. In Figure 6.31, a numerical simulation of the ideal Baseball Lens with a 10% decrease in the separation of the bias coils, i.e. $S = 0.9$, is shown. This

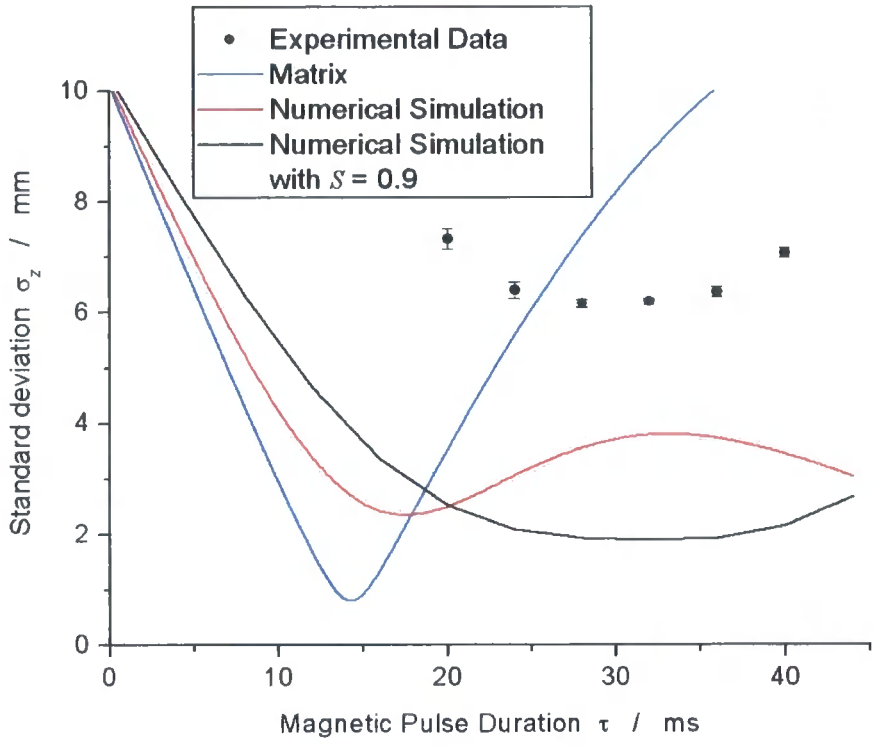

Figure 6.31. Numerical simulation of the variation of the standard deviation in the z-direction when using the lens in the configuration with R_{TUNE} removed. The matrix theory prediction using the characterised angular frequency $\omega_z = 38\ s^{-1}$ is also plotted along with the experimental data. The numerical simulation (of an ideal Baseball Lens) diverges from the matrix solution towards the experimental data, but does not account for the shape or minimum of the data. By decreasing the separation S of the bias coils by 10%, the shape of the experimental data can be more closely matched. However, this does not account for the observed minimum cloud size in the z-direction.

decreased-separation simulation goes some way to account for the shape of the experimental data, but does not account for the measured size. The experimental error on the separation of the bias coils of the experimental lens is estimated to be approximately 6%. The simulation also predicts a minimum standard deviation a factor of three smaller than the observed data. Changing the input values for the initial cloud width σ_{z_0} has little effect on the minimum cloud size and an input temperature of approximately 50 μK is required to account for the minimum observed value. This temperature is twice the estimated temperature, which appears to fit the data for σ_x extremely well. Indeed, using an input temperature of 50 μK predicts values for σ_x that are greater than the observed experimental data.

Since the configuration with R_{TUNE} removed is the case where the error in separation has the greatest effect (since this is the case where most current is passed through the bias coils), the other three lens configurations show considerably worse fits to the experimental data. It is thought that the discrepancy between the fitting of σ_x and the fitting of σ_z has much to do with the motion of the atoms through the lens in the *z*-direction. Indeed, numerical simulations show that, for an ideal Baseball Lens with $\omega_x = \omega_z = 40\ \text{s}^{-1}$, there is a discrepancy between the direction parallel and the direction perpendicular to the motion of the atoms, especially at larger values of τ (Figure 6.32).

At the time of writing of this thesis, the complex issue of the discrepancy between the predictions (both analytical and numerical) for σ_z and the obtained experimental data is an ongoing investigation.

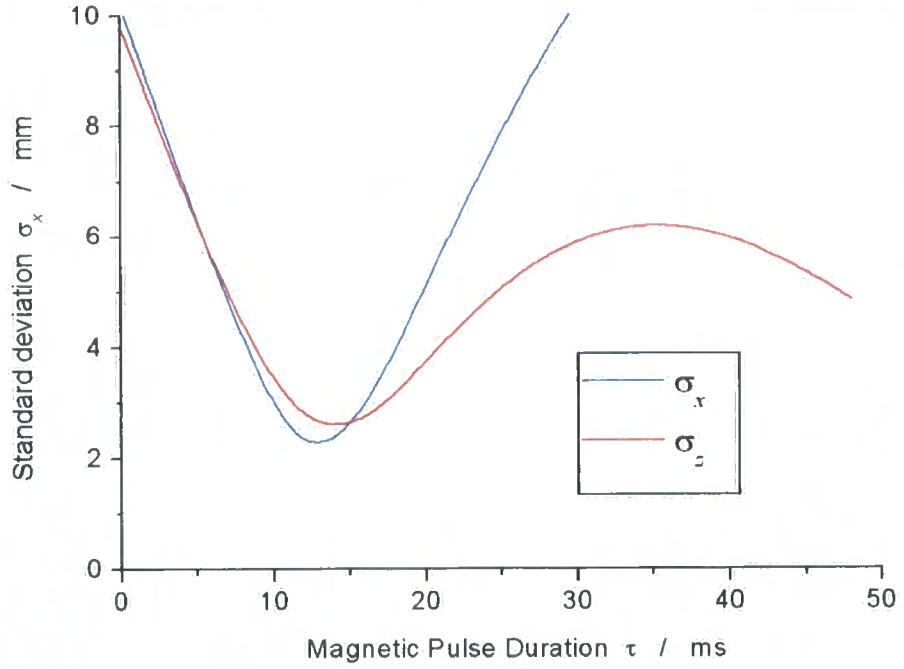

Figure 6.32. Numerical simulation of the variation of the standard deviation using an ideal Baseball Lens with $\omega_x = \omega_z = 40\,\mathrm{s}^{-1}$. For large pulse durations τ, the standard deviation perpendicular σ_x and the standard deviation parallel σ_z to the direction of motion diverge significantly.

[1] É Maréchal, S Guibal, J-L Bossennec, M-P Gorza, R Barbé, J-C Keller and O Gorceix, *Longitudinal Stern-Gerlach effect for slow cesium atoms*, Eur. Phys. J. D **2** 195 (1998)

[2] L Cognet, V Savalli, G Zs K Horvath, D Holleville, R Marani, N Westbrook, C I Westbrook and A Aspect, *Atomic Interference in Grazing Incidence Diffraction from an Evanescent Wave Mirror*, Phys. Rev. A **81** 23 (1998)

[3] M J Pritchard, A S Arnold, D A Smith and I G Hughes, *Single-impulse magnetic focusing of launched cold atoms*, J. Phys. B: At. Mol. Opt. Phys. **37** 4435 (2004)

Chapter 7

Conclusions

Conclusions

In summary, the use of pulsed magnetic lenses with cold atoms was investigated. Specifically, an experiment was designed and built to focus a launched cloud of cold rubidium atoms. An atomic fountain was realised, based on launching a compact cold cloud of atoms using the technique of moving molasses.

Analytical and numerical simulations were conducted to formulate the optimum strategies for focusing. Focusing aberrations are investigated and characterised, and techniques for minimising their deleterious effects were presented.

A Baseball Lens was constructed to enable the experimental 3-dimensional focusing of launched cold atoms with a single magnetic impulse.

Typically 7×10^7 ^{85}Rb atoms were loaded into a magneto-optical trap (MOT), before undergoing an optical molasses stage. Subsequently a moving molasses phase was realised to launch the atoms vertically at a speed of approximately 2 m s^{-1} to bring them to an apex 20.5 cm above the MOT in a remote vacuum chamber. During their flight the atoms were pumped into the weak-field-seeking $5^2S_{1/2}\left|F=3,m_F=3\right\rangle$ state. The centre of the Baseball Lens was located 16.5 ± 0.2 cm above the MOT. Fluorescence images were taken at the apex of flight to characterise the widths of the focussed clouds.

Results were obtained for four different configurations of the Baseball Lens, which varied the relationship between the axial and radial angular frequencies of the lens. Compact focussed clouds were seen for all four configurations with a minimum observed volume of 60 ± 3 mm^3, which is a factor of 17 smaller than the predicted unfocussed cloud volume of approximately 1000 mm^3.

Here, 3-dimensional magnetic focusing of cold atoms with a single-impulse magnetic lens has been observed for the first time.

$\mathcal{ABCD}$-matrix analysis of the experimental data for the variation of the focussed cloud size was in good agreement for the horizontal (x) direction, but did not account for the behaviour of the focussed cloud in the vertical (z) direction. Therefore, numerical simulations of the experiment were performed. The numerical simulations showed very good agreement with the horizontal cloud size, but were not able to account fully for the behaviour of the cloud size in the direction in which the atom cloud had been launched. At the time of the writing of this thesis, the complex issue of the

discrepancy between the predictions (both analytical and numerical) for vertical cloud size and the obtained experimental data is an ongoing investigation.

The results presented here form a method of transferring cold atoms from a MOT to a remote vacuum chamber. This method can be compared to two other very successful transfer mechanisms presented during the time of the work of this thesis. Greiner *et al.* [1] used a train of quadrupole coils to transfer cold atoms through over 30 cm, and around a corner, heating the atoms by less than 20 μK in the process. This compares favourably against the use of pulsed magnetic lenses, which (to gain a high spatial compression at the focus) involves considerable heating of the atom cloud. However, the train of coils requires multiple power supplies and proves more expensive to realise than the pulsed magnetic lens used with three truck batteries that is presented in this thesis.

The second extremely successful transfer mechanism involves the physical movement of a pair of quadrupole coils [2]. Atoms are collected in a MOT before being transferred into a quadrupole trap formed from a pair of coils. The coils are then physically translated using a controllable translation stage. This method does, however, place limitations on vacuum chamber design since enough space must be allowed for the translation mechanism. The pulsed magnetic lens presented in this thesis needs, realistically, only space for the lens itself since the wires for current supply can be easily incorporated.

In this work, spatial focusing was considered. A possible future extension would be to study velocity focusing. A wavepacket with very narrow momentum distribution is ideal for studying quantum tunnelling, and a 1-dimensional narrow momentum distribution could also be useful for other atom optics experiments, such as studying quantum accelerator modes.

The future is bright for pulsed magnetic lenses.

[1] M Greiner, I Bloch, T W Hänsch and T Esslinger, *Magnetic transport of trapped cold atoms over a large distance*, Phys. Rev. A **63** 031401 (2001)

[2] H J Lewandowski, D M Harber, D L Whitaker, E A Cornell, *Simplified system for creating a Bose-Einstein condensate*, J. Low Temp. Phys. **132** 309 (2003)